Intrinsic Dysfunction in Muscle Stem Cells Lacking Dystrophin Disrupts Secondary Myogenesis and Postnatal Muscle Regeneration

Marie Elizabeth Esper

Thesis submitted to the University of Ottawa
in partial fulfillment of the requirements for the
Doctorate in Philosophy in Cellular and Molecular Medicine

Department of Cellular and Molecular Medicine
Faculty of Medicine
University of Ottawa

Abstract

Dystrophin deficiency is the underlying cause of Duchenne Muscular Dystrophy (DMD), a severe neuromuscular disorder characterized by progressive muscle degeneration and a significantly diminished lifespan. While DMD is conventionally understood to manifest postnatally due to cumulative muscle damage, the intrinsic dysfunction of muscle stem cells (MuSCs) also contributes to disease progression. Specifically, the absence of dystrophin-MARK2 interactions in activated MuSCs impairs their polarity, resulting in fewer asymmetric divisions and progenitor cells. However, the role of impaired MuSC polarity in muscle development and regeneration has not been extensively studied *in vivo*. Here, we describe the consequences of MuSC dysfunction during fetal, neonatal, and regenerative myogenesis using the *mdx* mouse model of DMD. We first characterized disease progression, muscle regeneration, and MuSC function in postnatal muscle. Dystrophin-deficient muscle undergoes progressive changes with age and delayed regeneration in response to acute injury. Moreover, defective MuSC polarity results in fewer progenitor cells at 5 days post-cardiotoxin injury and at neonatal day 7, before chronic inflammation and severe necrosis. We also observe that *mdx* MuSCs exhibit elevated $PAX7^{+}$ cell engraftment with significantly fewer donor-derived myonuclei in regenerated myofibers. We next explored the developmental onset of *mdx* MuSC dysfunction. Examination of *mdx* mouse embryos lacking dystrophin revealed no impairment of the primary myogenic program. By contrast, histological and single cell RNA-sequencing analysis during secondary myogenesis uncovered a reduced proportion of progenitor cells relative to fetal (f) MuSCs, leading to fewer smaller-caliber myofibers. Wild type fMuSCs expressed full-length dystrophin that interacted with MARK2, whereas *mdx* fMuSCs downregulated MARK2 and NUMB and exhibited markedly reduced polarization. Strikingly, deletion of the Numb Associated Kinase, AAK1, restores NUMB

expression in *mdx* fMuSCs and rescues the proportion of myogenic committed progenitor cells in *mdx* fetal muscle. Our data provides evidence that dystrophin deficiency in MuSCs and myofibers contributes to the progression of DMD. We also elucidate an acute disease pathology during DMD fetal development and the potential for therapeutic intervention by targeting MuSC.

Acknowledgements

First, I would like to express my sincere gratitude to my supervisor, Dr. Michael Rudnicki, for his guidance and mentorship throughout my graduate studies. I am extremely thankful for his support of my curiosity and for indulging my occasional adventures down scientific rabbit holes. Thank you for keeping me focused; the freedom to explore and think critically in the lab has been crucial to my growth as a scientist.

I would like to express special appreciation to my thesis advisory committee members, Dr. Rashmi Kothari, Dr. Nadine Wiper Bergeron, and Dr. Pierre Mattar, for their support and guidance throughout my studies. I also extend my gratitude to the principal investigators who generously agreed to serve as examiners during my PhD defence: Dr. Pierre Mattar, Dr. Hanns Lochmüller, Dr. Blair Gage, and Dr. April Pyle.

I would also like to thank all current and former members of the Rudnicki lab for their collaboration, discussions, and friendship. I am genuinely grateful to my mentors for the opportunities, insight, and support they have provided me along my journey. A special thank you to Dr. Alex Lin, a fantastic guide and unwavering supporter of my research – I appreciate all the shared expertise, knowledge, and patience. I would also like to thank Dr. Derek Hall for his invaluable scientific advice, insightful discussions, and exceptional patience throughout the assay optimization process. His expertise and guidance have been instrumental in refining my research and writing my manuscripts. I am also grateful to Dr. Chloë Van Oostende-Triplet and Fernando Ortiz for always making time to provide guidance, support and encouragement. Chloë, thank you for nurturing my love of microscopy and always supporting my research, and Fernando, thank you for tolerating my sometimes-absurd sort schedule. I would also not be where I am today without the unwavering support of my friends and family, who have continuously encouraged me through

the highs and lows of my PhD. To my partner, Mike, my father, George, and huskies, Oscar and Buddy, I could not have done it without you!

I am grateful to have received financial support from the Canada Graduate Scholarship-Masters (CGS M), the Queen Elizabeth II Graduate Scholarship (QEII-GSST), and the Ontario Graduate Scholarship (OGS). I would also like to thank Jennifer Ritchie, Guo Hua Li, and Dallas Bennett for their assistance with animal husbandry, Fernando Ortiz for his help with FACS and flow, Christopher Porter for bioinformatics support, Chloë Van Oostende-Triplet for her microscopy expertise, and Sandy Martino for administrative support. Finally, I would like to acknowledge the following cores that have supported my studies: StemCore Laboratories Genomics Core Facility (RRID:SCR_012601), UOttawa Preclinical Imaging Core (RRID:SCR_021832), UOttawa Cell Biology and Image Acquisition Core (RRID:SCR_021845), and UOttawa Louise Pelletier Histology Core Facility (RRID:SCR_021737).

Copyright Acknowledgment

> **Marie E Esper***, Caroline E Brun*, Alexander YT Lin, Peter Feige, Marie J Catenacci, Marie-Claude Sincennes, Morten Ritso, and Michael A Rudnicki, Intrinsic Muscle Stem Cell Dysfunction Contributes to Impaired Regeneration in the *mdx* Mouse. Journal of Cachexia, Sarcopenia and Muscle. 2025;16(1):e13682. *Contributed equally to this work.

> **Marie E. Esper** ME, Kasun Kodippili, Michael A. Rudnicki. Immunofluorescence Labeling of Skeletal Muscle in Development, Regeneration, and Disease. Methods Mol Biol. 2023;2566:113-132.

Table of Contents

List of Tables

List of Figures

List of Supplemental Figures

List of Supplemental Data Files

Data File S1 Differential gene expression testing of bulk RNA-seq libraries.
Data File S2 GO term analysis of postnatal bulk RNAseq libraries.
Data File S3 Cluster markers for postnatal MuSC libraries.
Data File S4 Cluster markers for combined fetal MuSC libraries.
Data File S5 Myogenic cell subset cluster markers for combined fetal MuSC libraries.
Data File S6 Differentially expressed genes between wild type and *mdx* fetal libraries.
Data File S7 GO terms identified from downregulated genes in *mdx* fetal MuSC libraries.

List of Abbreviations

7-AAD	7-Aminoactinomycin D
Ach	Acetylcholine
ADP	Adenosine diphosphate
AMuSC	Activated muscle stem cell
ANP	Atrial Natriuretic Peptide
ASO	Antisense oligonucleotide
ATP	Adenosine triphosphate
cDNA	Complementary DNA
CTX	Cardiotoxin
DAG1	Dystroglycan
DAPI	4′,6-diamidino-2-phenylindole
DGC	Dystrophin glycoprotein complex
DMD	Duchenne muscular dystrophy
DMD	Dystrophin
DMEM	Dulbecco's modified Eagle's medium
DMSO	Dimethyl sulfoxide
DNA	Deoxyribonucleic acid
DSHB	Developmental Studies Hybridoma Bank
E	Embryonic day
ECL	Enhanced chemiluminescence
ECM	Extracellular matrix
EDL	*Extensor digitorum longus* muscle
EDTA	Ethylenediaminetetraacetic acid
EdU	5-ethynyl-2'-deoxyuridine
EGF	Epidermal growth factor
EGFR	Epidermal growth factor receptor
FACS	Fluorescence-activated cell sorting
FAP	Fibroadipogenic progenitors
FBS	Fetal bovine serum
FGF	Fibroblast growth factor
FGF2	Fibroblast growth factor 2
FiMuSC	Freshly isolated MuSC
fMuSC	Fetal MuSC
FSC	Forward scatter
GFP	Green fluorescent protein
HGF	Hepatocyte growth factor
Hi	High
hiPSC	human induced pluripotent stem cell
HRP	Horseradish peroxidase

IL	Interleukin
ITGA7	Alpha-7 integrin
KCl	Potassium chloride
Lo	Low
MACS	Magnetic activated cell sorting
MARK2	Microtubule Affinity Regulating Kinase
mdx	X chromosome-linked mouse mutant
miRNA	Micro RNA
MLC	Myosin light chain
MOM	Mouse over mouse
MRF	Myogenic regulatory factor
MRF4	Myogenic Regulatory Factor 4
mRNA	Messenger RNA
mRNP	Messenger ribonucleoprotein
mTOR	Mammalian target of rapamycin
MuSC	Muscle stem cell
MyD88	Myeloid differentiation primary response 88
MYF5	Myogenin factor 5
MyHC	Myosin heavy chain
MYOD1	Myogenic differentiation 1
MYOG	Myogenin
NCAM-1	Neural cell adhesion molecule
NF-κB	Nuclear factor-κB
nGFP	Nuclear green fluorescent protein
NGS	Next Generation Sequencing
NLS	Nuclear localisation signal
ns	Not significant
nTdT	Nuclear TdTomato
OCT	Optimal cutting temperature
P	Perinatal day
PAR	Partition-defective
PARD3	Par-3 Family Cogell Polarity Regulator
PAX3	Paired-box protein 3
Pax7	Paired-box protein 7
PBS	Phosphate buffered saline
PCR	Polymerase Chain Reaction
PFA	Paraformaldehyde
PSM	Presomitic mesoderm,
PTB	Phosphotyrosine binding
QMuSC	Quiescent muscle stem cell
RA	Retinoic acid

RIPA	Radio-Immunoprecipitation Assay
RNA	Ribonucleic acid
RNA-seq	RNA-sequencing
ROS	Reactive Oxygen Species
Rsp18	Ribosomal Protein S18
scRNA-seq	Single cell RNA-sequencing
SDS	Sodium dodecyl sulfate
SEM	Standard error of the mean
SSC	Side scatter
siRNA	Silencing RNA
SMASH	Semi-automatic muscle analysis using segmentation of histology
SHH	Sonic hedge hog
STAT	Signal transducer and activator of transcription
TA	*Tibialis anterior* muscle
TBS	Tris-buffered saline
TBST	Tris-buffered saline - 0.1% Tween20
TGF-β	Transforming growth factor-β
TLR	Toll-like receptor
TNF	Tissue necrosis factor
T-tubules	Transverse tubules
VCAM1	Vascular cell adhesion molecule 1
WGA	Wheat germ agglutinin
WT	Wild-type
YFP	Yellow fluorescent protein

Preface

The current body of work was generated during my studies in the Faculty of Medicine at the University of Ottawa. The contents of several of my first author works are included in Chapters 1-5 and in the appendix with permission from the publisher where necessary (see Copyright Acknowledgment).

Content from the publication titled *Intrinsic Muscle Stem Cell Dysfunction Contributes to Impaired Regeneration in the mdx Mouse* was reproduced with permission from Wiley.[1] The results from this publication are included in Chapter 3, where the data is unchanged, but the figure formatting and order have been modified to conform to the current format. Dr. Caroline E. Brun and I are co-first authors, and all listed authors' experimental and intellectual contributions to this paper were significant. My specific contributions include experiment design, animal work, data generation and analysis relating to histology, polarity assays, engraftment and transcriptomic experiments. I also wrote most of the manuscript and revised it during peer review. Co-authors contributed to the results and methodology sections.

Chapter 4 was adapted from the results of a manuscript titled *Intrinsic dysfunction in muscle stem cells lacking dystrophin begins during secondary myogenesis*, by Marie E Esper, Alexander Y. T. Lin, Dallas Bennett, and Michael A. Rudnicki, which is currently under revision for Nature Communications. Michael A. Rudnicki, Alexander Y. T. Lin, and I conceptualized the experiments. The experiments were conducted with the assistance of Alex Lin and Dallas Bennett, who helped with timed mating, genotyping, and larger-scale experiments. Alex Lin and Michael Rudnicki contributed intellectually to writing the manuscript.

This thesis also includes the content of a book chapter submitted to Cold Spring Harbor Perspectives titled *Satellite Cells in Regeneration and Disease*, by Marie E. Esper, John Saber, and

Michael A. Rudnicki. I wrote the chapter, except for the MuSC activation section that was mostly written by John Saber.

Appended is a detailed methods chapter detailing my immunostaining techniques, reproduced with permission from Springer Nature. In this chapter, I optimized the immunostaining assays, wrote the manuscript, and generated the images and illustrations. Kasun Kodippili processed and stained the canine tissues.

List of included work:

- **Marie E Esper***, Caroline E Brun*, Alexander YT Lin, Peter Feige, Marie J Catenacci, Marie-Claude Sincennes, Morten Ritso, and Michael A Rudnicki, Intrinsic Muscle Stem Cell Dysfunction Contributes to Impaired Regeneration in the *mdx* Mouse. Journal of Cachexia, Sarcopenia and Muscle. 2025;16(1):e13682.

  *Contributed equally to this work.
- **Marie E. Esper**, Alexander Y. T. Lin, Dallas Bennett and Michael A. Rudnicki Intrinsic dysfunction in muscle stem cells lacking dystrophin begins during secondary myogenesis. Nature Communication. 2025. *Revisions requested*.
- **Marie E. Esper**, John Saber, Michael A. Rudnicki. Satellite cells in Regeneration and Disease. Muscle Biology; Cold Spring Harbor Perspectives. 2025. *Accepted.*
- **Marie E. Esper** ME, Kasun Kodippili, Michael A. Rudnicki. Immunofluorescence Labeling of Skeletal Muscle in Development, Regeneration, and Disease. Methods Mol Biol. 2023;2566:113-132.

Chapter 1: Introduction

1.1 Skeletal Muscle Structure and Function

Three distinct types of muscle exist in the human body: skeletal, smooth, and cardiac. Skeletal muscle makes up approximately 40% of human body mass and is indispensable for voluntary locomotion, force production, stability, nutrient storage, metabolic processes, and heat production. Individual skeletal muscles consist of organized bundles called fascicles that are composed of long, multinucleated muscle cells known as myofibers. Myofibers, fascicles, and skeletal muscles are contained within complex extracellular matrices (ECM), broadly termed the endomysium, perimysium, and epimysium, respectively, that play both structural and signalling roles (**Figure 1.1A**).[3,4]

The epimysium, a collagen I and proteoglycan-rich ECM, surrounds the entire skeletal muscle and is continuous with the tendons that connect muscle and bone. Enriched in collagens I, III, V, and VI, proteoglycans, and glycoproteins, the perimysium connects surrounding fascicles. Adjacent to myofibers is the endomysium, composed of two compartments, the pericellular basal lamina and the exterior interstitial matrix connecting adjacent myofibers.[4,5] The basal lamina is a matrix of non-fibrous collagen IV, laminin-211, and other matrix proteins, including nidogen and proteoglycans perlecan, agrin, and biglycan. Laminin-211 physically tethers the basal lamina to the myofiber through interactions with the dystrophin glycoprotein complex (DGC), and collagen-IV integrates basal lamina proteins. The exterior interstitial matrix is composed of fibrillar collagens I and III, the microfibrillar collagen VI, elastin, and proteoglycans, including perlecan and decorin.[4–6] Adjacent to myofibers are diverse cell types that are essential for muscle function, adaptation, and maintenance, including motor neurons, immune cells, fibro-adipogenic progenitors (FAPs), endothelial cells, and resident muscle stem cells (MuSCs) (**Figure 1.1A**).[7]

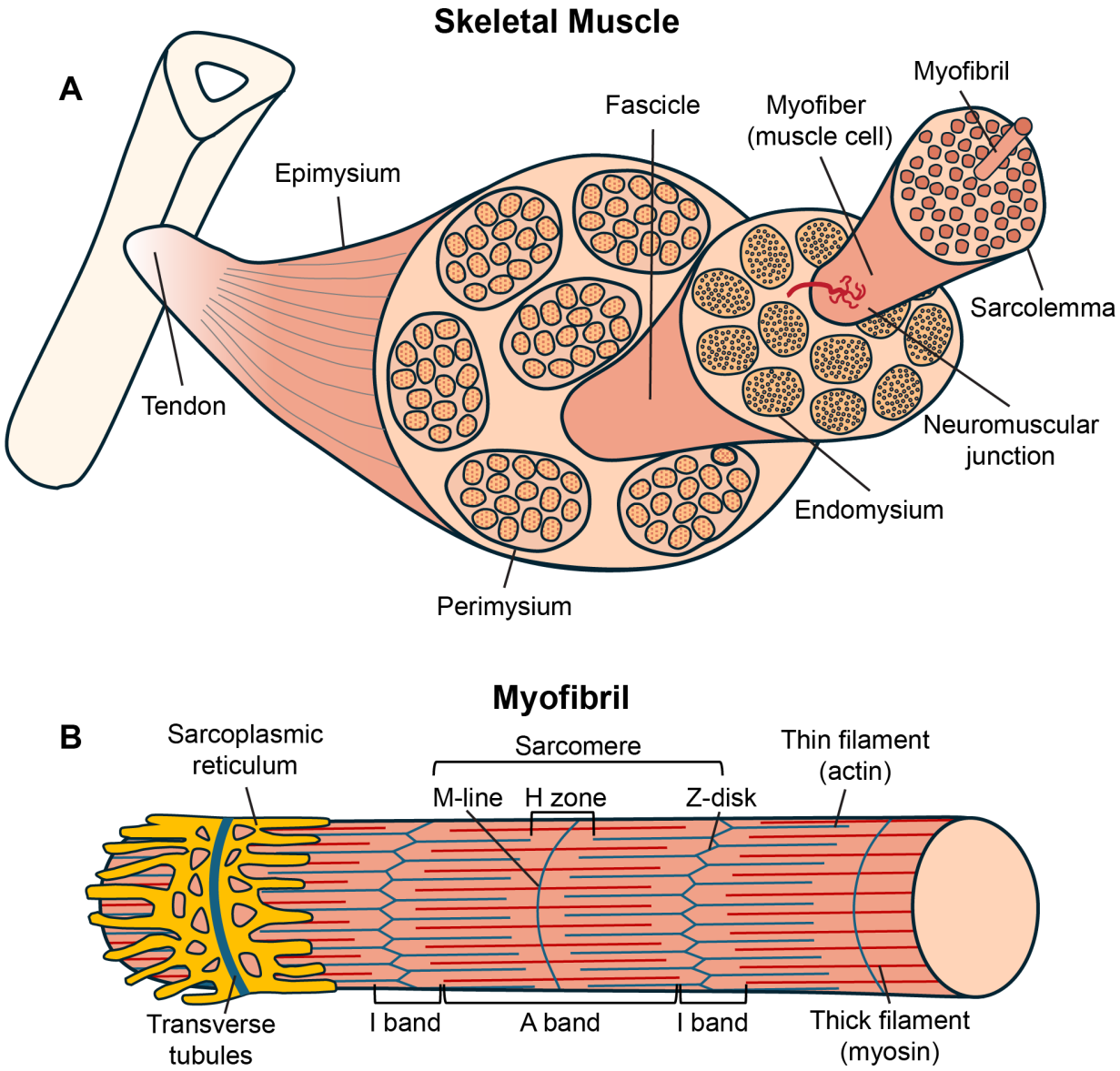

Figure 1.1 Skeletal muscle structure and function.
A Schematic representation of skeletal muscle organization. Three extracellular matrices surround the muscle. The outermost epimysium is continuous with the tendon, anchoring the muscle to the bone. The perimysium surrounds fascicles, and the endomysium encases individual myofibers. Each myofiber contains multiple myofibrils. The neuromuscular junction is the site of myofiber innervation by motor neurons. **B** Structure of a myofibril, the fundamental contractile unit of muscle. Myofibrils are composed of repeating sarcomeres connected at Z-disks. Within each sarcomere, thin (actin) and thick filaments (myosin) are arranged in an iterative overlapping pattern, creating bands that give muscle its striated appearance. The M-line is the center of the sarcomere, connecting myosin filaments and providing structural support to the sarcomere. Myofibrils are encased in the sarcoplasmic reticulum, a tubule network that stores Ca^{2+} ions. Transverse tubules, invaginations of the sarcolemma, propagate action potentials to coordinate muscle contraction. In response to an action potential, the sarcoplasmic reticulum releases Ca^{2+} to induce power strokes, pulling actin towards the M-line and resulting in sarcomere contraction.

Within the myofiber plasma membrane (sarcolemma) are organized stacks of longitudinal myofibrils that give skeletal muscle its striated appearance. Each myofibril consists of linearly joined sarcomeres, the basic functional contractile units in muscle. Transverse (T) tubules are extensions of the sarcolemma that perpendicularly surround myofibrils and facilitate the propagation of electrical signals during muscle contraction. T-tubules are associated with the sarcoplasmic reticulum, another tubular structure that surrounds myofibrils and plays an integral role in muscle contraction (**Figure 1.1B)**.[4]

Sarcomeres are made up of organized stacks of thin and thick filaments that are joined at the Z-disk. Filamentous actin is the major component of the thin filament, interacting with the contraction-related proteins troponin and tropomyosin. The thin filament extends from the Z-disk to the middle of the sarcomere (M-line), which overlaps with the thick filament. The thick filament, spanning the center of the sarcomere (A-band), is mainly composed of myosin II, a hexameric complex containing two myosin heavy chains (MyHCs) and four myosin light chains (MLCs). MyHCs contain catalytic head domains that bind actin and adenosine triphosphate (ATP) (**Figure 1.1B)**. Titin protein filaments stabilize the myosin filaments by extending from the Z-disk to the M-line and help with sarcomere relaxation. Sarcomeres are connected physically to the myofiber basal lamina through actin interactions with costamere protein complexes, namely the DGC and integrin-vinculin-talin complex.[4]

Each myofiber is innervated by a motor neuron at the neuromuscular junction (**Figure 1.1A)**. One motor neuron innervates multiple myofibers, collectively termed the motor unit. When an action potential reaches the motor end plate and sufficient acetylcholine (Ach) is released to induce membrane depolarization, the action potential propagates through the T tubules to the sarcoplasmic reticulum, triggering the release of Ca^{2+}. In resting conditions, tropomyosin is twisted

around the actin filament, inhibiting the binding of myosin cross-bridges to actin. The binding of Ca^{2+} to troponin induces a conformational change that moves tropomyosin away from myosin binding sites. The myosin head then tilts and binds the actin filament, at which time the catalytic cleavage of ATP by the myosin head domain to adenosine diphosphate (ADP) and free phosphate induces a brief dissociation and further hinging of the myosin head relative to the actin filament. The release of free phosphate then causes the power stroke, which pulls actin towards the M-line. Repeat power strokes lead to sarcomere contraction. This process allows myosin to move along the actin filament while ATP is available, pulling the actin filament toward the M-line. Without ATP, the myosin head remains bound to actin.[4]

Muscle fibre type influences the speed and force of muscle contraction and can be categorized into type I slow twitch myofibers and type II fast twitch myofibers. Type I myofibers, characterized by MYH7 expression, have slower ATPase activity and cross-bridging rates that generate reduced force but are resistant to fatigue. These myofibers are highly vascularized, rich in mitochondria and myoglobin, and metabolically rely on oxidative phosphorylation. Conversely, type II myofibers rely heavily on glycolysis, exhibit faster cross-bridging, and are more susceptible to fatigue. In humans, the type II myofibers are either type IIa or type IIx, while small animal models possess type IIa and IIb myofibers. Type IIa myofibers express MYH2 and contract faster than type I fibres but still rely on oxidative phosphorylation. In contrast, type IIb and IIx myofibers, expressing MYH4 and MYH1, are highly glycolytic, contract faster, and are the quickest to fatigue. While myofiber-type composition varies by muscle, nerve innervation, exercise, and hormones modulate fibre-type patterning throughout life.[8]

1.2 Embryonic Origin of Muscle Stem Cells and Skeletal Muscle

Skeletal muscle development occurs in four distinct phases. The first is the myogenic progenitor phase, which spans from conception to approximately embryonic day (E) 9.5 in mice and 5-6 weeks in humans when the first myogenic cells arise. This is followed by two successive waves of *in utero* myogenesis: primary (embryonic) and secondary (fetal) myogenesis. The transition from primary to secondary myogenesis occurs around E14.5 in mice and between 7-12 weeks in humans. Postnatally, neonatal MuSCs contribute to muscle growth through hypertrophy until around 3 weeks in mice (**Figure 1.2A**).[9–11]

The Mesodermal Origin of Skeletal Muscle

During early embryonic development (myogenic progenitor phase), the inner cell mass of the blastocyst generates two cell layers, the external epiblast and internal hypoblast. These two layers form the bilaminar disk, which is positioned between the amniotic sac and the yolk sac (**Figure 1.2B,C**).[12] Gastrulation is the morphogenetic process of epiblast cells migrating and differentiating into the three germ layers, the ectoderm, mesoderm, and endoderm, which together form the developing embryo. Gastrulation is initiated at around E6.25 by formation of the primitive streak in the bilaminar disk, which defines the rostral-caudal axis. Epiblast cells internalize at the primitive streak to form mesoderm and endoderm, while non-migrating cells form the ectoderm (**Figure 1.2A,B**).[12] The mesoderm segments into the axial mesoderm and bilaterally relative to the body axis into the paraxial, intermediate, and lateral mesoderm (**Figure 1.2C**).[9,13] Gastrulation is complete by the end of the myogenic progenitor phase at approximately E9.5 (**Figure 1.2A**).

Skeletal muscle and resident MuSCs of the trunk and limbs originate from the mesenchymal paraxial mesoderm, which segments bilaterally along the neural tube into epithelial structures termed somites. Conversely, multiple mesoderm lineages contribute to the development

of the head and neck muscles.[14,15] Cranial and cervical somites contribute to the formation of the tongue and some neck muscles, while the remaining cranial muscles arise from the unsegmented anterior paraxial mesoderm, the lateral plate splanchnic mesoderm, and the prechordal mesoderm, which is derived from the axial mesoderm (**Figure 1.2C**).[14]

The lateral plate mesoderm differentiates into the splanchnic mesoderm, somatic mesoderm, and extraembryonic mesoderm. The lateral splanchnic mesoderm and the unsegmented anterior paraxial mesoderm collectively form the pharyngeal arches, which serve as a common origin for cardiac and branchiomeric skeletal muscles, including the esophageal, craniofacial, masticatory, and several neck muscles.[16] Other derivatives of the lateral plate mesoderm include the smooth muscle of the gut and vasculature, the appendicular skeleton, and associated connective tissues (**Figure 1.2C**).

The axial mesoderm gives rise to the chordamesoderm, which forms the notochord, and the prechordal mesoderm. The notochord is a transient structure essential for rostral-caudal axial patterning and contributes to the formation of the nucleus pulposus in the vertebral column. The prechordal mesoderm, the most anterior mesodermal structure, contributes to anterior-posterior and ventral-dorsal neural patterning, forebrain formation, and the development of the extraocular muscles (**Figure 1.2C**).[14,17]

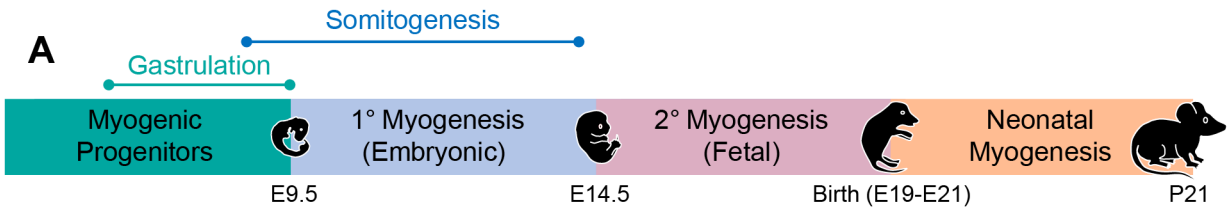

Myogenic Progenitor Phase

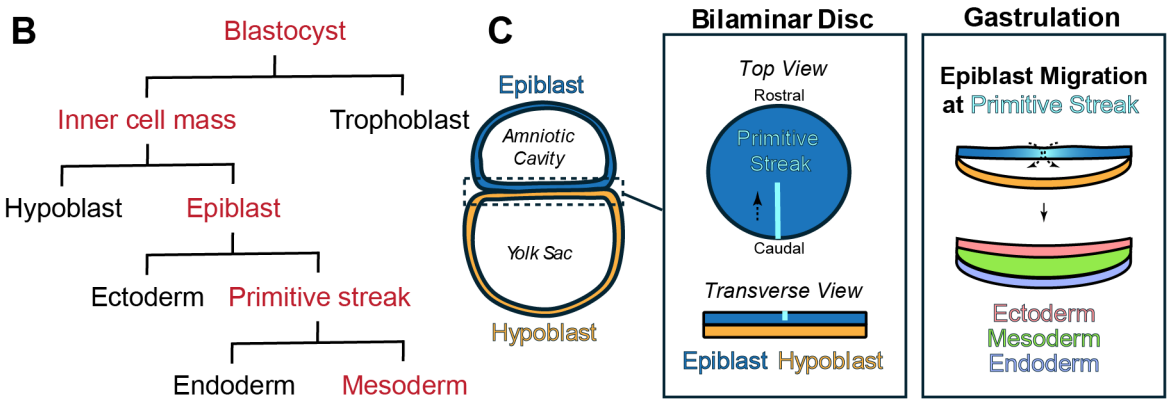

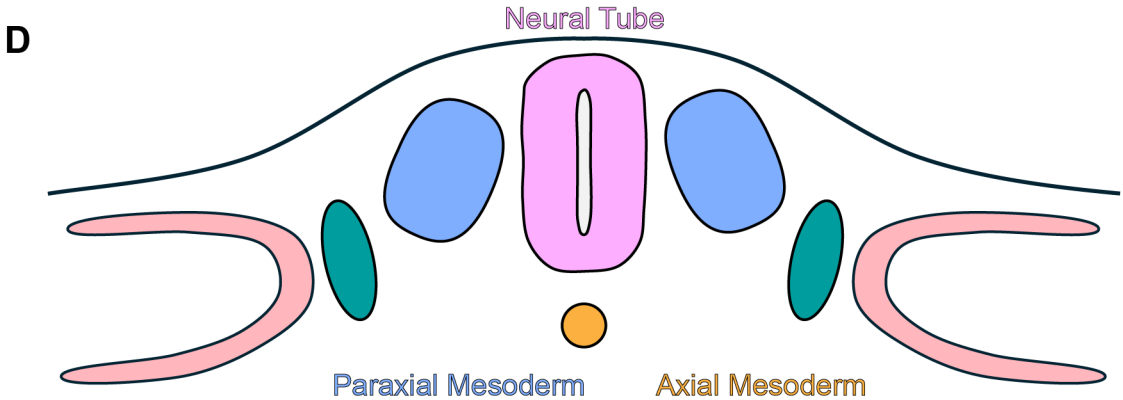

Lateral Plate Mesoderm → Splanchric, Somatic, Extraembryonic (Cardiac muscle, vasculature, smooth muscle, appendicular skeleton, connective tissue)

Paraxial Mesoderm → Somites, Head Mesenchyme (Skeletal muscle, dermis, axial skeleton/connective tissues)

Axial Mesoderm → Chordamesoderm (Notochord), Prechordal (Nucleus pulposus, extraocular muscles)

Intermediate Mesoderm → Urogenital system (Kidney, gonads)

Figure 1.2 Early embryonic origins of skeletal muscle.
A Visual representation of the four distinct phases of mammalian muscle development, with the murine-specific timeline highlighted. Schematic representation of the myogenic progenitor phase is presented in B-D. **B** Origin of mesoderm lineage during the myogenic progenitor phase of embryogenesis. **C** Schematic of epiblast and hypoblast formation during gastrulation. The epiblast and hypoblast layers between the amniotic cavity and the primitive yolk sac form the bilaminar disk. Gastrulation is the morphogenetic process of epiblast cells giving rise to the three germ layers. This is initiated by forming the primitive streak in the bilaminar disk, which defines the rostral-caudal axis. Epiblast cells are then internalized at the primitive streak to form the mesoderm and endoderm. The remaining epiblast cells differentiate into the ectoderm. **D** The mesoderm segments into the axial mesoderm and bilaterally into the paraxial, intermediate, and lateral mesoderm. Paraxial mesoderm gives rise to the skeletal muscle of the body and most head muscles. Extraocular muscles are derived from the prechordal mesoderm.

Paraxial Mesoderm Specification and Somitogenesis

WNT3A and FGF4/8, originating from the primitive streak and maintained in the presomitic mesoderm (PSM), signal paraxial mesoderm specification, maintenance, and elongation by targeting the transcription factors brachyury (T), TBX6, and MSGN1 (**Figure 1.3**).[13,18–22] *T* is the earliest mesoderm marker, followed by *Msgn1* and *Tbx6*, which are maintained in the uncommitted PSM.[23] Somite segmentation from the PSM, termed somitogenesis, occurs in a rostral-to-caudal progression concomitant with posterior PSM elongation, beginning around E8 in mice and 20 days post-fertilization in humans.[24,25] While this process is morphologically and genetically conserved among vertebrates, the rate of somite segmentation varies by species, spanning two hours in mice and six hours in humans.[26] Interestingly, the periodic segmentation of the paraxial mesoderm is intrinsically regulated, occurring independent of surrounding cues.[27]

Somitogenesis is regulated by gradients of WNT3A, FGF4/8, and retinoic acid (RA), along with the oscillating expression of Notch, FGF, and WNT target genes, collectively referred to as the "segmental clock," which progresses anteriorly from the posterior PSM.[28,29] Elevated WNT3A and FGF4/8 maintain the posterior PSM's immature identity and prevent cells from responding to oscillating segmental clock genes.[30–33] Anteriorly, reducing gradients of WNT3A and FGF4/8 reach a permissive threshold where oscillating Notch signalling upregulates the segmentation gene *Mesp2*, marking the new somite boundary.[34,35] This coincides with the downregulation of the mesoderm markers *Msgn1* and *Tbx6* and increased expression of the somite markers *Pax3*, *Meox1/2* and *Foxc1/2* in the soon-to-be segmented anterior PSM.[9,23] Anterior to this threshold, termed the "determination front," is an opposing gradient of RA from the maturing somites that counteracts FGF and WNT signalling, maintains somite symmetry by buffering the left-right body patterning cues, and regulates segmentation genes in some vertebrate species (**Figure 1.3)**.[36–38]

Interacting negative feedback loops in the Notch, FGF, and WNT signalling pathways regulate oscillations in segmental clock genes.[29] While *Notch1* RNA is uniformly expressed in the PSM, the NOTCH1 receptor and its targets *Hes7* and *Lfng* are cyclically expressed in mice.[39,40] The Notch ligand DLL1 activates the NOTCH1 receptor. This leads to the cleavage of the Notch intracellular domain (NICD), which then translocates to the nucleus and initiates the transcription of Notch target genes, including *Lgfn* and *Hes7*. LGFN then inhibits NICD cleavage, contributing to the oscillation of NOTCH1 and downstream signalling in the PSM.[41] FGF-ERK signalling, through FGF receptor 1 (FGFR1), induces expression of the negative feedback genes *Dusp4/6* and *Spry2*.[29,31–33] Further, canonical WNT3A signalling upregulates negative feedback genes, including *Axin2* and *Dkk1*. The regulation of the Notch, FGF, and WNT pathways is also interconnected. HES7 links the Notch and FGF pathways by repressing itself, *Lgfn*, and the FGF targets *Dusp4/6* and *Spry2*. Additionally, the *Hes7* gene is activated by the FGF-ERK cascade. MSGN1 and TBX6, targets of WNT3a and key PSM markers, also regulate Notch signalling by activating genes such as *Notch1*, *Dll1*, *Lfng* (MSGN1), and *Hes7* (TBX6).[42,43] However, oscillations in WNT signalling are likely independent of the *Hes7* negative feedback loop.[44]

Negative feedback loops permit segmental clock oscillation and the rhythmic expression of segmentation genes. *Mesp2* upregulation by Notch is dependent on TBX6, a direct WNT3A target. However, expression of the MESP2 target *Ripply2* leads to suppression of TBX6, which defines the new TBX6-positive anterior PSM border.[35,45] Interestingly, the upregulation of *Mesp2* by Notch also depends on the out-of-phase oscillation of the FGF signalling effector pERK.[37,46] Thus, while high FGF signalling inhibits *Mesp2* expression, low FGF activity is permissive to somite segmentation. This aligns with the finding that Notch and FGF signalling cycle in phase in

the posterior PSM but out of phase anteriorly.[45,46] Conversely, WNT and Notch oscillate out of phase in posteriorly and in-phase in the anterior PSM.[44]

The segmentation of somites requires a mesenchymal-to-epithelial transition that culminates in an epithelial boundary surrounding a mesenchymal centre. Multiple signalling pathways orchestrate the internal polarity and differentiation of somitic cells. In response to sonic hedgehog (SHH) signalling from the notochord and floor plate, the ventral segment of the somite forms the mesenchymal sclerotome, a structure that gives rise to tendons and the axial skeleton. The inhibition of bone morphogenetic protein 4 (BMP4) signalling in the dorsal somite and positive WNT signalling from the neural tube (WNT1/3A) and dorsal ectoderm (WNT6/7A) induces the dorsal somite to form the epithelial dermomyotome, a structure marked by the expression of PAX3 and PAX7 (**Figure 1.3)**. Cells of the dermomyotome give rise to all the skeletal muscle of the trunk and limbs, in addition to brown fat, endothelial cells, vascular smooth muscle, and dermis.[47]

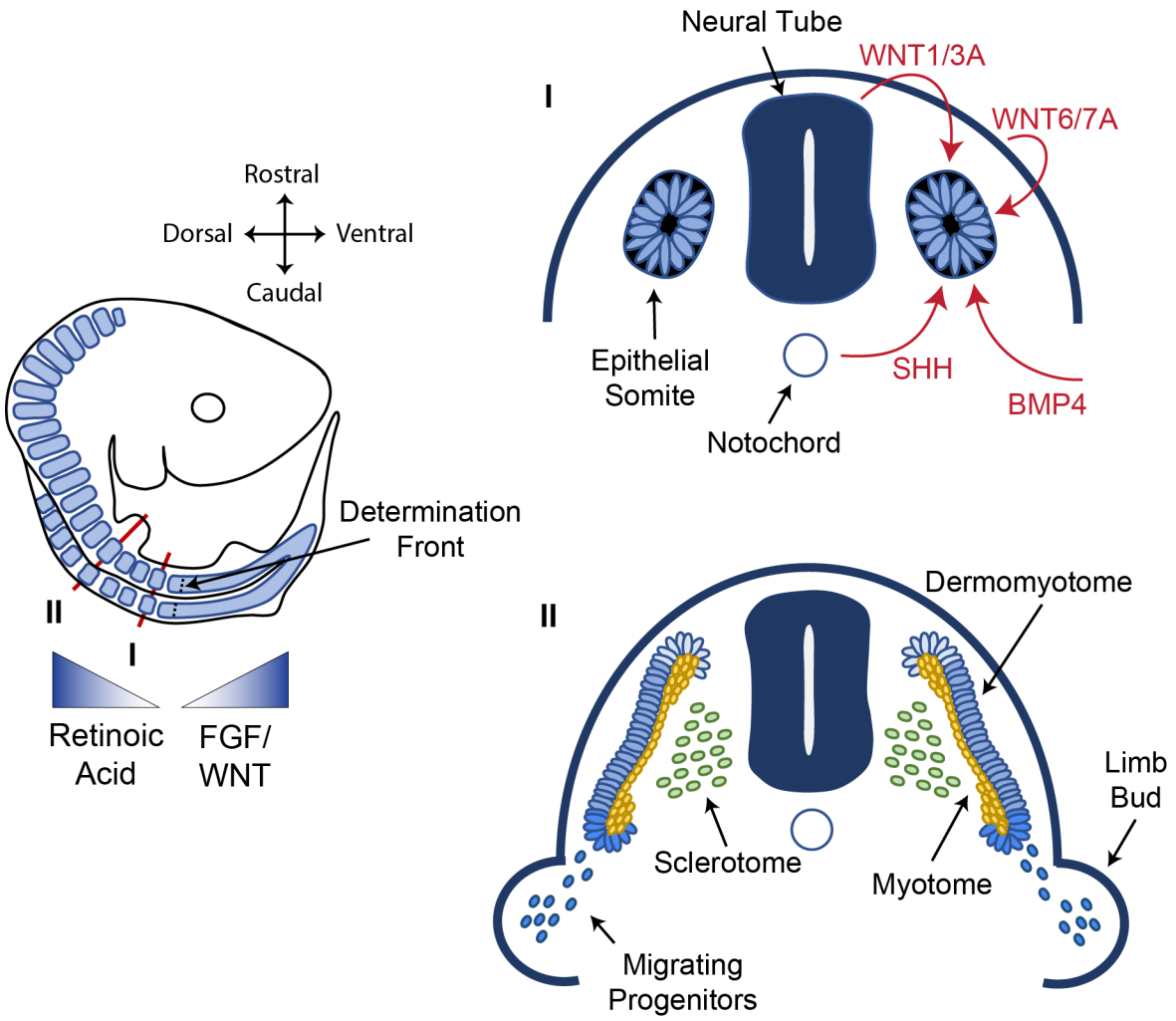

Figure 1.3 Somite formation and differentiation

The lateral view of somite formation illustrates segmentation from the presomitic mesoderm (PSM) in a rostral-to-caudal progression. Gradients of WNT and FGF from the posterior presomitic mesoderm, retinoic acid from the somite, and BMP from the lateral plate regulate the patterning and segmentation of new somites at the determination front. **I,II** Cross-section illustrations of the newly segmented somite. The ventral sclerotome is specified in response to SHH signalling from the Notochord. WNT signalling from the neural tube and dorsal ectoderm specify the dermomyotome. Cells from the dermomyotome translocate and differentiate into the myocytes of the primary myotome, delaminate from the hypaxial edge of the dermomyotome, and migrate to the limbs and trunk.

Skeletal Muscle Development

PAX3 is uniformly expressed in the nascent somite, then restricted to the dermomyotome where it importantly regulates the migration, determination, and self-renewal of myogenic progenitor cells. PAX3-expressing cells first upregulate PAX7 in the central dermomyotome domain, after which PAX3 and PAX7 are both expressed in the epaxial (dorsal medial) dermomyotome while only PAX3 is maintained in the hypaxial (ventral lateral) domain. At the beginning of primary myogenesis, PAX3 and PAX7-positive dermomyotome cells delaminate and differentiate into postmitotic myocytes adjacent to the dermomyotome, forming structures called the primary myotome (**Figure 1.2A** and **Figure 1.3)**. The first myocytes are mononuclear cells that elongate the segmented boundary's length, with myocyte fusion occurring later in primary myogenesis. The primitive muscle structure expands further, serving as a scaffold for subsequent waves of myogenic cell differentiation that form the axial muscles.[48,49] Specifically, the epaxial myotome domain gives rise to the deep back muscles. In contrast, the hypaxial myotome expands, providing the scaffold for newly added myofibers in the body wall, such as the intercostal and trunk muscles.[50,51]

PAX3 and PAX7-expressing cells in the dermomyotome divide asymmetrically, generating committed myogenic progenitor cells that subsequently translocate to the primary myotome. The asymmetric distribution of NUMB and N-cadherin towards the myotome in dermomyotome cell divisions is associated with a committed myogenic cell fate.[52–56] Notch signalling through DLL1 causes dermomyotome cells to delaminate, contribute to the developing myotome, and inhibit premature progenitor cell differentiation.[57,58] Notch signalling also maintains an undifferentiated subset of PAX7- and PAX3-positive dermomyotome-derived cells that later give rise to postnatal MuSCs necessary for muscle maintenance and regeneration.[59] Similarly, BMP4 from the lateral plate mesoderm inhibits differentiation of myogenic progenitor cells, thereby promoting the

expansion of the progenitor pool.[9,60] SHH and WNT signalling are essential in maintaining dermomyotome specification and promoting progenitor cell differentiation.[61] Finally, transforming growth factor-β (TGF-β) signalling through SMAD2/3 slows the fusion of myogenic progenitor cells during the formation of embryonic myofibers.[62]

Undifferentiated PAX3-expressing cells also delaminate from the hypaxial ventral lateral region of the dermomyotome and migrate to form the limb, diaphragm, tongue and pelvic muscles. PAX3 acts upstream of c-MET to induce myogenic progenitor migration from the ventral lateral dermomyotome to the limbs and trunk, which is critical for normal muscle development. This is demonstrated by the deletion of PAX3, precluding the development of the diaphragm and limb muscles. PAX3 also plays a crucial role in the myogenic program by activating the muscle regulatory factor (MRF) genes, *Myf5* and *Myod1*, in the hypaxial somite and limbs. PAX3 binding activates enhancers required for *Myf5* expression and indirectly regulates *Myod1* expression by activating *Pitx2*, a transcription factor that binds to an embryonic *Myod1* enhancer.[50,63,64] Independent of PAX3, SIX1/4 and the cofactors EYA1/2 also directly regulate *Myod1* activation through enhancer regulatory regions.[65] While this is also true for *Myf5* activation, *Myf5* enhancers depend on PAX3 binding.[63] Further, PAX3 regulates FGF signalling by directly binding a *Fgfr4* regulatory element that induces its expression. The loss of PAX3 also leads to the downregulation of SPRY1, an essential inhibitor of premature differentiation and depletion of myogenic progenitor cells.[66]

PAX3 and PAX7 are maintained in postnatal MuSCs of the diaphragm and trunk muscles, while PAX7 becomes the predominant MuSC marker in the hindlimb muscle.[50] Interestingly, while PAX3 and PAX7 have overlapping roles during development, the two transcription factors are not functionally redundant. *Pax7* is not expressed in the hypaxial somite and the early limb buds, while

Pax3 expression is required for muscle development. Conversely, *Pax7* knockout mice undergo normal skeletal muscle development; however *Pax7* is indispensable for specifying and maintaining the postnatal MuSC population.[67–69] The ablation of *Pax7* from MuSC leads to total population loss and complete failure to regenerate postnatal injured muscle.[70–73]

The hierarchical differentiation of myogenic progenitor cells into terminally differentiated muscle cells during embryonic development is coordinated by the expression of MRFs, a family of four basic helix-loop-helix transcription factors that can act as master regulators of myogenesis. *Myf5* is the first MRF expressed during myogenesis, followed by *Mrf4*, *MyoD1*, and *Myog*, which regulate myogenic cell determination, differentiation, and fusion.[49] Despite some key differences, the general hierarchical expression of MRFs during embryonic myogenesis is recapitulated during later phases of muscle development and postnatal muscle regeneration, where *Myf5*, *Myod1*, *Myog* and *Mrf4* are sequentially expressed (**Figure 1.4**). Murine knockout models have largely clarified the roles of the MRFs in the myogenic program.[49]

In mice, the loss of *Myf5* or *Myod1* expression alone does not ablate skeletal muscle development. Instead, developmental delays in epaxial and hypaxial muscle occur in the *Myf5* and *Myod1* mutants, respectively, but reciprocal compensation preserves muscle development.[74–76] Conversely, a severe phenotype is observed in the double *Myf5* and *Myod1* knockout mouse, where the loss of both MRFs abolishes the expression of *Myog* and the formation of skeletal muscle, leading to death shortly after birth.[77] Together, this demonstrated that epaxial and hypaxial myogenic progenitors differentially rely on MYF5 and MYOD1, though both MRFs can reciprocally and functionally compensate. However, it was later demonstrated that the early *Myf5* knockout mouse had compromised *Mrf4* expression due to the adjacent positioning of the genes. In a *Myf5:Myod1* double knockout mouse where *Mrf4* expression is preserved, myotome formation

initiates, suggesting that *Mrf4* plays an upstream role in myogenic lineage specification (**Figure 1.4** and **Figure 1.5**).[78]

As observed in the initial *Myf5:Myod1* double knockout mouse, the ablation of *Myog* leads to neonatal lethality due to severe loss of skeletal muscle. Myoblasts form and organize normally in these mice but never fuse. This demonstrates that MYOG does not regulate muscle lineage specification but rather the later stages of myogenic differentiation and fusion.[79,80] Interestingly, the *Mrf4*:*Myod1* double knockout mouse phenocopies the loss of MYOG, while the muscle of *Mrf4* mutants alone develops normally (**Figure 1.5**). This suggests that *Mrf4* plays a role in both early myotome myogenic lineage initiation and differentiation (**Figure 1.4**),[81,82] and is consistent with the findings in the mouse embryo that MRF4 is first expressed at E9, downregulated at E11.5, and re-expressed at E16.[49]

Interestingly, the loss of Notch signalling through the mutation of *Rbpj* leads to the upregulation of *Myod1* and precocious myogenic cell differentiation and loss of fetal muscle, suggesting MYOD1 plays an essential role in promoting progenitor cell differentiation.[83] However, studies using a $MyoD^{iCre}$ knock-in allele find that nearly all MuSCs express *Myod1* prenatally, suggesting MYOD1 is a myogenic cell determination factor, not only a regulator of differentiation.[84] Later studies demonstrated that MYOD1 and HES1 are expressed in an oscillatory manner. Oscillating MYOD1 expression promotes myogenic cell proliferation while sustained expression induces differentiation, again suggesting that MYOD1 plays multiple roles in lineage specification, proliferation, and differentiation.[85]

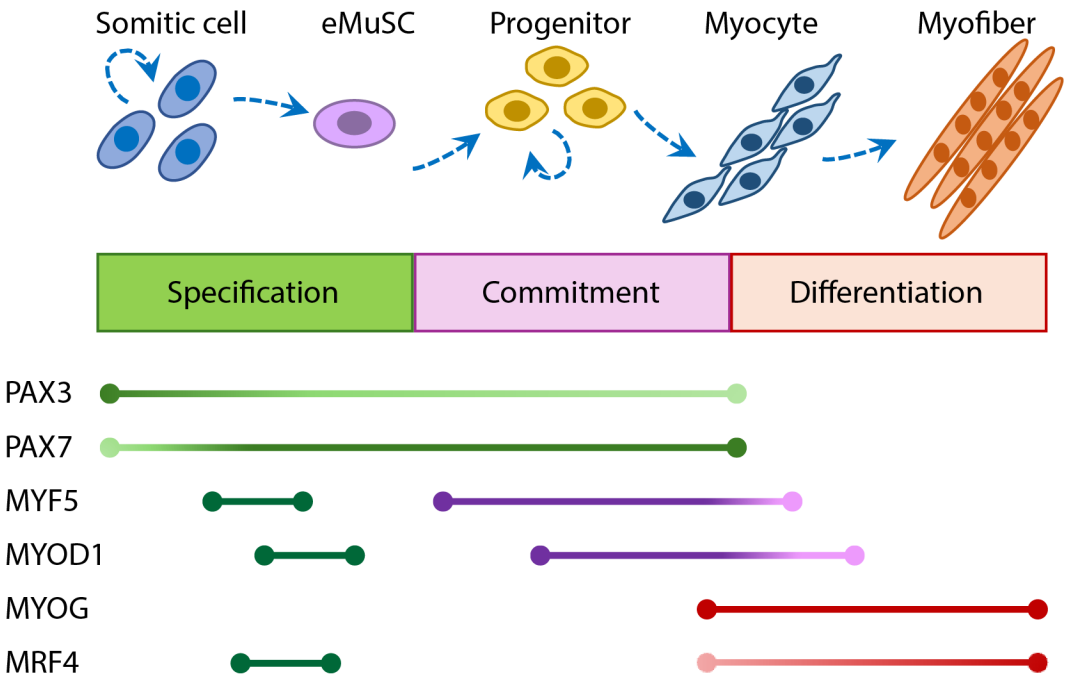

Figure 1.4 Hierarchy of transcription factors coordinates embryonic myogenesis.
The hierarchical differentiation of embryonic muscle stem cells (eMuSCs) into terminally differentiated muscle cells is coordinated by the expression of muscle regulatory factors (MRFs). *Myf5* is the first MRF expressed during murine myogenesis at E8.5, followed by *Mrf4* around E9.5, and *MyoD1* and *Myog* around E10.5. *Myf5*, *Mrf4*, and *Myod1* regulate myogenic lineage specification during myotome formation, while *Myod1* and *Myog* coordinate differentiation. *Mrf4* expression is briefly expressed during myotome specification and is re-expressed later in development, where it coordinates myogenic cell differentiation and fusion. The hierarchical expression of *Myf5*, *Myod1* and *Myog* is recapitulated in postnatal muscle regeneration.

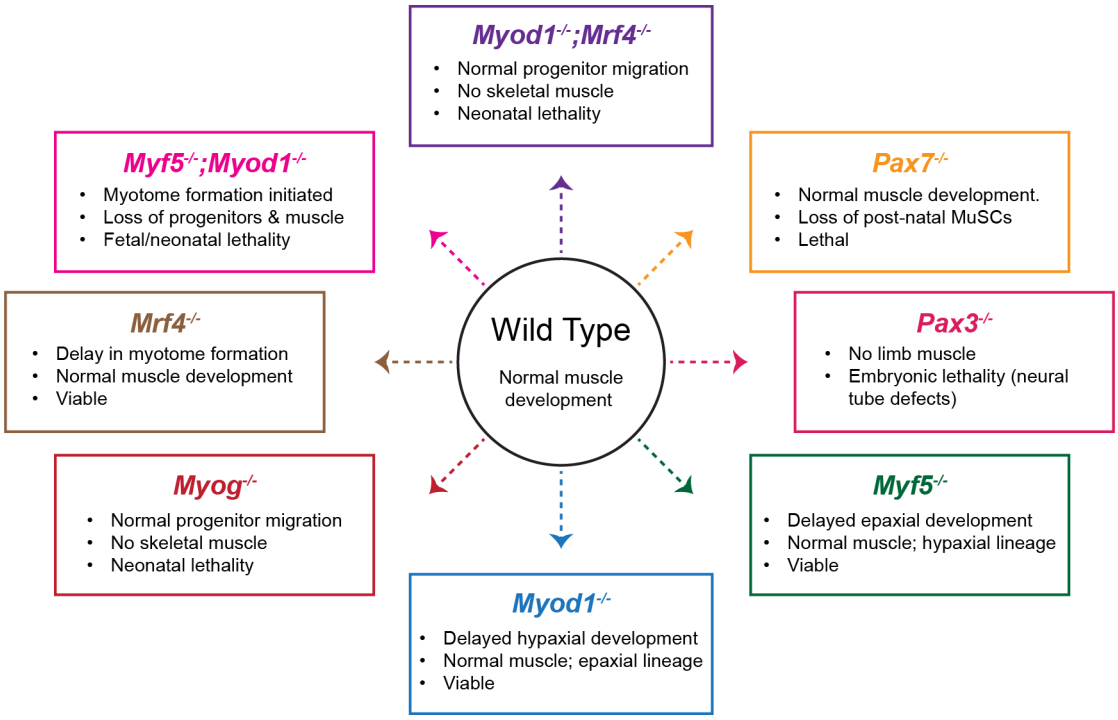

Figure 1.5 Summary of knockout models during development.
Diagram summarizing the effects of *Pax3*, *Pax7* and muscle regulatory factor (MRF) null mutations on muscle development. *Myf5*, *Mrf4* and *Myod1* play roles in myogenic cell specification during myotome formation, while *Myod1* and *Myog* are required for myogenic cell differentiation. *Pax3* is required for hypaxial myogenic cell migration and, thus, the formation of distal muscle. While not necessary for myogenic cell development, *Pax7* is required to maintain the postnatal MuSC pool and sustain muscle regeneration.

Developmental myogenesis occurs in two waves, termed primary (embryonic) and secondary (fetal) myogenesis, beginning at E9.5 and E14.5, respectively, in the mouse embryo (**Figure 1.6**). Primary myogenesis begins when PAX3- and PAX7-positive cells differentiate into myocytes of the primary myotome, and PAX3-expressing migrating progenitors generate primary myofibers at their destination in the body wall and limb buds. These fibres provide the scaffold and patterning for myofiber formation during secondary myogenesis. Interestingly, while all myogenic progenitor cells of the body are of somitic origin, the embryonic and fetal lineages have distinct gene expression profiles and behaviours. Primary myofibers express the embryonic MyHC isoform (MYH3) alongside slow MyHC (MYH7). By contrast, secondary myofibers express embryonic and neonatal (MYH8) MyHC, which shares high sequence homology with adult fast MyHCs (**Figure 1.6**).[8,86–88] Similarly, *in vitro* myoblasts derived from E11.5 and E16.5 *Myf5*-expressing cells form myotubes expressing genes related to slow and fast myofibers, respectively.[89]

Cultured embryonic and fetal myoblasts also exhibit different fusion competencies, proliferation, differentiation, and responses to myogenesis inhibitory signalling.[89] Consistent with *in vivo* observations,[48] embryonic myoblasts give rise to organized mononuclear myocytes and myotubes with few nuclei that do not contract. Conversely, multinuclear fetal myotubes contract spontaneously in culture. Moreover, embryonic and fetal myoblasts are more likely to fuse to their lineage; embryonic myoblasts are more prone to differentiation and are less proliferative compared to fetal myoblasts; and only fetal myoblasts differentiation is inhibited by TGF-β1, TPA and BMP4 signalling.[89] Profiling the transcriptome of GFP^+ cells freshly isolated from E11.5 and E16.5 $Myf5^{GFP\text{-}P\ /+}$ tissues also highlights key differences. As seen *in vitro*, fetal myoblasts express upregulated genes associated with TGF-β and BMP4 signalling pathways and adhesion genes, such

as integrins and laminins. In contrast, embryonic myoblasts express the TGF-β signalling inhibitors *Smad6* and *Smad7,* as well as genes involved in embryonic patterning.[89]

Embryonic myoblasts express SOX6, which positively regulates the expression of slowhcyHC (*Myh7*) through binding the *Mef2c* promoter.[90] The transcription factor nuclear factor one X (NFIX) functions as a switch from the embryonic to the fetal myogenic programme and is activated by PAX7 in fetal myogenic progenitor cells around E14.5. NFIX subsequently initiates the transcription of fetal muscle fibre genes, including *Mck* (muscle creatine kinase) and *Eno3* (β-enolase) and represses embryonic genes.[91] Specifically, NFIX cooperates with SOX2 during secondary myogenesis to suppress the expression of *Myh7*, demonstrating a different role for SOX2 in embryonic and fetal progenitors.[90] NFATC2 also cooperates with MYOD1 to initiate the expression of *Myh8* during secondary myogenesis.[92] Consistent with the upregulation of adhesion genes in fetal myogenic cells compared to embryonic cells, primary myogenesis occurs without a continuous basal lamina. This laminin-rich structure appears later during secondary myogenesis and is required for adult muscle regeneration.[93]

Lineage tracing studies using mouse embryos and chicken-quail chimeras convincingly demonstrate that postnatal MuSCs originate from $PAX3^+$/$PAX7^+$ dermomyotome cells, rather than from separate lineages, as previously suggested.[94–97] $PAX7^+$ cells take positions under the basal lamina in a Notch-dependent process around E16.5 in mice, where MuSCs remain postnatally.[83,94,95] Neonatal muscle growth is driven by myofiber hypertrophy, with the contribution of new myonuclei by neonatal MuSCs until 3 weeks of age, after which muscle growth occurs through protein synthesis.[11,98] Although active during early postnatal development, MuSCs gradually enter quiescence, becoming the resident stem cells responsible for maintaining and repairing adult muscle. At birth, approximately 32% of myogenic nuclei are MuSCs, declining

to around 4% in the adult mouse.[99] By around 8 weeks of age, the majority of MuSCs are quiescent.[100]

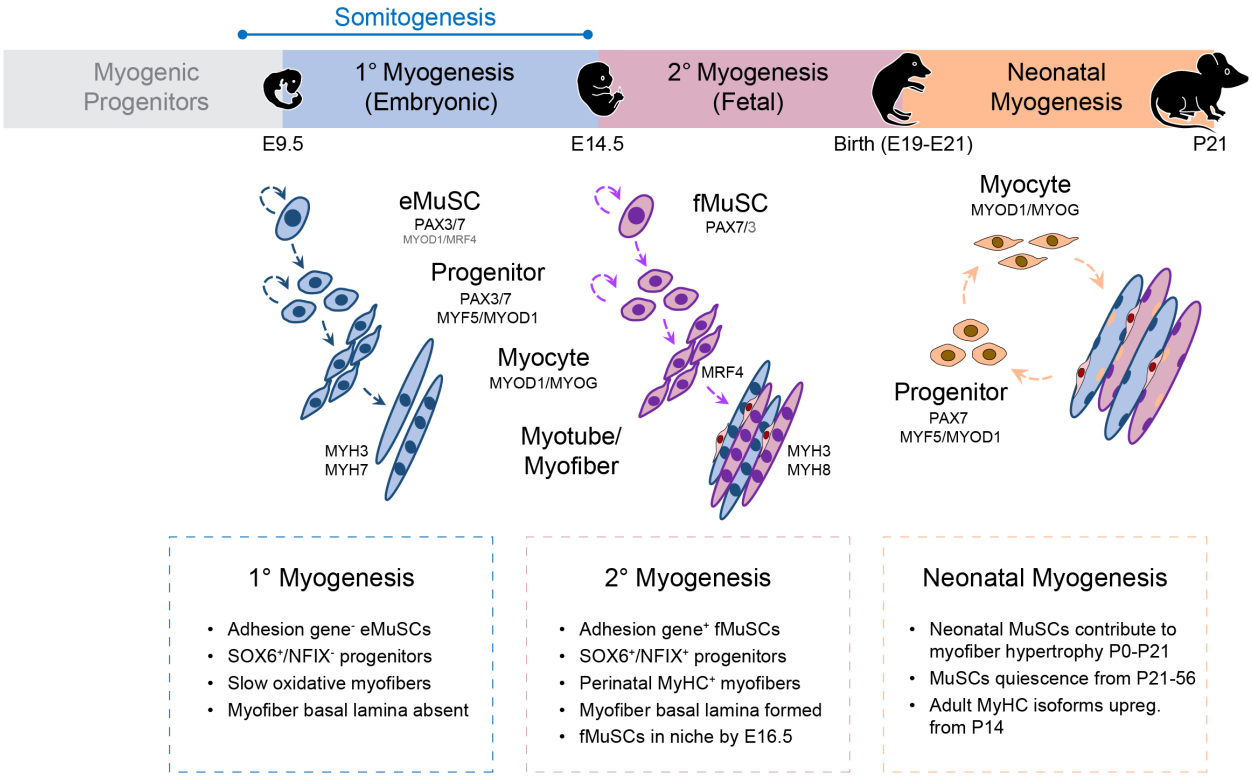

Figure 1.6 Stages of myogenesis in the embryo and fetus.
The differentiation of embryonic (e) and fetal (f) muscle stem cells (MuSCs) into terminally differentiated muscle cells occurs in two *in utero* waves, termed primary (embryonic) and secondary (fetal) myogenesis. $PAX3^+$ and $PAX7^+$ cells first differentiate into mononuclear myocytes of the primary myotome, and $PAX3^+$ migrating cells differentiate into primary myofibers in the body wall and limb buds. Primary myocytes become multinucleated during the later stages of primary myogenesis, providing the scaffold and patterning for secondary myofibers. Both eMuSCs and fMuSCs originate from the somites but are characteristically and functionally distinct and give rise to unique myofibers. Primary and secondary myofibers express MYH7 and MYH8, respectively. The transcription factor NFIX, in cooperation with SOX6, regulates the transition from primary to secondary myogenesis. After birth, neonatal MuSCs contribute to muscle growth by myofiber hyperplasia until P21, after which muscle growth occurs by protein synthesis. Myonuclei number plateaus around P21, coinciding with increased expression of adult MyHC isoforms. MuSCs quiescence is established around P21 and reaches adult levels by P56.

1.3 Postnatal Skeletal Muscle Stem Cells

In healthy individuals, skeletal muscle undergoes slow but continuous protein turnover with basal muscle maintenance and repair levels. This is accomplished through the fusion of intracellular vesicles,[101] and myogenic progenitors with damaged myofiber membranes. MuSCs, also termed satellite cells for their niche position between the myofiber plasma membrane and the basal lamina, are the source of myogenic progenitor cells that contribute to a weekly myonuclei turnover of 1-2% and have a remarkable ability to regenerate skeletal muscle following severe injury (**Figure 1.7A**).[102]

Following injury or exercise, quiescent MuSCs enter the cell cycle to generate self-renewing MuSCs and committed progenitor cells. Committed MuSCs proliferate as progenitors, differentiate into myocytes, and fuse with damaged myofibers (**Figure 1.7A**). The balance between MuSC self-renewal and commitment is a delicate interplay of intrinsic and extrinsic niche factors, and disruptions in these mechanisms can lead to functional impairment.[103]

MuSC Quiescence

Quiescent MuSCs are characterized by the expression of PAX7, low metabolic rates, fatty acid oxidation, cell cycle repression, elevated adhesion and ECM gene expression, and specific cell surface proteins, such as hematopoietic progenitor cell antigen (CD34), vascular cell adhesion molecule 1 (VCAM1), mesenchymal-epithelial transition factor (c-MET), β1-Integrin (ITGB1), α7-Integrin (ITGA7), C-X-C chemokine receptor type 4 (CXCR4), m-cadherin (CDH15), n-cadherin (CDH2), calcitonin receptor (CALCR), and Syndecan3/4 (SDC3/4) (**Figure 1.7A**).[103] A complex interplay between intrinsic and niche signalling mechanisms maintains MuSC quiescence.

MuSCs, expressing NOTCH1, NOTCH2 and NOTCH3, rely on DLL4 ligands from myofibers and endothelial cells to maintain quiescence (**Figure 1.7**).[104,105] Quiescent MuSCs mediate their proximity to vasculature through the expression of VEGFA.[106] Interestingly, a recent study found that the microvascular endothelium upregulates and releases soluble DLL4, which acts on NOTCH2 receptors in the myofiber.[107] This suggests that DLL4 from endothelial cells may act in a juxtacrine and paracrine fashion on MuSC Notch receptors to maintain quiescence. Regardless of the ligand's origin, downstream Notch signalling is critical for MuSC quiescence.

The loss of canonical Notch signalling leads to precocious differentiation and depletion of the MuSC pool, while overexpression of Notch inhibits the myogenic program. Similarly, the expression of Notch receptors and target genes in quiescence is progressively lost during myogenic differentiation.[108–111] Canonical signalling through NOTCH1 inhibits cell cycle entry and MYOD1 expression, in addition to the upregulation of *Pax7* through direct RBPJ binding to the *Pax7* promoter.[110] Interestingly, NOTCH1/RBPJ-bound regulatory elements are also located near collagen V and collagen VI genes in MuSCs, and collagen-V produced by MuSCs autonomously regulates quiescence through interactions with CALCR on MuSCs.[112] Notch similarly regulates basal lamina assembly in the MuSC niche, as fetal MuSCs never take up their niche in the Notch signal mutant model.[83] Notch also regulates MuSC quiescence through microRNA (miRNA) mechanisms.

Many miRNAs are upregulated in quiescent MuSCs, and the loss of the miRNA processing machinery causes MuSCs to enter the cell cycle.[113] Notch-mediated MuSC quiescence relies on miR-708 expression to inhibit MuSC motility and migration through TENSIN3.[114] miR-489 is also upregulated in quiescent MuSCs, and its overexpression inhibits MuSC commitment, resulting in pathogenic muscle regeneration. Conversely, siRNA against miR-489 induces MuSC activation.

Further, *Myf5* mRNA is sequestered in messenger ribonucleoprotein (mRNP) granules alongside miR-31, which targets its 3'UTR to prevent the translation of *Myf5* in quiescent MuSCs.[115] MuSC quiescence also relies on translational repression mediated by the phosphorylation of the translation initiation factor eIF2α.[116]

Additional pathways also regulate MuSC quiescence. WNT4 secreted from the myofiber regulates quiescence through non-canonical signalling. Here, the repression of YAP and activation of RHOA cytoskeleton signalling maintains mechanical tension and retains MuSCs in their niche under the basal lamina.[117] Signalling by the CALCR also maintains MuSC quiescence through the cAMP-PKA pathway.[118] Further, FOXO expression is vital for maintaining MuSC quiescence, as loss of FOXO1/3/4 leads to spontaneous MuSC activation and reduced regenerative potential, likely by IGF1 activation of AKT signalling.[119] Similarly, loss of the AKT antagonist PTEN leads to translocation of FOXO1 from the nucleus to the cytoplasm, causing MuSCs to exit quiescence.[120] Expression of the mechanosensitive cation channel *Piezo1* also preserves MuSC quiescence. It is required for MuSC self-renewal and differentiation, as deletion of *Piezo1* in quiescent MuSCs leads to increased reactive oxygen species (ROS) and TP53-mediated cell senescence, precocious differentiation and depletion of the stem cell pool.[121] Finally, small microtubular projections termed primary cilia are required for SHH signalling, which is critical for maintaining MuSC quiescence.[122,123] The proteolytic cleavage of GLI3 into its repressive form preserves MuSC quiescence by inhibiting mammalian target of rapamycin (mTOR) signalling. Without the repressive action of GLI3, MuSCs enter a state of activated quiescence.

Conventionally, MuSCs are thought to exist in a quiescent (G_0) or activated state (G_1). However, the observation that MuSCs in the leg contralateral to an injury site have different cell-cycle kinetics compared to MuSCs from uninjured and injured legs led to the discovery of a primed

state of quiescence, termed G_{Alert}. MuSCs in G_{Alert} are primed to divide, have greater mitochondrial activity, and are positioned to respond quickly to muscle injury.[124] In response to injury, hepatocyte growth factor (HGF) signalling activates c-MET/mTORC1, which causes MuSCs to transition into G_{Alert}.[125] Signalling through CXCL12 and CXCR4 are also implicated in this shift.[126]

The maintenance of quiescence is a complex and intricate process. Unsurprisingly, recent studies reveal that MuSCs isolated from uninjured tissues undergo rapid transcriptomic and epigenetic modifications. This led to the development of *in situ* fixation and isolation techniques that allow researchers to study genuine quiescence and the activation signatures of MuSCs.[127–130]

MuSC Activation and Asymmetric Cell Division

MuSC activation and proliferation are governed by a complex interplay of spatial cues, signalling pathways, and metabolic shifts toward glycolysis that induce transcriptional and functional changes. Activation signals arise from non-myogenic muscle resident cells, including fibroblasts, immune cells, FAPs, and endothelial cells, as well as modifications in the ECM, mechanical forces, and biochemical signals. Together, these factors regulate MuSC self-renewal and differentiation, ensuring the preservation of the MuSC population and muscle regeneration.[7,131]

Upon activation, MuSCs undergo symmetric or asymmetric cell divisions that determine cell fate and function (**Figure 1.7**). In a symmetric cell division, two functionally identical daughter cells are generated in a planar orientation relative to the myofiber basal lamina. Conversely, asymmetric cell divisions occur when the asymmetric distribution of intrinsic cell fate determinants leads to the generation of a self-renewing and committed MuSC in an apical-basal orientation. The majority of MuSCs divide symmetrically upon activation, with fewer than 10% of divisions occurring in the apical-basal orientation.[132]

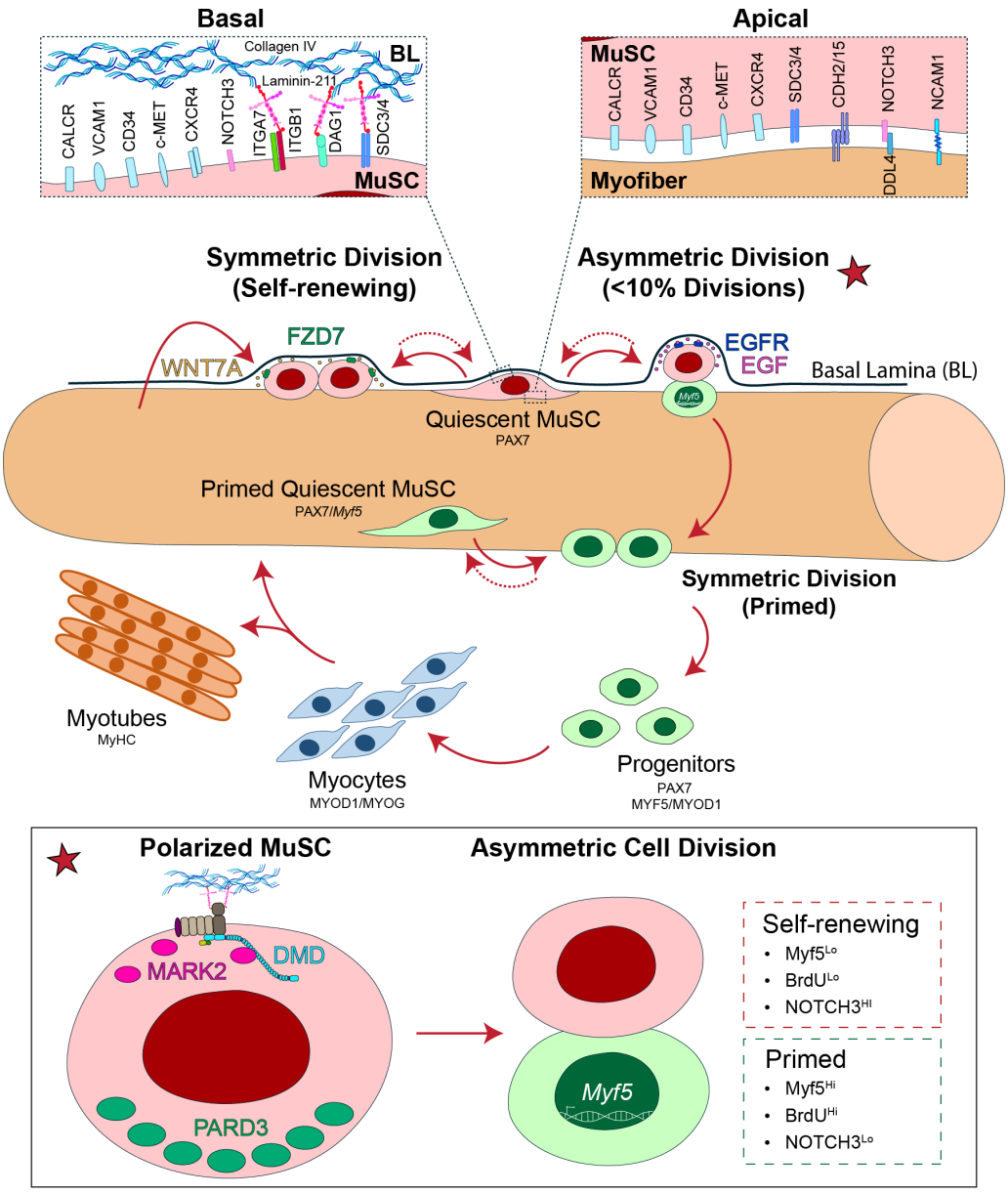

Figure 1.7 Quiescent MuSCs in polarized niches make cell fate decisions after activation. *Quiescence*: Quiescent MuSCs express unique cell surface markers and reside in polarized niches. MuSCs express α7β1-Integrin (ITGA7/ITGB1) basally, with the homophilic receptors m-cadherin (CDH15) and NCAM1 expressed apically at the sarcolemma. CALCR interacts with autonomously produced Collagen V. NOTCH3 interacts with DLL4 presented by endothelial cells basally and myofibers apically. *Myf5*^{Lo} MuSCs and *Myf5*^{Hi} (primed) are both quiescent. *Activation*: *Myf5*^{Lo} MuSCs undergo asymmetric divisions and are long-term self-renewing. Primed MuSCs readily proliferate and commit. Upon activation, *Myf5*^{Lo} MuSCs make a cell fate decision to undergo an asymmetric or symmetric cell division. The self-renewing MuSC remains *Myf5*^{Lo} and retains the template DNA strand (BrdU^{Lo}), while primed MuSCs are *Myf5*^{Hi} and BrdU^{Hi}. WNT7A signalling through FZD7 and EGF signalling by binding EGFR modulate the MuSC decision to undergo symmetric or asymmetric cell division, respectively.

Asymmetric cell fate was initially observed in MuSCs using BrdU labelling, where $BrdU^+$ DNA was asymmetrically segregated with NUMB during MuSC divisions.[133] Experiments using transgenic mice harboured the $Myf5^{Cre/+}$ and $ROSA^{loxP\text{-}STOP\text{-}loxP\text{-}EYFP/+}$ alleles (*Myf5-Cre.ROSA-YFP*) later demonstrated that MuSCs that have never expressed *Myf5-Cre* (YFP^- or $Myf5^{Lo}$) give rise to a self-renewing YFP^- stem cells and a committed progenitor cell expressing Myf5 (YFP^+ or $Myf5^{Hi}$) through asymmetric cell division. This contrasts with self-renewing symmetric cell divisions that generate identical YFP^- stem cells (**Figure 1.7**).[134] The polarized niche of MuSCs likely plays a role in regulating MuSC fate.

In the quiescent niche, MuSCs express ITGA7 and ITGB1 (α7β1-integrin) basally, with the homophilic receptors CDH15 (m-cadherin) and NCAM1 expressed apically at the sarcolemma (**Figure 1.7**).[103,135,136] Considering the importance of niche signalling in maintaining MuSC quiescence and self-renewal, MuSC associations with the niche likely contribute to self-renewal cues during asymmetric divisions. For example, Notch signalling from the niche regulates MuSC collagen gene expression, including *Col5a1* and *Col6a1*, and the loss of either collagen leads to deficits in MuSC self-renewal and muscle regeneration.[112] *Col6a1*-knockout mice have impaired MuSC self-renewal and muscle regeneration following injury,[137] and conditional deletion of *Col5a1* in mice results in loss of MuSC quiescence and gradual depletion of the MuSC pool.[112] Moreover, although the exact mechanisms that induce intrinsically mediated cell polarity are not fully resolved, polarized niche factors interact with regulators of intrinsic polarity in MuSCs. For instance, ITGA7 interacts with both dystrophin and dystroglycan during MuSC activation.

In activated MuSCs, dystrophin interacts with MARK2 (PAR1b), a serine/threonine kinase, to establish polarity in the PAR complex and mediate asymmetric cell divisions. During this process, dystrophin and MARK2 are retained in the YFP^- MuSC, and PARD3 is segregated in the

YFP$^+$ MuSC (**Figure 1.7**).[138] Downstream MuSC fate commitment is also dependent on dystrophin expression. ß1-syntrophin, a component of the DGC in MuSCs, is also apically polarized during asymmetric cell divisions. It interacts with the mitogen-activated protein kinase p38γ to prevent nuclear translocation of CARM1, an arginine methyltransferase that regulates the epigenetic activation of *Myf5* through PAX7 methylation. By phosphorylating CARM1, p38γ prevents its nuclear translocation and contributes to MuSC self-renewal apically.[139]

Beyond niche cues, other pathways govern MuSC fate decisions. WNT7A signalling through FZD7 is important for the symmetric expansion of MuSCs following activation through the planar cell polarity (PCP) pathway.[140] Conversely, EGF stimulates MuSC asymmetric division through the epidermal growth factor receptor (EGFR)-Aurora kinase A (AURKA) pathway by promoting asymmetric accumulation of EGFR, which recruits AURKA to facilitate mitotic spindle assembly (**Figure 1.7**).[141]

The Notch pathway regulates MuSC proliferation, activation and likely asymmetric cell division. NOTCH1 and NOTCH2 are highly expressed in the majority of MuSCs. Conversely, YFP$^-$ MuSCs express higher levels of NOTCH3, while YFP$^+$ MuSCs have elevated expression of the Notch ligand DDL1 (**Figure 1.7**).[134] Interestingly, this finding correlates with the observation that myofibers have increased DLL4 staining intensity in the niche of *Pax7*-high MuSCs, whereas the loss of DLL4 results in enhanced MuSC proliferation and commitment.[105] The Notch receptors also play distinct roles in MuSC function. The loss of *Notch1/2* expression prevents MuSC expansion, induces precocious MuSC differentiation, and has deleterious effects on muscle regeneration.[142] Conversely, *Notch3* suppression results in MuSC hyperplasia and muscle growth after repeat injury.[143] Notch signalling is generally downregulated during MuSC commitment, which is permissive to myogenic cell differentiation. However, some Notch target genes, such as

Hes6, are upregulated during cell differentiation.[111] Moreover, the mechanisms of Notch signalling antagonization are still elusive.

NUMB, the cell fate determinant and inhibitor of Notch signalling, is asymmetrically distributed in *ex vivo* MuSCs and segregates with the non-template strand during asymmetric divisions and progenitor cells,[133,144] suggesting that Notch signalling plays a role in regulating MuSC asymmetric divisions. However, the loss of NUMB does not lead to significant changes in the expression of Notch signalling genes in myogenic cells,[145] suggesting that further study is necessary to elucidate the mechanisms of Notch downregulation during myogenesis. Moreover, the role of NUMB in asymmetric MuSC divisions requires further investigation.

Other pathways involved in cell fate decisions and the activation and proliferation of MuSCs include SHH, mTOR, WNT, and FGF signalling. Ablation of mTOR impairs myoblast proliferation and differentiation.[146] During muscle regeneration, mTOR pathway activation also induces the expression of cyclin D1 through the activity of two miRNAs, miR-26a and miR-1.[147] FGF2 also activates MuSCs, which predominantly express FGFR1 and FGFR4, by promoting Ca^{2+} uptake through activation of the TRPC1 channel.[148–152] Moreover, the loss of primary cilia and SHH signalling reduces MuSC proliferation and impairs muscle regeneration.[123] Taken together, MuSC activation, proliferation, and self-renewal result from the simultaneous interaction of many pathways that regulate muscle regeneration.

MuSC Heterogeneity

Early studies proposed that satellite cells were a homogenous population of muscle progenitor cells. However, satellite cells are, not only distinct from myoblasts, but transcriptionally and functionally heterogeneous, with a subset of cells exhibiting elevated engraftment, self-renewal, and multipotency.[153] For instance, PAX3 expression is maintained at the protein level in the

diaphragm muscle,[154] and the RNA level in a rare radiation-resistant MuSC subpopulation capable of clonal expansion.[155,156] Studies also suggest that MuSCs exist within a hierarchy where MuSCs can differentiate along different trajectories. This is illustrated by the bi-potent potential of MuSCs to generate both myogenic progenitor cells and brown adipocytes.[157] MuSC hierarchies are further supported by studies demonstrating increased stemness potential within MuSC subpopulations.

MuSC subpopulations with increased stemness have been described using multiple mouse models. Label-retaining MuSCs, identified using *TetO-H2B-GFP* mice, give rise to label-retaining and non-label-retaining cells. However, only the former can self-renew, while the latter undergo differentiation.[158] Stemness can also be identified by *Pax7* expression using *Tg:Pax7-nGFP* transgenic mice and CD34 expression. *Pax7*-high and CD34-high MuSCs have delayed activation, lower metabolic activity, reduced rates of division, and greater resistance to differentiation compared to *Pax7*-low, CD34-low or CD34-negative MuSCs. *Pax7*-high and CD34-high MuSCs also have greater engraftment potential following transplantation.[119] Similarly, studies using *Myf5-Cre.ROSA-YFP* transgenic mice reveal that approximately 10% of MuSCs that never express *Myf5-Cre* have greater self-renewal, while the majority of MuSCs express *Myf5-Cre* and are primed to differentiate. Engraftment assays also demonstrate that YFP^- MuSCs can regenerate myofibers and repopulate the stem cell niche *in vivo*. Conversely, YFP^+ MuSCs undergo myogenic differentiation upon transplantation.[134] The relationship between these subpopulations is unresolved, and a full characterization of the long-term self-renewing multipotent MuSC is required.

Diseases and aging alter MuSC subpopulation function and composition. While clonal complexity is maintained in aging, functional heterogeneity and proliferation decline.[159] One study identified an age-related increase in CD47-high MuSCs, suppressing CD47-low MuSC

proliferation and impairing muscle regeneration.[160] Similarly, diseases disrupt the MuSC subpopulation balance by changing the proportions of symmetric and asymmetric cell divisions. Despite strong evidence of MuSC heterogeneity, whether it results from intrinsic differences or environmental influences remains a topic of debate.

MuSCs in Myopathies

MuSC dysfunction is implicated in several inheritable muscular dystrophies, congenital muscular dystrophies, and congenital myopathies, which share elements of impaired muscle regeneration and histopathology. Myopathic mutations compromise MuSC function intrinsically and/or by creating hostile niche microenvironments that cause chronic MuSC activation and impair muscle regeneration.[161–163]

Myopathic mutations that impair intrinsic MuSC function were termed "satellite cell-opathies" by Ganassi et al.[161] Primary satellite cell-opathies are caused by mutations that directly impair MuSC function and self-renewal, resulting in downstream myofiber dysfunction. For example, mutations to the *PAX7* gene lead to progressive congenital Myopathy with scoliosis (MYOSCO), a neuromuscular disease characterized by depletion of the MuSC pool, muscle atrophy, scoliosis, and respiratory failure. Conversely, secondary satellite cell-opathies result from mutations that directly perturb MuSC and myofiber function.[161] An example is Duchenne muscular dystrophy (DMD), a disease of myofiber fragility and impaired MuSC commitment caused by the absence of the cytoskeleton protein dystrophin.[138,139]

1.4 Duchenne Muscular Dystrophy

Duchenne Muscular Dystrophy (DMD) is a fatal neuromuscular disease caused by loss-of-function mutations in the X-linked dystrophin gene (*DMD*). The largest known gene in the human genome,

DMD spans 2.3 million base pairs, contains expansive intronic regions, and requires over 16 hours to transcribe.[164,165] Unsurprisingly, *DMD* is highly susceptible to genetic mutations, making DMD the most common inherited neuromuscular disorder in children worldwide.[166,167] Strikingly, an estimated 1 in 3 DMD cases results from *de novo* mutation in the *DMD* gene.[168–170] Approximately 60-70% of *DMD* loss-of-function mutations result from deletions of one or more exons, while exon duplication events or point mutations cause the remainder. Approximately 47% of DMD-causing mutations occur between exons 45 and 55, with a second hotspot between exons 3 and 9 accounting for 7% of patients.[171]

DMD contains seven known tissue-specific promoters in mice and humans, with loss of the full-length 427kDa muscle isoform (Dp427m) driving DMD pathology.[166,172] Dp427m is expressed in both skeletal muscle myofibers and MuSCs, where it plays important structural and signalling roles through the DGC (**Figure 1.7**).[138,173] Without dystrophin, the DGC does not assemble and is unable to tether the ECM to the intracellular actin cytoskeleton through the sarcolemmal protein dystroglycan.[5] This results in two overarching consequences, myofiber fragility and disrupted MuSC function (**Figure 1.8**).[138,139,174,175]

Knowledge of DMD pathophysiology is largely based on studies in the genetically homologous *mdx* mouse, harbouring a nonsense point mutation in exon 23.[172,176–179] While the progression of muscular dystrophy in *mdx* mice is less severe compared to humans, dystrophin-deficient murine and human muscles both display characteristic lesions, elevated inflammation, and similar mechanisms of dysregulation.[180] DMD is conventionally thought to manifest at 3-5 years of age in humans, equivalent to 3-4 weeks of age in mice, when the accumulation of contraction-induced muscle injuries, caused by myofiber fragility, leads to gross motor delays, abnormal gait, frequent falls and difficulty standing.[180,181] Despite ongoing muscle regeneration by

MuSCs, continuing muscle degeneration, cell necrosis, and fibrotic deposition ultimately lead to muscle weakening and dysfunction. Moreover, the impaired regenerative ability of MuSCs in dystrophic muscle exacerbates this phenotype.

Muscle fragility leads to continual sarcolemma insult and cytoplasm leakage, which result in chronic immune responses and activation of inflammatory pathways in the MuSC niche, including the nuclear factor-κB (NF-κB), TGF-β, tissue necrosis factor (TNF), toll-like receptor (TLR), Myeloid differentiation primary response 88 (MyD88), and interleukin (IL) pathways.[182,183] Chronic exposure to inflammatory signals negatively impacts MuSC function, while limiting the immune response improves the regenerative ability of dystrophic MuSCs. For instance, directly antagonizing the inflammatory cytokine IL6 or STAT3 leads to improved dystrophic MuSC differentiation.[184,185] However, the direct loss of Dp427m in MuSCs also contributes to disease progression.[138]

Human and murine MuSCs express Dp427m and components of the DGC in a temporally regulated manner during myogenic commitment and differentiation.[138,175] As previously noted, the polarity kinase MARK2 interacts with Dp427m at repeats 8-9 to establish the MuSC polarity required for asymmetric cell division (**Figure 1.7**). In the absence of Dp427m, MARK2 is downregulated, and MuSCs undergo fewer asymmetric divisions, producing fewer progenitor cells (**Figure 1.9**).[138,186] Additionally, without the assembly of the DGC, its role in asymmetrically regulating the epigenetic activation of MuSCs is perturbed, further contributing to MuSC expansion and reduced progenitor generation.[139] Considering that postnatal muscle regeneration is reminiscent of developmental myogenesis, intrinsic MuSC dysfunction may begin earlier than overt symptom manifestation.

Although DMD patients seem asymptomatic at birth, an increasing number of studies indicate that the etiology of DMD begins *in utero*. For instance, studies describe disrupted muscle development in 12-week fetal human muscle,[187] and the muscle of dystrophin-deficient animal models, including the neonatal dystrophic golden retriever (GRMD), the *mdx* mouse fetus and the *sapje* zebrafish embryo.[188–190] Further, transcriptional dysregulation occurs in DMD patient muscle before 2 years of age and in disease modelling of myogenesis using patient-derived induced pluripotent stem cells (hiPSCs).[191–193] Another recent study demonstrated that, during *in vitro* somitogenesis, hiPSCs diverge to an alternative branch of myogenic trajectory, and these cells have dysregulated gap junction genes.[192] Overall, the developmental manifestation of DMD further suggests that factors beyond myofiber fragility play a role in DMD progression before the debilitating phenotype seen in young patients.

Myofiber fragility, chronic inflammation and MuSC impairment in DMD patients manifest as wheelchair dependency during the teenage years, reliance on ventilators by the third decade of life, and premature death at a median age of 22 years despite intensive clinical intervention.[174,194] While improvements in clinical care have extended the life expectancy of DMD patients, available treatments remain palliative.[171]

Despite nearly 50 years since the discovery of the dystrophin gene,[164] glucocorticoid treatment to slow the decline of muscle strength remains the gold standard and most effective treatment for DMD.[195] However, several treatment advances have emerged over the last decade. Antisense oligonucleotide (ASO) exon skipping technology, which aims to restore the *DMD* gene reading frame and produce a truncated dystrophin protein, was among the first modern treatments approved by the United States Food and Drug Administration (FDA) to treat DMD. However, the available ASOs target a subset of DMD mutational hotspots, including exon 45 (casimersen), exon

51 (epeplirsen) and exon 53 (golodirsen and viltolarsen), which could benefit only 30% of DMD patients.[171,196] Moreover, first-generation ASOs restore less than 6% of dystrophin protein, and the long-term treatment benefit is unclear.[196] After 8 years, the first approved ASO, Eteplirsen, showed only a smaller, albeit significant, survival benefit compared to corticosteroid-treated control patients.[197] Exon skipping using CRISPR Cas9-mediated gene editing to restore the *DMD* gene reading frame is another therapeutic area of investigation. However, many barriers remain to its implementation in the clinic, including delivery efficiency, immunogenicity against the bacterial-derived Cas9 protein, off-target genomic editing potential, and the diversity of *DMD* gene mutations.[198]

Gene therapy is another conceptually appealing avenue of therapeutic intervention. However, the large size of the *DMD* gene makes engineering effective, deliverable vectors challenging. Furthermore, treatment is contraindicated in patients with exon 1-17 mutations due to the heightened risk of severe immune-mediated myositis, believed to result from T-cell-mediated reactions to N-terminal micro-dystrophin segments that the patient's immune system has not previously encountered.[199] Despite these limitations, the FDA recently approved the first gene therapy for DMD, Elevidys, under the Accelerated Approval pathway.[200] Like other gene therapies in clinical trials, Elevidys is an adeno-associated virus (AAV; specifically AAV serotype rh74[201]) vector-based gene therapy that aims to deliver a truncated, partially functional version of *DMD* to restore a level of connection between the myofiber sarcolemma and basal lamina. Promisingly, patients treated with Elividys had decreased creatine kinase levels, sustained micro-dystrophin expression, and promising functional outcomes.[200] However, MuSCs are refractory to AAV transduction,[202] and the transduction efficiency of rAAVrh74 in MuSCs has not been reported. Moreover, truncated dystrophin constructs lack the MARK2 binding site on dystrophin's rod

domain, which together questions the long-term therapeutic benefit from Elevidys alone. The limitations of existing therapies for treating DMD suggest that further therapeutic innovation is necessary.

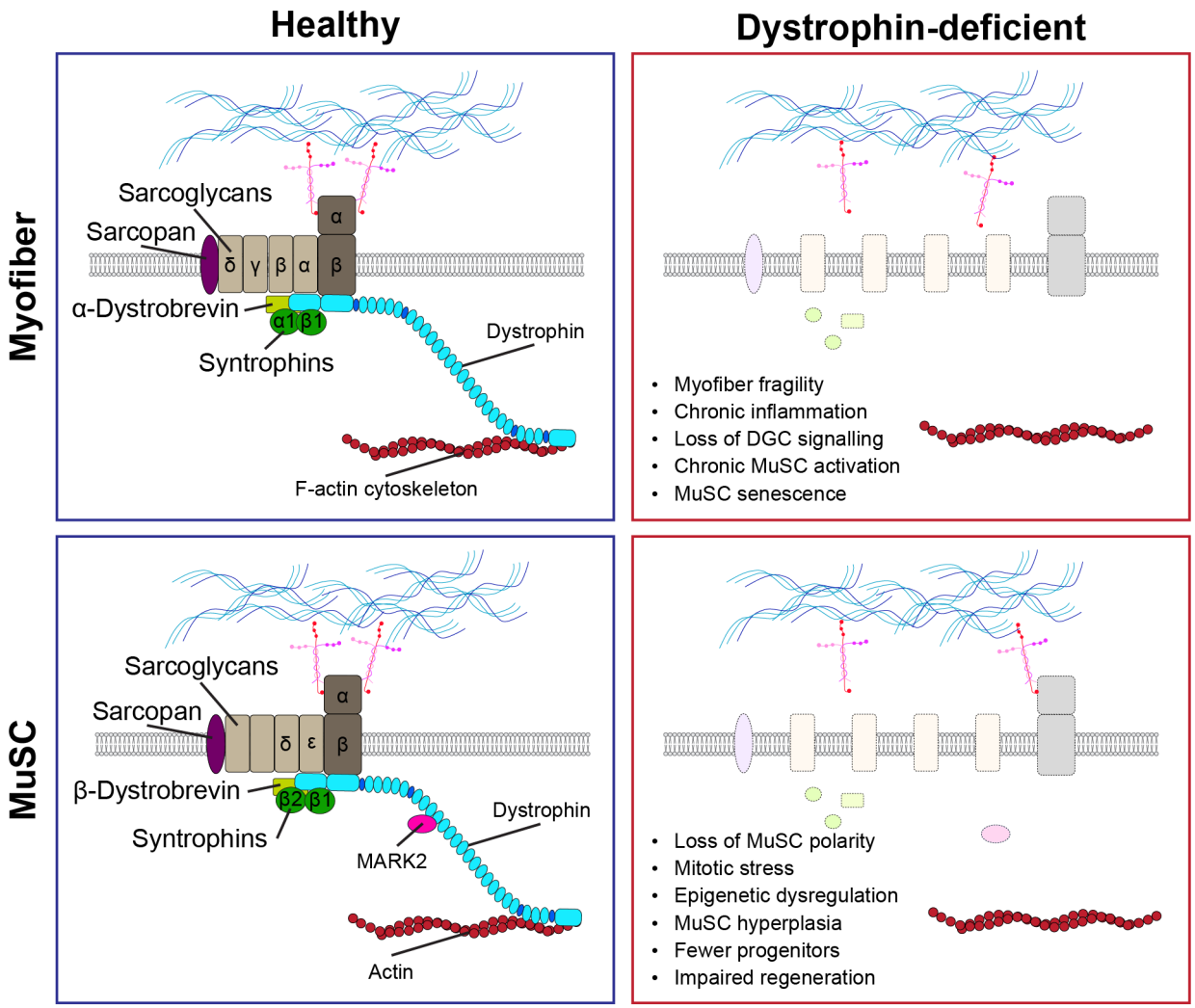

Figure 1.8 Dystrophin associated glycoprotein complex does not form without dystrophin. In healthy muscle, the dystrophin associated glycoprotein complex (DGC) tethers the extracellular matrix (ECM) to the intracellular actin cytoskeleton in myofibers (top left) and muscle stem cells (MuSCs; bottom left; predicted DGC components[138]). However, the absence of dystrophin causes the dissolution of the DGC in myofibers (top right) and MuSCs (bottom right). Myofibers are prone to contraction-induced damage that leads to chronic inflammation, further impairing myofiber and MuSC function. In MuSCs, the loss of the DGC results in intrinsic polarity impairments that induce mitotic stress and epigenetic dysregulations. Together, these cause MuSC hyperplasia, the generation of fewer progenitor cells, and impaired muscle regeneration.

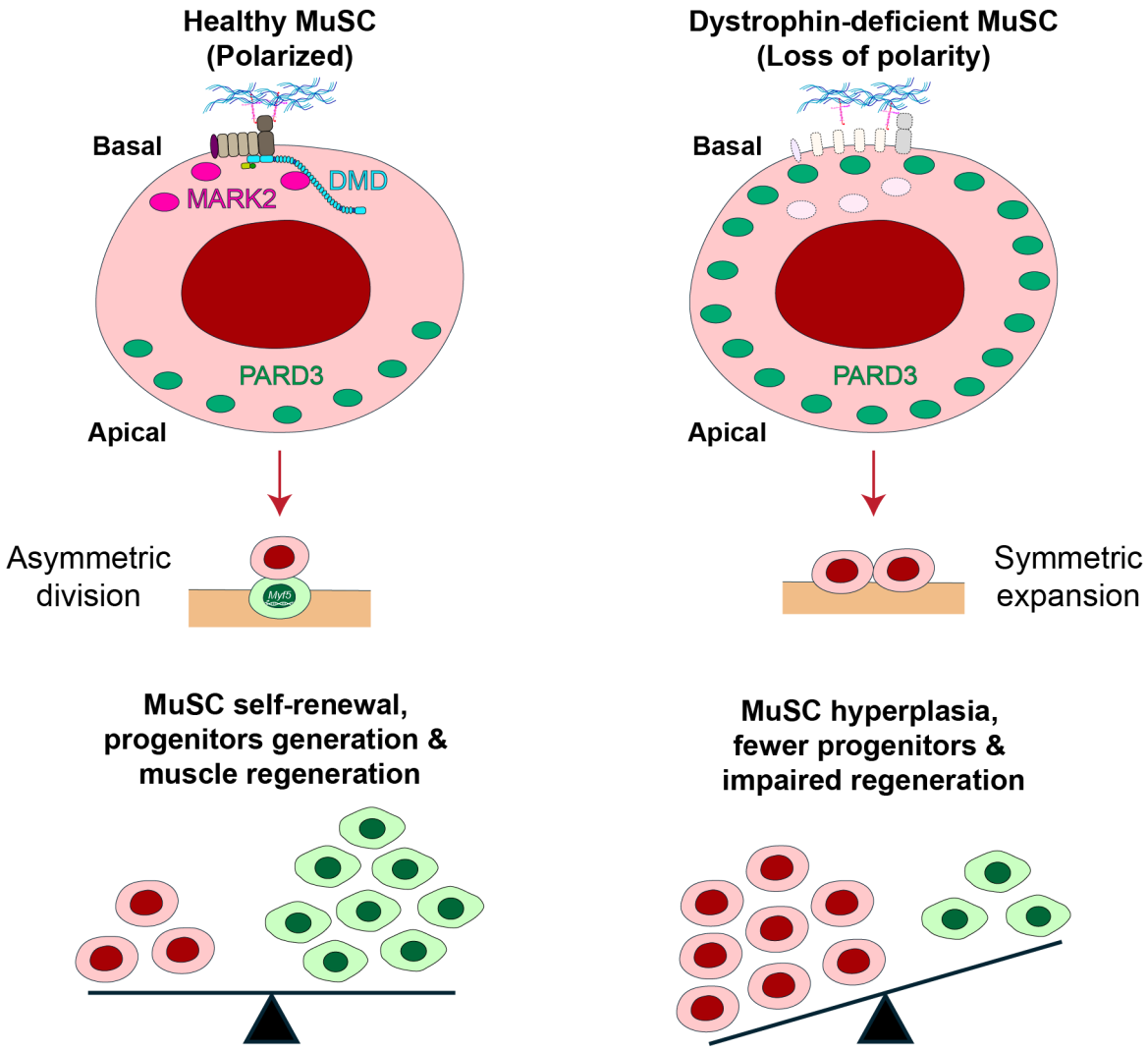

Figure 1.9 The absence of dystrophin impairs MuSC polarity and asymmetric division. Healthy MuSCs undergo asymmetric cell division upon activation, repopulating the MuSC pool and generating differentiation-competent progenitors (left). Impaired polarity results from the loss of dystrophin-MARK2 interactions in dystrophic MuSCs, leading to symmetric MuSC expansion and fewer progenitor cells.

1.5 Rational and Hypothesis

Studies from our lab establish DMD as a MuSC disease.[138,139] However, the role of impaired asymmetric MuSC divisions and reduced myogenic commitment in muscle regeneration has not been extensively studied *in vivo*, and controversy surrounding the contribution of intrinsic MuSC dysfunction to muscle regeneration deficits in DMD remains. Moreover, despite reports of full-length *Dmd* expression as early as murine and human myotome development, the role of dystrophin in development is unknown.[203,204] Given our findings that the absence of dystrophin disrupts MuSC polarity in *ex vivo* myofiber culture, we theorized that intrinsic polarity deficits in dystrophin-deficient MuSCs contribute to skeletal muscle development and regeneration defects *in vivo*. To clarify these hypotheses, we employed the *mdx* mouse model of DMD to investigate MuSC dynamics and function during primary, secondary, and neonatal myogenesis, as well as chronic and acute adult muscle regeneration.

1.6 Objectives

1. Clarify the contribution of intrinsic MuSC dysfunction to regeneration deficits in the *mdx* mouse.

2. Investigate the effects of dystrophin deficiency on primary and secondary myogenesis and assess the mechanisms underlying potential disruptions in muscle development.

3. Restore MuSC function during myogenesis by targeting pathways to restore polarity.

Chapter 2: Experimental Methods

Antibodies are listed in **Table 2.1**, reagents are listed in **Table 2.2**, primers are listed in **Table 2.3**, software is listed in **Table 2.4**, and mouse strains are listed in **Table 2.5**.

2.1 Experimental Approval, Models and Procedures

All housing, husbandry and experiments were performed per the University of Ottawa Animal Care Committee guidelines and approved by the Animal Research Ethics Board at the University of Ottawa. The following mouse lines were used: C57BL/10ScSnJ (referred as WT, JAX #000476), C57BL/10ScSn-*Dmd*^{mdx}/J (referred as *mdx*; JAX #001801), *Myf5-LacZ* (JAX #018626),[205] *Pax7-nGFP* (JAX #036759),[206] *ROSA-nTnG* (JAX #023035),[207] *Myf5-Cre* (JAX #007893),[208], *CAG-GFP* (JAX #006567), *Myf5*^{CreER}*; R26R*^{mTmG} (JAX #023342 and JAX #007576), NOD.Cg-*Prkdc*^{scid} *Il2rg*^{tm1Wjl}*/SzJ* (NSG; JAX #:005557), and *Aak1*$^{tm1a(EUCOMM)Hmgu}$ (*Aak1*$^{-/-}$, EMMA ID #EM:08493).[209] Full strain names are identified in **Table** 2.5.. All transgenic lines except for *Myf5-LacZ* were bred onto the *mdx* background before timed mating experiments. All experiments presented in **Chapter 3** were performed on male mice and initiated at 6-10 weeks-old unless stated otherwise. In **Chapter 4**, male and female adult *Pax7-nGFP* mice were used in equal numbers between 10 and 20 weeks of age to access the expression of dystrophin protein and RNA.

Cardiotoxin Injury

For muscle injury, mice were anesthetized using isoflurane (2% in oxygen), then injected with 50 µL of 10 µM Cardiotoxin (CTX) solution (Latoxan) directly into the *tibialis anterior* (TA) muscle. For fluorescence cell sorting of activated MuSCs, both TA and *gastrocnemius* muscles were injected with 40-50 µL and 80-100 µL of 10 µM CTX, respectively. Mice were provided either

0.1mg/kg buprenorphine (CTX-injury experiments in **Chapter 3**) or 50 µL of 5 mg/mL carprofen (polarity and engraftment experiments in **Chapter 3**; **Chapter 4**) for pain management.

In Situ Force Measurement

Mice were anesthetized using isoflurane (2% in oxygen) by nose cone throughout the procedure. As previously described, muscle force measurements were performed on TA muscle using an Aurora Scientific 300C-LR-FP dual mode muscle lever system equipped with a 1N force transducer and 1cm lever arm.[122] Electrical stimulation was performed using monopolar needle electrodes attached to an Aurora Scientific 701C High-Power, Bi-Phase Stimulator. Force transducers were calibrated before each study using precision weights.

Two monopolar needle electrodes were positioned adjacent to the tibial nerve proximal to the kneecap and distal to the kneecap adjacent the *extensor digitorum longus* (EDL) muscle. Traction was applied to the transducer to maintain 20 mN of measured tension for an initial 15 min stretching period with 100 ms trains of 0.3 ms, 5 V supramaximal voltage pulses at 1 Hz stimulation every 100 seconds. Following stretching, muscles were maintained at 20 mN static tension and tetanic contractions were measured every 100 seconds following 200 ms trains of 0.3 ms, 5V supramaximal voltage pulses at serial frequencies from 1 Hz to 200 Hz. Maximal force was defined by the difference in maximal force measured during stimulation to that of the static tension immediately before stimulation.

Following force measurement, muscle mass and volume were measured. Specific force of muscles was calculated as follows: $\frac{F_{measured}}{PCSA}$ and $PSCA = \frac{M_{displacement}}{M_{FL}} \times Cos(M_{PA})$, where $F_{measured}$ is the force measured in mN, $PSCA$ is the physiological cross-sectional area in mm^2, $M_{displacement}$ is the measured muscle displacement in µL (mm^3), M_{FL} is the experimentally determined muscle fibre length in mm, M_{PA} is the experimentally determined muscle pennation

angle in °. For non-volumetric analysis, muscle mass was related to the assumed density of mammalian tissue (1.06g.m^{-3}). Muscle fibre length and pennation angles were determined previously.[210]

Satellite Cell Engraftment Assay

Transplantation experiments were modified from previously described protocols.[211] Recipient immunodeficient NSG (NOD.Cg-*Prkdc*^{scid} *Il2rg*^{tm1Wjl}*/SzJ*, JAX #005557) mice were anesthetized by isofluorane and treated with subcutaneous carprofen (50 µL of 5 mg/ml). Under anesthesia, the hindlimbs were irradiated with 8Gy X-rays delivered at 0.71 Gy.min^{-1} (X-RAD 320, Precision X-Ray) using a lead barrier to protect the body. Immediately following irradiation, the TA was injured using 50µL of 10µM CTX (Latoxan). Two days later, 10,000 donor MuSCs from 6-8-week-old WT and *mdx CAG-GFP* or *ROSA-nTnG* mice were injected into the contralateral TAs of NSG mice. Fluorescent donor MuSC (tdTomato$^+$ or GFP$^+$) were isolated using fluorescence-activated cell sorting (FACS) based on forward scatter (FSC), side scatter (SSC), 7-Aminoactinomycin D (7-AAD) (STEM CELL Technologies) viability dye, lineage-negative (Lin$^-$) selection (CD31$^-$, CD11b$^-$, CD45$^-$, SCA1$^-$), and positive selection (α7-integrin$^+$, VCAM1$^+$) (see section **2.4**). Donor muscle stem cells were washed with PBS and resuspended in 0.9% NaCl solution at a concentration of 10,000 cells per 20µL prior to engraftment into the TA muscle of irradiated and injured NSG mice. Two- and four-weeks following transplantation, NSG mice were perfusion-fixed and processed as previously described.[2] Briefly, the fixed TA muscles were harvested, fixed overnight in 1% PFA at 4°C, submerged in a 15% to 30% sucrose gradient at 4°C, embedded in Tissue-Tek OCT and frozen in liquid nitrogen-cooled isopentane. Embedded muscles were transversely sectioned at 10 µm-thickness. Antibody staining was performed as described above beginning from the permeabilization step. Antibodies are listed in **Table 2.1**.

Timed Mating Experiments

Timed mating was performed using post-coital plug visualization where the day of conception was assigned as E0.5. To reduce false-positive pregnancies at early timepoints, maternal weight was measured at day E0.5 and at E9.5. A threshold weight gain of 1.75g at E9.5 was used to determine pregnancy.[212] On the day of embryo collection, pregnant mice were humanely euthanized and c-sectioned, and the embryos removed at corresponding time points between E10.5 and E17.5. All embryos were immediately placed in ice cold PBS and fetal mice were euthanized by decapitation. To obtain neonatal mice, breeding pairs were monitored for births after 18 days in the same enclosure. The day of discovery was labelled as perinatal day 0 (P0). Perinatal mice (P7) were euthanized by decapitation. All experiments using embryonic, fetal, and neonatal mice were conducted post-mortem.

Both male and female embryos were used in equal numbers for comparative analysis, except for experiments using the *Myf5-LacZ* transgene. Male *Myf5-LacZ* mice not carrying the loss-in-function mutation to *Dmd* on the X-chromosomes ($Dmd^{+/y}$) were crossed with *mdx* dams ($Dmd^{-/-}$) and the male embryos were selected by sex genotyping. As *Dmd* is X-linked, all males offspring from an *mdx* mother possess just one copy of *the Dmd* gene ($Dmd^{-/y}$) and display the dystrophic phenotype. In contrast, female embryos carried only one mutated copy ($Dmd^{+/-}$). Male offspring from *Myf5-LacZ* male mice crossed with WT females were used as controls.

2.2 Genotyping

Genetic Sex

The DNA extraction and PCR protocol for determining genetic sex was adapted from previously published methods.[213] SX primers amplified intron 8 of *Sly* on the Y chromosome (~300bps) and

intron 6 of *Xlr* 6 on the X chromosome (~500-700bps) and are listed in **Table 2.3.** DNA was extracted from portions of the yolk sac or tail. The tissue was placed in 200µL of DNA extraction buffer (50mM KCl, 10mM Tris-HCl pH8.3, 2.5mM $MgCl_2$, 0.1mg/mL gelatin, 0.45% (v/v) Nonidet P-40, 0.45% (v/v) Tween-20; autoclaved and stored frozen) supplemented with 150µg/mL proteinase K. Samples were incubated at 55°C, vertexing every 15min for 1hr then overnight. The proteinase K was then heat-inactivated at 95°C for 5min. DNA was diluted 5X then 1µL of each sample was added directly to a PCR reaction. The PCR reaction was performed in a final volume of 25µL with High-Fidelity Phusion Polymerase (Thermo Fisher Scientific), 1X Phusion buffer, 1µL DMSO, 0.2mM dNTPs, 0.5µM primers and 1µL DNA. The PCR parameters were as follows: initial denaturation at 94°C for 2min, 35 cycles with 94°C for 30s, 57°C for 30s, and 72°C for 30s, followed by final elongation at 72°C for 5min. The PCR product was electrophoresed with 1 Kb Plus DNA Ladder (Invitrogen) on a 2% agarose gel with ethidium bromide and visualized using UV illumination.

Aak1 Mutants

Genotyping for *Aak1* mutants requires the purification of DNA from tissues. According to the manufacturer's protocol, DNA was extracted from fetal tail clippings using the NucleoSpin Tissue kit for DNA from cells and tissue (Macherey-Nagal). *Aak1* primers are listed in **Table 2.3**. The PCR products were 328 bps for the WT and 392 bps for the mutant allele. The PCR reaction was performed in a final volume of 20µL with High-Fidelity Phusion Polymerase (Thermo Fisher Scientific), 1X Phusion buffer, 1µL DMSO, 0.2mM dNTPs, 2µM primers and 2µL DNA. The PCR parameters were as follows: initial denaturation at 94°C for 4min, 35 cycles with 94°C for 30s, 62°C for 30s, and 72°C for 1min, followed by final elongation at 72°C for 7min. The PCR product

was electrophoresed with 1 Kb Plus DNA Ladder (Invitrogen) on a 2% agarose gel with ethidium bromide and visualized using UV illumination.

2.3 Embryo Staging

Fixed embryos were visualized for embryo staging using a Zeiss Stereo Discovery V8 microscope equipped with an achromat S 1,0X objective. Images were acquired using AxioVision software. Somites were enumerated manually using FIJI, and limb ontology staging was conducted utilizing the forelimb and the Embryonic Mouse Ontogenetic Staging System (https://limbstaging.embl.es/).[214]

2.4 Fluorescence-Activated Cell Sorting

Adult Myogenic Cell Isolation

Adult MuSCs were FACS-isolated from uninjured or CTX-injured adult hindlimb muscles that were dissected, minced briefly, and dissociated in Hams F10 (Wisent) containing collagenase/dispase using a gentle MACS Octo Dissociator (Miltenyi Biotec). A single cell suspension was generated using a 100µm filter and centrifugation. The cell pellet was then treated with red blood cell lysis buffer according to the manufacturer's recommendation (Sigma, Hybri-Max). Staining was performed in 1mL FACS buffer (5% FBS, 5 mM EDTA in PBS) volume using lineage-negative (Lin^-) antibodies against CD31, CD11b, CD45, and SCA1 conjugated to BV421, and positive selection markers specified under each experimental method. Cell preparations isolated without formaldehyde fixation were stained with 7-AAD viability dye (STEM CELL Technologies). Alternatively, fixable viability Zombie NI dye (BioLegend) was used, followed by a 10 min formaldehyde-fixation (4% PFA) and cell sorting. All myogenic cells were isolated using

a MoFlo XDP cell sorter (Beckman Coulter) based on FSC/SSC, viability dye and lineage markers. Antibodies are listed in **Table 2.1**.

Developmental MuSC isolation

Pax7^{+} cells were isolated from *Pax7-nGFP* E10.5 and E12.5 embryos with the head removed by manually mincing tissues in 3mL of Hams F10 (Wisent) containing collagenase/dispase using razor blades. *Pax7*$^{+}$ MuSCs were isolated from *Pax7-nGFP* E14.5 and E17.5 fetal limbs dissociated in 3mL of Hams F10 (Wisent) containing collagenase/dispase-containing using a gentle MACS Octo Dissociator (Miltenyi Biotec).

Three conditions were used to isolate fetal MuSCs. For all assays not examining protein polarity, GFP^{+} or cells stained with 7-AAD were isolated from fetal limbs of *Pax7-nGFP* mice. A second method was used for experiments that examined protein polarity. GFP^{+} cells were isolated from *Pax7-nGFP* hindlimb muscle that were dissociated, filtered, stained with the fixable viability Zombie NI dye (BioLegend), and formaldehyde-fixed (4% PFA) for 10 min before cell sorting. Finally, the MARK2 and dystrophin polarity analysis was conducted on E17.5 PAX7^{+} cells isolated from WT and *mdx* fetal limbs. Following limb dissociation and filtering, the cell pellet was stained overnight against antibodies for Lin^{-} conjugated to PE-Cy7 (BD Biosciences) and unconjugated PAX7 (DHSB), followed by 1 hour of staining with an AlexaFluor secondary antibody. All cells were isolated with a MoFlo XDP cell sorter (Beckman Coulter). Antibodies are listed in **Table 2.1**.

2.5 Single Cell Assays

To assess adult MuSC polarity, Lin^{-} α7-integrin^{+} VCAM1^{+} Zombie^{-} cells were FACS-isolated from CTX injured hindlimb muscle 48 hours following injury. Fetal and neonatal day 7 GFP^{+} Zombie^{-} MuSCs were isolated from *Pax7-nGFP* dissociated limb muscles. Following a short dissociation

(30 min for adult MuSCs; 20 min for fetal neonatal MuSCs), antibody incubation (adult MuSCs only) and viability dye stain, an additional 10-minute fixation with 4% paraformaldehyde was conducted prior to cell sorting to preserve the polarization of polarity proteins.

Fixed and live isolated myogenic cells were adhered to 12-well removable chambers Ibidi slides coated with Cell-Tak (Corning) for immunostaining, RNA scope and proximity ligation assay (PLA). Live cells were fixed with 4% paraformaldehyde following adhesion for 20 min at RT.

NIH 3T3 cells, used as negative control cells for the single cell assays, were grown on 12-well chamber slides in high glucose DMEM supplemented with 10% FBS and 1% penicillin/streptomycin. The cells were then fixed with 4% paraformaldehyde for 20 min at RT.

Immunostaining

Immunostaining was modified from previously described methods.[2] Fixed cells were permeabilized (0.1% Triton X-100, 0.1 M Glycine in PBS), blocked (5% horse serum, 2% BSA, and 0.1% Triton X-100 in PBS), and stained overnight at 4°C in blocking buffer with a combination of primary antibodies against EGFP, PARD3, MARK2, NUMB, DMD and PAX7. The following day, the cells were incubated with Alexa Fluor-conjugated secondary antibodies (1:1500) for 1 hr at room temperature (RT), counterstained with DAPI (0.5 μg/mL in PBS) and mounted with PermaFluor (Fisher). Antibodies are listed in **Table 2.1**.

RNAscope

In situ hybridization assays using the RNAscope Multiplex Fluorescent Reagent Kit v2 (Advanced Cell Diagnostics) kit were conducted according to the manufacturer's protocol for cultured adherent cell samples. Protease III was diluted 1:15 and incubated for 10 min. Probes that target *Pax7* (RNAscope Probe- Mm-Pax7-C2, ACD) and exons 4-10 of the full-length *Dmd* ($Dmd^{ex4\text{-}10}$)

(RNAscope Probe- Mm-Dmd, ACD) were used. Control 3T3 cells that do not express *Pax7* or appreciable *Dmd* were assayed in parallel.[215] The cells were counterstained with DAPI (0.5 μg/mL in PBS) and mounted with PermaFluor (Fisher).

Proximity Ligation Assay (PLA)

Cells were permeabilized, blocked using Duolink Blocking solution for one hour at 37°C, then incubated in Duolink Antibody diluent containing primary antibodies against GFP (Abcam; 1:1500, Cat# ab13970), MARK2 (LS Bio, 1:1000, #LS-B7503; 1:1000) and DMD (MANDYS16; 1:10, DSHB; # AB_2618166) overnight at 4°C. PLA was then performed using Duolink mouse plus and rabbit minus probes, and the assay was conducted using the In Situ Detection Reagents in Texas Red (Duolink; # DUO92008) according to the manufacturer's guidelines. Secondary antibodies against GFP were added to the PLA amplification step. The cells were counterstained with DAPI (0.5 μg/mL in PBS) and mounted with PermaFluor (Fisher).

Image Acquisition and Analysis

All single cell assays were imaged on a Zeiss LSM900 confocal microscope with Z-stacks using a Plan-Apochromat 20X/0.8 M27 objective in conventional pinhole microscopy mode. Where possible, all image analysis was automated using IMARIS and FIJI software. To analyze cell polarity, where cells were assigned a polarity status manually, all images were blinded by a third party with no knowledge of the experimental details.

High magnification images were acquired using a Plan-Apochromat 63X/1.4 NA Oil objective and Zeiss Airyscan 2 Super Resolution technology. Airyscan processing was performed using Zen 3.7 blue edition software and the image analysis module.

2.6 X-gal Staining

Heterozygous *Myf5-LacZ* mice (*Dmd*$^{+/y}$.*Myf5*$^{+/LacZ}$) were bred with WT and *mdx* female mice (*Dmd*$^{-/-}$.*Myf5*$^{+/+}$), and male offspring were examined. Genetic sex genotyping was conducted as described above. The embryos were stained with the synthetic X-gal substrate to examine *Myf5-LacZ* transgene expression. The protocol has been previously described by the Joshua Wythe Laboratory (https://wythelab.squarespace.com/). E10.5 embryos were fixed for 10 min in fixing solution (2% Formaldehyde, 0.2% Glutaraldehyde, 0.02% Na Deoxycholate and 0.01% NP-40 in 1X PBS), permeabilized overnight in permeabilization solution (0.02% Na Deoxycholate and 0.01% NP-40 in 1X PBS), and incubated at RT for 3-4 hrs in fresh staining solution (5 mM K-Ferricyanide, 5 mM K-Ferrocyanide, 2 mM $MgCl_2$, 0.02% Na Deoxycholate and 0.01% NP-40 in 1X PBS and 1mg/mL X-gal) filtered through a 0.45µM filter. Following staining, the embryos were washed in a permeabilization solution and fixed overnight in 4% PFA. The embryos were then visualized using a Zeiss Stereo Discovery V20, imaged using AxioVision software and FIJI software was used to measure myotome length.

2.7 RNA Extraction and RT-qPCR

Total RNA was extracted from approximately 100,000 (E14.5) and 250,000 (E17.5) sorted GFP$^+$ cells isolated from *Pax7-nGFP* fetal limbs using the PicoPure RNA Isolation Kit (Life Technologies Inc). For these experiments, WT, *mdx*, *mdx.Aak1*$^{+/+}$ and *mdx.Aak1*$^{-/-}$ lines were crossed with *Pax7-nGFP* transgenic mice. Reverse transcriptase cDNA was synthesized using the iSCRIPT Synthesis Kit (Bio-Rad). The RT-qPCR reaction was performed in a final volume of 20µL with SYBR Green PCR Master Mix (Bio-Rad), ROX reference dye (Invitrogen), 0.5µM primers and DNA diluted 1:10. The PCR parameters were as follows: 95°C for 3min, 40 cycles

with 95°C for 20 s, 58°C for 20s, and 72°C for 30s, then 95°C for 10s, and melt curve at 65°C for 5s and 95°C for 5s. *Tbp* and *Gapdh* were used as reference genes at E14.5, while *Rps18* and *Ppia* were used as references genes at E17.5. *Nfix* primer sequences were previously published.[216] Primers are listed in **Table 2.3**.

2.8 Cross-Section Histology

All cross-section staining protocols were previously described (**Appendix A1**).[2] Tissues from embryos and fetal limbs were processed differently. Embryos were embedded in paraffin, while fetal limbs and adult muscles were cryopreserved.

Embryo Tissue Processing and Staining

E10.5 embryos were fixed in fresh 4% PFA for 24 hr, then sent to the Louise Pelletier Histology Core Facility at the University of Ottawa for paraffin embedding and sectioning. Four-micron sections were deparaffinized in xylene for 10min and rehydrated in an ethanol series of 100% EtOH, 95% EtOH, 70% EtOH, and 50% EtOH for 5min each at RT. Sections were rinsed in dH_2O, and antigen retrieval was performed using citrate butter (10mM Sodium Citrate, 0.05% Tween 20, pH 6.0) in a pressure cooker set to 12psi for 10 mins. Sections were then permeabilized (0.1% Triton-X 100, 0.1 M Glycine in PBS) for 10min, treated with 1X TrueBlack Lipofuscin Autofluorescence Quencher (Biotium; #23007) in 70% EtOH for 30-60s, and incubated in blocking solution (5% horse serum, 2% BSA in PBS) for 1hr. M.O.M. blocking reagent (1:40; Vector Laboratories) was added to the blocking buffer for all stains using mouse primary antibodies. Primary antibodies were incubated overnight at 4°C in blocking solution. The following primary antibodies were used: γ-tubulin (1:1000, Abcam), Laminin (1:500, Sigma), MF20 (DSHB, 1:10), Mandag2 (DSHB, 5 μg/mL), Utrn (BD biosciences, 1:200), PAX7

(DSHB,1:1), PAX3 (DSHB, 1:1), and MYOG (Abcam, 1:500). Isotype and species-specific cross absorbed Alexa Fluor secondary antibodies were incubated for 1 hr at RT, followed by DAPI (0.5 μg/mL in PBS) counterstaining and mounting in PermaFluor (Thermo Fisher Scientific). Cross-sections stained with antibodies against TUBG1 for quantifying cell division orientation were acquired on an LSM900 confocal microscope using a Plan-Apochromat 20X/0.8 M27 objective. Using a Plan-Apochromat 20X/0.8 M27 objective, cross-sections stained with PAX7 and MYOG antibodies were imaged using a Zeiss Axio Observer.D1 inverted microscope, while laminin and UTRN stained cross-sections were imaged on an LSM800.

Fetal And Neonatal Limb Processing and Staining

Fetal and neonatal limbs were carefully cut from the body, immersed in 4% PFA for 12 hr at 4°C, and placed in a sucrose gradient of 15% and 30% sucrose (w/V) in PBS overnight at 4°C. The limbs were then embedded in OCT compound (Tissue-Tek), frozen in liquid nitrogen-cooled isopentane, stored at -80°C, and sectioned at 10μm intervals. Antigen retrieval, described above, was performed when staining with an antibody that required epitope unmasking.

Sections were permeabilized for 10 min and incubated in blocking solution with M.O.M. blocking reagent (1:40) for 1hr. Primary antibodies were incubated overnight at 4°C in blocking solution. The following primary antibodies were used: PAX7 (DSHB,1:1), MYOG (Abcam, 1:500), Laminin (Sigma, 1:500), DAG1 (Abcam; 5μg/mL), and COL4A1 (Abcam; 1:500). Slides were incubated with cross absorbed Alexa fluor secondary antibodies in blocking buffer for 1hr at RT, followed by DAPI (0.5 μg/mL in PBS) counterstaining and mounting in PermaFluor (Thermo Fisher Scientific). Antibodies are listed in **Table 2.1**.

Adult Muscle Staining

In the aging and acute injury studies, mice were euthanized, and TA muscles were harvested, weighed, and embedded in Tissue-Tek OCT and frozen in liquid nitrogen-cooled isopentane. Embedded muscles were transversely sectioned at 10 µm-thickness.

Masson's trichrome staining. Muscle sections were fixed in Bouin's solution overnight. After washing in tap water, sections were incubated in Weigert's hematoxylin solution for 10 min and rinsed under running tap water for 10 min. After washing in distilled water, sections were stained with Biebrich scarlet-acid fuchsin solution for 5 min and rewashed in distilled water. Sections were then incubated in a phosphomolybdic-phosphotungstic acid solution for 15 min and transferred to an aniline blue solution for 5 min. Sections were briefly rinsed in water and incubated in 1% glacial acetic acid for 2 min. After washing in distilled water, sections were dehydrated in a 95-100% graded ethanol series and cleared in xylene for 5min. Samples were mounted using DPX mounting media.

Immunostaining. Cross-sections were fixed in 4% PFA 10 min at room temperature, permeabilized in 0.1M glycine, 0.1% Triton X-100 in PBS, and blocked in 5% goat serum, 2% BSA in PBS supplemented with M.O.M. Blocking reagent (Vector Laboratories). Sections were then incubated with primary antibodies overnight at 4°C. The list of primary antibodies is available in **Table 2.1**. Samples were washed 3 times in PBS, incubated 1h at room temperature with Alexa Fluor-conjugated cross-absorbed secondary antibodies at 1:1,000 (ThermoFisher), washed 3 times in PBS and counterstained with Hoechst or DAPI at 1µg/mL in PBS before mounting.

2.9 Histological Cross-Section Analysis

Postnatal sections

Cross-sectional area. Acute and chronic injury images were taken on a Zeiss Axio Observer.D1 inverted microscope or a Zeiss Axio Imager M2 Microscope equipped with a 10x objective and stitched using Fiji software (http://fiji.sc/Fiji). Trichrome-stained cross-sections were used to measure the total cross-sectional area using the trace tool in Fiji. Transplantation images were acquired using a Zeiss Axio Observer.D1 and stitching using Fiji (2 weeks) or a Zeiss Observer7 using a 20x apo objective and stitched using Zeiss ZEN 3.7 blue edition software (4 weeks).

Minimum Feret's diameter. Laminin immunostaining was used to delineate myofibers. Minimum Feret's diameters were measured using the semi-automated SMASH software plugin for MATLAB 2015a for acute and chronic injury experiments.[217] Over 90% of myofibers were quantified for each cross-section studied. FIJI's analyzed particle function was used to assess Minimum Feret's diameters for the transplantation study.

Fiber number. Total myofiber count per cross-section was verified by manual validation of SMASH myofiber masks and original images of injury series experiments for acute and chronic injury time courses. The total myofiber count per cross-section was enumerated for transplantation studies using FIJI's analyze particle function.

Collagen deposits. Collagen area was analyzed using Masson's trichrome staining by measuring the area of thresholded pixels in images extracted from the red channel. The positively stained tissue was calculated as a fraction of the total cross-sectional area.

Lipid droplets. Fat infiltration was calculated using Bodipy staining by measuring the area of thresholded pixels in Bodipy single channel images. The positive stained tissue was calculated as a fraction of the cross-sectional area.

Diaphragm thickness measurements. Diaphragm hypertrophy was assessed by measuring the thickness of diaphragm cross-sections at a minimum of 15 points along each muscle using FIJI.

Muscle stem cell number. Chronic and acute injury images of PAX7 immunostaining were taken on a Zeiss Axio Observer.D1 inverted microscope using a 20x apochromatic objective and analyzed on ZEN software. The number of $PAX7^+$ cells per mm^2 was averaged from 6 to 12 fields to cover more than 90% of the tissue. During disease progression, we aimed to compare regions of non-acute injury. Thus, abnormal frames with exceptionally high numbers of PAX7 cells and small centrally nucleated myofibers (regions of microinjury) were excluded. For transplantation study and neonatal sections, the entire graft/muscle was imaged using a Zeiss Axio Observer.D1 and stitching using Fiji (2-week grafts) or a Zeiss Observer7 (4-week grafts and neonatal muscle) using a 20x apochromatic objective and stitched using Zeiss ZEN 3.7 blue edition software. The entire graft was enumerated for $PAX7^+$ cells, while the whole *tibialis anterior* (TA) and EDL cross-section was enumerated for neonatal hindlimb sections.

Embryonic Sections

Characterization of myogenic progenitor cell division. The number of asymmetric and symmetric cell division were counted along the dermomyotome/ myotome border. Asymmetric divisions were considered any cell division with an orientation of 60-90 degrees to the myotome plane. Divisions with a 0- and 30-degree division plane along the myotome were considered symmetric.

Myogenic cell analysis. Fetal and neonatal limb cross-sections were imaged with a Zeiss Observer 7 widefield microscope or an LSM900 confocal microscope, both equipped with a Plan-Apochromat 20X/0.8 M27 objective. Automated cell counting was conducted using IMARIS software (v9) with the count spot function, or FIJI analyze particle function. Only one type of

automation was used per individual experiment. Myofiber size analysis was conducted with IMARIS using the outline cell function and dystroglycan or collagen IV staining.

2.10 Whole Mount Embryo Immunostaining

Whole mount staining was modified from the 2016 iDISCO protocol (https://idisco.info/idisco-protocol/).[218] Embryos were fixed in 4% PFA for 12 hours, permeabilized (0.4% Tx-100, 10% DMSO and Glycine 0.1M in PBS) for 4 hr at RT and blocked overnight at 4°C (125nM Glycine, 5% Donkey serum, 2% BSA, 0.2% Tx-100 and 5% DMSO in PBS). The embryos were then incubated in primary antibodies diluted in staining solution (5% DMSO, 3% Donkey Serum, and 0.2% Tween 20 in PBS) for 24 hr at 4°C. The following primary antibodies were used: PAX7 (DHSB), PAX3 (DHSB), MYOG (Abcam, 1:250), and dystroglycan (Mandag1, DHSB, 5µg/mL). PAX3 and PAX7 hybridoma supernatants grown in house were purified using a commercial kit and used at a 10µg/mL concentration (Abcam ab109207). Following extensive washes in PBS with 0.2% Tween (PSB-Tw) at RT, the embryos were incubated for 24 hr at 4°C in AlexaFluor secondary antibodies diluted in a staining solution. After additional washing, DAPI (1 µg/mL in staining solution) counterstaining was performed for 1 hr at RT. Antibodies are listed in **Table 2.1**.

Optical clearing was performed using a glycerol series of 20%-90%, after which the embryos were mounted on glass slides in glycerol mounting media (90% glycerol, 0.5% N-propyl gallate in TBS pH 8.5). Images illustrated in Fig. 1 were acquired using a Leica SP8 confocal microscope equipped with a galvo stage and a Plan- Apochromat 20X/0.75 IMM CORR CS2 objective. Automated cell counting was conducted using IMARIS software count spot function (version 9). Fig. S1F depicting dystroglycan whole mount staining was acquired using an LSM800 using a Plan-Apochromat 20X/0.8 M27 objective. FIJI's despeckle function or gaussian filtering

(sigma value of 1) was applied to 20X confocal images for immunofluorescence image illustrations. The same processing was performed within each experiment.

2.11 Western Blot

Embryonic tissues were collected, snap frozen in liquid nitrogen, homogenized and extracted in RIPA lysis buffer (150mM NaCl, 0.1% TritonX_100, 0.5% sodium deoxycholate, 0.1% SDS, 50mM Tris_HCl pH8.0) supplemented with proteinase inhibitors (Roche) for 1 hour on ice with vertexing every 10 min. Extracts were heated in Laemmli buffer for 5 minutes at 95°C then resolved by SDS-PAGE, transferred to a PVDF membrane and analyzed by western blot with antibodies against dystrophin (DYS1, Leica,1:20), utrophin (BD Bioscience, 1:500) and GAPDH (1:1000). Blocking was done using 5% milk in TBST and primary antibodies were incubated overnight in. blocking buffer. Secondary antibodies conjugated to HRP (1:5000) were diluted in blocking buffer for 1 hr. The blots were visualized using ECL with a BioRad digital imager. Antibody details are listed in **Table 2.1**.

2.12 Bulk RNA-Sequencing Library Generation and Gene Expression Analysis

Myoblast Isolation, Culture, and RNA Extraction

Primary myoblasts were derived from hindlimb muscles of 6–8-week-old male mice by magnetic cell separation (MACS) as previously described.[219] Briefly, cells were isolated based on lineage-negative markers ($CD31^-$, $CD11b^-$, $CD45^-$, $SCA1^-$) and positive selection for α7-INTEGRIN. Myoblasts were cultured on collagen-coated dishes in Ham's F10 medium (Wisent, 318-051-CL) supplemented with 20% FBS, 1% penicillin/streptomycin, and 5ng/mL of FGF2 (Millipore, GF003AFMG). Myoblast differentiation was induced for 2 days in Ham's F10:DMEM 1:1

(Wisent, 319-016-CL) supplemented with 5% horse serum and 1% penicillin/streptomycin. Total RNA was extracted using the Nucleospin RNA II kit (Macherey-Nagel), according to the manufacturer's instructions.

MuSC Isolation and RNA Extraction

MuSCs were obtained from uninjured and 3-day CTX-injured *Pax7-nGFP* TA and *gastrocnemius* muscle. MuSCs were sorted by gating a mononuclear cell population of α7-INTEGRIN$^+$, GFP$^+$ (PAX7$^+$), CD31$^-$, CD45$^-$, SCA1$^-$, CD11b$^-$ using a MoFlo XDP cell sorter (Beckman Coulter). Antibodies are listed in **Table 2.1**. Total RNA was isolated using Arcturus Picopure RNA extraction kit (Thermo Fisher).

Sample sizes. 24 biological samples were used for RNA-sequencing analysis: n = 3 quiescent MuSCs, n = 3 activated MuSCs, n = 3 myoblasts and n = 3 myotubes for each genotype (WT and *mdx*). For quiescent MuSCs, all hindlimb muscles from 2-3 mice were combined to obtain one sample. For activated MuSCs, myoblasts and myotubes, each sample corresponded to one mouse.

Library Construction, Sequencing, and Analysis

Library construction was performed with 20ng of input total RNA using the NEBNext Ultra II Directional RNA Library Prep Kit for Illumina - polyA mRNA workflow (New England Biolabs). The libraries were sequenced with a NextSeq 500 High Output 75-cycle kit (Illumina). RNA-seq reads were mapped to transcripts from GRCm38_GENCODE.vM19 using salmon v0.13.1.[220]. The data was loaded into R using the tximport package, and the gene/count matrix was filtered to retain only genes with five or more mapped reads in two or more samples. Differential gene expression testing and PCA plotting were performed using DESeq2.214. An adjusted *p*-value less than 0.05 defined differentially expressed genes. Fold change was determined using lfcShrink, applying the apeglm method (v1.6.0).[221] Differentially expressed genes were based on a log2 fold change

greater than 2 and an adjusted *p*-value less than 0.05. Functional analysis of the differentially expressed genes was examined using Gene Ontology Biological Processes,[222,223] and the R application clusterProfiler.[224]

2.13 Single Cell RNA-Sequencing

Postnatal libraries

WT and *mdx Myf5creER;ROSA-mTmG* were subjected to four intraperitoneal tamoxifen injections (100 µL of 20 mg/mL in corn oil) at 24h intervals prior to injury. MuSCs ($mGFP^+$ α7-$INTEGRIN^+$,GFP^+, $CD31^-$, $CD45^-$, $SCA1^-$, $CD11b^-$) were isolated from the uninjured and 5-days post CTX injured hindlimb muscles of male WT and *mdx* tamoxifen-treated *Myf5creER;ROSA-mTmG* mice. Antibodies are listed in **Table 2.1**. The isolated cells were then captured using the 10X Genomics Chromium Platform and sequenced to a mean read depth of 21,000 reads/cell using the Illumina NextSeq 500. The CellRanger v7.1.0 pipeline (10X Genomics) with default parameters aligned reads to GENCODE vM25 (GRCm38/mm10).

Filtering, qualify control and analysis were performed using R (v4.3.1) and the package Seurat (v4.3.0).[225] Genes expressed in less than 3 cells, and cells expressing fewer than 200 genes were excluded from the analysis. Cells with more than 30% mitochondrial reads were also removed. Following cell doublet removal using scDblFinder,[226] 4205 WT and 6980 *mdx* high-quality cells were captured in the uninjured libraries. Similarly, 4616 WT and 5396 *mdx* cells were captured in the injured libraries.

Individual libraries were analyzed separately prior to integration using standard Seurat processing steps. We then performed Harmony integration on the combined data using the RNA assay.[227] Following normalization and scaling of the data, we performed principal component

analysis on the top 3000 genes in the integrated object, followed by Uniform Manifold Approximation Projection (UMAP) embedding using the top 20 principal components. Clustering was performed using a resolution of 0.3, after which clusters were annotated using a combination of known cell markers and Seurat's Find All Markers function that were inputted into the online tool Metascape.[228] The AddModuleScore Seurat function was used to evaluate the enrichment of 400 quiescence-enriched genes.[119] Publication graphics were generated using Seurat, SCpubr and scCustomize.[225,229,230]

Fetal Libraries

The libraries were generated in biological duplicates using GFP^+ cells isolated from WT and *mdx Pax7-nGFP* fetal limbs with the 10X Genomics 3' v3 platform. The libraries were sequenced together to a mean read depth of 17,013 reads/cell using the Illumina NextSeq 500. Reads were aligned to the GENCODE vM25 (GRCm38/mm10) reference genome using CellRanger (v7.1.0) with default parameters.

Filtering, qualify control and analysis were performed using R (v4.3.1) and the package Seurat (v5.1.0).[225,231] The following were excluded from analysis: genes expressed in fewer than 3 cells, cells expressing fewer than 500 or greater than 5000 genes, and cells expressing greater than 20% mitochondrial genes. Doublets were also excluded using the package scDblFinder.[226] Following filtering, 10,921 and 11,168 cells were observed in the two WT libraries, respectively, while 10,292 and 15,050 cells remained in the two *mdx* libraries.

The combined libraries were normalized using SCTransform (v2),[232,233] after which we performed principal component analysis, Uniform Manifold Approximation Projection (UMAP) embedding with the top 30 principal components, and cell clustering with a resolution of 0.2. Custers were then annotated using known cell markers and Seurat's FindAllMarkers function,

where cluster markers were inputted into online tools, including Metascape and gprofiler.[228,234] Mitosis S and G2/M phase scores were assigned using Seurat's CellCycleScoring function. A contaminating cluster of *Ptprc*$^{+}$ immune cells and low-quality cells, characterized by lower relative nfeatures and ncount RNA and lack of meaningful biological identity, accounted for less than 2% of the libraries and were omitted from downstream analysis.

Next, we analysed the myogenic cell clusters alone using Seurat's subset function. First, cell cycle regression was performed using SCTransform normalization, after which PCA analysis, UMAP embedding with the top 25 principal components, and clustering with a resolution of 0.6 was repeated. Clusters were annotated by known cell markers and Seurat's FindAllMarkers function. Graphics were generated using Seurat, SCpubr, and scCustomize.[225,229,230] Adobe Illustrator (v29) was used for minor edits to line size, text, and colour.

Differential gene expression testing between the WT and *mdx* libraries was conducted using the Seurat FindMarkers function using a minimum cell fraction (min.pct) of 0.1 and an adjusted *p*-value less than 0.05. Functional analysis of enriched genes was conducted using Gene Ontology Biological Processes,[222,223] and the R application clusterProfiler using an adjusted *p*-value of 0.05 and log2 fold change greater than 0.4.[224]

2.14 Quantification and Statistical Analysis

Statistical evaluation was performed using the Student's two-tailed t-test tests between two groups and using a one-way ANOVA followed by a post hoc test between more than two groups. Two-way ANOVA with post hoc tests was conducted when more than two groups and variables were compared. Correction for multiple comparisons was conducted. All statistical tests and graph visualization were performed using GraphPad Prism v10. The number of independent

experimental replications and the statistical test used is reported in the figure legends. Data is presented using a box plot where the whiskers indicate the maximum and minimum values or bar plots where the data is presented as mean ± SEM. For all statistical tests, p-value < 0.05 was considered statistically significant. Unless otherwise indicated, the significance level is indicated as follows: *$p < 0.05$, **$p < 0.01$, ***$p < 0.001$.

2.15 Figures

All figures included in Chapters 1-5 were designed and created using Adobe Illustrator V29. Schematics were created in Illustrator or adapted from drawings originally drawn in Microsoft PowerPoint.

2.16 Data Availability

All bulk RNA-seq and scRNA-seq data related to Chapter 3 have brna deposited in GEO under accession GSE268316 (RNA-seq: GSE268313; scRNA-seq: GSE268314). Data relating to Chapter 4 have been deposited in GEO under accession GSE274925.

Table 2.1 List of antibodies

Primary Antibody	Company	Reference
y-Tubulin	Abcam	Cat#ab11317; RRID:AB_297921
Laminin	Sigma	Cat#L9393; RRID:AB_477163
Laminin [4H8-2]	Sigma-Aldrich	Cat#L0663; RRID:AB_
Myosin (MF 20)	DSHB	Cat#MF 2; RRID:AB_2147781
Dystroglycan MANDAG2 (7D11)	DSHB	Cat# MANDAG2; RRID: AB_2618140
Utrophin, clone 55	BD Biosciences	Cat# 610896; RRID: RRID:AB_398213
PAX7	DSHB	Cat#PAX7; RRID:AB_2299243
PAX3	DSHB	Cat#PAX3; RRID: AB_528426
Myogenin [EPR4789]	Abcam	Cat#ab124800, RRID: AB_10971849
Myogenin [F5D]	Santa Cruz	Cat#sc12732;RRID:AB
DAG1 [IIH6C4]	Abcam	Cat#ab234587; RRID:AB_2910177
PARD3	Millipore	Cat# 07-330; RRID:AB_2101325
NUMB	Cell Signaling Technology	Cat# 2756; RRID:AB_2154298
MARK2	LSBio (LifeSpan)	Cat#LS-B7503-50; RRID:AB_11233034
GFP	Abcam	Cat# ab13970; RRID:AB_300798
Dystrophin MANDYS16(1B12)	DSHB	Cat#MANDYS16(1B12); RRID:AB_2618166
DMD (Dys1)	Leica Biosystems	Cat#NCL-DYS1; RRID:AB_442080
Dystrophin	Abcam	Cat#ab15277; RRID:AB
Collagen I (COL1)	Abcam	Cat#ab21286; RRID:AB
GAPDH	UBC Ablab	Cat#21-0017-01; RRID:AB
Alexa647 mouse anti-Integrin alpha7 (clone R2F2)	UBC AbLab	Cat#67-0010-10; RRID:AB
Integrin alpha7-Biotin (clone 3C12)	Miltenyi Biotec	Cat#130-102-125; RRID:AB
Satellite Cell Isolation Kit	Miltenyi Biotec	Cat#130-104-268; RRID:AB
BV421 mouse anti-SCA1 (clone D7)	BD Biosciences	Cat#553108; RRID:AB
BV421 mouse anti-CD45 (clone 30-F11)	BD Biosciences	Cat#12-0451-83; RRID:AB
BV421 mouse anti-CD31 (clone 390)	BD Biosciences	Cat#12-0311-81; RRID:AB
BV421 mouse anti-CD11b (clone M1/70)	BD Biosciences	Cat#12-0112-81; RRID:AB
PE-Cy7 mouse anti-CD106 (VCAM1)	BioLegend	Cat#105719; RRID:AB
PerCP/Cyanine5.5 Streptavidin	BioLegend	Cat#405214; RRID:AB
PE-Cy7 CD45	BD Biosciences	Cat#552848; RRIB: AB_394489
PE-Cy7 CD31	BD Biosciences	Cat#561410; RRIB: AB_1061200
PE-Cy7 Ly-6A/E (Sca-1)	BD Biosciences	Cat#561021; RRIB: AB_647253
Collagen IV	Abcam	Cat# ab6586; RRID:AB_305584
Goat Anti-Rabbit IgG (H+L), Alexa Fluor 488	Thermo Fisher Scientific	Cat# A-11008; RRID:AB_14316
Goat Anti-Rabbit IgG (H+L), Alexa Fluor 546	Thermo Fisher Scientific	Cat#A-11010; RRID:AB_2534077
Goat Anti-Rabbit IgG (H+L), Alexa Fluor 647	Thermo Fisher Scientific	Cat# A-21244; RRID:AB_2535812
Goat Anti-Mouse, Alexa Fluor 488	Thermo Fisher Scientific	Cat#A-21121; RRID:AB_2535764
Goat Anti-Mouse IgG1 Antibody, Alexa Fluor 546	Thermo Fisher Scientific	Cat#A-21123; RRID:AB_2535765
Goat Anti-Mouse IgG1, Alexa Fluor 647	Thermo Fisher Scientific	Cat#A-21240; RRID:AB_2535809
Goat anti-Mouse IgM, Alexa Fluor 488	Thermo Fisher Scientific	Cat#A-21042; RRID:AB_2535711

Goat Anti-Mouse IgG2a, Alexa Fluor 488	Thermo Fisher Scientific	Cat#A-21131; RRID:AB_2535771)
Goat Anti-Mouse IgG2a, Alexa Fluor 546	Thermo Fisher Scientific	Cat# A-21133; RRID:AB_2535772

Table 2.2 List of Reagents

Primary Antibody	Company	Reference
Ibidi 12-well slides	Ibidi	81201
1 Kb Plus DNA Ladder	Invitrogen	10787026
7-AAD (7-Aminoactinomycin D)	STEMCELL Technologies	75001.1
Agarose (Low-EEO/Multi-Purpose/Molecular Biology Grade)	Thermo Fisher Scientific	BP160-500
bisBenzimide Hoechst 33342 trihydrochloride	Sigma-Aldrich	B2261
BD Cytofix/Cytoperm™ Fixation/Permeabilization Kit	BD Biosciences	554714
Cardiotoxin	Latoxan	L8102
Chromium Single Cell 3' GEM Library & Gel Kit v3	10X Genomics	
Collagenase B	Sigma-Aldrich	11088831001q
cOmplete™, Mini, EDTA-free Protease Inhibitor Cocktail	Roche	11836170001
Corning™ Cell-Tak Cell and Tissue Adhesive	Thermo Fisher Scientific	CB40240
DAPI (4',6-Diamidino-2-Phenylindole, Dihydrochloride)	Thermo Fisher Scientific	D1306
Dispase II	Sigma-Aldrich	4942078001
DMEM, high glucose, Pyruvate	Thermo Fisher Scientific	11995065
Duolink® In Situ Detection Reagents Red	Sigma-Aldrich	DUO92008
Ethidium Bromide, UltraPure	Thermo Fisher Scientific (Invitrogen)	15585011
FBS Performance	Wisent	098-150
Hams F10 medium	Wisent	318-051-CL
High-Fidelity Phusion Polymerase	Thermo Fisher Scientific	F530S
iSCRIPT Synthesis Kit	BioRad	1708891EDU
M.O.M. (Mouse on Mouse) Blocking Reagent	Vector Laboratories	VECTMKB22131
NucleoSpin Tissue kit for DNA from cells and tissue	Macherey-Nagal	740952.50
Precision Plus Protein Kaleidoscope Prestained Protein Standards	BioRad	1610375
Paraformaldehyde 32% Aqueous Solution EM Grade	Electron Microscopy Sciences	15714
Paraformaldehyde, crystalline	Sigma-Aldrich	P6148
Penicillin Streptomycin	Thermo Fisher Scientific	SV30010
Permafluor	Thermo Fisher Scientific	TA006FM
PicoPure™ RNA Isolation Kit	Applied Biosystems	KIT0204
Red Blood Cell Lysing Buffer Hybri-Max	Sigma	R7757
RNAscope Multiplex Fluorescent Reagent Kit V2	ACD	
ROX reference dye	Invitrogen	12223012
Sucrose	Thermo Fisher Scientific	S5-500
SYBR Green PCR Master Mix	Bio-Rad	1708884
Tamoxifen	Sigma-Aldrich	T5648
Wheat Germ Agglutinin Alexa 647 conjugate	Fisher	W32466
Xylene	MilliporeSigma	534056
Zombie NI dye	BioLegend	423106

Table 2.3 List of Primers

RT-qPCR	**Sequence**
Gapdh-F	TGTGTCCGTCGTGGATCTGA
Gapdh-R	CCTGCTTCACCACCTTCTTGA
Tbp-F	TTTGGCTAGGTTTCTGCGGT
Tbp-R	GCCCTGAGCATAAGGTGGAA
Ppia-F	CACTGCCAAGACTGAATG
Ppia-R	GTCGGAAATGGTGATCTTC
Rps18-F	AACGGTCTAGACAACAAGCTG
Rps18-R	AGTGGTCTTGGTGTGCTGAC
Nfix-F	CTGGCTTACTTTGTCCACACTC
Nfix-R	CCAGCTCTGTCACATTCCAGAC
Myog-F	CAA CCC AGG AGA TCA TTT G
Myog-R	CAT ATC CTC CAC CGT GAT
Pax7-F	GACGACGAGGAAGGAGACAA
Pax7-R	ACATCTGAGCCCTCATCCAG
Genotyping	**Sequence**
SX-F	GATGATTTGAGTGGAAATGTGAGGTA
SX-R	CTTATGTTTATAGGCATGCACCATGTA
Aak1-F	GCAAGAGGGAGATCCAGATCATGG
Aak1-R	CTACCATCCTTCTGGACAGGCTC

Table 2.4 List of Software

Software	Company	Reference
FlowJo v10	FLOWJO, LLC	RRID:SCR_008520
Zen 3.7 blue edition	Zeiss	RRID:SCR_013672
AxioVision Imaging System	Zeiss	RRID:SCR_002677
Leica Application Suite X (LasX)	Leica Microsystems	RRID:SCR_013673
IMARIS v9	Oxford Instruments	RRID:SCR_007370
FIJI	Open Source	RRID: SCR_002285
R V4.3.1	R Core Team	RRID:SCR_001905
RStudio	Posit Software	RRID:SCR_000432
Seurat V5	(Stuart *et al*, 2023)	RRID:SCR_016752
Cell Ranger v7	10X Genomics	RRID:SCR_017344
scCustomize	(Marsh, 2021)	doi.org/10.5281/zenodo.5706430
SCpubr	(Blanco-Carmona, 2022)	github.com/enblacar/SCpubr
g:Profiler	(Raudvere *et al.*, 2019)	RRID:SCR_006809
Gene Ontology	The Gene Ontology Consortium	RRID:SCR_002811
Tximport	(Soneson *et al.*, 2015)	RRID:SCR_016752
DoubletFinder	(McGinnis *et al.*, 2019)	RRID:SCR_018771
ggplot2	(Wickham, 2009)	RRID:SCR_014601
GraphPad Prism V10	Graphpad Software Inc.	RRID:SCR_002798
Adobe Illustrator V29	Adobe Inc	RRID:SCR_010279
PowerPoint	Microsoft	

Table 2.5 List of Mouse Strains

Referred name	Full stain name	Identifier
WT	C57BL/10ScSnJ	JAX #000476
mdx	C57BL/10ScSn-*Dmd*^{mdx}/J	JAX #001801
Myf5-LacZ	*Myf5*^{tm1Pas}/J	JAX #018626
Pax7-nGFP	B6.Cg-Tg(Pax7-EGFP)15Tajb/J	JAX #036759
ROSA-nTnG	B6N.129S6-*Gt(ROSA)26Sor*$^{tm1(CAG-tdTomato*,-EGFP*)Ees}$/J	JAX #023035
Myf5-Cre	B6.129S4-*Myf5*$^{tm3(cre)Sor}$*/J*	JAX #007893
CAG-GFP	C57BL/6-Tg(CAG-EGFP)131Osb/LeySopJ	JAX #006567
Myf5CreER	*Myf5*$^{tm1(cre/Esr1*)Trdo}$/J	JAX #023342
R26R^{mTmG}	*Gt(ROSA)26Sor*$^{tm4(ACTB-tdTomato,-EGFP)Luo}$/J	JAX #007576
NSG	NOD.Cg-*Prkdc*^{scid} *Il2rg*^{tm1Wjl}*/SzJ*	JAX #:005557
Aak1$^{-/-}$	*Aak1*$^{tm1a(EUCOMM)Hmgu}$	EMMA ID: EM:08493

Chapter 3: Intrinsic Muscle Stem Cell Dysfunction Contributes to Impaired Regeneration in the *mdx* Mouse

The results presented in Chapter 3 were reproduced from the following publication with permission from Wiley (see Preface and Copyright Acknowledgment):

Marie E Esper*, Caroline E Brun*, Alexander YT Lin, Peter Feige, Marie J Catenacci, Marie-Claude Sincennes, Morten Ritso, and Michael A Rudnicki, Intrinsic Muscle Stem Cell Dysfunction Contributes to Impaired Regeneration in the *mdx* Mouse. Journal of Cachexia, Sarcopenia and Muscle. 2025;16(1):e13682.

*Contributed equally to this work.

3.1 Myofiber Hypertrophy, Hyperplasia, and Reduced Force Generation in *mdx* Muscle

To characterize the physiological consequences of dystrophin deficiency, we first assessed the TA muscle of wild type (WT) and *mdx* mice from 13 to 56 weeks of age. Despite the significantly lower body weight of *mdx* mice compared to age- and sex-matched WT mice (**Figure 3.1A**), the *mdx* TA was heavier from 26 to 56 weeks of age (**Figure 3.1B**), in agreement with previous reports.[235–237]

In DMD patients, muscle mass is progressively substituted by fat and fibrotic tissue, thus reducing muscle force generation.[168] To assess whether fat infiltration or fibrosis correlates with changes in *mdx* muscle function, we performed trichrome and Biodipy staining to label collagen deposits and lipid droplets on age-matched WT and *mdx* TA cross-sections. Muscle fibrosis did not change in the WT muscle but increased from 26 weeks in *mdx* mice (**Figure 3.1C,B**). No significant change in fat deposition occurred in either WT or *mdx* TA muscles from 13 to 36 weeks, while *mdx* muscles had a marked reduction in lipid droplets at 52 weeks compared to WT animals (**Figure 3.1E,F**).

Histological analysis of TA cross-sections revealed that the number of *mdx* myofibers increased with age (**Figure 3.2A,B**). As previously observed,[238] the mean diameter of TA myofibers did not change significantly from 13 to 56 weeks in WT or *mdx* mice (**Figure 3.2C**). However, the *mdx* myofiber size distribution broadened with the presence of larger myofibers and elevated numbers of small myofibers (**Figure 3.3A,B**).[238] The distributional change in myofiber size with age differed for each genotype. WT myofibers increased in size from 13 to 36 weeks, while the number of large *mdx* myofibers remained unchanged, and small myofibers increased significantly from 36 to 52 weeks (**Figure 3.3C**).

To study the functional consequence of altered *mdx* muscle morphology, we measured *in situ* isometric force of the TA muscle. WT and *mdx* mice maintained comparable maximum tetanic force that declined with age (**Figure 3.4A**). However, when accounting for the TA displacement volume, *mdx* mice had significantly decreased specific force at all time points (**Figure 3.4B,C**), aligning with previous reports.[236,239] The normalized maximum specific force declined with age in WT mice, while no significant change was observed from 13 to 52 weeks in *mdx* mice (**Figure 3.4C)**.

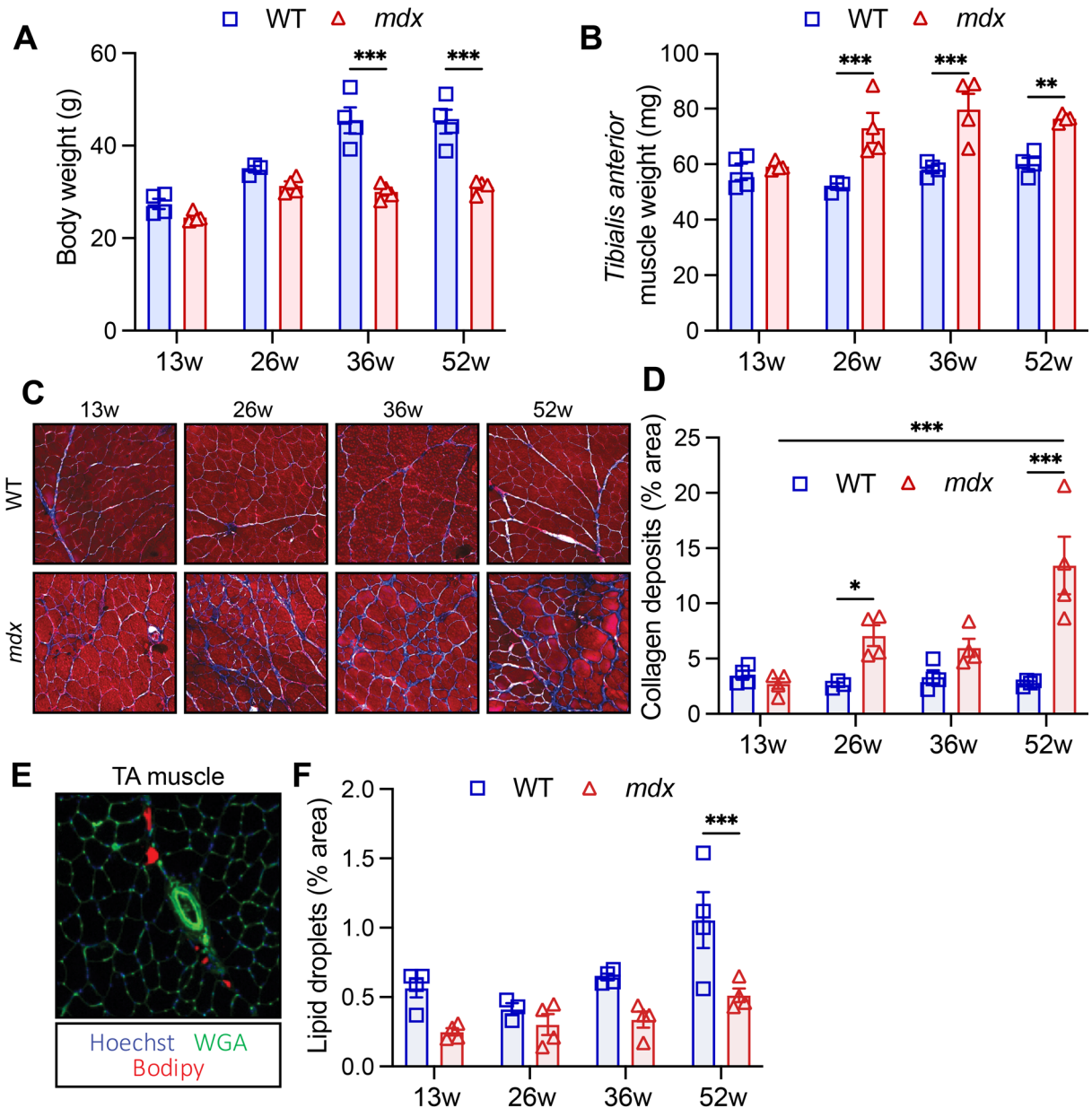

Figure 3.1 Progressive changes in the *tibialis anterior* occur with age in the *mdx* mouse.
A Body weight of wild type (WT) and *mdx* mice from 13 to 56 weeks of age. **B** Weight of WT and *mdx tibialis anterior* (TA) muscle from 13 to 56 weeks of age. **C** Representative Trichrome staining of TA cross-sections 13 to 56 weeks of age. **D** Quantification of collagen content (blue) in TA muscle cross-sections stained by Trichrome from 13 to 56-week-old WT and *mdx* mice. **E** Representative image of lipid droplets labelled by Bodipy on TA muscle cross-section. **F** Lipid droplet quantification in WT and *mdx* TA cross-sections from 13 to 56 weeks of age. Data presented as mean values ± SEM. Two-way ANOVA corrected for multiple comparisons using Sidak's test (*$p < 0.05$; **$p < 0.01$; ***$p < 0.001$). n = 4 WT and 4 *mdx* 13-week-old mice, n = 3 WT and 4 *mdx* 26-week-old mice, n = 4 WT and 4 *mdx* 36-week-old mice, n = 4 WT and 4 *mdx* 52-week-old mice.

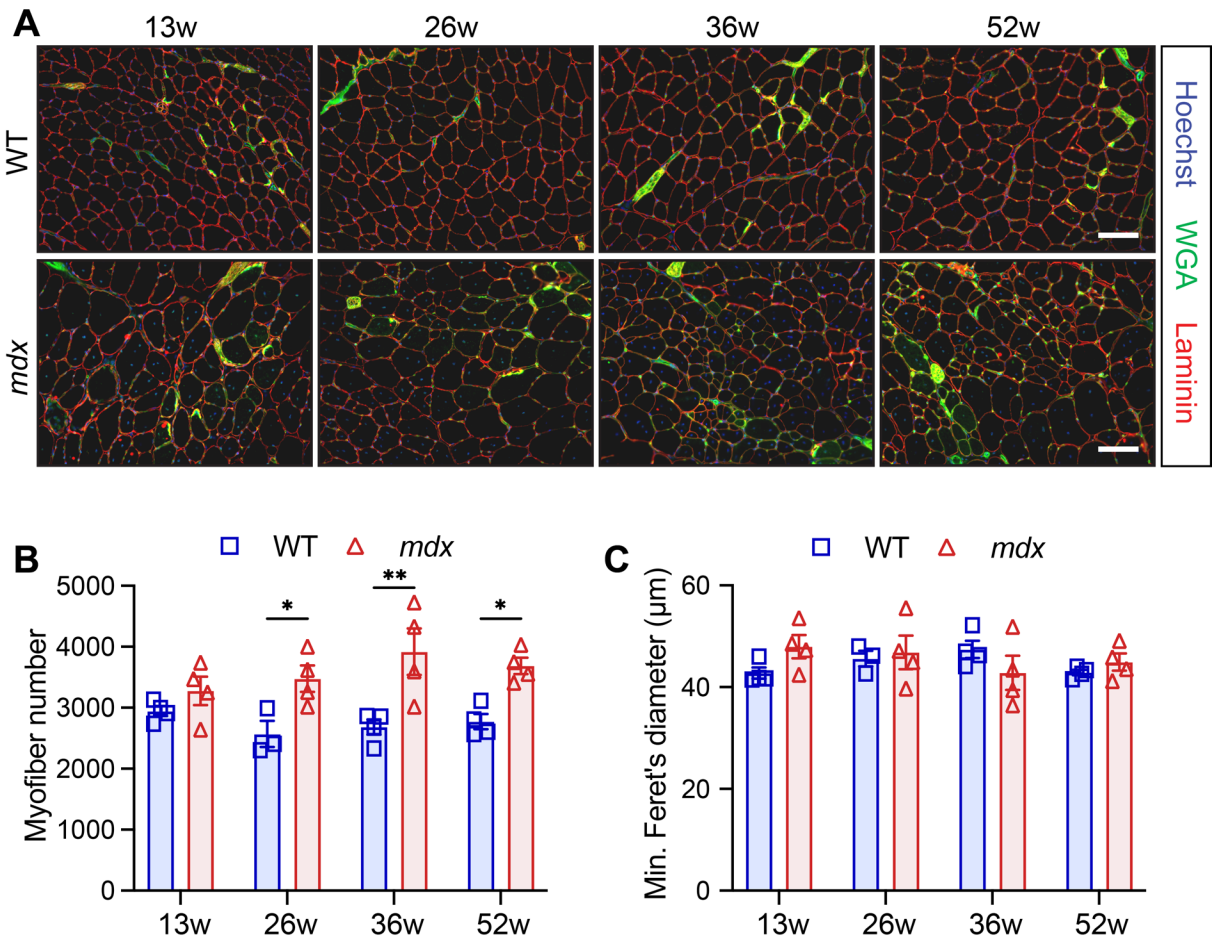

Figure 3.2 Increased number of myofibers on *mdx tibialis anterior* muscle cross-sections
A Representative immunofluorescence images of transversal *tibialis anterior* (TA) muscle sections from 13-, 26-, 36- and 52-week-old wild type (WT) and *mdx* mice. LAMININ (red) delineates the myofibers, WGA (green) stains the connective tissues, and Hoechst (blue) labels the nuclei. **B** Quantification of the number of myofibers per transversal TA muscle sections. **C** Mean TA myofiber size using the minimum Feret's diameter. Two-way ANOVA corrected for multiple comparisons using Sidak's test (*$p < 0.05$; **$p < 0.01$). n = 4 WT and 4 *mdx* 13-week-old mice, n = 3 WT and 4 *mdx* 26-week-old mice, n = 4 WT and 4 *mdx* 36-week-old mice, n = 4 WT and 4 *mdx* 52-week-old mice.

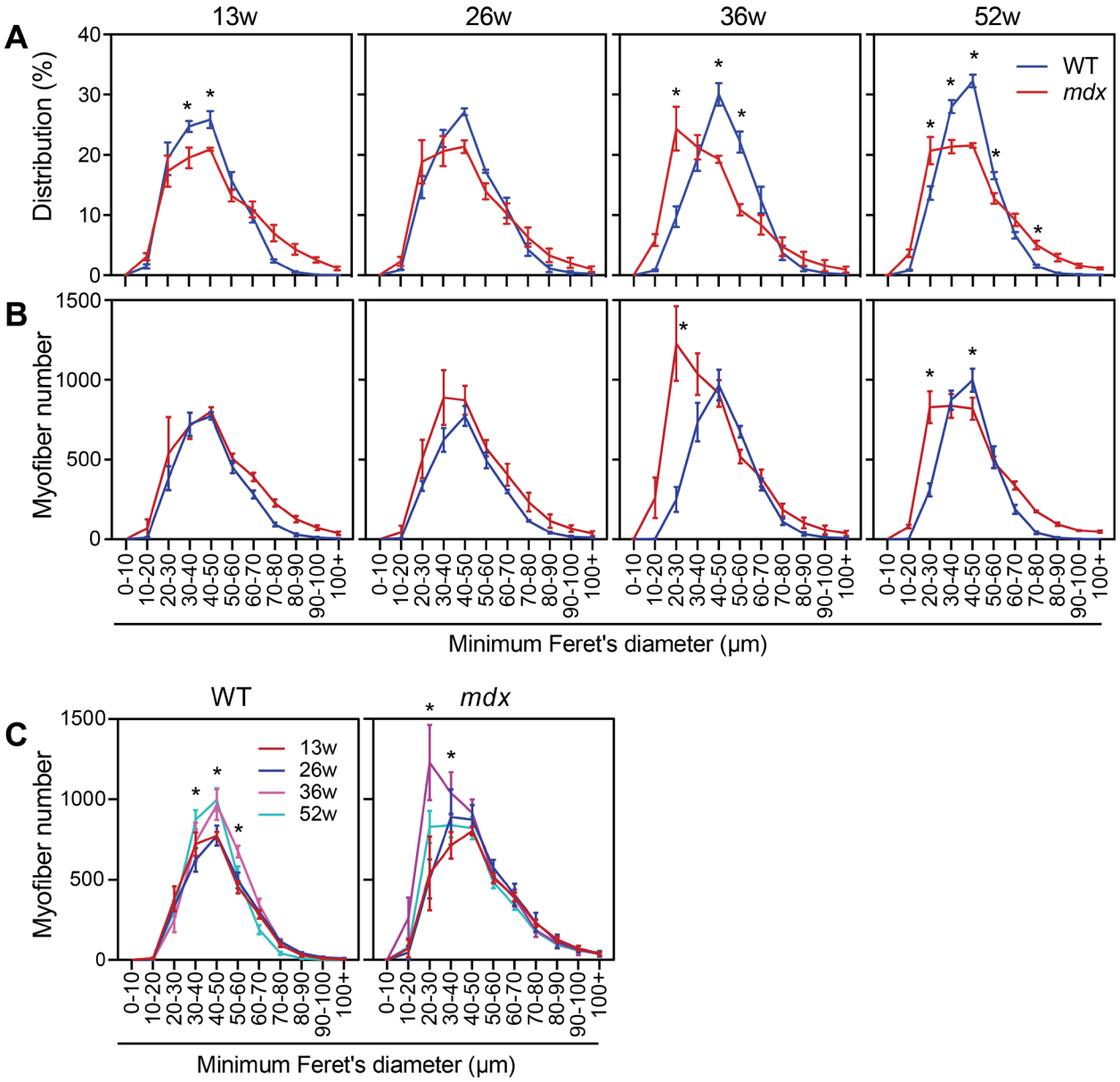

Figure 3.3 Broadened myofiber size distribution in the *mdx tibialis anterior* muscle.
A-B Myofiber size distribution quantified on *tibialis anterior* (TA) cross-sections using minimum Feret's diameter and illustrated by number of myofibers (A) and proportional distribution (B) from 13-, 26-, 36- and 52-week-old wild type (WT) and *mdx* mice. **C** TA myofiber size distribution using minimum Feret's diameter and divided by genotype. Data presented as mean values ± SEM. Two-way ANOVA corrected for multiple comparisons using Sidak's test (*$p < 0.05$). n = 4 WT and 4 *mdx* 13-week-old mice, n = 3 WT and 4 *mdx* 26-week-old mice, n = 4 WT and 4 *mdx* 36-week-old mice, n = 4 WT and 4 *mdx* 52-week-old mice. (Related to **Figure 3.2**)

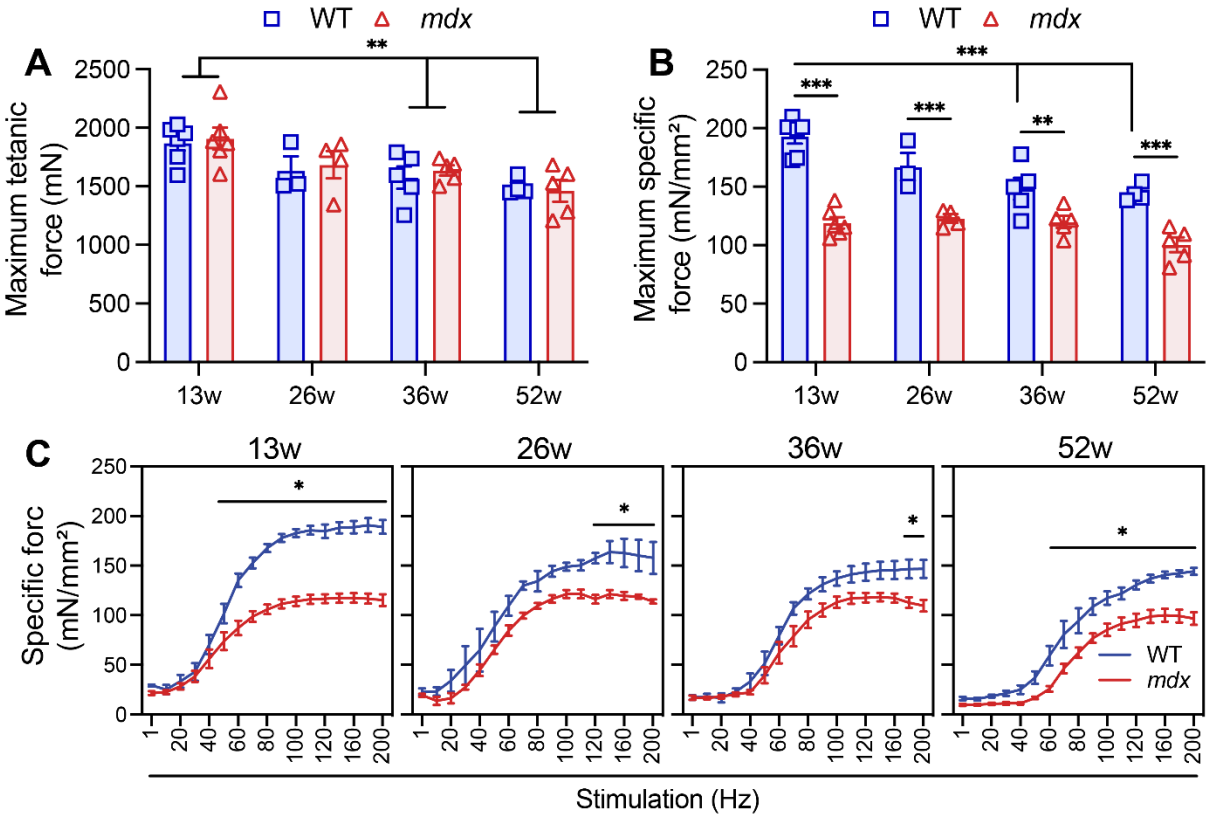

Figure 3.4 Reduced specific force in *mdx* tibialis anterior muscle is consistent with age.
A-B Maximum tetanic force (A) and maximum specific force (B) of *tibialis anterior* (TA) muscles from 13-, 26-, 36- and 52-week-old wild type (WT) and *mdx* mice. **C** Specific force of WT and *mdx* TA muscle from 13 to 56 weeks of age. Data presented as mean values ± SEM. Two-way ANOVA corrected for multiple comparisons using Sidak's test (*$p < 0.05$; **$p < 0.01$; ***$p < 0.001$). n = 6 WT and 6 *mdx* 13-week-old mice, n = 3 WT and 4 *mdx* 26-week-old mice, n = 5 WT and 5 *mdx* 36-week-old mice, n = 4 WT and 5 *mdx* 52-week-old mice.

3.2 Severe Fibrosis and Decreased Myofiber Diameter in the *mdx* Diaphragm

The *mdx* diaphragm closely recapitulates the degenerative pathology of DMD skeletal muscle.[240] To examine the effect of chronic regeneration cycles on the *mdx* diaphragm, we assessed histological changes in the diaphragm of WT and *mdx* mice from 13 to 52 weeks. We first examined muscle hypertrophy by measuring the diaphragm cross-section width. Diaphragm thickness did not change in WT mice, whereas the *mdx* diaphragm was significantly thickened at 26 and 36 weeks. At 52 weeks, we observed diaphragm atrophy (**Figure 3.5A,B**). Further, trichrome staining revealed a progressive increase (up to 9.5-fold) in interstitial collagen deposition in the diaphragm of *mdx* mice, representing up to 51% of the total diaphragm area (**Figure 3.5A,C)**. A variable decrease in lipid deposition within the diaphragm of *mdx* mice was observed, however, this accounted for <1% of the muscle (**Figure 3.5D**).

The number of myofibers in the WT and *mdx* diaphragm could not be directly compared due to variability in cross-section coverage **(Figure 3.6A,B**). We therefore assessed the minimum myofiber diameter and the proportional change in myofiber size distribution, which did not change with age in the WT diaphragm (**Figure 3.6C,D**). In the *mdx* diaphragm, the minimum myofiber diameter decreased linearly with age (**Figure 3.6A,C**), due to a dramatic increase in small myofibers and the concurrent loss of large myofibers from 26 weeks of age (**Figure 3.6D**). Myofiber hypertrophy was not observed in the *mdx* diaphragm (**Figure 3.6D,E)**. Considering the absence of myofiber hypertrophy in the *mdx* diaphragm, the increase in collagen deposition and the elevated numbers of small myofibers likely contributed to diaphragm thickening at 26 and 36 weeks in the *mdx* mouse.

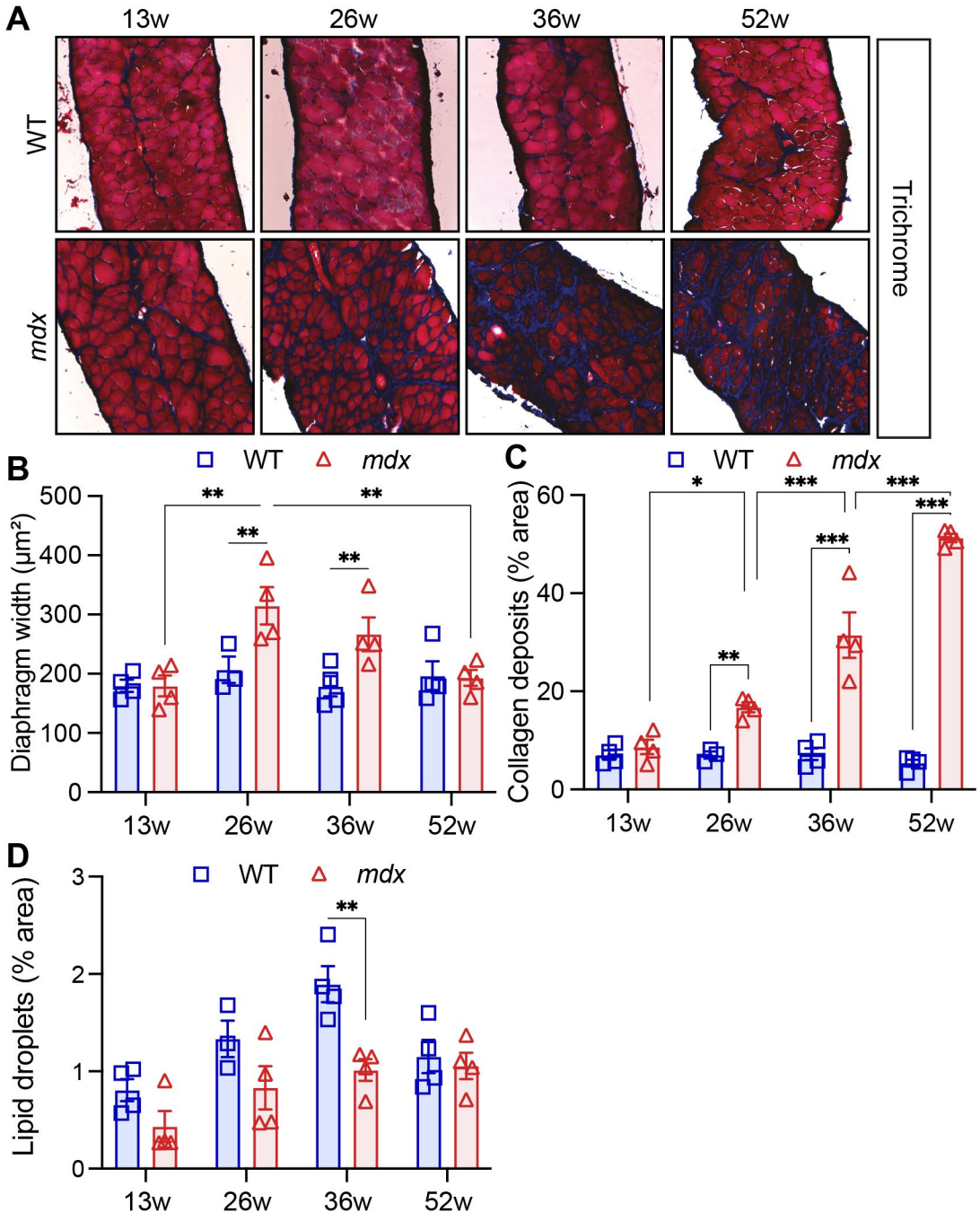

Figure 3.5 Severe pathology occurs in the *mdx* diaphragm.
A Representative Trichrome stained wild type (WT) and *mdx* diaphragm muscle cross-section images from 13- to 56-week-old mice. **B** WT and *mdx* diaphragm cross-section width from 13 to 56 weeks of age. **C** Quantification of collagen content (blue) in WT and *mdx* diaphragm muscle sections stained by Trichrome. **D** Lipid droplet quantification in diaphragm muscle sections. Data presented as mean values ± SEM. Two-way ANOVA corrected for multiple comparisons using Sidak's test (*$p < 0.05$; **$p < 0.01$; ***$p < 0.001$). n = 4 WT and 4 *mdx* 13-week-old mice, n = 3 WT and 4 *mdx* 26-week-old mice, n = 4 WT and 4 *mdx* 36-week-old mice, n = 4 WT and 4 *mdx* 52-week-old mice.

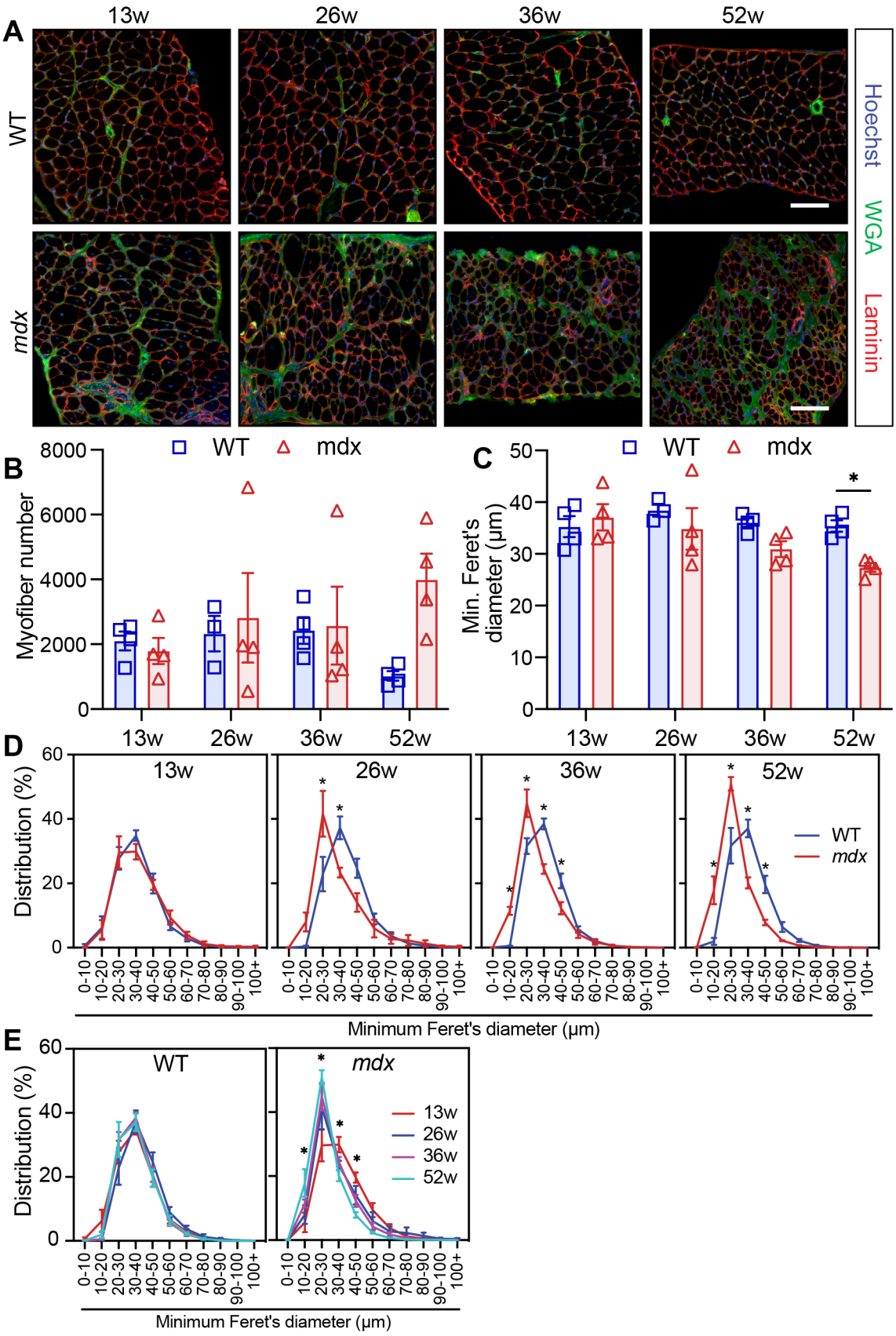
A
13w
26w
36w
52w
WT
mdx
Hoechst
WGA
Laminin
B
WT
mdx
Myofiber number
8000
6000
4000
2000
0
13w
26w
36w
52w
C
WT
mdx
Min. Feret's diameter (μm)
50
40
30
20
10
0
*
13w
26w
36w
52w
D
Distribution (%)
60
40
20
0
13w
26w
36w
52w
WT
mdx
0-10
10-20
20-30
30-40
40-50
50-60
60-70
70-80
80-90
90-100
100+
Minimum Feret's diameter (μm)
E
Distribution (%)
WT
mdx
13w
26w
36w
52w
Minimum Feret's diameter (μm)

Figure 3.6 Progressively smaller diaphragm myofibers with age in the *mdx* mouse.
A Representative immunofluorescence images of transversal diaphragm muscle sections from 13-, 26-, 36- and 52-week-old wild type (WT) and *mdx* mice. Laminin (red) delineates the myofibers, WGA (green) stains the connective tissues, and Hoechst (blue) labels the nuclei. Scale bar, 100µm. **B** Quantification of the number of myofibers per quantified diaphragm section. **C** Mean diaphragm myofiber size using the minimum Feret's diameter. **D** Normalized TA myofiber size distribution using minimum Feret's diameter. **E** Normalized diaphragm myofiber size distribution according to size using minimum Feret's diameter and divided by genotype. Data presented as mean values ± SEM. Two-way ANOVA corrected for multiple comparisons using Sidak's test (*$p < 0.05$). n = 4 WT and 4 *mdx* 13-week-old mice, n = 3 WT and 4 *mdx* 26-week-old mice, n = 4 WT and 4 *mdx* 36-week-old mice, n = 4 WT and 4 *mdx* 52-week-old mice.

3.3 Delayed Recovery After Acute Injury Caused by Myofiber Hyperplasia in *mdx* Mice

To study muscle regeneration following acute injury, we injected CTX into the TA of WT and *mdx* mice and harvested the muscle at multiple timepoints from 3 to 90 dpi (**Figure 3.7A**). CTX injury did not affect body weight in either WT or *mdx* mice within their respective genotypes (**Figure 3.7B**). However, decreased TA mass due to myolysis was observed at 5 dpi, after which the muscle weight increased (**Figure 3.7C**). By 21 dpi, the WT TA recovered its pre-injury mass, while the *mdx* TA weight increased by 62% compared to uninjured muscle (**Figure 3.7C**), as previously observed.[241] Between 21 and 90 dpi, the WT and *mdx* TA weights increased by 40% and 20%, respectively. However, the *mdx* TA weighed significantly more than the control WT TA at 21 and 90 dpi (**Figure 3.7C**). This was not due to increased fibrosis, as collagen deposition was also not significantly changed in the WT or *mdx* TA at 90 dpi (**Figure 3.7D,E**).

The morphology of regenerating WT and *mdx* muscle was visually comparable up to 90 dpi, but several differences were observed (**Figure 3.8A,B**). Compared to non-injured (N.I.) muscle, the number of WT myofibers remained unchanged at 90 dpi, but the mean minimum myofiber diameter increased (**Figure 3.8C,D**). By contrast, the number of small *mdx* myofibers increased dramatically, and the mean myofiber diameter decreased (**Figure 3.8C,D**). Moreover, compared to the WT TA muscle, hypertrophic myofibers were not observed, which contrasts with uninjured conditions (**Figure 3.8E**).

We also observed worsened *mdx* TA histopathology after triple CTX injury, with 21 days of recovery after each injection (63 dpi total; 3X CTX). The number of myofibers increased in the *mdx* TA muscle, and the mean minimum myofiber diameter decreased. Conversely, the WT TA morphology was unaffected (**Figure S1A-C**). However, consistent with a single injury, collagen deposition did not significantly change in the WT or *mdx* TA after three CTX injections (**Figure**

S1D-F). Together with the lack of fibrosis, this suggests that muscle growth following acute injury occurs by myofiber hypertrophy in WT muscle and myofiber hyperplasia in *mdx* muscle.

To determine the physiological consequences of architectural changes following acute injury, we measured *in situ* isometric force of the WT and *mdx* TA at 21 and 90 dpi. The maximum titanic force was recovered by 21 dpi in WT mice but not until 90 dpi in the *mdx* TA (**Figure 3.9A**). Specific force was significantly reduced at both 21 and 90 dpi (**Figure 3.9B,C)**. Following triple injury, the maximum tetanic force increased in the WT TA but was unchanged in the *mdx* TA compared to N.I. conditions. Similarly, the maximum tetanic force of the *mdx* TA was reduced compared to the WT muscle (**Figure S1F**).

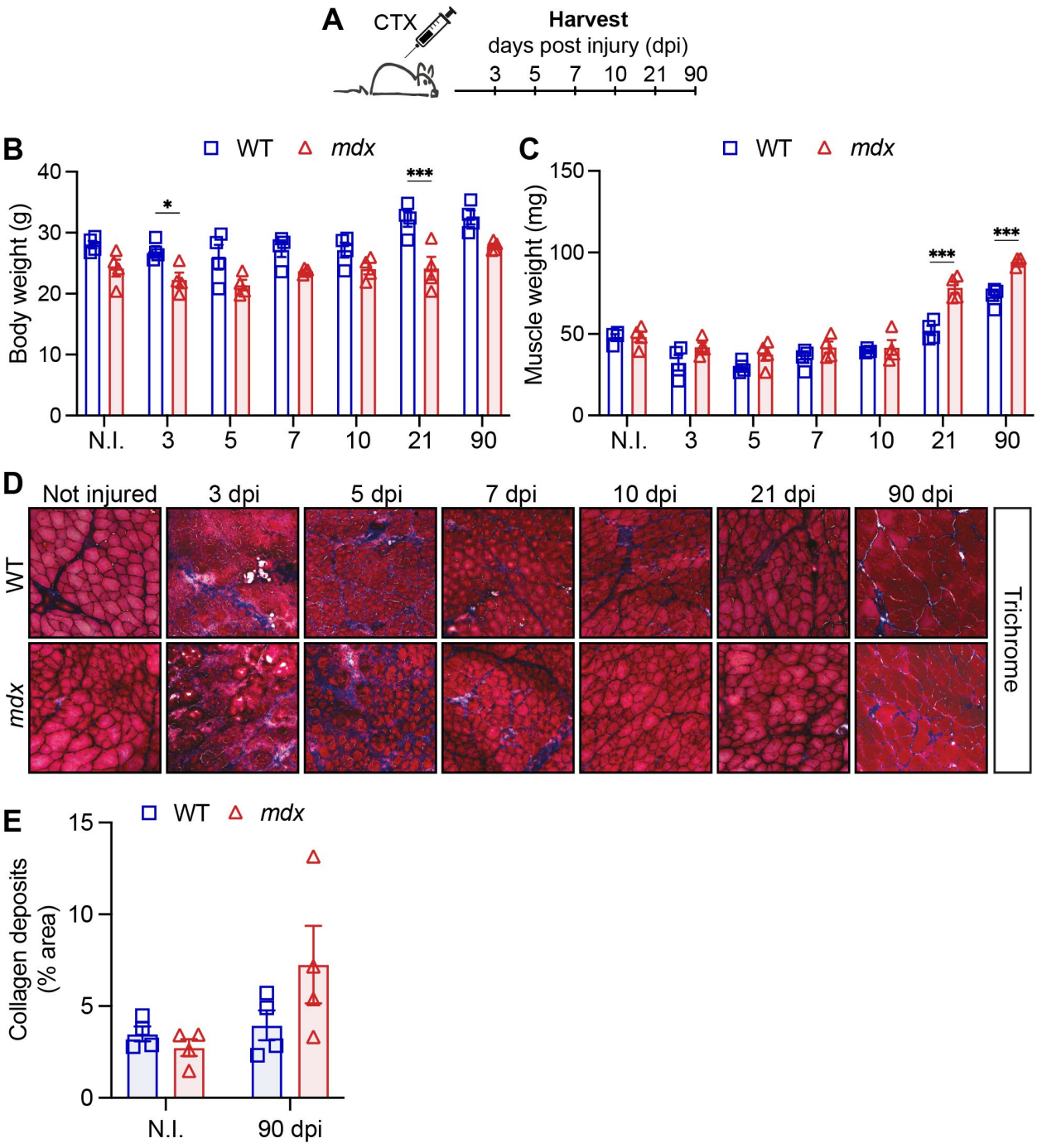
A
CTX
Harvest
days post injury (dpi)
3 5 7 10 21 90
B
WT
mdx
Body weight (g)
40
30
20
10
0
*
***
N.I. 3 5 7 10 21 90
C
WT
mdx
Muscle weight (mg)
150
100
50
0
***
***
N.I. 3 5 7 10 21 90
D
Not injured
3 dpi
5 dpi
7 dpi
10 dpi
21 dpi
90 dpi
WT
mdx
Trichrome
E
WT
mdx
Collagen deposits (% area)
15
10
5
0
N.I.
90 dpi

Figure 3.7 Increased muscle weight after acute injury is not caused by fibrosis in *mdx* mice. **A** Time course schematic of cardiotoxin (CTX)-induced injury in the *tibialis anterior* (TA) muscle of wild type (WT) and *mdx* mice, with tissues collected at multiple timepoints following injury. **B** Body weight of WT and *mdx* mice before CTX-induced injury (N.I., non-injured) and at 3, 5, 7, 10, 21 and 90 days post-injury (dpi). **C** *Tibialis anterior* (TA) muscle weight of WT and *mdx* mice before and following CTX-injury. **D** Representative trichrome staining images of N.I. and injured WT and *mdx* TA muscle cross-sections. **E** Quantification of collagen content (blue staining) in Trichrome-stained TA. Data presented as mean values ± SEM. Two-way ANOVA corrected for multiple comparisons using Sidak's test (*$p < 0.05$; **$p < 0.01$; ***$p < 0.001$).

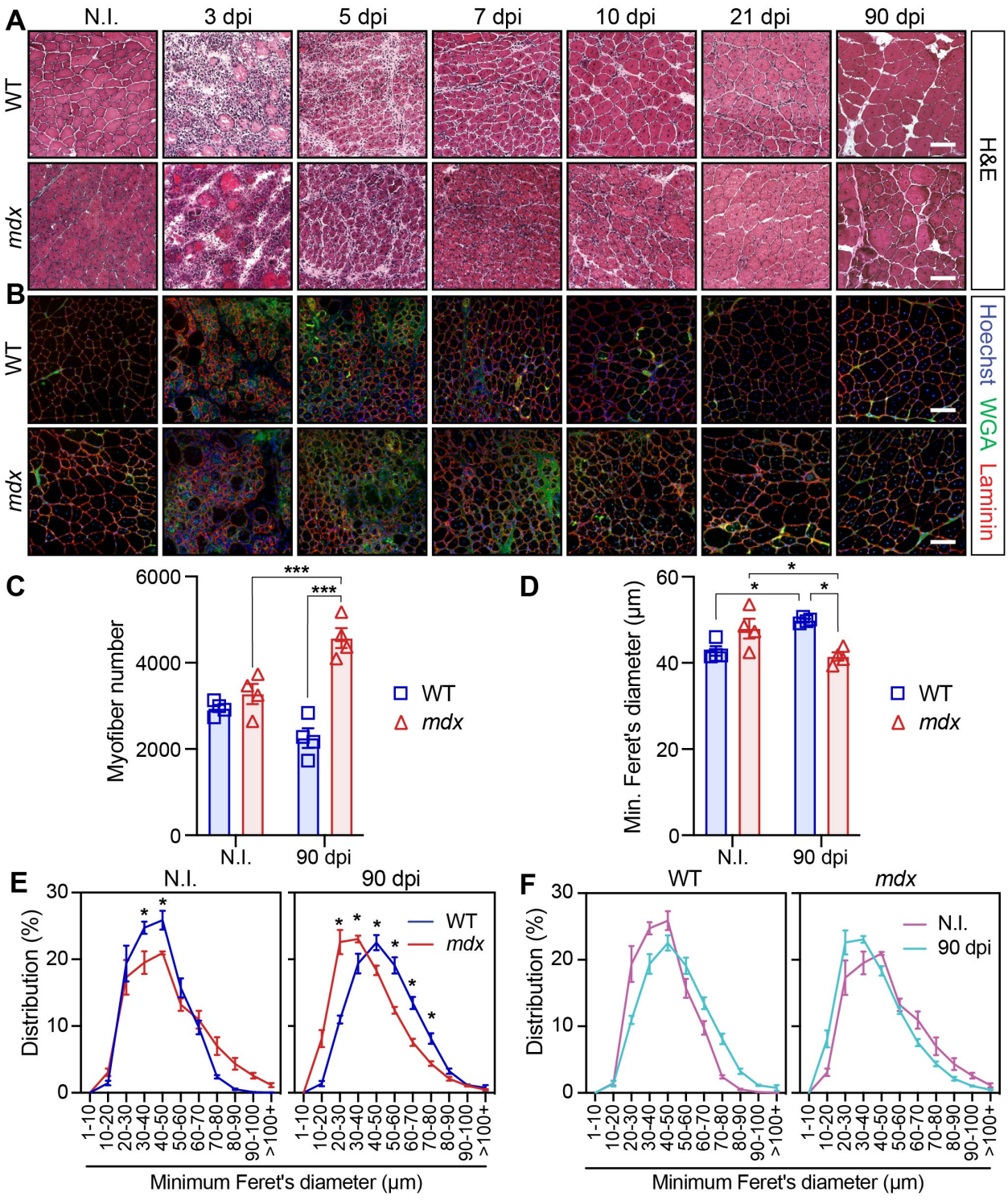
A
N.I.
3 dpi
5 dpi
7 dpi
10 dpi
21 dpi
90 dpi
WT
mdx
H&E
B
WT
mdx
Hoechst WGA Laminin
C
Myofiber number
6000
4000
2000
0
***
***
N.I.
90 dpi
WT
mdx
D
Min. Feret's diameter (µm)
60
40
20
0
*
*
*
N.I.
90 dpi
WT
mdx
E
N.I.
90 dpi
Distribution (%)
30
20
10
0
WT
mdx
1-10
10-20
20-30
30-40
40-50
50-60
60-70
70-80
80-90
90-100
>100+
Minimum Feret's diameter (µm)
F
WT
mdx
Distribution (%)
N.I.
90 dpi
Minimum Feret's diameter (µm)

Figure 3.8 Altered myofiber distribution in the *mdx* tibialis anterior after acute injury.
A-B Representative haematoxylin and eosin (H&E) (A) and immunofluorescence images (B) of transversal sections of non-injured (N.I.) and cardiotoxin (CTX)-injured *tibialis anterior* (TA) muscle at 3, 5, 7, 10, 21 and 90 days post-injury (dpi) from wild type (WT) and *mdx* mice. Laminin (red) delineates the myofibers, WGA (green) stains the connective tissues, and Hoechst (blue) labels the nuclei. **C** Cross-sectional TA myofiber quantification at 90 dpi compared to NI. **D** Mean WT and *mdx* TA myofiber size using the minimum Feret's diameter in N.I. and CTX-injured muscles at 90 dpi. **E** Proportional myofiber size distribution quantified on uninjured and 90 dpi TA cross-sections using minimum Feret's diameter. **F** Proportional distribution of TA myofiber size divided by genotype. Scale bars, 100 µm. Data presented as mean values ± SEM. Two-way ANOVA corrected for multiple comparisons using Sidak's test (*$p < 0.05$; **$p < 0.01$; ***$p < 0.001$). N.I. = non-injured. $n = 4$ WT and 4 *mdx*.

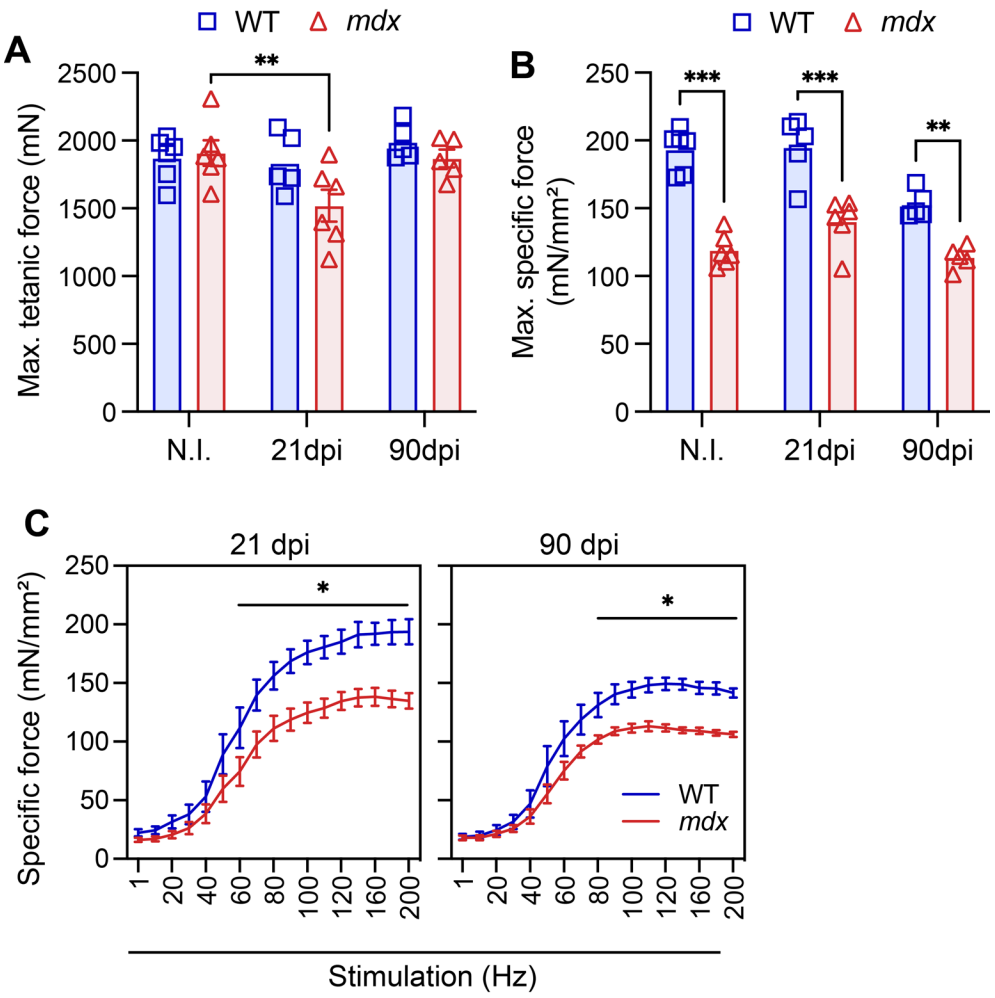

Figure 3.9 Delayed recovery of maximum tetanic force after acute muscle injury.
A Maximum tetanic force of non-injured (N.I.) and cardiotoxin (CTX)-injured WT and *mdx tibialis anterior* (TA) muscle at 21- and 90-days post-injury (dpi). **B** Maximum specific force of TA muscles from N.I., 21 and 90 dpi WT and *mdx* mice. **C** Specific force of WT and *mdx* TA muscle at 21 and 90 dpi. Data presented as mean values ± SEM. Two-way ANOVA corrected for multiple comparisons using Sidak's test (*$p < 0.05$; **$p < 0.01$; ***$p < 0.001$). $n = 6$ WT and 6 *mdx* 'non-injured' mice, $n = 5$ WT and 6 *mdx* '21 dpi' mice, $n = 5$ WT and 5 *mdx* '90 dpi' mice.

3.4 Perturbed Muscle Stem Cell Homeostasis and Injury Response in *mdx* Muscle

The regenerative capacity of skeletal muscle relies on PAX7$^+$ MuSCs. Despite initial reports that dystrophic MuSCs become progressively exhausted due to ongoing demands of muscle regeneration,[242,243] it is now accepted that the number of PAX7$^+$ MuSCs is elevated 3-5 fold in both *mdx* mice and DMD at all stages of the disease.[174,244,245] Studies in *ex vivo* myofiber culture suggest that the hyperplasia of PAX7$^+$ MuSCs is due to a loss of polarity control caused by dystrophin deficiency, which leads to reduced asymmetric divisions.[138]

To investigate the dynamics of *mdx* MuSCs in response to chronic repeat injury, we compared the number of PAX7-expressing (PAX7$^+$) cells in WT and *mdx* muscle from 13 to 56 weeks of age. Consistent with previous reports,[244,245] the number of PAX7$^+$ cells was elevated in the *mdx* TA and diaphragm at all time points (**Figure 3.10A,B**). However, while the number of PAX7$^+$ cells did not change in the WT TA or diaphragm, the number of *mdx* MuSCs declined in both muscles between 13 and 52 weeks (**Figure 3.10A,B**).

We next assessed the response of PAX7$^+$ MuSCs to acute CTX injury by immunostaining a regeneration time course of WT and *mdx* TA cross-sections (**Figure 3.11A**). Significant expansion of WT and *mdx* PAX7$^+$ cells occurred at 5 dpi, followed by a progressive decrease to N.I.-levels at 21 dpi (**Figure 3.11B**). However, fewer *mdx* PAX7$^+$ were enumerated at 5 dpi (**Figure 3.11B**). We also normalized the number of PAX7$^+$ cells at 5 dpi to uninjured conditions within both genotypes and observed reduced expansion in *mdx* PAX7$^+$ cells (8-fold) relative to WT cells (20-fold) at 5 dpi (**Figure 3.11C**).

We also investigated the effects of repeat CTX injury on the WT and *mdx* MuSC population in the TA muscle. After triple CTX injection into the TA muscle, with 21 days of recovery after each injury (63 dpi total), the number of PAX7$^+$ cells increased in the WT TA muscle. Fewer *mdx*

PAX7^{+} cells were quantified following repeat injury (**Figure S1G,H**). Since progenitor cells retain the expression of PAX7, we theorize, based on our previous findings, that the reduced numbers of PAX7^{+} cells result from defective MuSC asymmetric divisions and subsequent diminished progenitor generation.[138]

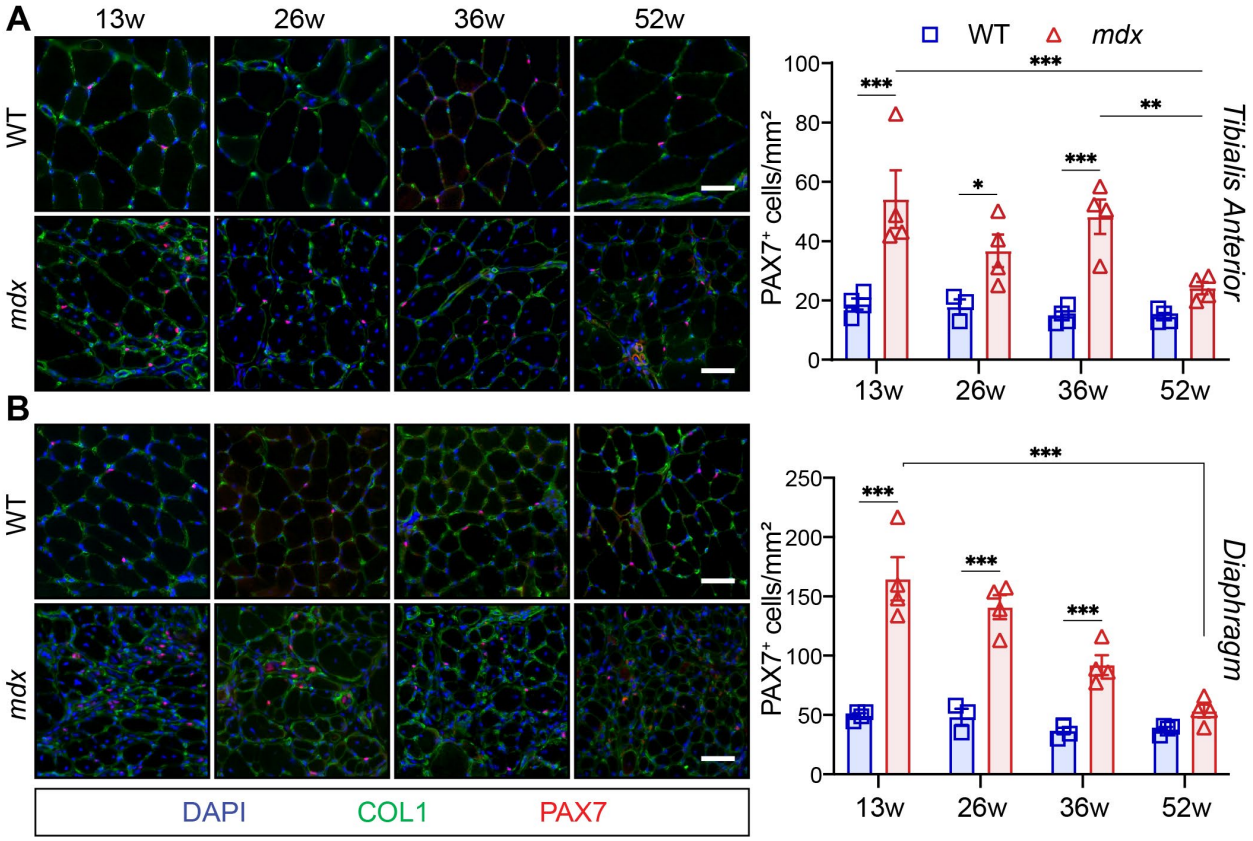

Figure 3.10 Perturbed MuSC homeostasis in *mdx* muscle.
A-B Immunofluorescence labelling and quantification of PAX7-expressing muscle stem cells (MuSCs, red) on WT and *mdx tibialis anterior* (TA, top, Panel A) and diaphragm (bottom, Panel B) muscle cross-sections. Collagen1 (COL1, green) labels the extracellular matrix, and Hoechst (blue) labels the nuclei. n = 4 WT and 4 *mdx* 13-week-old mice, n = 3 WT and 4 *mdx* 26-week-old mice, n = 4 WT and 4 *mdx* 36-week-old mice, n = 4 WT and 4 *mdx* 52-week-old mice. Two-way ANOVA corrected for multiple comparisons using Sidak's test (*$p < 0.05$; **$p < 0.01$; ***$p < 0.001$). Scale bar, 100 µm. Data presented as mean values ± SEM.

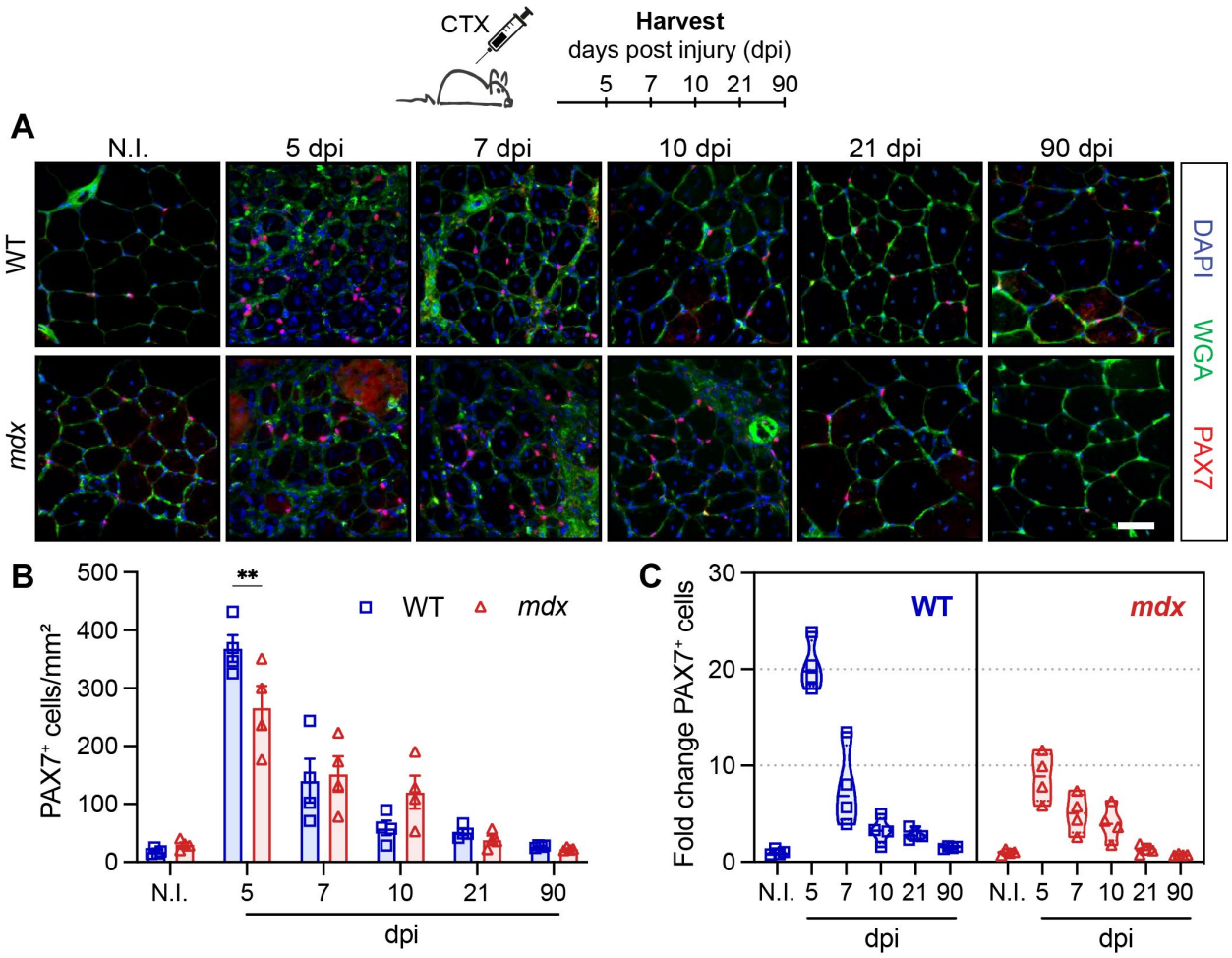

Figure 3.11 Perturbed *mdx* MuSC activation

A Representative immunofluorescence images of transversal sections from wild type (WT) and *mdx* non-injured (N.I.) and cardiotoxin (CTX)-injured TA muscles at 5, 7, 10, 21 and 90 days post-injury (dpi). PAX7 (red) marks the muscle stem cells (MuSCs), WGA (green) stains the connective tissues, and Hoechst (blue) labels the nuclei. **B** PAX7-expressing MuSC number per mm^2 on TA sections at the corresponding days following injury. $n = 4$ mice/genotype. **C** Fold change of $PAX7^+$ MuSCs at each timepoint post-CTX injury relative to N.I. conditions. n = 4 mice/genotype. Two-way ANOVA corrected for multiple comparisons using Sidak's test ($*p < 0.05$; $**p < 0.01$; $***p < 0.001$). Scale bar, 100 µm. For B, data presented as mean values ± SEM.

3.5 Dystrophin-Deficient MuSCs Display Features of Activation in *mdx* Muscle

To characterize the impact of Dp427m-deficiency on MuSCs in homeostatic and injured muscle, we studied the transcriptomic profile of WT and *mdx* MuSCs by bulk and single cell RNA-sequencing (RNA-seq) at multiple stages in the myogenic differentiation trajectory.

Bulk RNA-seq was performed in biological triplicates on myogenic cells prospectively isolated from WT and *mdx* mice before injury and at 3 dpi, termed freshly isolated (Fi)MuSC and activated (A)MuSCs, and from cultured primary myoblasts and 2-day differentiated myotubes (**Figure 3.12A,B**). Principal component analysis (PCA) of the bulk RNA-seq libraries revealed that cell state is a primary driver of variance (**Figure 3.12C,D**). While the FiMuSC and 2-day differentiated myotube grouped by myogenic state regardless of genotype, greater variance between genotypes was observed in the AMuSC and myoblast libraries. Next, we tested differential gene expression between genotypes for all conditions (**Data File S1**).

Differential gene expression (DGE) analysis between the WT and *mdx* FiMuSC libraries identified 1089 upregulated and 613 downregulated genes in *mdx* FiMuSCs (**Figure 3.13A** and **Data File S1**). Gene ontology (GO) analysis of the upregulated genes in the *mdx* FiMuSC library identified terms including ‘cell population proliferation,’ ‘tissue development,’ ‘response to external stimulus,’ and ‘cell motility’ (**Figure 3.13B** and **Data File S2**), indicating that *mdx* MuSCs are not completely quiescent. Further, terms related to the immune response were identified that reflect the inflammatory milieu surrounding *mdx* MuSCs. GO analysis on the downregulated genes in the *mdx* FiMuSC library highlighted terms such as ‘cell differentiation’ and ‘muscle tissue development,’ suggesting that despite increased proliferation, *mdx* MuSCs have reduced commitment capacities (**Figure 3.13C** and **Data File S2**).

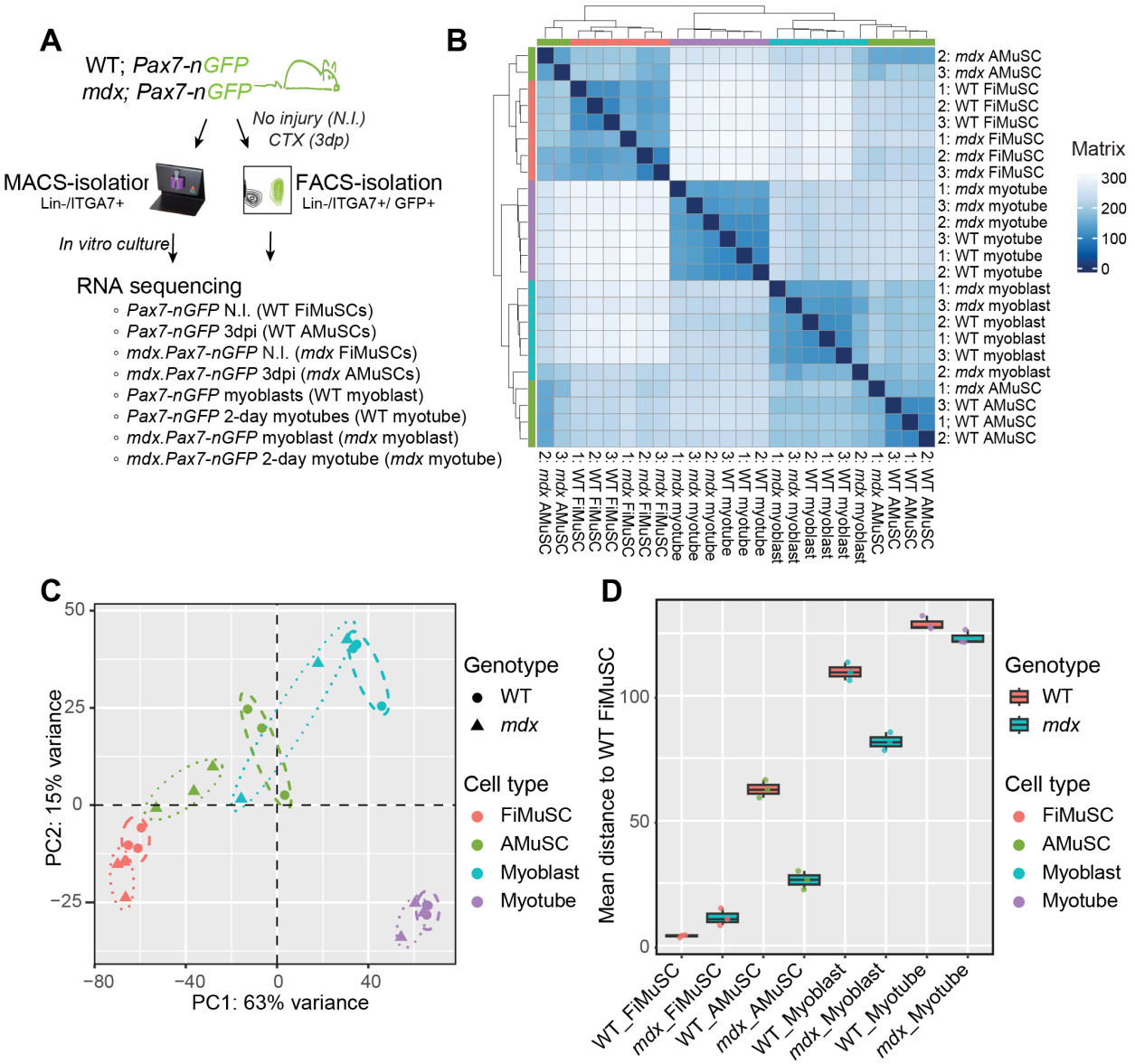

Figure 3.12 Transcriptomic differences in *mdx* myogenic cells identified by bulk RNA-seq. **A** Experimental design for fluorescence sorting and sequencing of the total population of GFP^{+} ITGA7^{+} freshly isolated (Fi) and activated (A) muscle stem cells (MuSCs) from the wild type (WT) and *mdx Pax7-nGFP* mice. *In vitro* myoblasts (MBs) derived from MuSCs of WT and *mdx Pax7-nGFP* mice were amplified or differentiated for 2 days before sequencing. Biological triplicates were included for each genotype and condition (n = 3 biological samples × 4 conditions). **B** Correlation heat map of bulk RNA-sequencing libraries following differential gene expression analysis of *mdx* FiMuSC and AMuSCs libraries compared to WT. **C** Principal component analysis of global transcriptomes of WT and *mdx* FiMuSCs, AMuSCs, myoblasts and 2-day differentiated myotubes. **D** Mean distance on PCA plot to WT FiMuSCs.

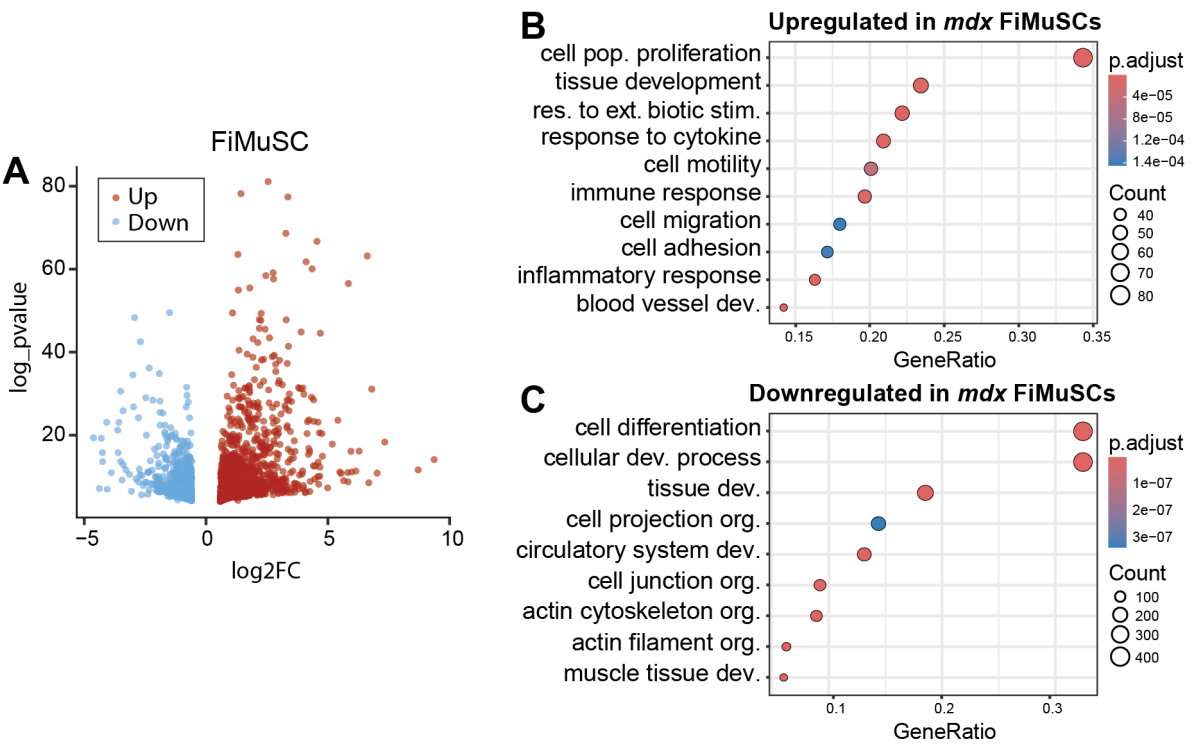

Figure 3.13 Differential gene expression in *mdx* freshly isolated MuSCs
A Volcano plot illustrating the significantly down- and up-regulated genes in bulk RNA-sequencing libraries generated from *mdx* freshly isolated (Fi) muscle stem cells (MuSCs) libraries compared to wild type (WT). **B,C** Gene ontology term enrichment for the upregulated (B) and downregulated (C) genes ($p_{adjusted} < 0.05$, Log2FC > 2) in *mdx* compared to WT FiMuSCs.

Four single cell RNA-seq (scRNA-seq) libraries were also generated from MuSCs isolated from N.I. and 5 dpi WT and *mdx* hindlimb muscle (**Figure 3.14A)**. After integration, ten clusters were identified and annotated based on differential gene expression and known cell markers (**Figure 3.14B** and **Data File S3**). Three contaminating clusters, namely *Cdh5*$^{+}$ 'Endothelial Cells', *Ckm*$^{+}$ 'Myonuclei,' and *Ptprc*$^{+}$ 'Immune Cells,' were equally distributed in all four libraries (1.5% and 2.4 % of the WT and *mdx* cells, respectively) and were excluded from downstream analysis (**Figure 3.14B,C**).

The seven myogenic clusters encompassed the trajectory from quiescent MuSCs to myocytes, and expressed canonical myogenic cell markers (**Figure 3.14D,E**). By assigning a quiescence module score to individual cells based on previously published 'quiescence core signature' genes, we identified three MuSC clusters with higher quiescence signatures (**Figure 3.14F**),[119] termed freshly isolated MuSCs 1 ('FiMuSCs 1'), 'FiMuSCs 2' and 'Early Activated MuSCs' (**Figure 3.14B,D**). Elevated expression of *Pax7*, *Calcr*, and oxidative phosphorylation (OxPhos) genes,[246] together with the absence of myogenic regulatory factor (MRF) gene expression suggested FiMuSCs 1 were the most quiescent (**Figure 3.14D,E**). Early Activated MuSCs were enriched in early activation and stress-response associated genes that are induced upon tissue dissociation, including *Jun*, *Junb*, and *Fos* (**Figure 3.14D,E**).[127] The *Pax7*$^{+}$ 'Activated MuSC' cluster, identified by reduced expression of quiescence genes and extracellular matrix gene enrichment, expressed negligible markers of myogenic cell proliferation, including *Mki67, Cenpa*, and *Myod1* (**Figure 3.14D**). Similarly, Seurat's CellCycleScoring function categorized less than 15% of Activated MuSCs having entered mitosis, which was consistent with the FiMuSCs 1, FiMuSC2 and Early Activated MuSCs clusters. In contrast, two myogenic progenitor clusters were identified. 'Progenitor' and 'Cycling Progenitor' expressed elevated *Myf5* and *Myod1*, while the

latter was enriched for S/G2/M-associated genes, including *Mki67* and *Cenpa*. 'Committed Progenitors' and 'Myocytes' were largely post-mitotic (*Cdkn1c*$^{+}$) and expressed *Myog*. 'Myocytes' expressed elevated levels of commitment markers, including *Mymk* and *Acta1* (**Figure 3.14D**).

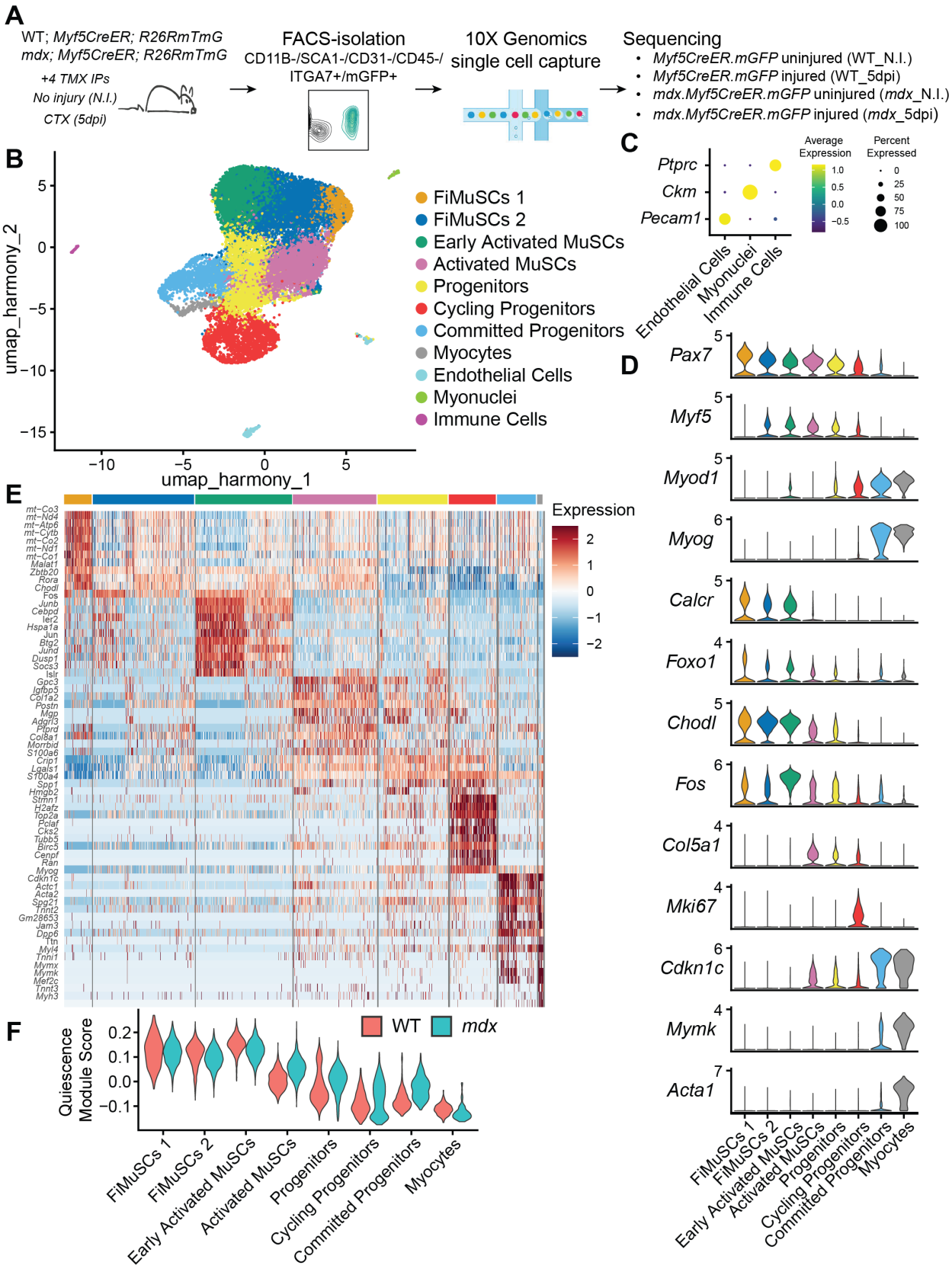
A
WT; Myf5CreER; R26RmTmG
mdx; Myf5CreER; R26RmTmG
+4 TMX IPs
No injury (N.I.)
CTX (5dpi)
FACS-isolation
CD11B-/SCA1-/CD31-/CD45-/
ITGA7+/mGFP+
10X Genomics
single cell capture
Sequencing
Myf5CreER.mGFP uninjured (WT_N.I.)
Myf5CreER.mGFP injured (WT_5dpi)
mdx.Myf5CreER.mGFP uninjured (mdx_N.I.)
mdx.Myf5CreER.mGFP injured (mdx_5dpi)
B
umap_harmony_2
umap_harmony_1
FiMuSCs 1
FiMuSCs 2
Early Activated MuSCs
Activated MuSCs
Progenitors
Cycling Progenitors
Committed Progenitors
Myocytes
Endothelial Cells
Myonuclei
Immune Cells
C
Ptprc
Ckm
Pecam1
Endothelial Cells
Myonuclei
Immune Cells
Average Expression
Percent Expressed
D
Pax7
Myf5
Myod1
Myog
Calcr
Foxo1
Chodl
Fos
Col5a1
Mki67
Cdkn1c
Mymk
Acta1
E
Expression
F
Quiescence Module Score
WT
mdx

Figure 3.14 Sequencing of single myogenic cells identifies cell identity.
A Experimental design for fluorescence sorting and sequencing of single ITGA7^{+} GFP^{+} muscle stem cells (MuSCs) from uninjured (non-injured, N.I.) and 5-day cardiotoxin-injured (5 dpi) hindlimb muscle of WT and *mdx Myf5-Cre;RmTmG* mice. **B** Uniform manifold approximation and projection (UMAP) visualization of integrated uninjured and 5 dpi injured libraries (21,352 cells total) before myogenic subset and coloured by cluster identity. **C** Dotplot of contaminating cluster markers. **D** Violin plots of select identity markers for each cluster. **E** Heat map of top 10 differentially expressed genes per cluster. **F** Violin plots illustrating quiescence module score (top 400 enriched from Garcia-Prat et al. 2020[119]) across the myogenic clusters, divided between WT and *mdx* libraries.

To investigate the intrinsic state and activation of dystrophic MuSCs, we assessed the scRNA-seq libraries isolated from WT and *mdx* uninjured muscle. FiMuSCs 1, FiMuSCs 2 and Early Activated MuSCs accounted for 93% and 59% of the uninjured WT and *mdx* libraries, respectively. The *mdx* library instead consisted of cells across the entire myogenic continuum, from *Pax7*$^{+}$ quiescent MuSCs to cycling progenitors and terminally differentiating myocytes (**Figure 3.15A,B**). Further, markers of proliferation and differentiation, such as *Mik67*, *Myog*, and *Mymk*, were expressed in the *mdx* but negligibly in the WT uninjured libraries (**Figure 3.15C**).

To examine the proportion of actively proliferating MuSCs in homeostatic muscle, we first regressed the Cell Cycle score from the Seurat object using the scale.data function to ensure that cell cycle was not the primary driver of clustering. We then examined the proportion of myogenic cells from the uninjured libraries expressing any cell cycle markers *Cenpa*, *Mki67* and *Cdk1*. We found that 4% of WT and 18% of *mdx* myogenic cells were actively proliferating. Within this analysis, we divided cells into two groups, categorizing the four stem cell clusters as 'MuSCs' and the remaining clusters as 'progenitors.' Notably, the number of proliferating MuSCs was comparable between genotypes, while the number of proliferating *mdx* progenitors increased (**Figure 3.15D**). Moreover, pseudo-bulk analysis of the uninjured libraries revealed an overall lower quiescence module score in *mdx* myogenic cells (**Figure 3.15E**).[119] Together, this suggests that dystrophin-deficient MuSCs from homeostatic muscle are in an asynchronous state of activation, leading to increased numbers of progenitor cells and differentiation.[244,247] Importantly, WT MuSCs are normally quiescent in uninjured muscle, while *mdx* MuSCs are pathogenically activated. Therefore, the presence of progenitors in the uninjured *mdx* libraries does not reflect the relative activation ability of *mdx* MuSCs compared to WT.

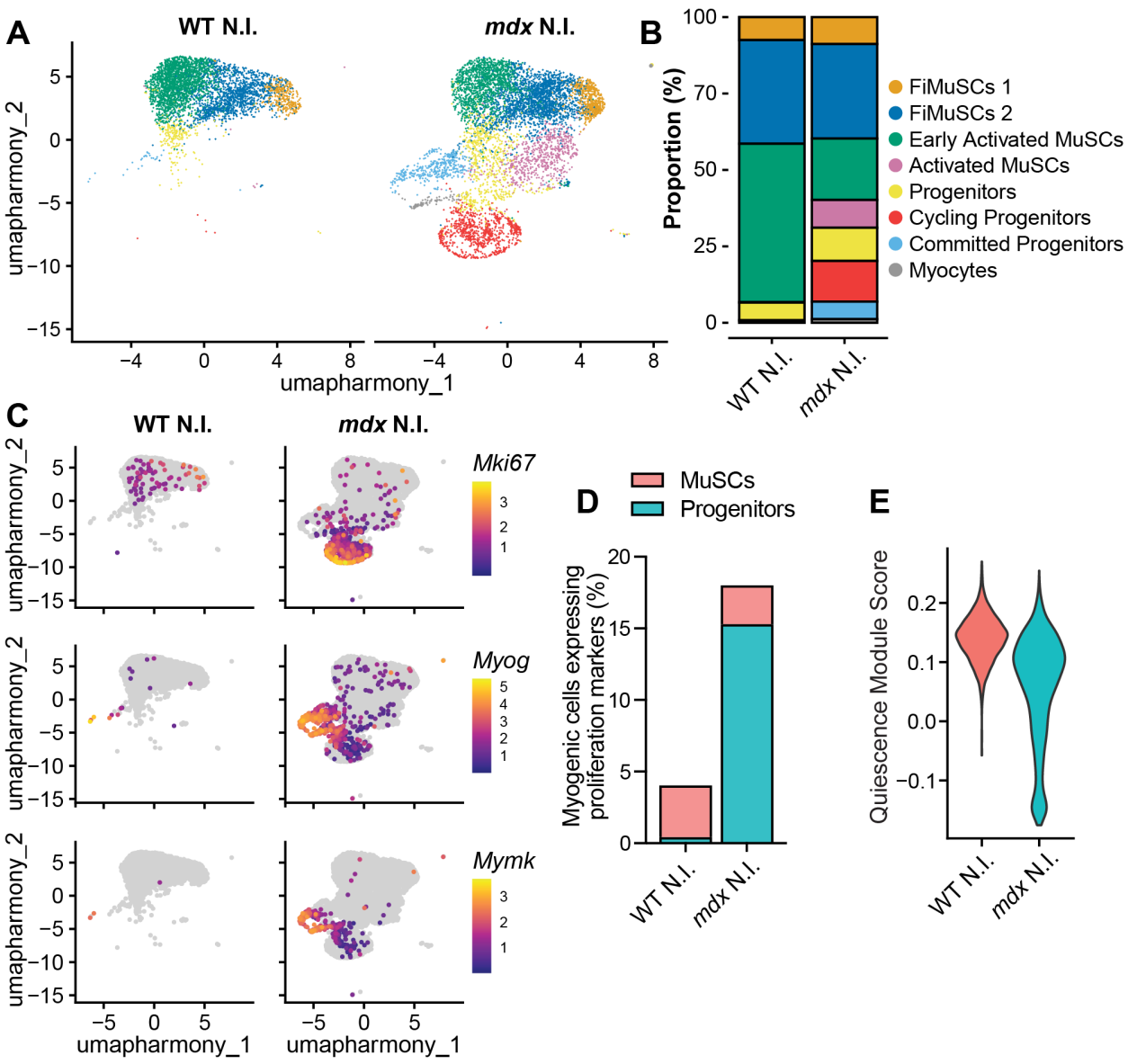

Figure 3.15 Increased activation of *mdx* MuSCs in homeostatic muscle.
A Uniform manifold approximation and projection (UMAP) visualization of myogenic libraries (4205 WT and 6980 *mdx*) isolated from uninjured hindlimb muscle and coloured by cluster identity. **B** Bar plot representing cluster proportions for uninjured WT and *mdx* MuSC libraries. **C** Feature plot illustrating the expression of proliferation marker *Mki67* and commitment markers *Myog* and *Mymk*. **D** Proportion of myogenic cells expressing *Cenpa*, *Mki67* or *Cdk1*, split by MuSC and progenitor cell identity. **E** Violin plot demonstrating pseudo bulked quiescence module score (top 400 enriched from Garcia-Prat *et al.*[119]) divided between uninjured WT and *mdx* libraries.

3.6 Reduced Commitment of *mdx* Muscle Stem Cells

The cyclic muscle degeneration and regeneration that results from myofiber fragility in *mdx* mice is not comparable to the basal level of muscle turnover that occurs in healthy muscle. Therefore, to compare the regenerative capacity of WT and *mdx* MuSCs, we examined bulk and single cell RNA-seq MuSC libraries isolated from CTX-injured muscle.

PCA analysis of the bulk RNA-seq libraries revealed that *mdx* AMuSC were transcriptionally more like WT FiMuSCs, while WT AMuSCs were more like *in vitro* cultured myoblasts than FiMuSCs (**Figure 3.12C,D**). DGE assessment between WT and *mdx* AMuSCs identified 2558 upregulated and 3415 downregulated genes (**Figure 3.16A** and **Data File S1**). GO term analysis showed *mdx* AMuSCs have decreased expression of genes involved in 'cell cycle', 'cell catabolic process', and 'RNA processing', while maintaining increased gene expression related to 'inflammatory response' and 'cell activation' (**Figure 3.16B,C** and **Data File S2**).

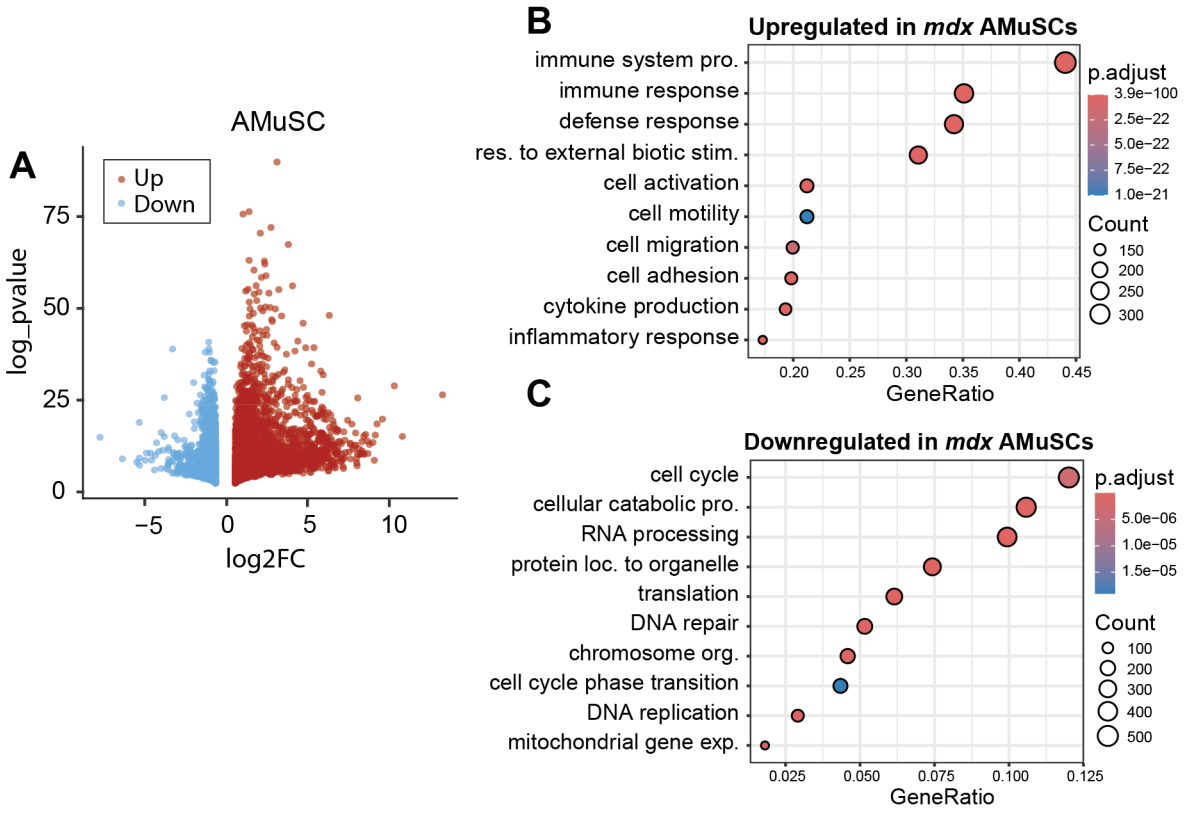

Figure 3.16 Differential gene expression in *mdx* activated MuSCs
A Volcano plot illustrating the significantly down- and up-regulated genes in bulk RNA-sequencing libraries generated from *mdx* activated (A) muscle stem cells (MuSCs) libraries compared to wild type (WT). **B,C** Gene ontology term enrichment for the upregulated (B) and downregulated (C) genes ($p_{adjusted} < 0.05$, Log2FC > 2) in *mdx* compared WT AMuSCs.

To study progenitor dynamics and the granularity of individual cell behaviour following MuSC activation, we next examined the scRNA-seq libraries generated from WT and *mdx* MuSCs at 5 dpi (**Figure 3.14A**). The WT and *mdx* libraries encompassed the myogenic trajectory from MuSCs to myocytes, but the proportion of uncommitted MuSCs relative to the total number of myogenic cells was elevated in the *mdx* library. Specifically, 40% of the WT compared to 63% of the *mdx* library were categorized as either FiMuSCs 1, FiMuSCs 2 or Early Activated MuSCs. The remaining 60% and 37% of cells clustered as progenitor cells or myocytes (**Figure 3.17A,B**). Moreover, the activated WT libraries expressed elevated differentiation markers including *Myog* and reduced stemness markers, such as *Calcr* (**Figure 3.17C**).

Interestingly, 26% of WT and 16% of *mdx* myogenic cells expressed one of the proliferation markers *Cenpa*, *Mki67* and *Cdk1* following Cell Cycle regression (**Figure 3.17D**). We again divided the myogenic cells into two categories, 'MuSCs' and 'progenitors,' and found that the proportion of proliferating MuSC was unchanged between genotypes, while the proportion of proliferating progenitors decreased in the *mdx* library (**Figure 3.17D**). This suggests that the reduced number of $PAX7^{+}$ cells quantified on *mdx* TA cross-sections at 5 dpi (**Figure 3.11A-C**) results from impaired generation of progenitors, and not from differences in the proliferation kinetics of MuSCs. Finally, the pseudo-bulked 5 dpi *mdx* library expressed elevated levels of quiescence genes compared to the WT library (**Figure 3.17E**). These results suggest that *mdx* MuSCs have fewer differentiation-competent progenitors relative to WT MuSCs.

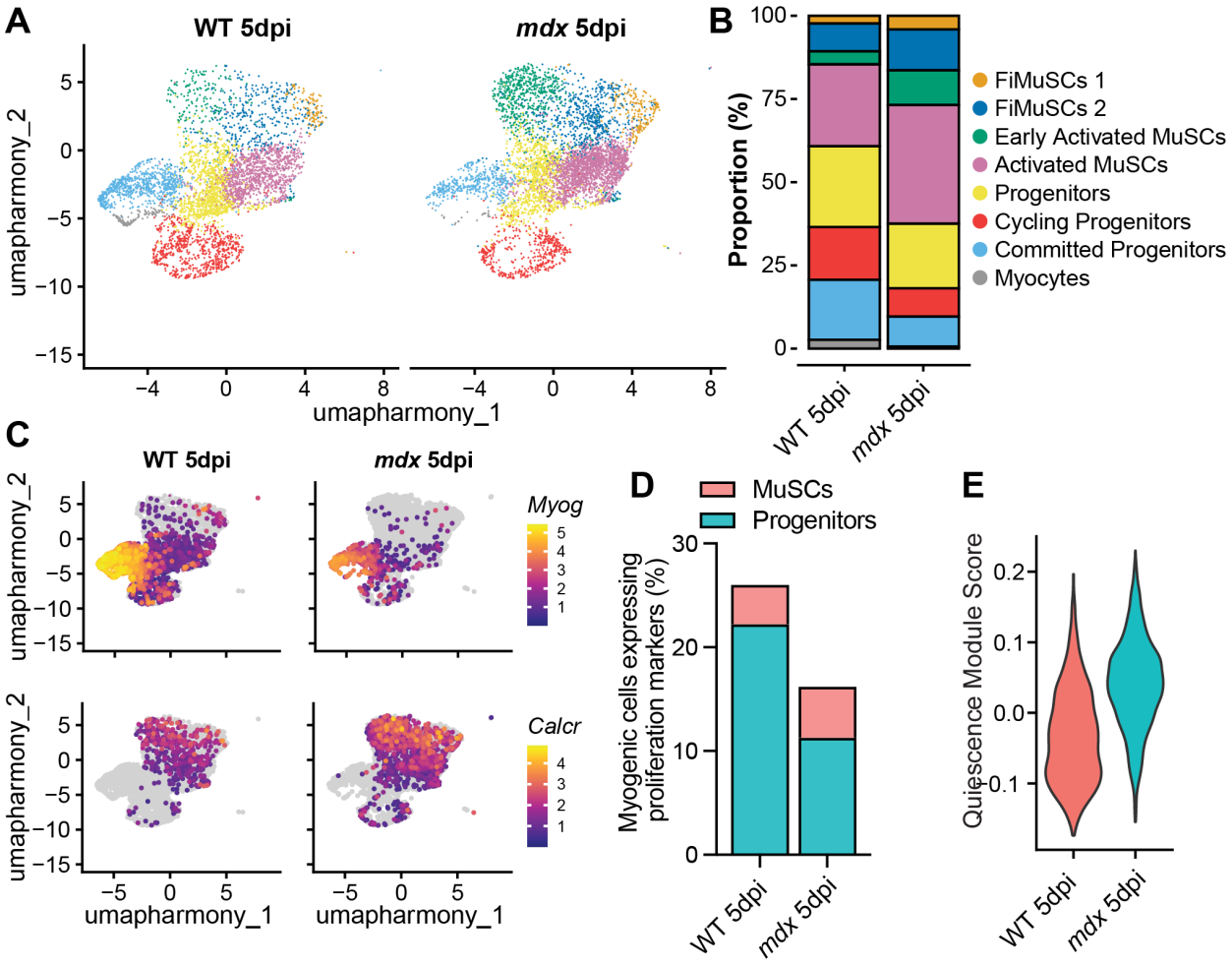

Figure 3.17 Reduced generation of *mdx* progenitor cells following acute injury.
A Uniform manifold approximation and projection (UMAP) visualization of cells (4616 WT and 5396 *mdx*) from scRNA-seq libraries captured 5-day post cardiotoxin-injured (5 dpi) and coloured by cluster identity. **B** Bar plot representing cluster proportions for WT and *mdx* MuSC libraries at 5 dpi. **C** Feature plot illustrating the expression of commitment markers *Myog* and *Mymk* and quiescence marker *Calcr*. **D** Proportion of myogenic cells expressing *Cenpa*, *Mki67* or *Cdk1*, divided by MuSC and progenitor cell identity. **E** Violin plot demonstrating pseudo bulked quiescence module score (top 400 enriched from Garcia-Prat et al[119]) divided between 5 dpi WT and *mdx* libraries.

We previously discovered that the direct loss of MARK2-DMD interactions in MuSC cultured on myofibers results in the loss of PARD3 polarity, fewer asymmetric cell divisions, and reduced numbers of committed myogenin (MYOG)-expressing cells.[138,139] To investigate *mdx* MuSC polarity *in vivo*, we isolated WT and *mdx* MuSCs 48 h following CTX injury and examined polarization of the PAR complex protein PARD3. Strikingly, we observed a significant reduction in the number of *mdx* MuSCs with polarized PARD3 expression (**Figure 3.18A-C**).

To determine if impaired MuSC polarity leads to fewer committed progenitors *in vivo*, as suggested by our transcriptomic analysis, we quantified $MYOG^+$ cells on TA muscle cross-sections at 5 dpi. A 2-fold decrease in $MYOG^+$ cells was observed on *mdx* muscle cross-sections (**Figure 3.18D,E**). To account for the reduced number of *mdx* $PAX7^+$ cells at 5 dpi that may generate fewer $MYOG^+$ progeny, we also calculated the proportion of $MYOG^+$ cells within the total $PAX7^+$ and $MYOG^+$ myogenic population. We observed a decreased proportion of *mdx* differentiated cells compared to WT (**Figure 3.18F**). Finally, we observed fewer GFP^+ nuclei on TA cross-sections from WT and *mdx Myf5cre;ROSA-nTnG* mice at 7dpi, which includes all primed MuSCs, progenitors, and myonuclei that have expressed *Myf5-Cre* **(Figure 3.18G,H**). Our results support the finding that *mdx* MuSCs have intrinsic polarity deficits that lead to fewer asymmetric divisions and reduced $MYOG^+$ progenitor generation.[138,139]

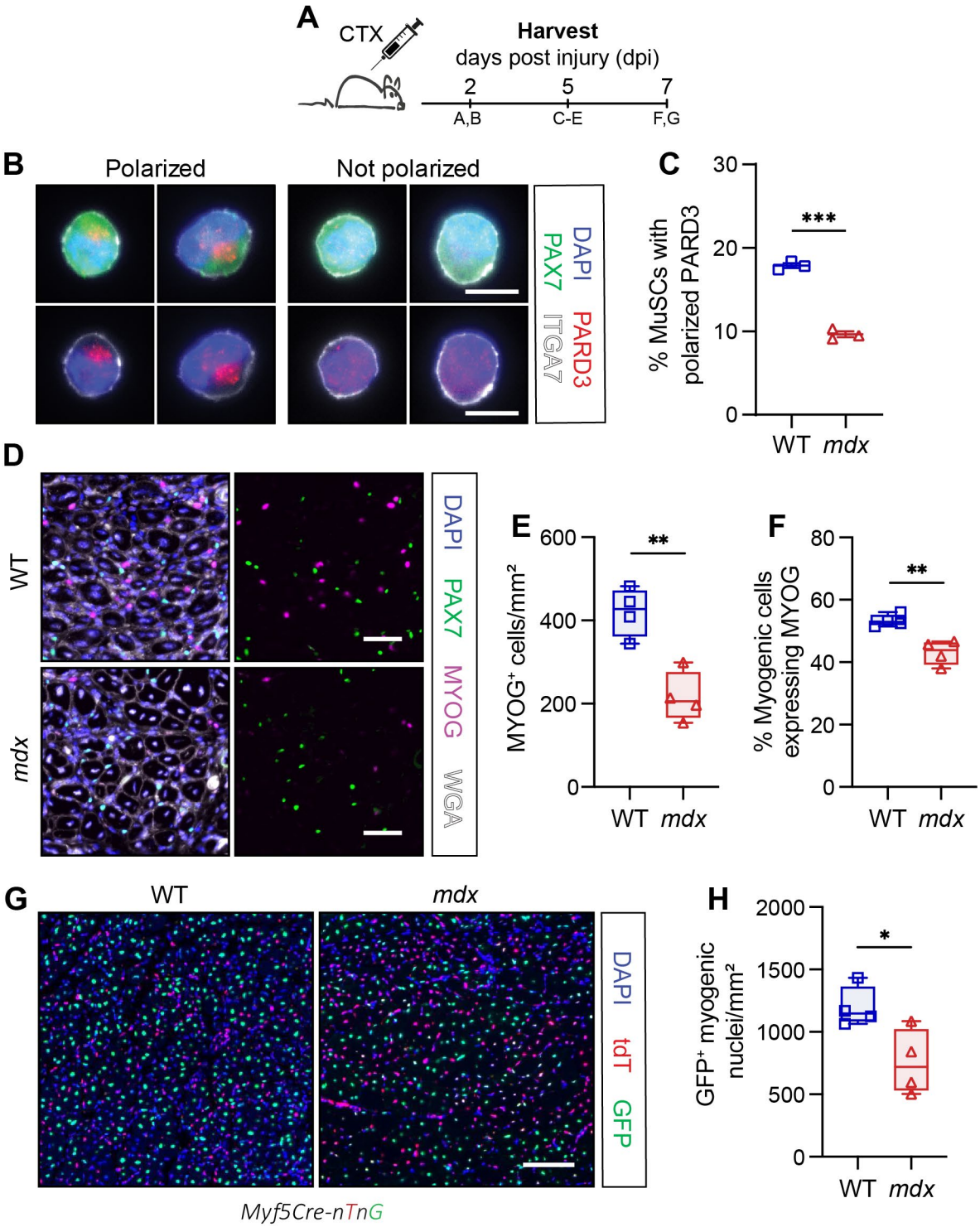
A
CTX
Harvest
days post injury (dpi)
2
5
7
A,B
C-E
F,G
B
Polarized
Not polarized
DAPI
PAX7
PARD3
ITGA7
C
% MuSCs with polarized PARD3
30
20
10
0
***
WT
mdx
D
WT
mdx
DAPI
PAX7
MYOG
WGA
E
MYOG+ cells/mm2
600
400
200
0
**
WT
mdx
F
% Myogenic cells expressing MYOG
80
60
40
20
0
**
WT
mdx
G
WT
mdx
DAPI
tdT
GFP
Myf5Cre-nTnG
H
GFP+ myogenic nuclei/mm2
2000
1500
1000
500
0
*
WT
mdx

Figure 3.18 Impaired *mdx* MuSC polarity results in reduced generation of myocytes.
A Schematic representation of cardiotoxin (CTX) injury time course of hindlimb muscles. **B** Representative immunostaining of polarized and non-polarized PARD3 (red) MuSCs (PAX7, green; ITGA7, white) isolated 48 hours after CTX-injury (left) from hindlimb muscles. Scale bar: 10µm. **C** Quantification of the number of wild type (WT) and *mdx* MuSCs with polarized PARD3 (right). n = 3 mice/genotype, greater than 500-1000 cells quantified per condition. **D** Representative immunofluorescence image of WT and *mdx tibialis anterior* (TA) muscle transverse sections 5 days following CTX-injury (5 dpi). PAX7 (green) denotes the MuSCs, MYOG (magenta) stains the differentiated myogenic cells, WGA (white) labels the connective tissues and DAPI (blue) labels the nuclei. Scale bar: 50µm **E** Enumeration of MYOG-expressing ($MYOG^+$) cell number normalized to mm^2 on TA sections at 5 dpi. **F** $MYOG^+$ cell proportion relative to total $PAX7^+$ and $MYOG^+$ myogenic cells at 5 dpi. **G** Representative immunofluorescence images of WT and *mdx* TA cross-sections from WT and *mdx Myf5cre;ROSA-nTnG* mice at 7 dpi. Myogenic nuclei that transcribe the muscle regulatory factor *Myf5* express nuclear EGFP (green), while the remainder that never express *Myf5* express nuclear tdTomato (tdT, red). DAPI (blue) labels the nuclei. Scale bar: 200µm. **H** Quantification of WT and *mdx* GFP^+ myogenic nuclei at 7 dpi on TA cross-sections. Panel D-H, n = 4 mice/genotype. Boxplot whiskers represent maximum and minimum data values. Statistical analysis performed using unpaired *t*-tests where $*p < 0.05$; $**p < 0.01$; $***p < 0.001$.

3.7 Intrinsic MuSC Dysfunction Impairs Myogenesis

To assess whether *mdx* MuSCs are intrinsically dysfunctional, we first analyzed MuSC polarity and myogenic cell commitment on perinatal day 7 (P7) before muscle weakness induces cyclic regeneration, chronic inflammation, and severe necrosis.[180] Interestingly, disrupted PARD3 polarity was observed in GFP^+ cells isolated from the limbs of P7 *mdx Pax7-nGFP* mice (**Figure 3.19A,B**). Further, EDL and TA muscle cross-section analysis of WT and *mdx* neonates at P7 revealed no difference in the number of $PAX7^+$ cells between genotypes (**Figure 3.19C,D**). However, *mdx* neonatal muscle contained fewer $MYOG^+$ cells, and the proportion of $MYOG^+$ cells in the total $PAX7^+$ and $MYOG^+$ cell population was reduced **(Figure 3.19E,F).** This notably correlates with the previous finding that *mdx* neonatal myofibers are hypotrophic.[248]

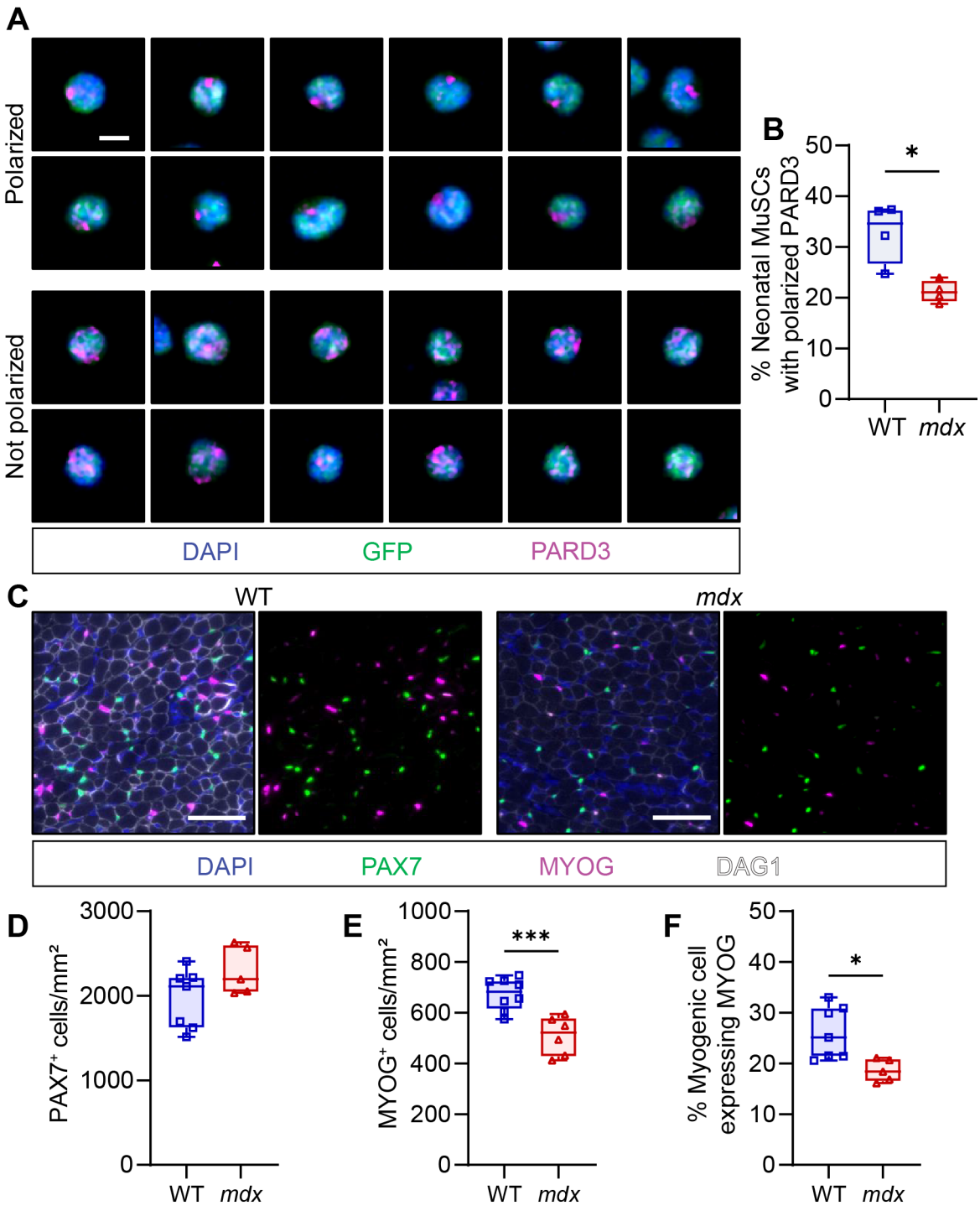
A
Polarized
Not polarized
DAPI
GFP
PARD3
B
% Neonatal MuSCs with polarized PARD3
50
40
30
20
10
0
*
WT
mdx
C
WT
mdx
DAPI
PAX7
MYOG
DAG1
D
PAX7⁺ cells/mm²
3000
2000
1000
0
WT
mdx
E
MYOG⁺ cells/mm²
1000
800
600
400
200
0
***
WT
mdx
F
% Myogenic cell expressing MYOG
50
40
30
20
10
0
*
WT
mdx

Figure 3.19 Reduced polarity and commitment of neonatal *mdx* MuSCs.
A Representative immunostaining of polarized and non-polarized PARD3 (magenta) in MuSCs (GFP, green) isolated from the limbs of *Pax7-nGFP* neonatal day 7 mice. Scale bar, 5 μm. **B** Quantification of PARD3 polarization in neonatal MuSCs. An average of 536 cells quantified per replicate. **C** Example immunofluorescence image of neonatal day 7 WT and *mdx* hindlimb muscle transverse section. PAX7 (green) denotes the neonatal MuSCs, MYOG (magenta) stains the differentiated myogenic cells, DAG1 (white) labels the connective tissues, and DAPI (blue) labels the nuclei. Scale bar, 50 μm. **D,E** Enumeration of PAX7-expressing ($PAX7^+$) (D) and MYOG-expressing ($MYOG^+$) (E) cells on *extensor digitorum longus* (EDL) and *tibialis anterior* (TA) cross-sections at neonatal day 7 and normalized to mm^2. **F** $MYOG^+$ cell proportion relative to total $PAX7^+$ and $MYOG^+$ myogenic cells at neonatal day 7. Boxplot whiskers represent the maximum and minimum data values. Statistical analysis performed using unpaired *t*-tests where $*p < 0.05$; $**p < 0.01$; $***p < 0.001$.

Next, we conducted transplantation experiments to remove the external contributions of the dystrophic environment. 10,000 MuSCs isolated from WT and *mdx* fluorescent reporter mice were injected contralaterally into the TAs of NSG mice 2 days following CTX-injury and irradiation. The engraftment potential of WT and *mdx* MuSCs was assessed at 2 and 4 weeks following the transplantation of donor MuSCs from *CAG-GFP* (GFP^+) mice and *ROSA-nTnG* (tdTomato or tdT^+) mice, respectively (**Figure 3.20A**). The absence of dystrophin staining on *mdx* transplants at 2- and 4-weeks post-engraftment confirmed the negligible contribution of host NSG MuSCs to donor grafts (**Figure 3.20B,C**). This was further confirmed by the colocalization of nuclear tdT with the majority of myonuclei and $PAX7^+$ cells at 4 weeks following MuSC delivery **(Figure 3.20D)**.

MuSCs from both genotypes were capable of self-renewal and differentiation,[249] shown by the presence of $PAX7^+$ cells and engrafted myofibers (**Figure 3.20B,D**). The total number of engrafted WT and *mdx* $PAX7^+$ cells was also not significantly different (**Figure 3.21A**). However, *mdx* donor MuSCs formed significantly smaller transplants with fewer myofibers and myonuclei compared to WT MuSCs (**Figure 3.21B-D**). The number of *mdx* $PAX7^+$ donor cells normalized to graft area in mm^2 was also elevated at 2- and 4-weeks post engraftment (**Figure 3.21E**), and the ratio of myonuclei to MuSCs (differentiation index) was significantly decreased in the 4-week *mdx* graft (**Figure 3.21F**). Further, myofiber size distribution analysis demonstrated that engrafted *mdx* MuSC form smaller myofibers four weeks following engraftment (**Figure 3.21G**). Overall, this suggests that *mdx* MuSCs possess enhanced self-renewal, while also having a reduced capacity to generate the progenitors necessary for myofiber formation.

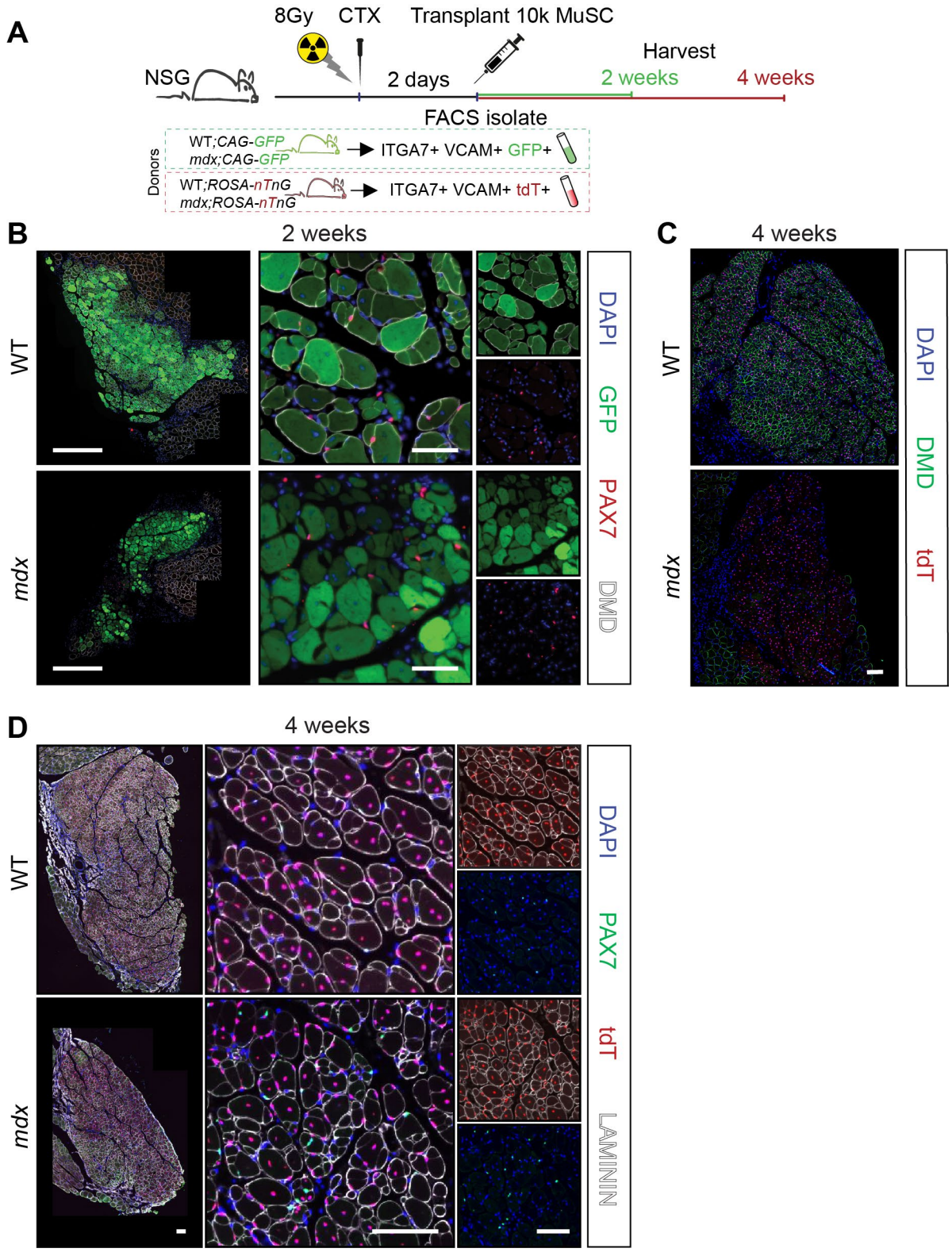
A
8Gy
CTX
Transplant 10k MuSC
NSG
2 days
Harvest
2 weeks
4 weeks
FACS isolate
Donors
WT;CAG-GFP
mdx;CAG-GFP
ITGA7+ VCAM+ GFP+
WT;ROSA-nTnG
mdx;ROSA-nTnG
ITGA7+ VCAM+ tdT+
B
2 weeks
WT
mdx
DAPI
GFP
PAX7
DMD
C
4 weeks
WT
mdx
DAPI
DMD
tdT
D
4 weeks
WT
mdx
DAPI
PAX7
tdT
LAMININ

Figure 3.20 Engraftment of wild type and *mdx* MuSCs.
A Experimental design for fluorescence sorting and injecting 10,000 donor ITGA7^{+}VCAM^{+} MuSCs from wild type (WT) and *mdx CAG-GFP* (2-week harvest) or *ROSA-nTnG* (4-week harvest) mice into the contralateral *tibialis anterior* (TA) muscles of 2 days post-cardiotoxin (CTX) injured and irradiated NSG mice. For 2-week harvest, n = 5 mice/genotype; and 4-week harvest, n = 6 mice/genotype. **B** Immunostaining of host TA muscle cross-sections 2 weeks after the transplantation of MuSCs from WT and *mdx CAG-GFP* mice. Both MuSCs (PAX7, red) and myofibers (DMD, white) from the donors express GFP (green). DAPI stains the nuclei. Scale bars: left panels, 500µm; right panels, 50µm. **C** Immunostaining of host TA muscle 4 weeks after engraftment of WT and *mdx* MuSC from *ROSA-nTnG* mice. Donor myogenic nuclei express tdTomato (tdT, red). Dystrophin staining denotes WT myofibers (green) and DAPI labels nuclei (blue). Scale bars are all 100µm. **D** Immunostaining of host TA muscle cross-sections 4 weeks following the engraftment of 10,000 MuSCs isolated from *WT;ROSA-nTnG* or *mdx; ROSA-nTnG* mice. Donor MuSCs (PAX7, green) and myonuclei express nuclear tdTomato (tdT, red). Laminin (white) stains myofiber membrane and DAPI (blue) stains the nuclei. Scale bars: left panels, 250µm; middle and right panels, 100µm.

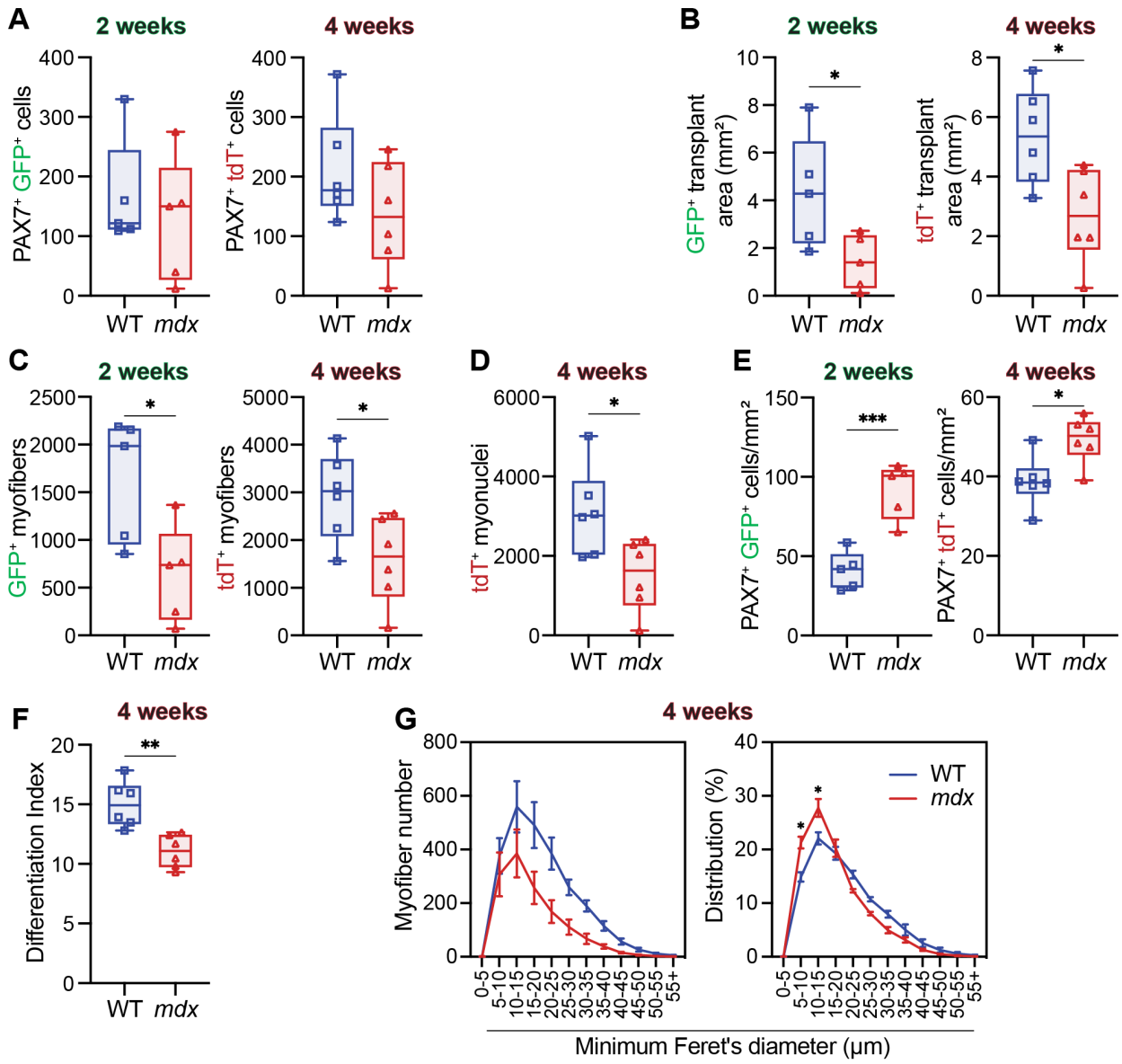

Figure 3.21 Intrinsic *mdx* MuSC dysfunction impairs muscle regeneration
A Quantification of wild type (WT) and *mdx* donor PAX7$^+$ cells on *tibialis anterior* (TA) muscles cross-sections at 2 weeks (GFP$^+$, left) and 4 weeks (tdT$^+$, right) following muscle stem cell (MuSC) transplantation. **B** Transplant area 2 weeks (GFP$^+$, left) and 4 weeks (tdT$^+$, right) following donor MuSC injection in mm^2. **C** Number of engrafted GFP$^+$ and tdT$^+$ myofibers per transverse sections of transplanted TA muscles. **D** Number of tdT$^+$ myonuclei per transverse sections of transplanted TA muscle 4 weeks following engraftment. **E** PAX7$^+$/tdT$^+$ MuSC number normalized to mm^2 of transplanted muscle cross-sections. **F** Differentiation index is the ratio of tdT$^+$ myonuclei to tdT$^+$ MuSCs. **G** Myofiber size distribution using minimum Feret's diameter and illustrated by number of myofibers (left) and proportional distribution (right). Panels A-F: boxplot whiskers represent the maximum and minimum data values, and statistical analysis performed using unpaired *t*-tests. Panel G: Data presented as mean values ± SEM, and statistical analysis using two-way ANOVA corrected for multiple comparisons with Sidak's test. *$p < 0.05$; **$p < 0.01$; ***$p < 0.001$. Related to **Figure 3.20**.

3.8 Findings Summary

In Chapter 3, we observe myofiber hypertrophy, myofiber hyperplasia, and reduced force generation in dystrophin-deficient muscle. The pathology of the diaphragm progresses earlier and more severely than the TA. Moreover, acute injury of the *mdx* TA leads to myofiber hyperplasia and delayed recovery, contrasting with the hypertrophic response in WT mice. While the ongoing muscle damage caused by myofiber fragility stimulates MuSC activation in *mdx* muscle, intrinsic polarity deficits in dystrophin-deficient MuSCs also impair muscle regeneration. This is evidenced by the expansion of MuSCs and the smaller proportion of progenitor cells observed through transcriptomic and histological analysis of *mdx* MuSCs after acute injury. The diminished regenerative capacity and intrinsic MuSC impairment are further evidenced by the smaller grafts following *mdx* MuSCs transplantation and the disrupted neonatal MuSC polarity and progenitor production, both of which occur without chronic inflammation. In summary, our study provides *in vivo* validation that polarity deficits in dystrophin-deficient MuSCs impair the regenerative abilities of dystrophin-deficient MuSCs compared to healthy cells.

Chapter 4: Intrinsic Dysfunction in Muscle Stem Cells Lacking Dystrophin Begins During Secondary Myogenesis

The results presented in Chapter 4 are adapted from the following manuscript, currently under revision for Nature Communications:

> **Marie E. Esper**, Alexander Y. T. Lin, Dallas Bennett and Michael A. Rudnicki Intrinsic dysfunction in muscle stem cells lacking dystrophin begins during secondary myogenesis. Nature Communication. 2025. *Revisions requested*.

4.1 Primary Myogenesis is Not Affected by Dystrophin Deficiency

To investigate the significance of dystrophin deficiency during primary myogenesis, a comparative analysis was conducted between C57BL/10ScSnJ WT and *mdx* embryos at E10.5, shortly after the formation of the primary myotome (**Figure 1.3**).[23] *Myf5* is the first MRF expressed during development and postnatal myogenesis.[250] We first examined *Myf5*, expression at E10.5 using the *Myf5-LacZ* transgene bred with the WT and *mdx* strains.

Timed mating was conducted using post-coital plug visualization, where the day of conception was assigned as E0.5, and the embryos were harvested at the same time daily. X-gal staining demonstrated decreased mean *mdx* somite length and reduced *Myf5* expression in *mdx* limb buds (**Figure 4.1A,B**). We next questioned whether the delay in *Myf5* expression stemmed from upstream dysregulation in paraxial mesoderm specification or disrupted primary myogenesis. To clarify this, we stage-matched embryos for further comparative analysis at E10.5.

Interestingly, staging of E10.5 WT and *mdx* embryos using somite enumeration and the Embryonic Mouse Ontogenetic Staging System (eMOSS[214]) revealed a subtle delay in *mdx* somitogenesis. On average, WT embryos had 1.2 additional somite pairs and were staged 1.9 hours ahead of *mdx* embryos (**Figure 4.1C,D**), which is consistent with the mean segmentation rate of one somite pair every two hours in mice.[251] This suggested that the reduced myotome length and limb bud expression of *Myf5-LacZ* may result from upstream delay in somitogenesis.

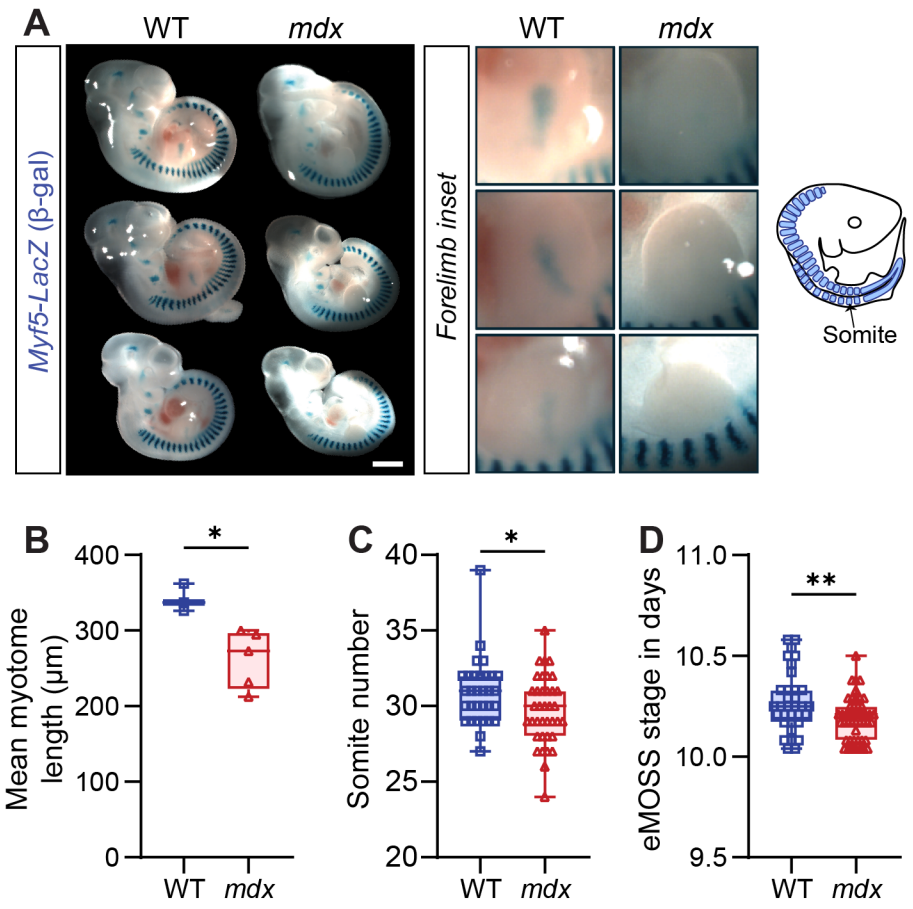

Figure 4.1 Somitogenesis is delayed at E10.5 in *mdx* embryos.
A X-gal staining (blue) of wild type (WT) and *mdx* E10.5 *Myf5-LacZ* embryos. Scale bar is 1 mm. Forelimb bud magnification is illustrated on the right. **B** Means myotome length enumerated from E10.5 *Myf5-LacZ* embryos. n = 3 WT and 5 *mdx*. **C** Number of enumerated somites at embryonic day 10.5 (E10.5) in wild type (WT) and *mdx* embryos. n=31 for WT and n=37 for *mdx*. **C** Age determined by forelimb morphology using the Embryonic Mouse Ontogenetic Staging System (eMOSS[214]). n=33 for WT and n=47 for *mdx*. Boxplot whiskers represent the maximum and minimum data values. Statistical analysis was performed using unpaired *t*-tests. *$p < 0.05$; **$p < 0.01$.

To directly evaluate myogenic cell commitment, we stage-matched WT and *mdx* E10.5 embryos by somite number and eMOSS age prior to whole mount (**Figure 4.2A,B**) and cross-section histological analysis (**Figure 4.2C,D**). In both analyses, the number of $PAX7^+$ and $MYOG^+$ cells in the dermomyotome and myotome was similar between genotypes at the forelimb bud level (**Figure 4.2B,D**). Similarly, the proportion of $MYOG^+$ cells in the entire $PAX7^+$ and $MYOG^+$ cell population, as determined by whole mount and cross-section analysis combined, was not significantly changed (**Figure 4.2E)**. We also observed no difference in the number of $PAX3^+$ cells in the E10.5 dermomyotome (**Figure 4.2C,D**).

In avian and murine embryos, $PAX3^+$ and $PAX7^+$ myogenic cells in the dermomyotome divide asymmetrically in an apical-basal orientation, generating committed myogenic cells that translocate to the primary myotome[52,53,56,96]. A basement membrane also forms adjacent to the dorsal dermomyotome (**Figure 4.3A**),[252] leading us to question whether dystrophin plays a role in dermomyotome asymmetric cell division. Consistent with the lack of changes in myogenic cell commitment, no differences in the proportion of apical-basal or planar divisions were observed in the WT and *mdx* E10.5 dermomyotome (**Figure 4.3B,C**).

Promoters on exon 1 of *Dmd* initiate transcription of isoforms encoding the full-length dystrophin protein, which is required for MARK2-mediated cell polarity and is universally lost in null DMD patients and *mdx* mice. Internal promoters downstream of the *mdx* mouse mutation generate N-terminal truncated isoforms.[138,253] Western blot analysis of the E10.5 trunk and limbs using a C-terminal dystrophin antibody identified short but not full-length dystrophin (**Figure 4.3D**). However, full-length utrophin (UTRN) and β-dystroglycan were expressed at the dermomyotome basal lamina (**Figure 4.3D-F**). Thus, dystrophin does not appear to play a role in regulating embryonic (e) MuSC polarity during primary myogenesis.

The subtle delay in somitogenesis suggests that dystrophin may play a role in upstream paraxial mesoderm specification. Moreover, recently published studies observed dysregulation of *in vitro* somitogenesis using dystrophin-deficient hiPSCs.[192] We therefore extracted cells of the paraxial mesoderm lineage from a recently published E8.5 single cell dataset and examined *Dmd* expression (**Figure 4.4A,B**).[254] Consistent with hiPSC modelling, *Dmd* was expressed in cells of the 'somite' and 'late somite,' before notable *Myf5* expression (**Figure 4.4B**). Interestingly, while the scRNA-seq assay employed 3' read enrichment, exon-spanning sequence alignment was observed in regions specific to the full-length *Dmd* transcript (data not shown).

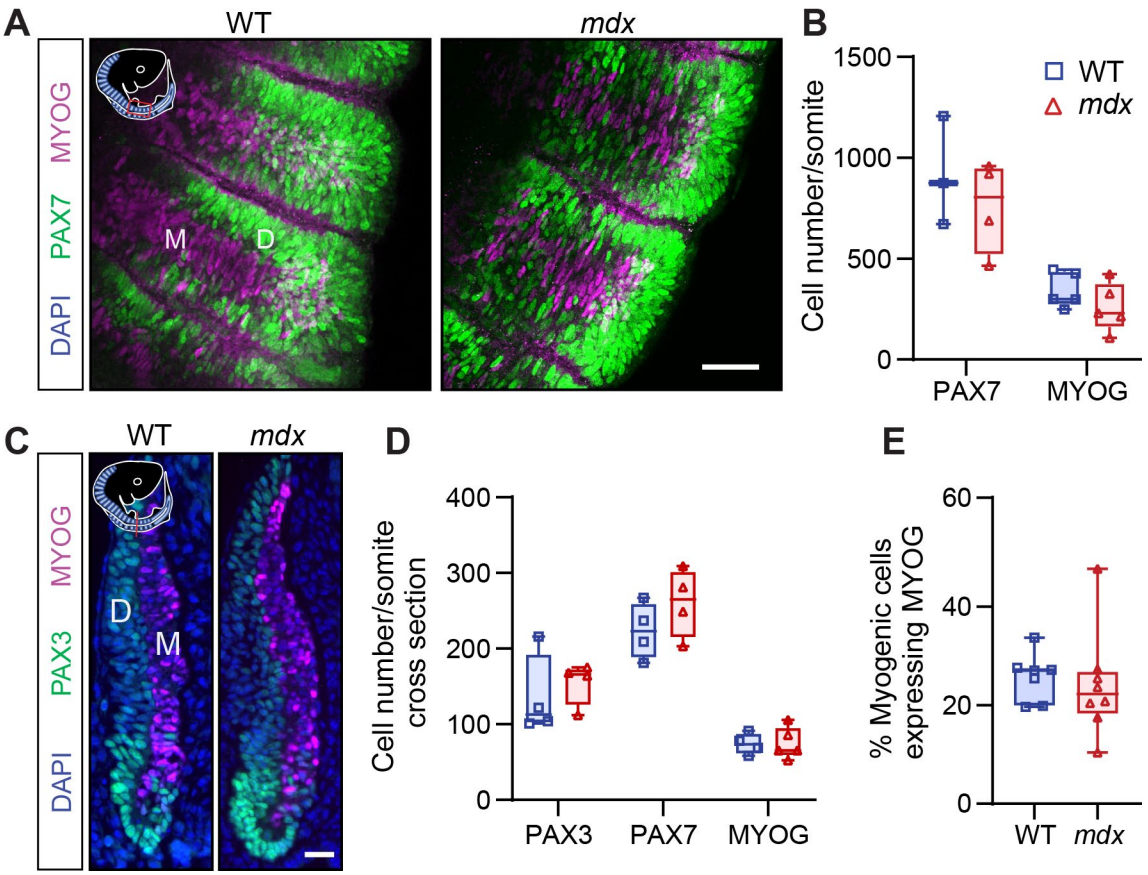

Figure 4.2 Myogenic cell commitment is not regulated by dystrophin at E10.5.
A Whole mount staining illustrates dermomyotome (D) and myotome (M) of E10.5 wild type (WT) and *mdx* embryos. PAX7 in green and MYOG in magenta. Scale bar is 50µm. **B** Average number of $PAX7^+$ and $MYOG^+$ cells per somite based on whole mount embryo staining at E10.5. For PAX7 staining, n=3 for WT and n=5 for *mdx*. For MYOG staining, n=5 per genotype. **C** Representative transverse cross-section of WT and *mdx* embryonic day 10.5 (E10.5) dermomyotome (D) and myotome (M) stained for PAX3 (green) and MYOG (magenta). Scale bar is 25µm. **D** Mean enumeration of myogenic cells per cross-section from ≥ 4 cross-section. **E** Proportion of $MYOG^+$ cells relative to total $PAX7^+$ and $MYOG^+$ cells at E10.5, including whole mount and cross-section analysis. n=7 for WT and n=8 for *mdx*. Data was not significantly different. Boxplot whiskers represent the maximum and minimum data values.

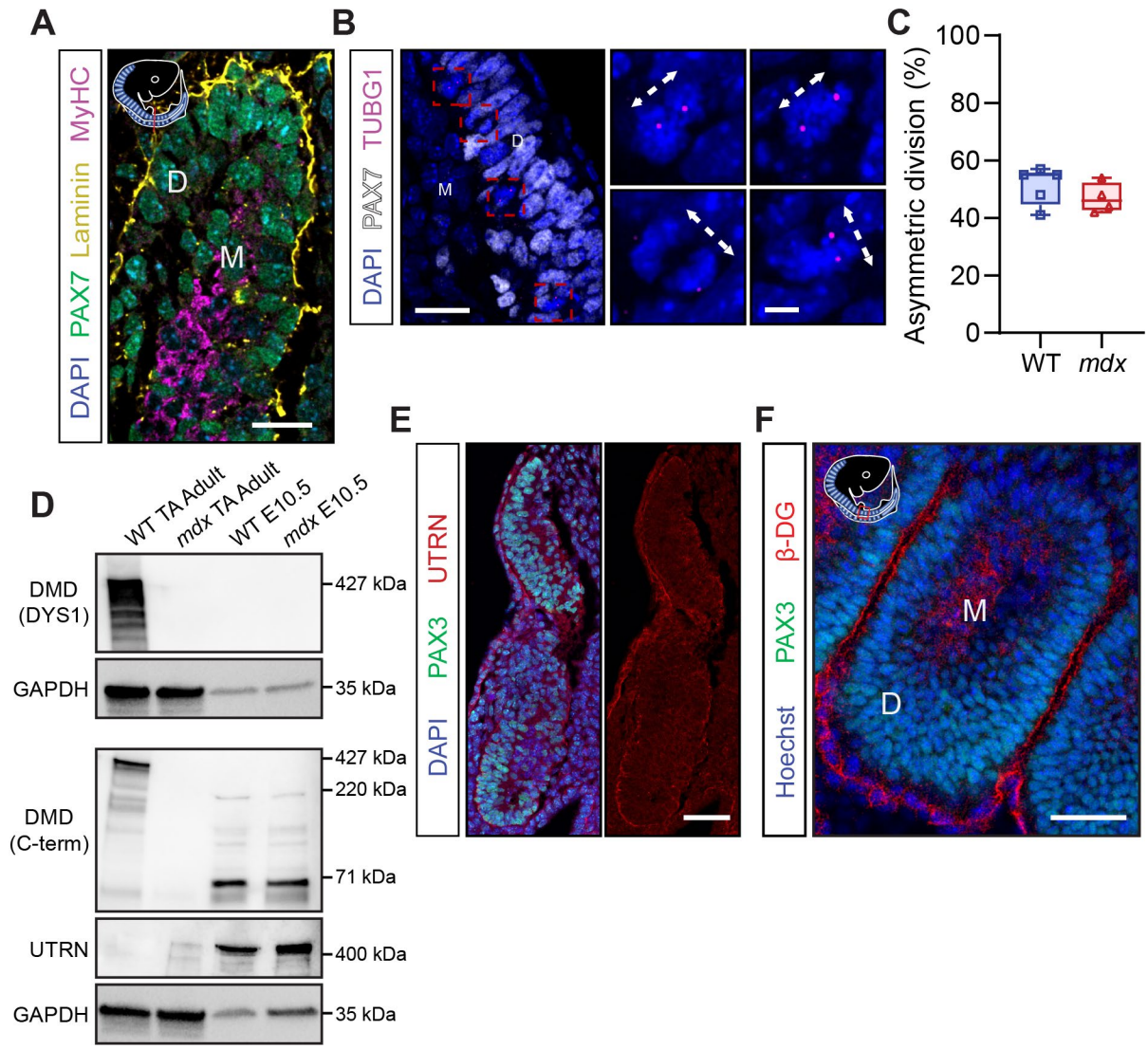

Figure 4.3 Dystrophin does not regulate asymmetric cell division in the dermomyotome. **A** Immunostaining depicts basal lamina surrounding the dermomyotome (D) and myotome (M). Dermomyotome illustrated by PAX7 (green), myotome by myosin heavy chain (MyHC; magenta) and basal lamina by laminin (yellow). Scale bar is 25µm. **B** Illustration of E10.5 dermomyotome (D) and myotome (M) stained for PAX7 (white) and TUBG1 (magenta). Right insets are magnified asymmetric (top) and symmetric (bottom) cell divisions denoted by white arrows and measured using the angle of cell divisions relative to the dermomyotome/myotome border. Scale bar is 25µm (left) and 5 µm (right). **C** Quantification of dermomyotome asymmetric cell division on serial wild type (WT) and *mdx* embryo transverse cross-sections relative to total cell divisions at E10.5. An average of 110 cell divisions was scored per embryo. n = 5 WT and 4 *mdx*. Statistical analysis was performed using unpaired t-tests. **D** Western blot with antibody against full-length dystrophin (DMD; DYS1), C-terminal dystrophin (c-term), N-terminal UTRN and GAPDH. **E** Continuous UTRN (red) staining around the epithelial dermomyotome marked by PAX3 (green) on E10.5 cross-section. Scale bar is 50µm. **F** Whole mount staining shows continuous β-dystroglycan (β-DG; red) staining surrounding the PAX3^{+} (green) dermomyotome at E10.5. Scale bar is 50µm.

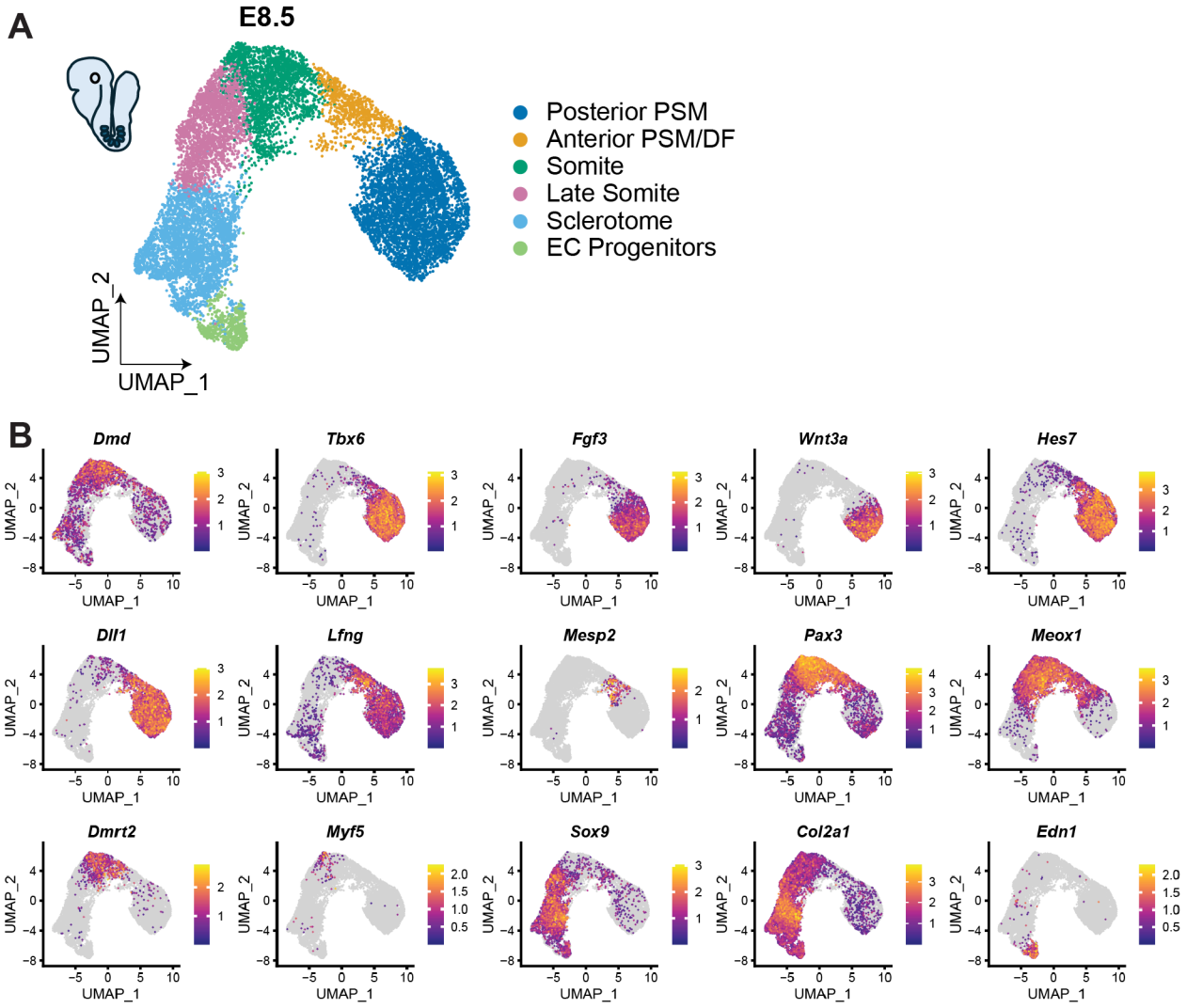

Figure 4.4 *Dmd* transcript is expressed in E8.5 somitic cells.
A UMAP projection of paraxial mesoderm lineage cells extracted from previously published E8.5 sci-RNA-seq3 dataset (Qiu et al.,2022[254]). **B** Features plots illustrate cluster identity markers and *Dmd* expression.

4.2 Delayed Development of *mdx* Fetal Muscle Occurs During Secondary Myogenesis

To assess the consequence of dystrophin deficiency during secondary myogenesis, cross-section sarcolemmal and ECM staining of WT and *mdx* fetal hindlimbs was performed at E14.5 and E17.5. We also examined muscles collected from WT and *mdx* fetuses that were crossed with the *Myf5-Cre* and *ROSA-nTnG* transgenic alleles. In this model, cells are nuclear tdTomato-positive (tdT^+) until *Myf5-Cre* expression permanently induces a switch to nuclear EGFP (GFP^+), which marks committed fMuSCs, progenitors, and myonuclei (**Figure 4.5A**).

At the beginning of secondary myogenesis, laminin staining of the E14.5 WT and *mdx* EDL revealed delayed organization of the basal lamina in the *mdx* fetus. While WT myofibers were surrounded by continuous laminin-rich matrices, intermittent laminin staining bordered *mdx* myofibers (**Figure 4.5B**). The laminin staining area was also reduced in the *mdx* EDL compared to WT muscle (**Figure 4.5C**). Taking advantage of the *Myf5-Cre;RnTnG* transgene, we also observed significantly fewer GFP^+ myogenic nuclei in the *mdx* EDL and TA at E14.5, which included progenitors and myonuclei that have expressed *Myf5-Cre* (**Figure 4.5B,D**).

We next questioned whether the changes in basal lamina formation and number of myogenic nuclei resulted from a delay in the transition from the primary to secondary myogenic program in *mdx* fMuSCs. The transcription factor NFIX is normally upregulated in fetal myogenic cells, serving as a transcriptional switch to regulate the transition from primary to secondary myogenesis.[91] RT-qPCR analysis of GFP^+ fMuSC isolated from WT and *mdx Pax7-nGFP* fetal limbs revealed that *Nfix* expression was unchanged between genotypes at E14.5 (**Figure 4.5E**). This suggests that the phenotype observed at E14.5 does not result from a delay in the transition from the embryonic to fetal transcriptional program, which we would expect if the architectural changes were a result of upstream developmental delays.

COL4A1 staining revealed a continuous ECM surrounding both WT and *mdx* myofibers by E17.5 (**Figure 4.6A**). However, sarcolemmal DAG1 staining of the E17.5 TA and EDL demonstrated fewer myofibers and reduced total cross-section area (CSA) in *mdx* muscle (**Figure 4.6A-C**). Moreover, the distribution of TA and EDL myofiber area shifted, with a greater proportion of small E17.5 *mdx* myofibers compared to age-matched WT muscle (**Figure 4.6D**). Visually, dystroglycan expression was downregulated in fetal *mdx* hindlimb muscle, as previously observed in postnatal *mdx* muscle (**Figure 4.6A**).[255] Confirming that this did not affect our myofiber analysis, we observed decreased myofiber number and CSA in *mdx* fetal EDL cross-sections using COL4A1 staining (**Figure S2A-C**). Consistent with findings at the beginning of secondary myogenesis, we also observed significantly fewer GFP^+ myogenic nuclei in the *mdx* EDL and TA at E17.5 using the *Myf5-Cre;RnTnG* transgene (**Figure 4.6E,F**). Finally, *mdx* fetal muscle was less dense at E17.5 than WT muscle, as demonstrated by the decreased number of myofibers per mm^2 in the EDL and TA (**Figure S2D,E**), and the increased ratio of ECM relative to myofiber area (**Figure S2F**). These results align with studies in *mdx* neonates, where myofibers are hypotrophic and have fewer myonuclei compared to WT muscle until approximately three weeks of age.[248] Similarly, our findings on myofiber morphology are consistent with the discovery that human fetal muscle has reduced myofiber density and size.[187]

To further assess whether the observed phenotype in *mdx* fetal muscle resulted from a delay in the transition from primary to secondary myogenesis, we next enumerated $MYH7^+$ primary myofibers on WT and *mdx* TA and EDL cross-sections at E17.5. We observed no difference in the number of $MYH7^+$ primary myofibers (**Figure 4.7A,B**) or the relative MYH7 expression area (**Figure 4.7C**) between WT and *mdx* TA and EDL cross-sections. Therefore, the difference in

myofiber morphology observed in *mdx* fetal muscle is likely not due to developmental delays prior to secondary myogenesis.

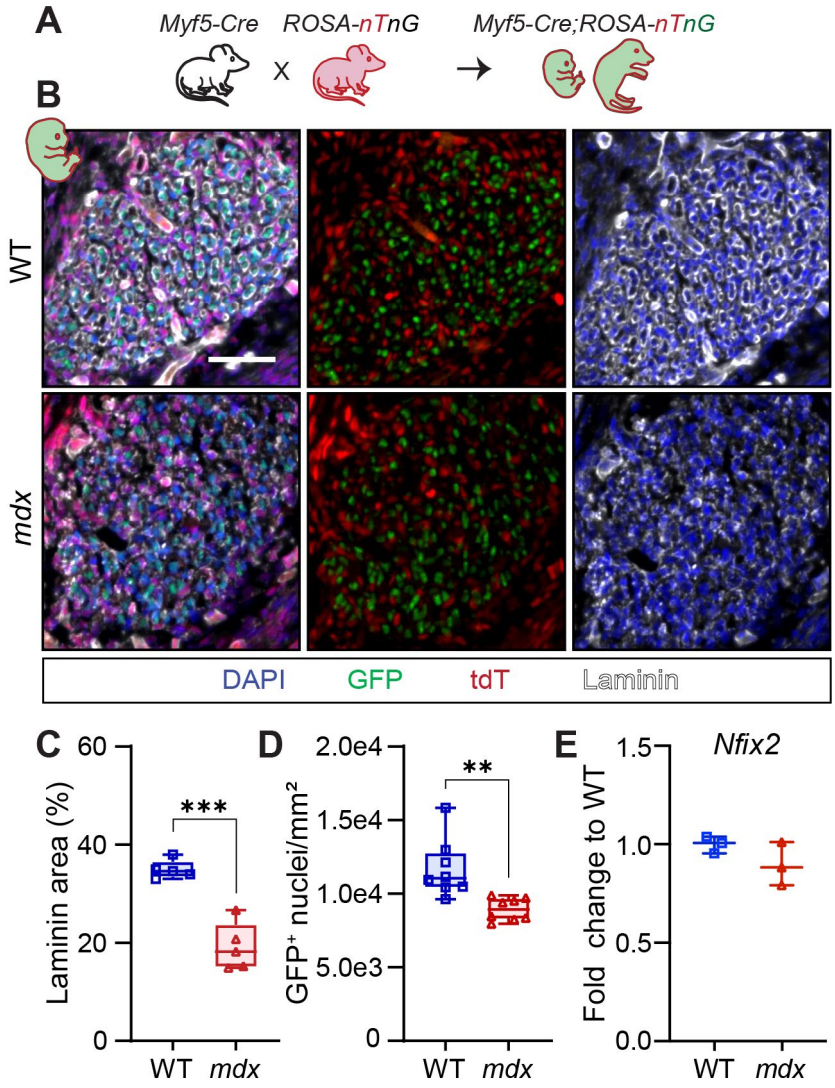

Figure 4.5 Hindlimb muscle basal lamina formation is delayed in the E14.5 *mdx* fetus.
A Schematic of *Myf5-Cre* and *ROSA-nTnG* breeding pairs used to obtain embryos for analysis of fetal MuSC commitment. Nuclei are tdTomato-positive (tdT$^+$) until *Myf5-Cre* expression induces recombination of the *ROSA* allele and expression of EGFP (GFP$^+$). **B** Representative immunofluorescence images of E14.5 *extensor digitorum longus* (EDL) from wild type (WT) and *mdx Myf5-Cre;ROSA-nTnG* fetuses with DAPI counterstain (blue), endogenous GFP (green) and tdT (yellow), and laminin staining (magenta). Scale bar is 50µm. **C** Percent of EDL area stained with anti-laminin. n=5 per genotype. **D** Number of GFP$^+$ nuclei normalized to mm^2 enumerated on WT and *mdx Myf5-Cre;R-nTnG* hindlimb TA and EDL cross-sections at E14.5. n=8 per genotype. **E** RT-qPCR analysis of *Nfix* expression in GFP$^+$ fMuSC isolated from WT and *mdx Pax7-nGFP* E14.5 fetal limbs. Data presented as fold change to WT. Box plot whiskers indicate the maximum and minimum values. Statistical analysis performed using unpaired t-tests, where ** $p < 0.01$ and *** $p < 0.001$.

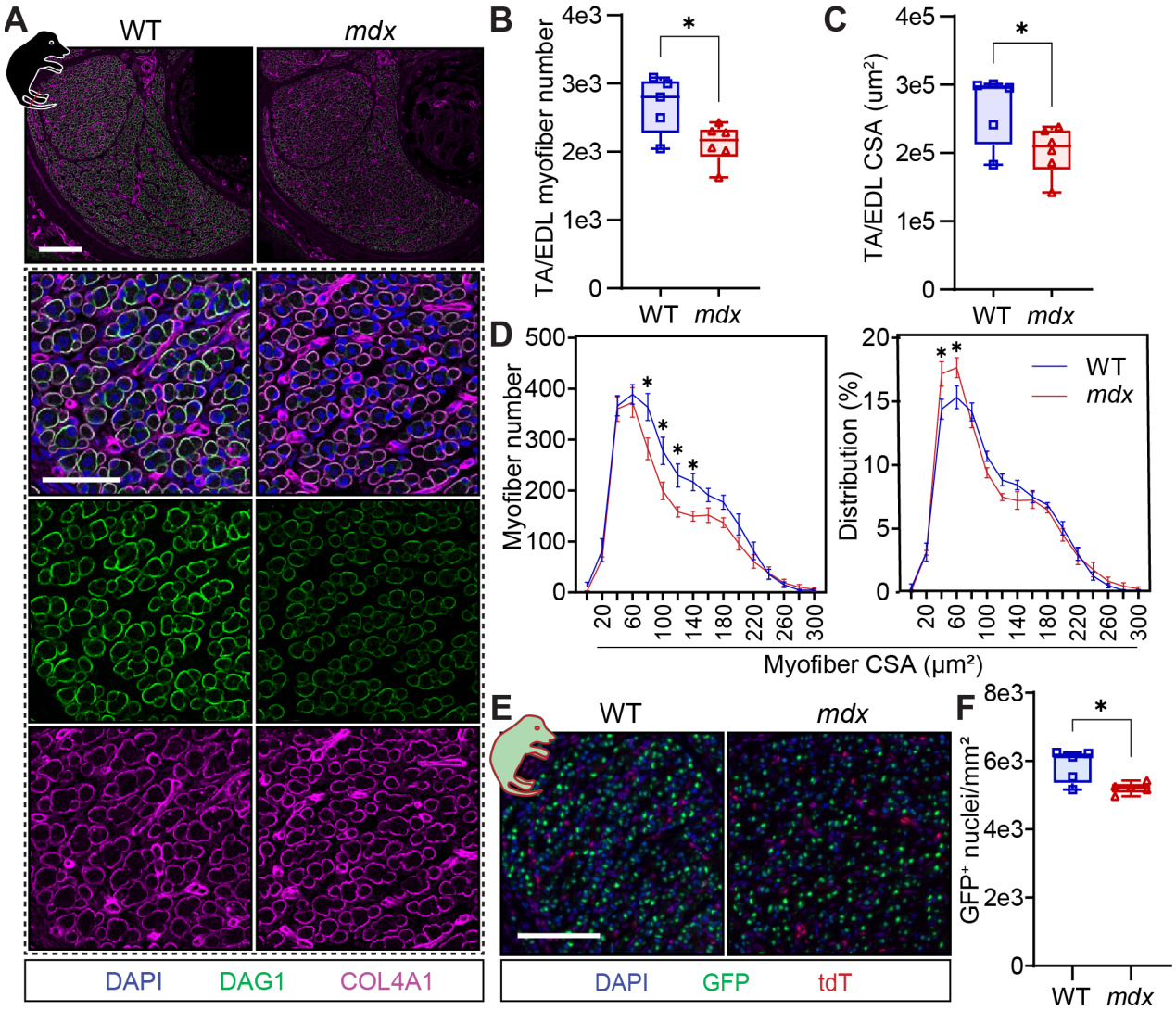

Figure 4.6 Fetal myofibers are smaller in the hindlimb muscle of E17.5 *mdx* mice.
A Example immunofluorescence images of entire wild type (WT) and *mdx extensor digitorum longus* (EDL) and *tibialis anterior* (TA) at E17.5 (top; scale bar is 100µm) and magnified insets (bottom; scale is 50µm). DAPI counterstain (blue), DAG1 (green) denotes sarcolemma and COL4A1 (magenta) marks the extracellular matrix. **B-C** Total TA and EDL myofibers number (B) and myofiber cross-section area (CSA; µm^2) (C) at E17.5 based on DAG1 staining. **D** Size distribution of E17.5 myofibers using myofiber CSA (µm^2) based on DAG1 staining. Left is number of fibres and right is normalized size distribution. **E** Representative immunofluorescence images of E17.5 EDL cross-section from WT and *mdx Myf5-Cre;ROSA-nTnG* fetuses expressing endogenous GFP (green) and tdT (red), counterstained with DAPI (blue). Scale bar is 100µm. **F** Number of GFP$^+$ nuclei normalized to mm^2 enumerated on WT and *mdx Myf5-Cre;R-nTnG* hindlimb TA and EDL cross-sections at E17.5. n=5 per genotype. For B,C, and F, box plot whiskers indicate the maximum and minimum values. For D, data presented as mean ± SEM. For B-D, n=5 for WT and n=6 for *mdx*. Statistical analysis performed using unpaired t-tests, except for D where a two-way ANOVA followed by Sidak's test for multiple comparisons was performed (*$p < 0.05$, ** $p < 0.01$, *** $p < 0.001$).

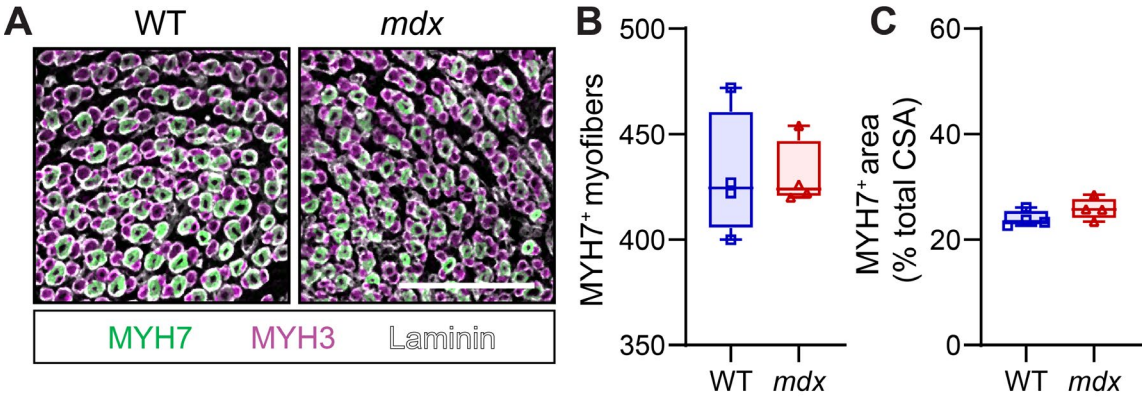

Figure 4.7 No change in the number of primary myofibers in E17.5 *mdx* muscle.
A Representative immunofluorescence images of wild type (WT) and *mdx extensor digitorum longus* (EDL) muscles at E17.5 (scale bar,100µm). MYH7 (green) denotes primary myofibers, and MYH3 (magenta) marks all myofibers. Laminin (white) highlights the myofiber basal lamina. **B** Number of MYH7-expressing primary myofibers in the WT and *mdx tibialis anterior* (TA) and EDL muscles. **C** Proportion of TA and EDL muscle cross-section area expressing MYH7. n=4 per genotype. Not statistically significant by unpaired t-test.

4.3 Fewer Myogenic Cells in *mdx* Fetal Muscle

In *mdx* muscle, fewer asymmetric MuSC divisions occur in the absence of dystrophin, leading to the reduced generation of progenitor cells.[138] To assess whether perturbations in fetal myofiber development correlated with a decreased number of progenitor cells, we enumerated the number of $PAX7^+$ and $MYOG^+$ cells on TA and EDL cross-sections at E14.5 and E17.5 (**Figure 4.8A,B**). The total number of myogenic cells, including both $PAX7^+$ and $MYOG^+$ cells, was reduced at both stages (**Figure 4.8C,D**). To account for the global reduction in myogenic cells and examine myogenic cell commitment, we assessed the proportion of $MYOG^+$ cells in the entire $PAX7^+$ and $MYOG^+$ populations. Interestingly, the proportion of $MYOG^+$ cells was reduced at both time points but more profoundly at E17.5 (**Figure 4.8E**). Our findings align with the previously observed decrease in PAX7 expression in *mdx* fetal muscle by western blot,[190] and our study of neonatal myogenesis (**Figure 3.19E,F).** Because both uncommitted myogenic and progenitor cells express PAX7, our results suggest that the decrease in PAX7 cells results from fewer progenitor cells in the *mdx* embryo.

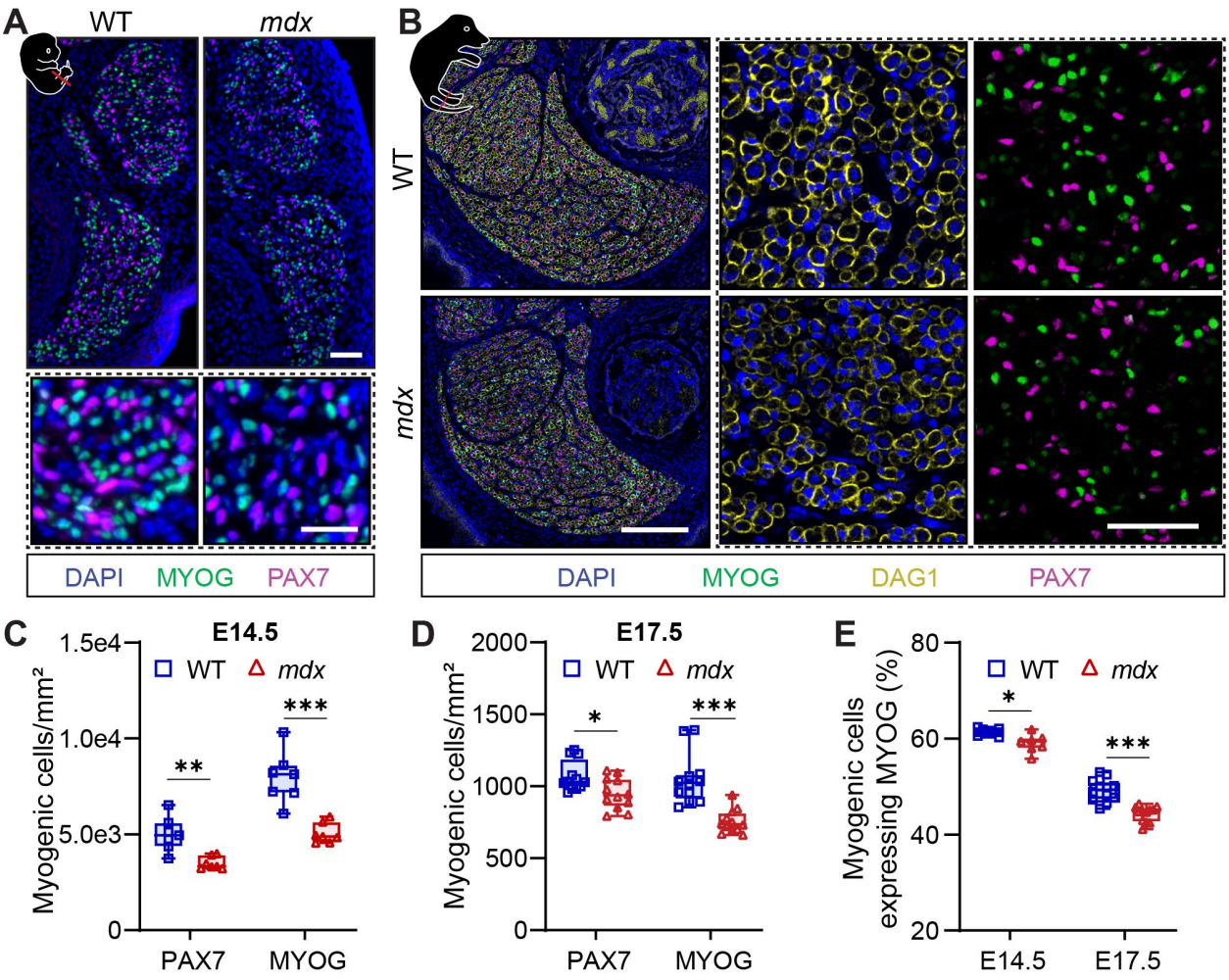

Figure 4.8 Fewer committed myogenic cells in E17.5 *mdx* muscles.
A Representative immunofluorescence images of wild type (WT) and *mdx tibialis anterior* (TA) and *extensor digitorum longus* (EDL) from hindlimb transverse sections at embryonic day (E) 14.5 (top; scale bar is 50µm) and magnified inset (bottom; scale bar is 25µm). MYOG (green) denotes differentiating progenitor cells, and PAX7 (magenta) labels fetal MuSCs. **B** Immunofluorescence image examples of WT and *mdx* TA and EDL from hindlimb transverse sections at E17.5 (scale bar is 200µm) and magnified inset (scale bar is 50µm). MYOG (green) denotes differentiating progenitor cells, DAG1 (yellow) marks fetal sarcolemma, and PAX7 (magenta) labels fetal MuSCs. **C-D** Enumeration of myogenic cells expressing either PAX7 or MYOG at E14.5 (C) and E17.5 (D) and normalized to mm^2. **E** Proportion of $MYOG^+$ cells relative to entire $PAX7^+$ and $MYOG^+$ cell population at E14.5. and E17.5. For C-E, n=7 per genotype at E14.5 and n=12 per genotype at E17.5. Box plot whiskers indicate the maximum and minimum values. Data analysed using two-way ANOVA corrected for multiple comparisons using Sidak's test where $*p < 0.05$, $**p < 0.01$, and $***p < 0.001$.

The expression of *Myf5* is a metric of developmental and adult MuSC commitment upstream of MYOG.[94,134] Using the *Myf5-Cre* and *ROSA-nTnG* knock in lines bred into the WT and *mdx* background, we quantified the number of $PAX7^+$ cells that have never expressed *Myf5-Cre* at E14.5 and E17.5 (**Figure 4.9A,B**). We observed fewer $PAX7^+$ tdT^+ cells at E14.5, and a 3.5-fold increase in $PAX7^+$ tdT^+ at E17.5 (**Figure 4.9C**). Taking into consideration the decrease in total $PAX7^+$ cells that was more pronounced at E14.5, we quantified the proportion of total $PAX7^+$ cells that express tdT. No change in the relative proportion of $PAX7^+$ tdT^+ cells was observed at E14.5, while a notable increase in the proportion of uncommitted $PAX7^+$ tdT^+ cells occurred at E17.5 (**Figure 4.9D**). This suggests that the uncommitted fMuSC population is expanded in dystrophin-deficient muscle by E17.5 during secondary myogenesis.

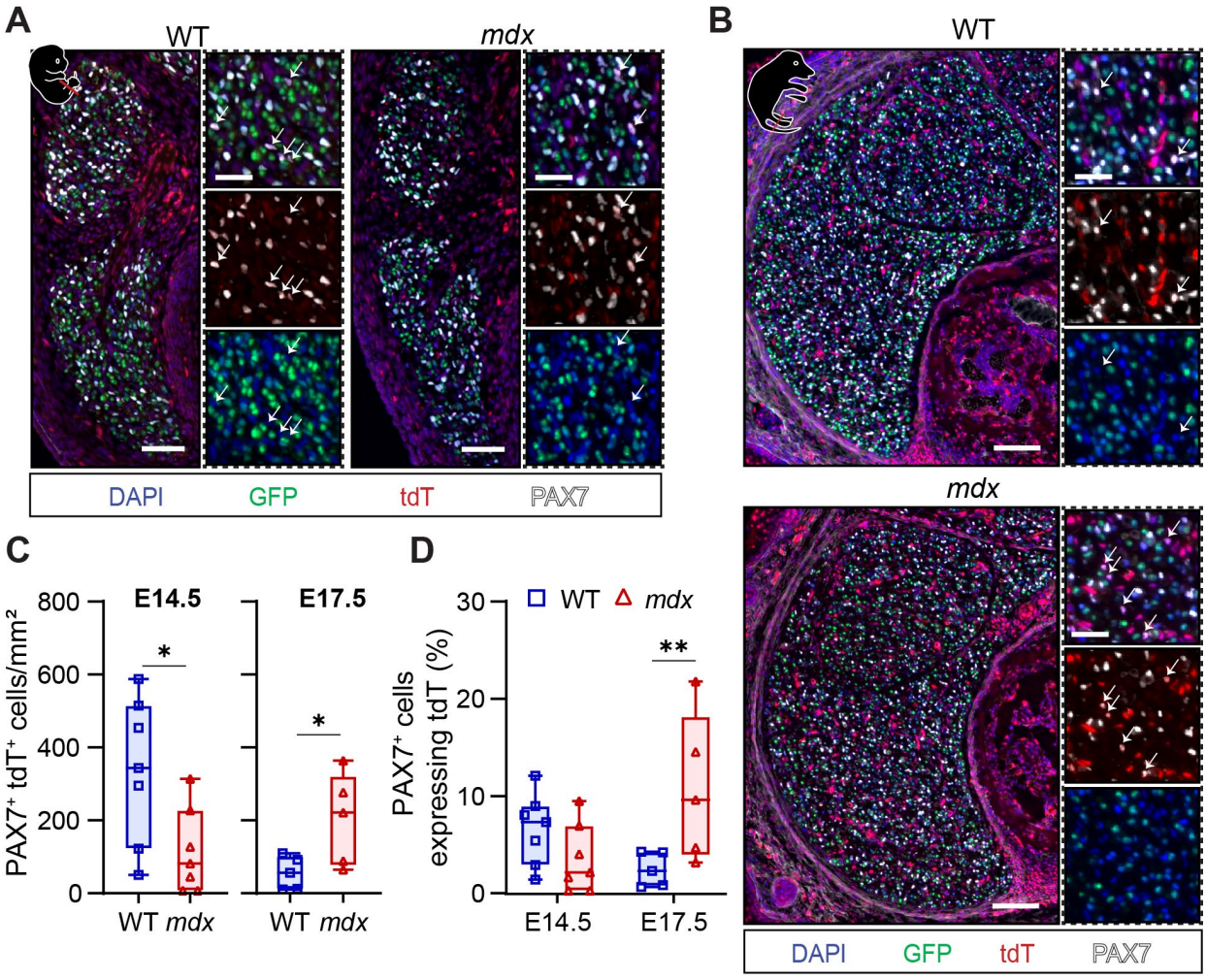

Figure 4.9 Fewer *mdx* fetal MuSCs have expressed *Myf5*.
A-B Representative image of the TA and EDL from WT and *mdx Myf5-Cre;R-nTnG* hindlimb cross-sections at E14.5 (A) and E17.5 (B). Cell express endogenous tdTomato (tdT^+; red) or EGFP (GFP^+; green), and PAX7 (white) marks fetal MuSCs (fMuSCs). In A, the scale bar is 50µm and 25µm (insets). In B, scale bars are 100µm and 25µm (insets). White arrows denote $PAX7^+$ tdT^+ cells. **C** Enumeration of $PAX7^+$ tdT^+ myogenic cells normalized to mm^2 at E14.5 and E17.5. Statistical analysis performed using unpaired t-tests (*$p < 0.05$). **D** Proportion of total $PAX7^+$ cells that express tdT at E14.5 and E17.5 from WT and *mdx Myf5-Cre;R-nTnG* hindlimb TA and EDL cross-sections. Data analyzed using two-way ANOVA corrected for multiple comparisons using Sidak's test where ** $p < 0.01$. For **C-D**, n=7 per genotype at E14.5 and n=5 per genotype at E17.5. Box plot whiskers indicate the maximum and minimum values.

4.4 Fetal MuSCs Generate Fewer Progenitor Cells During Secondary Myogenesis

To further investigate myogenic cell state and gene expression profiles of fMuSCs in dystrophin-deficient fetal muscle, we isolated GFP^+ cells in biological duplicates from the limbs of WT and *mdx Pax7-nGFP* embryos at E17.5 for single cell RNA-seq (scRNA-seq) (**Figure 4.10A** and **Figure S3A**). Residual GFP allowed us to study the progression from uncommitted fMuSCs to terminally differentiated myocytes. Following quality control, filtering and dimensional reduction of the combined libraries, 7 clusters containing 21,734 WT and 25,064 *mdx* cells were identified and annotated based on differential gene expression testing (**Figure 4.10B** and **Data File S4**).

Two of the identified clusters were omitted from downstream analysis. The first were $Pax7^+$ '$Tex14^+$ Cells,' which represented 3.3% and 2.3% of the WT and *mdx* libraries, respectively, and likely originated from the fetal testes.[256,257] The second were $Pdgfra^+$ $Cd34^+$ fetal fibro-adipogenic progenitors ('fFAPs'), accounting for 1.3% of the WT and 2.1% of the *mdx* libraries. This cluster expressed previously documented fFAP markers and was likely derived from $Pax7^+$ lineages. (**Figure 4.10C**).[258] The five remaining clusters represented the myogenic continuum, from undifferentiated fMuSCs to post-mitotic myocytes, and were the focus of further analyses (**Figure 4.10B,C**). Myogenic cells comprised approximately 95% of each library, regardless of genotyping. Together, this suggests that the absence of dystrophin does not lead to an expansion of the $Pax7^+$ non-myogenic lineage. However, increased ECM deposition in *mdx* and DMD fetal muscle has been reported.[187,190] Thus, the small increase in the fFAPs could represent a larger difference that is not reflected in the GFP^+ libraries.

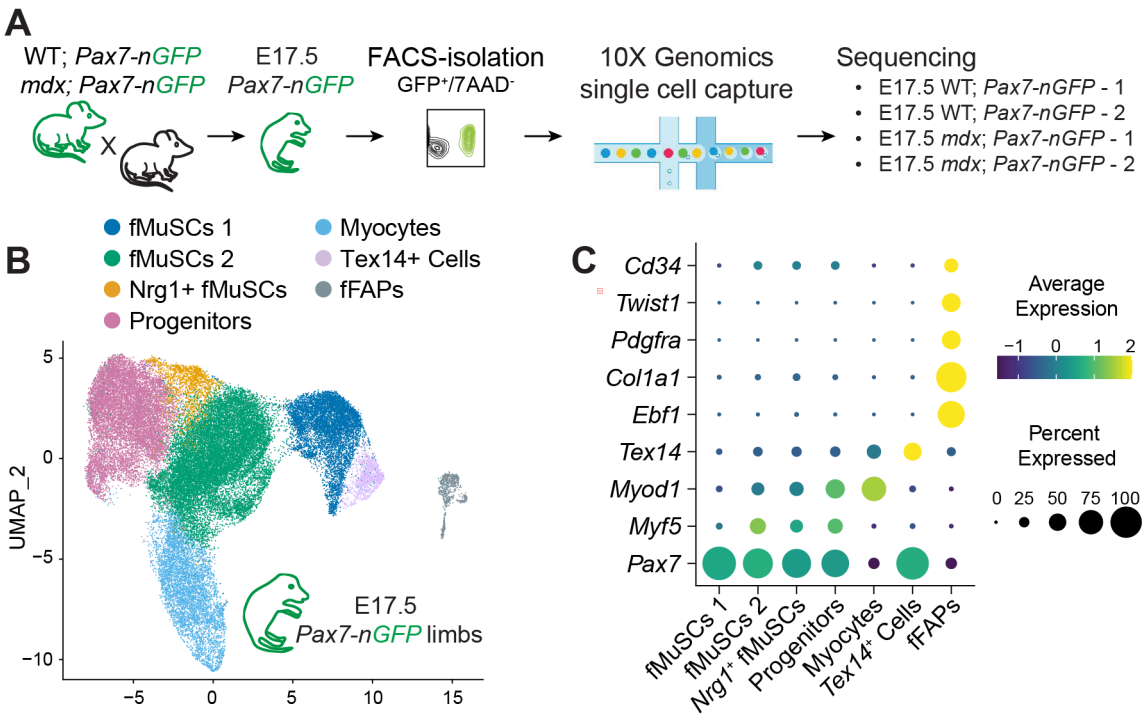

Figure 4.10 Myogenic cell heterogeneity observed by single cell RNA.
A Experimental design for fluorescence sorting and sequencing of live single GFP^{+} fetal muscle stem cells (fMuSCs) from wild type (WT) and *mdx Pax7-nGFP* fetal limbs. **B** Uniform manifold approximation and projection (UMAP) visualization of 21734 WT and 25064 *mdx* cells across four single cell RNA-sequencing libraries with illustration of low-resolution clusters. Myogenic cells are schematically depicted in hierarchical order from fetal (f) MuSCs to myocytes. **C** Dot plot illustrates cluster markers illustrated in panel B.

To minimize the effect of cell cycle on clustering, we assigned mitosis scores using Seurat's CellCycleScoring function, then regressed the S and G2/M phase scores using scTransform. Dimensional reduction and re-clustering identified 11 myogenic cell clusters with unique features (**Figure 4.11A** and **Data File S5**). The clusters were ordered hierarchically based on decreasing *Notch3* expression,[134] the concurrent emergence of the notch ligand *Srrt*,[109] the progressive increase in *Hes6*,[111] and the general sequence of MRF and differentiation marker expression (**Figure 4.11A-C** and **Data File S5**).

fMuSC clusters were generally characterized by elevated *Pax7* expression, the absence of *Myog*, and the expression of notch and ECM genes that are linked to postnatal MuSC quiescence and activation (**Figure 4.11B,C** and **Data File S5**).[83,111,112] 'fMuSCs 1' and 'fMuSCs2' were enriched in oxidative phosphorylation genes and expressed elevated *Pax7*, *Notch3*, *Col4a1*, *Lama2*, and *Itgb1*, and negligible *Myf5* and *Myod1*. Based on the elevated expression of quiescent MuSC niche genes and the metabolic gene signature, we theorized fMuSCs 1 and 2 are fMuSCs residing in the nascent fetal myofiber niche and contributing to its formation. 'fMuSCs 3' and 'fMuSCs4' expressed *Myf5* but not *Myod1*, while 'fMuSC 5' and 'fMuSCs 6' expressed both MRFs. All four *Myf5*-expressing fMuSC clusters shared increased expression of activation related genes such as the AP1 transcription factors *Junb* and *Fos*, the ECM genes *Lama5* and *Col5a1*, and the proliferation and activation-related notch genes *Notch1*, *Notch2*, *Notch3*, *Srrt*, *Hes1*, and *Hes6*.[85,112,127,137,259] 'fMuSCs 7' shared similarities to the four 'active' clusters, but with reduced expression of MuSC and activation-related genes including *Pax7*, *Notch2*, *Notch3*, *Lama2*, *Lama5*, and *Col5a1*, and elevated expression of ribosomal and cell cycle genes such as *Ccnd1*, *Ccnb2*, and *Pttg1,* suggesting this was a committed fMuSC cluster.

Interestingly, we observed striking fMuSC heterogeneity. The fMuSCs 4 cluster expressed elevated genes related to TGF-β and MAPK signalling, focal adhesions, and smooth muscle, including *Igf1*, *Ltbp1*, *Rgma*, *Pitx2*, *Tgfb2*, *Met*, *Itga1*, *Nppc* and *Cav1*. fMuSCs 2 and fMuSCs 5 expressed elevated *Nrg1*, *Col19a1*, *Adgrb3*, *Fgf12*, *Slit2*, *Bmpr1b*, *Meis1*, and *Nell1*, genes linked to BMP signalling and neurogenesis. Finally, fMuSCs 6 were enriched for the interleukin 1 receptor family gene *Il1rapl2*, in addition to *Eya2*, *Sfrp2*, *Exoc6*, *Fat3*, *Nckap5,* and *Zic1* (**Figure 4.11B,C** and **Data File S5**).

Four progenitor cell clusters were identified in the WT and *mdx* libraries. 'Progenitors' expressed *Pax7*, *Myf5*, *Myod1*, *Mki67*, and low levels of *Myog*, while 'Committed progenitors' expressed very little *Pax7*, and elevated *Myod1*, *Myog*, and *Mymx*. Two distinctly different myocyte clusters were also observed. The larger 'Myocytes' cluster expressed dogmatic differentiation markers such as *Myog*, *Mymx*, and *Acta1*, the cell cycle inhibitor *Cdkn1a*, and very little *Dmd*. The smaller 'Oxidative Myocyte' cluster expressed elevated OxPhos genes, *Myog*, and *Utrn*. The oxidative myocyte cluster also shared upregulated genes with the two *Nrg1*$^{+}$ fMuCS clusters, including *Bmpr1b*, and *Col19a1* (**Figure 4.11B,C** and **Data File S5**).

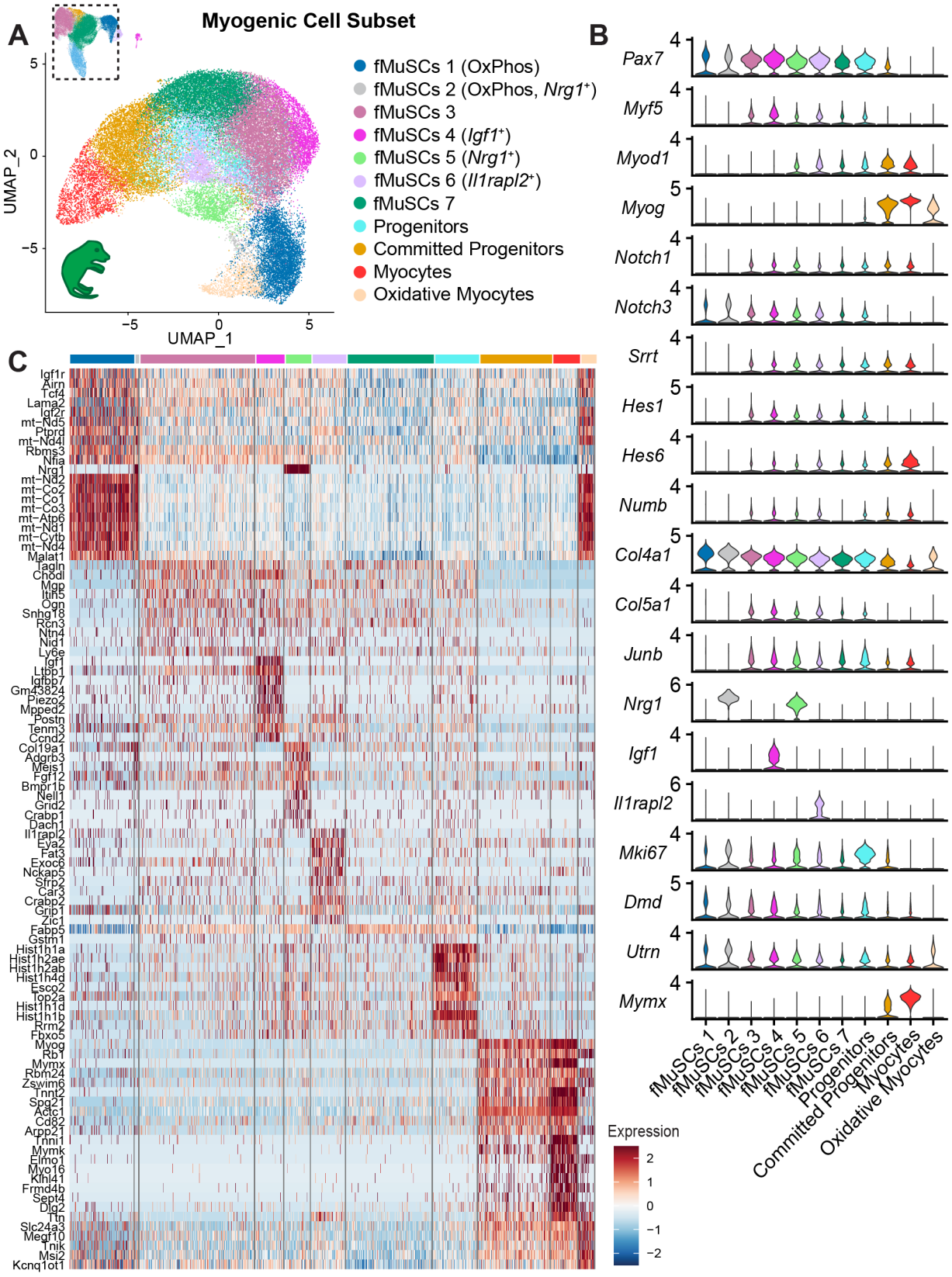
A
Myogenic Cell Subset
fMuSCs 1 (OxPhos)
fMuSCs 2 (OxPhos, Nrg1+)
fMuSCs 3
fMuSCs 4 (Igf1+)
fMuSCs 5 (Nrg1+)
fMuSCs 6 (Il1rapl2+)
fMuSCs 7
Progenitors
Committed Progenitors
Myocytes
Oxidative Myocytes
UMAP_1
UMAP_2
B
Pax7
Myf5
Myod1
Myog
Notch1
Notch3
Srrt
Hes1
Hes6
Numb
Col4a1
Col5a1
Junb
Nrg1
Igf1
Il1rapl2
Mki67
Dmd
Utrn
Mymx
fMuSCs 1
fMuSCs 2
fMuSCs 3
fMuSCs 4
fMuSCs 5
fMuSCs 6
fMuSCs 7
Progenitors
Committed Progenitors
Myocytes
Oxidative Myocytes
C
Expression

Figure 4.11 Clustering of the myogenic cell subset reveals cellular heterogeneity.
A Uniform manifold approximation and projection (UMAP) visualization of myogenic cell subset from libraries generated from GFP^+ cells isolated from WT and *mdx Pax7-nGFP* E17.5 fetal hindlimbs. **B** Violin plots of representative markers for the clusters illustrated in A. **C** Heat map of top 10 differentially expressed genes by cluster.

Unlike the adult scRNA-seq libraries, cells in the WT and *mdx* libraries clustered together without bioinformatic integration (**Figure 4.12A**). However, as seen by histological analysis, *Pax7*$^{+}$ fMuCSs clusters were over-represented in the *mdx* libraries. The fMuSC clusters constituted 62% and 76% of the WT and *mdx* libraries, respectively, while the *Myog*$^{+}$ progenitor cell clusters accounted for the remaining 38% and 24% (**Figure 4.12B**). Interestingly, the *Myf5*-low fMuSCs1 cluster represented 12% of the WT library and 20% of the *mdx* libraries, which corroborates our findings using the *Myf5-Cre;ROSA-nTnG* allele, where we observed an expansion of the uncommitted fMuSC population at E17.5 (**Figure 4.9**). Comparing similar numbers of WT and *mdx* cells using feature plots further illustrates the overrepresentation of *Pax7*$^{+}$ cells, and the reduced expression of the commitment markers *Myog*, *Mymk*, and *Acta1* (**Figure 4.12C**).

Cell cycle scoring indicated that slightly more than half of both WT and *mdx* libraries were in G2M or S phase, with no major differences between genotypes (**Figure 4.12D**). However, the proportion of *Mki67*$^{+}$ progenitors was drastically reduced in the *mdx* libraries (**Figure 4.12A,B**), which should account for a large portion of proliferating cells. We therefore examined the number of cells expressing the proliferation markers *Cenpa*, *Mki67* and *Cdk1* and categorized these into fMuSC or progenitor clusters. As observed by cell cycle scoring, the overall number of proliferating cells was nearly identical (64%) between genotypes. However, proliferating fMuSCs accounted for 39% of the WT and 48% of the *mdx* libraries, whereas proliferating progenitors comprised 25% of the WT and 16% of the *mdx* libraries, respectively (**Figure 4.12E**). This corresponded to a 22% increase in proliferating fMuSCs concomitant with a 34% reduction in proliferation progenitors in the *mdx* libraries compared to WT. The transcriptomic data supports the finding that *mdx* fMuSCs have a reduced ability to generate progenitor cells.

Next, we performed differential gene expression testing on the WT and *mdx* libraries and found 1604 downregulated and 580 upregulated genes in the *mdx* libraries (**Data File S6**). Further corroborating the reduced commitment of *mdx* fMuSCs, we observed downregulated genes related to muscle commitment, including *Actc1*, *Myog*, *Mymx*, *Tnnt2*, and *Acta1*, in addition to genes such as *Camk1d*, *Lars2*, *Erh*, *Cdv3*, *Eno1*, *Igf2*, and *Ddx6*. Gene ontology (GO) analysis of the downregulated genes similarly highlighted terms such as 'muscle system process,' 'muscle contraction,' and 'muscle cell differentiation' (**Figure 4.12F** and **Data File S7**).

In the *mdx* libraries, upregulated genes included *Hes1*, *mt-Nd2*, and *Igf1r*, in addition to genes related to TGF-β signalling (*Bmpr1b*, *Id1*, *Thsd4* and *Ltbp1*), and genes associated with the fMuSCs 5 cluster (*Meis1*, *Fgf12*, *Col19a1*, *Slit2*, *Robo2*, and *Nrg1*). *Prkca*, a calcium-dependent protein kinase C, was also elevated, which was previously observed in fetal human DMD muscle (**Data File S6**).[187] Given that Notch and TGF-β signalling inhibit myogenic cell differentiation, this provides further evidence of reduced differentiation of *mdx* myogenic cells.[260,85,109] Unlike the adult libraries, the aberrant proportion of fMuSCs and progenitor cells occurred in the absence of inflammatory response gene upregulation. This supports the finding that intrinsic deficits, rather than solely the inflammatory microenvironment, contribute to MuSC polarity dysfunction in *mdx* postnatal muscle.

Notably, fMuSC clusters were enriched for adhesion, ECM, and DGC genes, requirements for dystrophin-mediated cell polarity. These included collagens, laminins, cadherins, integrins, immunoglobulin adhesion molecules, syndecans, and fibronectin (**Figure 4.11B**, **Figure 4.12G** and **Data File S6**). DGC genes expressed in the fMuSC clusters included *Dag1*, *Sgce*, *Dtnb*, *Sspn*, and importantly *Dmd*. Interestingly, the PAR complex genes *Mark2* and *Pard6g* were also enriched

in the 'activate' fMuSC clusters, while *Pard3* was ubiquitously expressed (**Figure 4.11B** and **Figure 4.12G**).

Because *Hes1* was highly upregulated in *mdx* fMuSCs, we also examined the expression of Notch signalling genes in the combined libraries (**Figure 4.11B** and **Figure 4.12G**). Unlike *Notch3,* which was most expressed in the *Myf5*-low OxPhos fMuSCs, *Notch1* and *Notch2* were upregulated in the *Myf5*-high expressing clusters. This agrees with previous studies that indicate *Notch3* and *Notch1* act in opposition to regulate postnatal MuSC activation.[143] Similarly, the Notch target gene *Hes1* was upregulated in the *Myf5*-high clusters, while the Notch ligand *Srrt* was upregulated in *Myf5*-high and progenitor cell clusters. The Notch signalling antagonist *Numb*, a known determinant of asymmetric cell fate,[261] was also expressed in most *Myf5*-high and progenitor clusters.

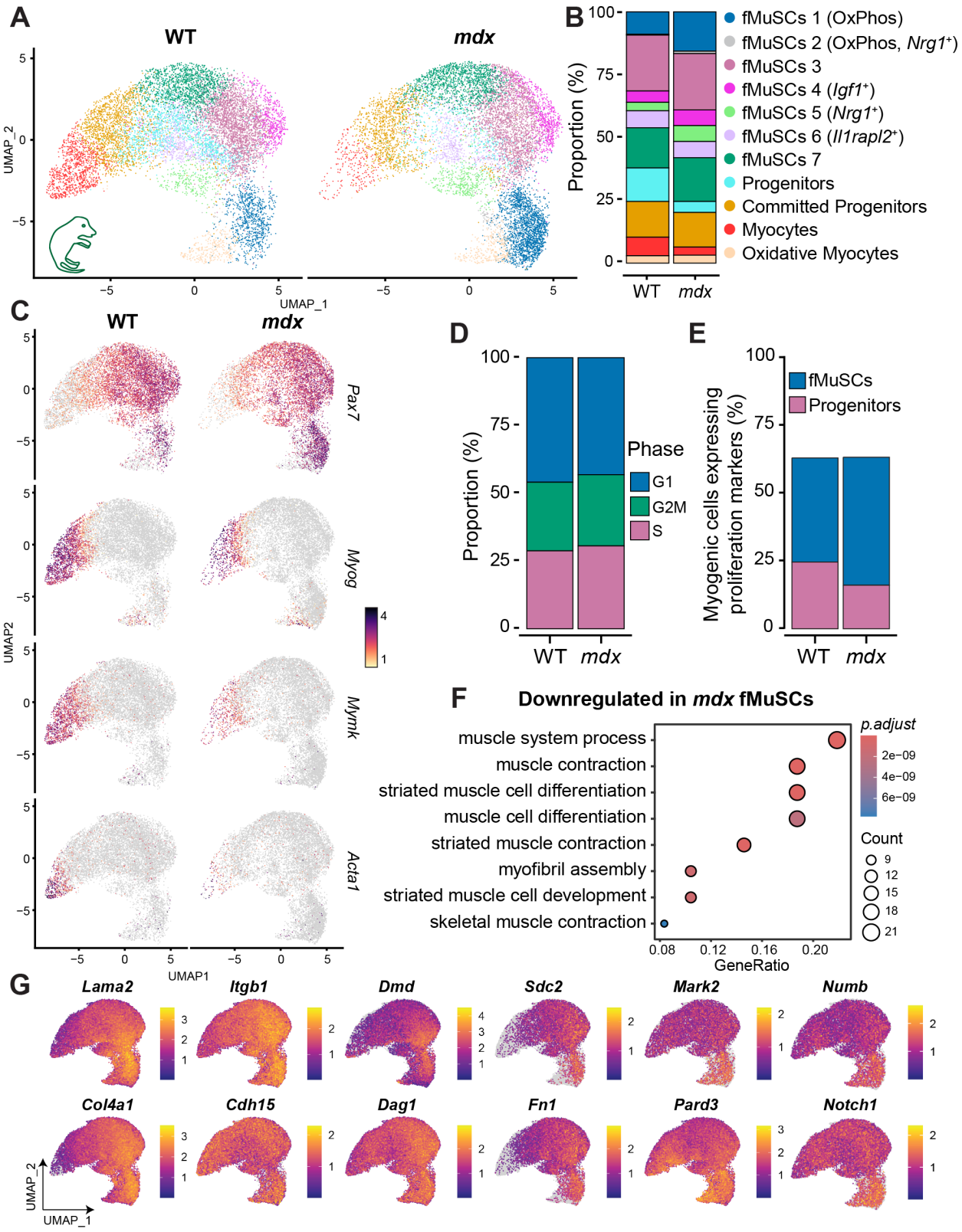
A
WT
mdx
UMAP_2
UMAP_1
B
Proportion (%)
WT
mdx
fMuSCs 1 (OxPhos)
fMuSCs 2 (OxPhos, Nrg1+)
fMuSCs 3
fMuSCs 4 (Igf1+)
fMuSCs 5 (Nrg1+)
fMuSCs 6 (Il1rapl2+)
fMuSCs 7
Progenitors
Committed Progenitors
Myocytes
Oxidative Myocytes
C
WT
mdx
Pax7
Myog
Mymk
Acta1
UMAP2
UMAP1
D
Proportion (%)
Phase
G1
G2M
S
E
Myogenic cells expressing proliferation markers (%)
fMuSCs
Progenitors
F
Downregulated in mdx fMuSCs
muscle system process
muscle contraction
striated muscle cell differentiation
muscle cell differentiation
striated muscle contraction
myofibril assembly
striated muscle cell development
skeletal muscle contraction
p.adjust
Count
GeneRatio
G
Lama2
Itgb1
Dmd
Sdc2
Mark2
Numb
Col4a1
Cdh15
Dag1
Fn1
Pard3
Notch1
UMAP_2
UMAP_1

Figure 4.12 Single cell RNA-sequencing uncovers fewer progenitor cells in *mdx* muscle.
A Uniform manifold approximation and projection (UMAP) visualization of 10,000 wild type (WT) and *mdx* myogenic cells isolated from *Pax7-nGFP* E17.5 fetal limbs. Clusters are schematically depicted in hierarchical order from fetal (f) MuSCs to myocytes and grouped by genotype. **B** Bar plot illustrating library cluster proportions for WT and *mdx* fetal MuSC libraries (biological duplicates). **C** Feature plot illustrating the expression of PAX7 and commitment markers *Myog*, *Mymk* and *Acta1*. **D** WT and *mdx* library proportions split by cell cycle phase, as determined by Seurat's cell cycle scoring. **E** Proportion of library expressing proliferation markers (*Cenpa*, *Mki67* or *Cdk1*), split by fMuSC and progenitor cell identity. **F** Gene ontology term enrichment for down-regulated genes in *mdx* compared to WT myogenic cells. **G** Examples of enriched extracellular matrix, adhesion and polarity genes in myogenic libraries.
See also **Figure 4.11**.

4.5 Dystrophin and MARK2 are Expressed and Polarized in fMuSCs

MARK2 interacts with dystrophin (DMD) at repeats 8-9 of the full-length 427kDa protein, which is necessary for PAR complex-mediated MuSC polarity, asymmetric division and the generation of myogenic progenitors.[138,186] To assess whether full-length dystrophin was expressed in fMuSCs, we isolated GFP$^+$ cells from *Pax7-nGFP* limb muscles at multiple time points, and conducted RNAscope and immunostaining using probes and antibodies specific to the full-length isoform. MuSCs isolated from adult *Pax7-nGFP* mouse hindlimb muscles were included as controls (**Figure 4.13A,B, Figure S3A**).

Building on our previous findings,[138] we observed that 95% of freshly isolated (Fi) MuSCs from healthy adult hindlimb muscle expressed full-length *Dmd,* which dropped to 31% in activated (A) MuSCs 48 hours following CTX-injury (**Figure 4.13A,C**). The drop in dystrophin RNA aligns with *Dmd* expression data extracted from bulk RNA-seq conducted on postnatal FiMuSC, AMuSCs, cultured primary myoblasts, and 2-day differentiated myotubes (**Figure 3.12A,B** and **Figure S4**). Inversely, DMD protein was not expressed in FiMuSCs, but 25% of AMuSCs were DMD$^+$ (**Figure 4.13B,D**).[138] This suggests that *Dmd* transcript is either continuously transcribed or sequestered in quiescent MuSCs. Interestingly, we also observe elevated relative *Dmd* expression in the OxPhos MuSC clusters, which we predict are fMuSCs taking up or laying down their niche (**Figure 4.11B**).

As anticipated, neither full-length dystrophin transcript nor protein was expressed in GFP$^+$ cells isolated from E12.5 embryos (**Figure 4.13A-D**). However, full-length RNA and protein were observed in 33% and 13% of GFP$^+$ cells, respectively, at E15.5, and in 39% and 13% of cells at E17.5. At P7, 33% and 19% of neonatal GFP$^+$ cells expressed full-length dystrophin RNA and protein, respectively (**Figure 4.13A-D**).

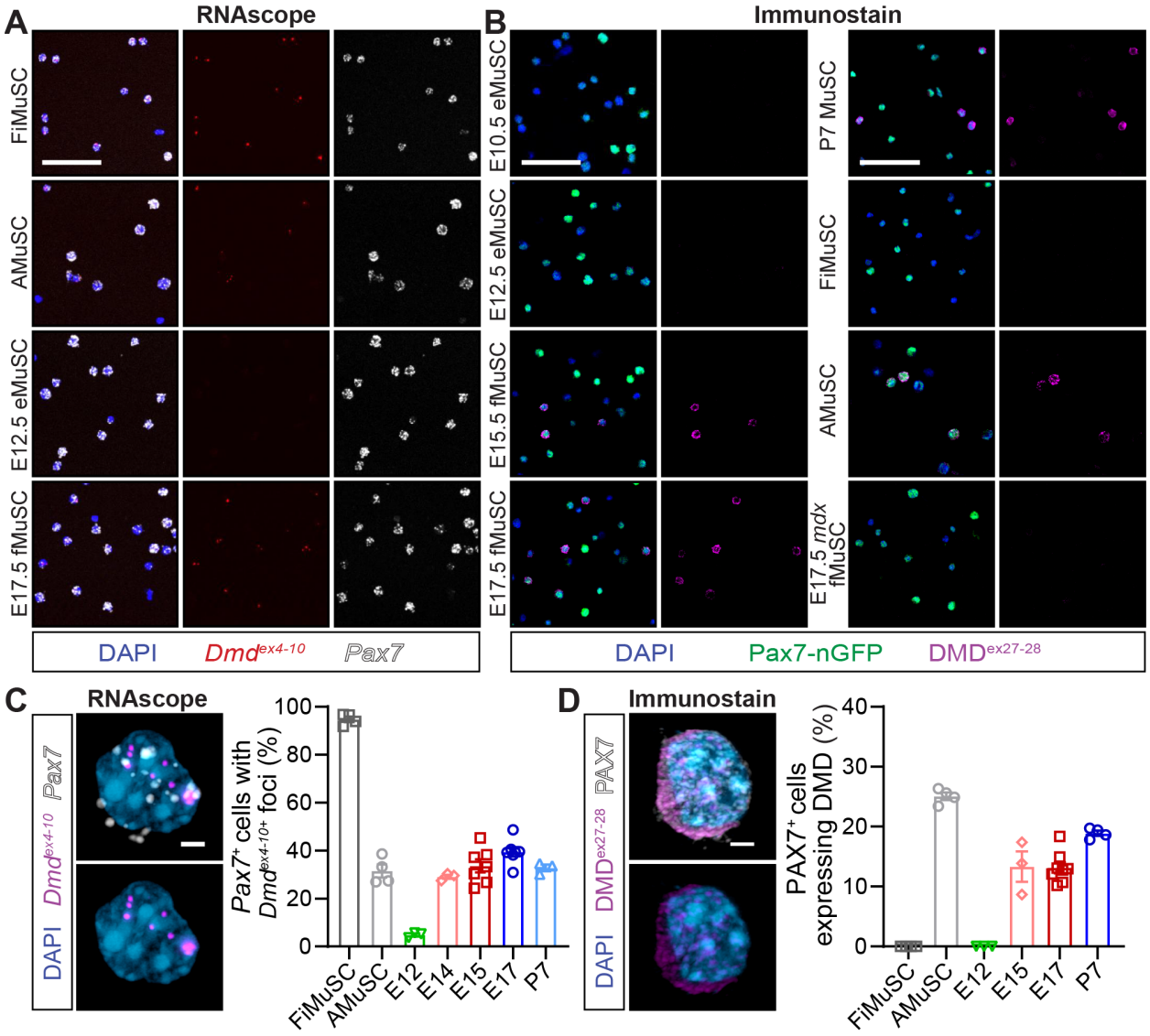

Figure 4.13 Dystrophin is expressed in fetal MuSCs from E14.5.
A Immunofluorescence images of freshly isolated (Fi) MuSC, activated (A) MuSCs 48-hours following cardiotoxin injury, embryonic (e) MuSCs (E12), and fetal (f) MuSCs (E17) isolated from *Pax7-nGFP* muscle based on GFP expression. Cells are treated with RNAscope probes that recognize exons 4-10 of the full-length *Dmd* (*Dmd*$^{ex4-10}$; red) and *Pax7* (white), and counterstained with DAPI (blue). Scale bar is 50µm. **B** Immunofluorescent images of GFP^{+} (green) FiMuSCs, AMuSCs, eMuSCs (E10.5, E12), fMuSCs (E15, E17) and perinatal day 7 (P7) MuSCs isolated from *Pax7-nGFP* mice and stained with an antibody specific to repeats 8-9 of the full-length dystrophin (DMD$^{ex27/28}$; magenta) and counterstained with DAPI (blue). Scale bar is 50µm. **C** Left: High-resolution images of E17.5 fMuSCs treated with RNAscope probes targeting *Dmd*$^{ex4-10}$ (magenta) and *Pax7* (white). Scale bar is 2µm. Right: Quantification of *Pax7*$^{+}$ myogenic cells expressing *Dmd*$^{ex4-10}$ foci. **D** Left: E17.5 GFP^{+} (green) fMuSCs stained with anti-DMD$^{ex27/28}$ (magenta). Scale bar is 2µm. Right: Quantification of GFP^{+} myogenic cells expressing DMD$^{ex27/28}$. For C-D, n = 3-8 per condition. Data presented as mean values ± SEM.

To validate the expression of MARK2 and study fMuSC polarity, we next isolated $PAX7^+$ cells from E17.5 WT hindlimbs and examined MARK2 and full-length DMD by immunostaining. To preserve cell polarity, fetal hindlimbs were quickly dissociated, formaldehyde-fixed, and sorted based on PAX7 staining (**Figure S3B**). In this experiment, MARK2 was expressed in approximately 30% of $PAX7^+$ cells, and 3% of fMuSCs expressed colocalized and polarized MARK2 and DMD (**Figure 4.14A,B**). Interestingly, several fMuSCs expressing polarized DMD and MARK2 displayed uniform PAX7 staining in the cell cytoplasm and bright chromosome staining, suggesting that these cells were entering mitosis.

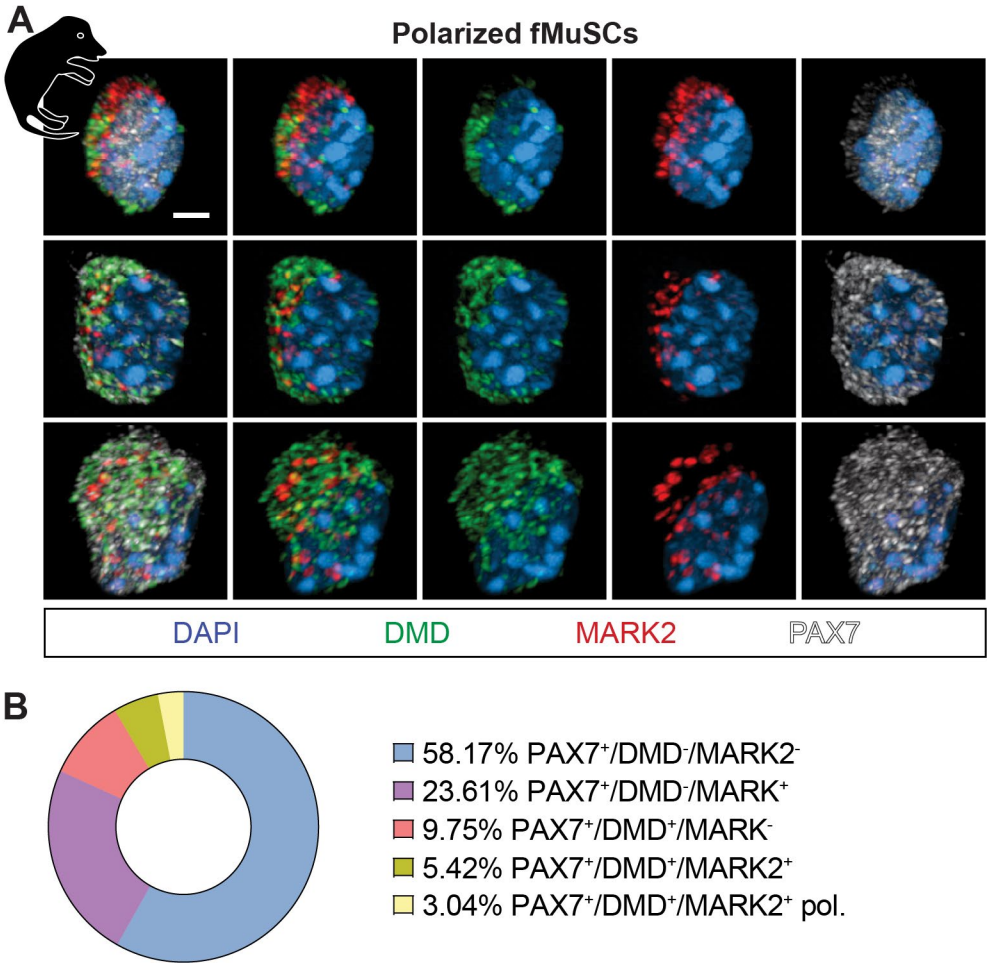

Figure 4.14 Dystrophin and MARK2 polarize in fetal MuSCs
A Representative high-resolution 3D images of E17.5 WT fMuSCs expression polarised dystrophin (DMD; green) and MARK2 (red). Images were counterstained with DAPI (blue). **B** Proportion of WT E17.5 fMuSCs expressing MARK2 and DMD. Greater than 450 cells enumerated per replicate. n=3. See also Figure S3.

4.6 Dystrophin-MARK2 Interactions Regulate fMuSC Polarity

To assess the interaction of dystrophin and MARK2 in fMuSCs, we isolated WT and *mdx* GFP$^+$ cells isolated from *Pax7-nGFP* limb muscles and performed proximity ligation assay (PLA) using antibodies against MARK2 and repeats 8-9 of DMD (**Figure S3A**). Interestingly, we observed bright foci in the WT fMuSCs that were not present in control *mdx* cells (**Figure 4.15A-C**). To determine whether MARK2 expression is impacted in dystrophin-deficient fMuSCs, we next stained WT and *mdx* GFP$^+$ cells for MARK2 (**Figure 4.15D**). As seen in adult MuCSs, the number of *mdx* GFP$^+$ cells expressing MARK2 was reduced relative to WT cells (**Figure 4.15E**). Further, the overall expression of MARK2 was reduced in GFP$^+$ cells isolated from E17.5 *mdx* muscle, demonstrated by reduced mean fluorescence intensity (MFI) (**Figure 4.15F**).[138]

The absence of MARK2-DMD interactions in postnatal MuSCs results in the loss of PARD3 polarization, fewer asymmetric divisions and the generation of fewer progenitor cells in myofiber culture.[138] To study whether polarity is perturbed in *mdx* fMuSCs, we examined PARD3 polarization in PAX7$^+$ fMuSCs isolated from WT and *mdx* fetal limbs at E17.5 (**Figure S3A**). As seen at the RNA level by scRNA-seq, PARD3 was ubiquitously expressed at similar intensities in WT and *mdx* fMuSCs (96.7% and 97.4% respectively; **Figure 4.16A-C**). However, the number of PAX7$^+$ cells expressing polarized PARD3 was reduced from 62% in WT conditions to 27% in *mdx* cells (**Figure 4.16D**). Thus, while the ability of *mdx* fMuSCs to express PARD3 is not impacted, we find that mechanisms directing PARD3 polarization rely on dystrophin.

Considering the distinct morphological and cellular differences observed in *mdx* fetal muscle at E14.5 and E17.5 compared to age-matched WT muscle, we also explored whether fMuSC polarity deficits arise at the onset of secondary myogenesis. Immunostaining of PARD3 on GFP$^+$ cells isolated from E14.5 WT and *mdx* Pax7-nGFP fetal limbs revealed that PARD3

expression was reduced in *mdx* fMuSCs (**Figure 4.17A,B**). Further, the proportion of GFP^+ $PARD3^+$ cells with polarized PARD expression was also decreased in the absence of dystrophin (**Figure 4.17C**). These findings suggest that fMuSC polarity disruptions arise at the onset of secondary myogenesis in the *mdx* fetus.

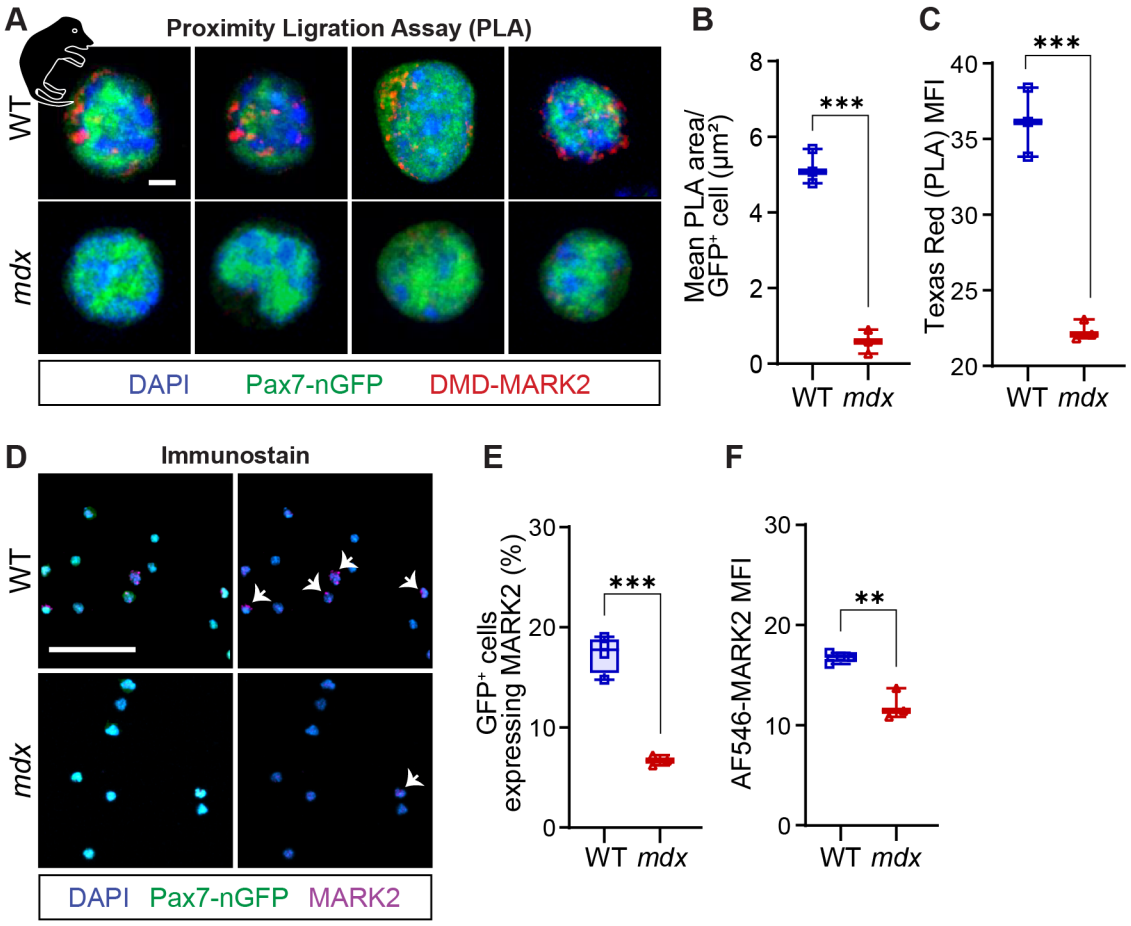

Figure 4.15 MARK2 is downregulated in dystrophin-deficient fetal MuSCs.
A Proximity ligation assay (PLA; red) performed on wild type (WT) and *mdx* GFP$^+$ (green) cells isolated from E17.5 *Pax7-nGFP* fetal limbs using antibodies specific to MARK2 and repeats 8 and 9 of DMD (DMD$^{ex27/28}$). Cells counterstained with DAPI. Scale bar is 2µm. **B** Mean PLA fluorescence area per cell measured in µm^2. **C** Mean fluorescence intensity (MFI) of PLA reaction in Texas Red in GFP$^+$ cells. **D** Representative immunofluorescence images of GFP$^+$ (green) cells isolated from E17.5 *Pax7-nGFP* fetal limbs expressing MARK2 (magenta; scale bar, 50µm). **E** Proportion of E17.5 GFP$^+$ (green) cells expressing MARK2. **F** MFI of MARK2-Alexa Fluor 546 in GFP$^+$ cells. For E and F, greater than 300 cells per replicate were enumerated. For B,C n=3 per genotype. For E-D, WT n=4 and *mdx* n=3. Statistical analysis performed using unpaired t-tests (** $p < 0.01$, *** $p < 0.001$). See also Figure S3. Box plot whiskers indicate the maximum and minimum values.

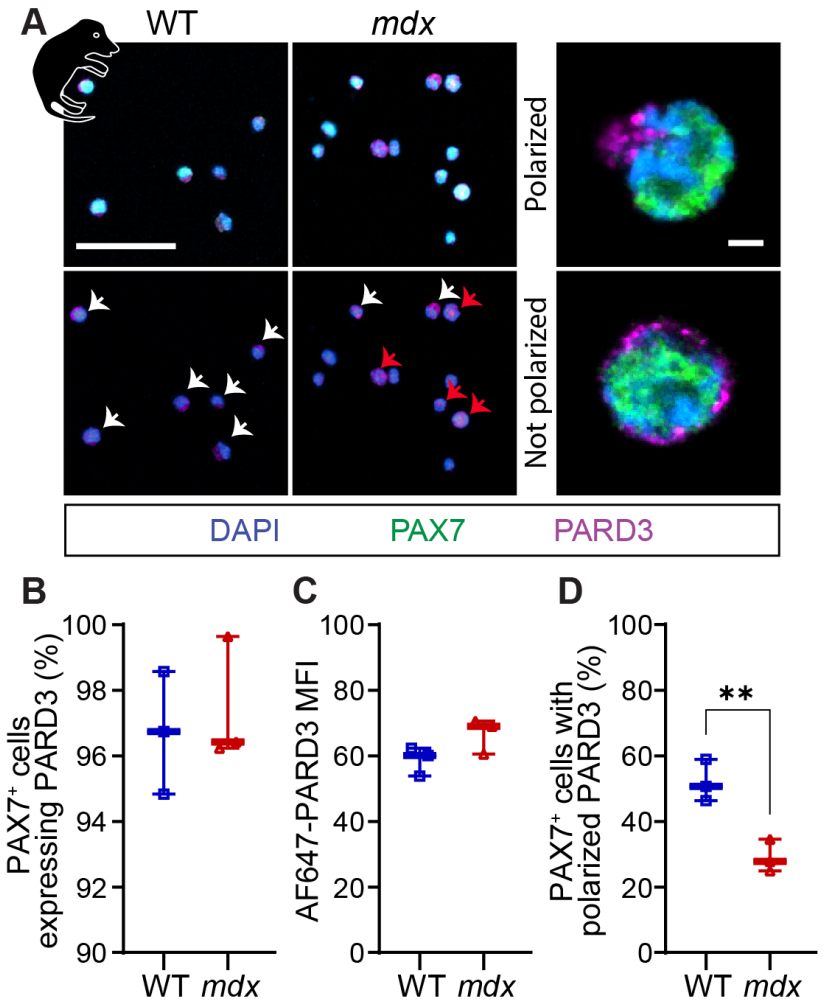

Figure 4.16 PARD3 polarization is disrupted in *mdx* fetal PAX7-expressing cells.
A Immunofluorescence staining of wild type (WT) and *mdx* PAX7$^+$ (green) cells isolated from E17.5 fetal limb muscle expressing PARD3 (magenta) and counterstained with DAPI. Scale bars are 50µm (left) and 2µm (right). White arrows denote polarized cells, while red arrows mark non-polarized cells. Illustrated on the right are high-magnification 3D projected images of a fMuSC with polarized and non-polarized PARD3 expression. **B** Proportion of PAX7$^+$ (green) cells that express PARD3. **C** MFI of PARD3-Alexa Fluor 546 in PAX7$^+$ cells. **D** Proportion of PAX7$^+$ (green) cells that express polarized PARD3. Greater than 150 cells assessed per replicate, and n=3 per genotype. Statistical analysis performed using unpaired t-tests (** $p < 0.01$, ***$p < 0.001$). See also Figure S3. Box plot whiskers indicate the maximum and minimum values.

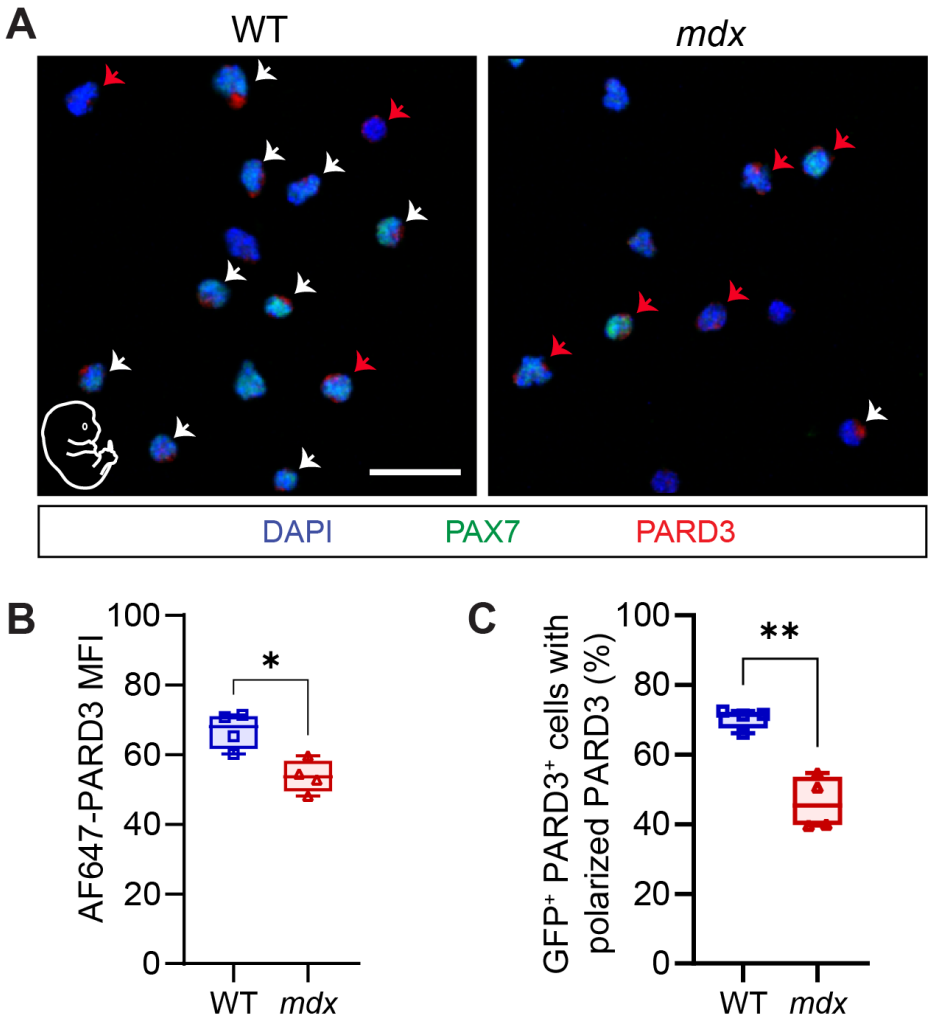

Figure 4.17 Polarity deficits in *mdx* fetal MuSCs begin at E14.5.
A Representative immunofluorescence images of GFP$^+$ (green) cells isolated from E14.5 *Pax7-nGFP* fetal limbs expressing PARD3 (red). Scale bars are 25µm. White arrows denote polarized cells and red arrows mark non-polarized cells. **B** MFI of PARD3-Alexa Fluor 546 in GFP$^+$ cells. **C** Proportion of GFP$^+$ PARD3$^+$ cells expressing polarized NUMB. Greater than 200 PARD3$^+$ cells assessed per replicate, and n=4 per genotype. Statistical analysis performed using unpaired t-tests (* $p < 0.05$** $p < 0.01$). Box plot whiskers indicate the maximum and minimum values.

4.7 Notch Signalling is Dysregulated in fMuSCs

Included in the top ten most upregulated genes in the *mdx* fMuSC scRNA-seq library was the Notch signalling gene *Hes1*, suggesting that Notch signalling is upregulated in dystrophin-deficient fMuSCs (**Figure 4.18A** and **Data File S6**). Interestingly, PARD3 is a positive regulator of Notch signalling that acts through NUMB and NUMBL to promote asymmetric radial glial cell fate.[262] NUMB is an endocytic adaptor protein, a Notch inhibitor, and a cell fate determinant that regulates asymmetric cell divisions through its polarized accumulation.[261,263–265] In mammalian cells, PARD3-dependent phosphorylation of NUMB by aPKC leads to the asymmetric distribution of NUMB and PARD3/aPKC.[262] Moreover, mammalian NUMB overexpression antagonizes the transactivation of the *Hes1* promoter in a NOTCH1-dependent manner.[266] Given that *mdx* fMuSCs have decreased PARD3 polarization (**Figure 4.16D**) and increased *Hes1* expression (**Figure 4.18A**), we questioned whether NUMB could be downregulated in *mdx* fMuSCs. We therefore analyzed NUMB expression in WT and *mdx* GFP^+ cells isolated from *Pax7-nGFP* E17.5 fetal limbs.

The expression of *Numb* RNA was unchanged between genotypes in the scRNA-seq libraries (**Figure 4.18B**). However, the overall expression of NUMB protein decreased (**Figure 4.18C-E**), and fewer GFP^+ cells expressed NUMB (**Figure 4.18F**). Although no differences in NUMB polarity were observed within the GFP^+ $NUMB^+$ fMuSC population (**Figure 4.18G**), fewer *mdx* GFP^+ cells with polarized NUMB were present in the total GFP^+ fMuSC population (**Figure 4.18H**). These findings suggest that the absence of dystrophin leads to NUMB downregulation, ultimately reducing the number of fMuSCs with polarized NUMB expression.

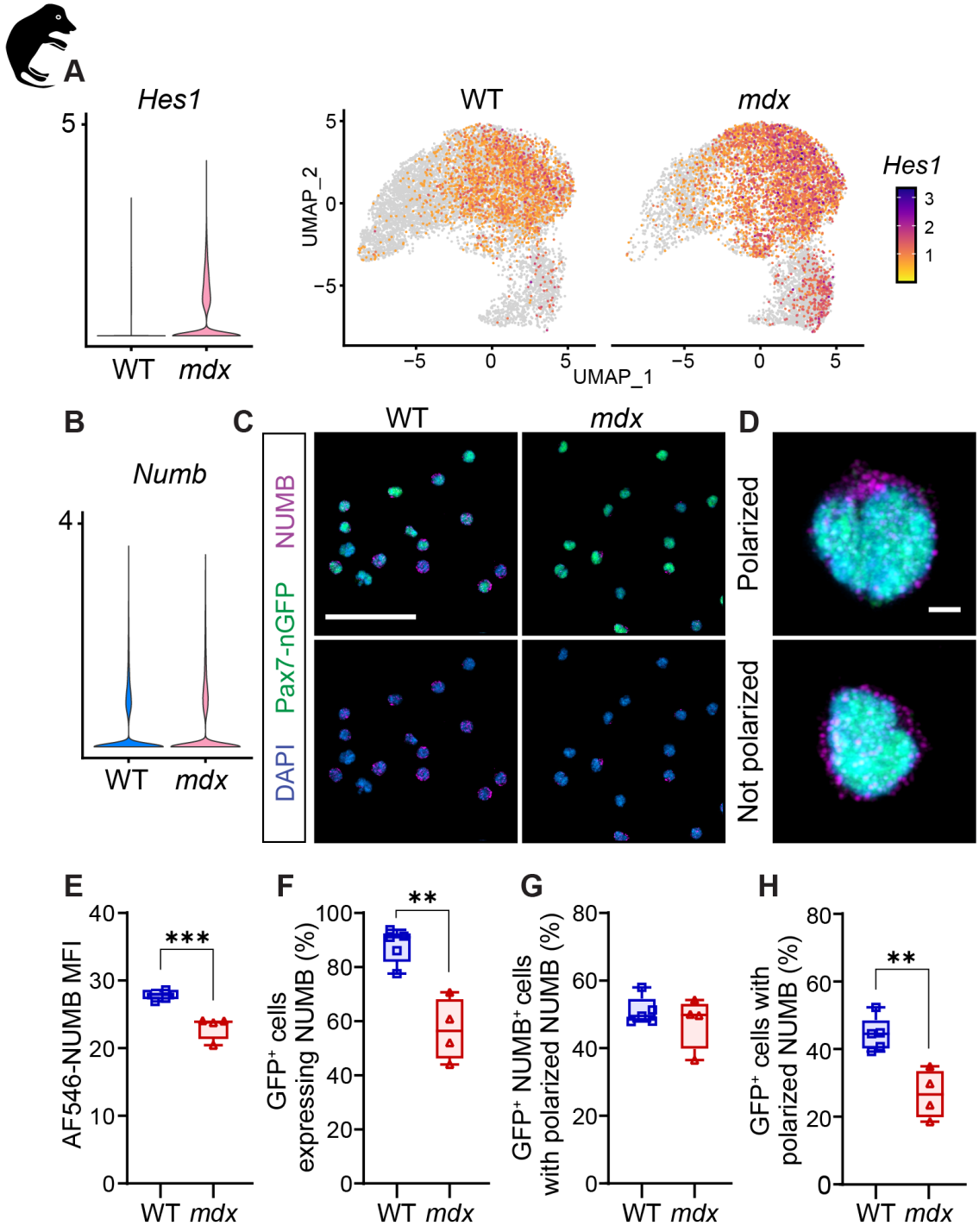
A
Hes1
5
WT
mdx
WT
mdx
UMAP_2
UMAP_1
Hes1
3
2
1
B
Numb
4
C
NUMB
Pax7-nGFP
DAPI
D
Polarized
Not polarized
E
AF546-NUMB MFI
***
F
GFP⁺ cells expressing NUMB (%)
**
G
GFP⁺ NUMB⁺ cells with polarized NUMB (%)
H
GFP⁺ cells with polarized NUMB (%)
**

Figure 4.18 Reduced NUMB expression and polarization in *mdx* fetal MuSCs.
A Violin plot (left) and feature plot (right) of *Hes1* expression in WT and *mdx* scRNA-seq libraries derived from GFP^+ cells isolated from *Pax7-nGFP* E17.5 limbs. **B** Violin plot of *Numb* expression from WT and *mdx* scRNA-seq libraries. **C** Representative immunofluorescence images of GFP^+ (green) cells isolated from E17.5 wild type (WT) and *mdx Pax7-nGFP* limbs expressing NUMB (magenta) and counterstained with DAPI. Scale bar, 50μm. **D** Example 3D projected images of a fMuSC expressing polarized and non-polarized NUMB expression. Scale bar, 2μm. **E** Mean fluorescence intensity (MFI) of NUMB-Alexa Fluor 546 in GFP^+ cells. **F** Proportion of GFP^+ cells isolated expressing NUMB. **G** Proportion of GFP^+ $NUMB^+$ cells expressing polarized NUMB. **H** Percent of entire GFP^+ cells expressing polarized NUMB. Between 180 and 1600 cells assessed per replicate. n=5 WT, n=4 *mdx*. Statistical analysis performed using unpaired t-tests (** $p < 0.01$, *** $p < 0.001$). Box plot whiskers indicate the maximum and minimum values. See also Figure S3.

4.8 Ablating AAK1 Rescues the Generation of Progenitors in *mdx* Fetal Muscle

During embryonic and adult myogenesis, NUMB polarization in MuSCs is suggested to inhibit Notch signalling asymmetrically, promote asymmetric cell division, and thus generate myogenic progenitor cells.[54,56,133,144,267] Considering that NUMB is a known Notch inhibitor that plays a role in asymmetric cell divisions, and that both *Hes1* and *Notch3* are upregulated genes in *mdx* scRNA-seq libraries (**Figure 4.18A** and **Data File S6**),[263,265] we hypothesized that modulating NUMB expression and polarization could rescue fMuSC polarity and the generation of myogenic progenitor cells in *mdx* fetal muscle.

Drosophila Numb associated kinase (NAK) regulates asymmetric cell fate through association with Numb.[268] In mammals, the NAK family consists of four homologues: adaptor-associated kinase 1 (AAK1), BMP-2-inducible kinase (BMP2K), cyclin G-associated kinase (GAK), and myristoylated and palmitoylated serine/threonine kinase 1 (MPSK1 or STK16), among which only AAK1 has been shown to phosphorylate NUMB.[269] Importantly, AAK1 is the closest ortholog to *drosophila* NAK and a positive regulator of Notch signalling that phosphorylates and antagonizes NUMB. Mutation of the AAK1 phosphorylation site results in a marked increase in membrane localization of NUMB.[265,269,270] Moreover, downregulating *Aak1* gene expression leads to the accumulation of NUMB at the plasma membrane of HeLa cells.[270] Thus, considering the polarized accumulation of NUMB during cell division confers asymmetric daughter cell fates,[264] AAK1 phosphorylation likely induces polarized NUMB accumulation to promote asymmetric divisions. Therefore, we asked whether targeting AAK1 could restore the commitment of *mdx* myogenic cells.

We first analyzed NAK expression in our scRNA-seq libraries, observing that *Aak1,* followed by *Stk16,* was the most expressed gene in fMuSCs (**Figure 4.19A**). *Aak1* was similarly

expressed between genotypes, while *Stk16* was significantly downregulated in the *mdx* libraries (**Figure 4.19B** and **Data File S6**). A similar phenotype was observed in adult *mdx* MuSC libraries, where *Aak1* was identified as an upregulated gene and *Stk16* was downregulated (**Figure S5**).[1]

We next performed timed mating to obtain *mdx.Aak1*$^{+/+}$ and *mdx.Aak1*$^{-/-}$ fetuses. Quantification of PAX7^{+} and MYOG^{+} cells on E17.5 EDL and TA cross-sections revealed that loss of AAK1 had no impact on the number of PAX7^{+} cells but increased MYOG^{+} cells by 30% (**Figure 4.19C,D**). The similar number of PAX7^{+} cells between genotypes suggested that the loss of AAK1 does not cause precocious differentiation or depletion of the fMuSC pool. We then compared the proportion of MYOG^{+} cells within the total PAX7^{+} and MYOG^{+} population between *mdx.Aak1*$^{+/+}$ and *mdx.Aak1*$^{-/-}$ fetuses. Not only was the proportion of committed MYOG^{+} cells elevated in *mdx.Aak1*$^{-/-}$ fetal muscle, but the loss of AAK1 restored the proportion to WT levels (**Figure 4.19E**). Analysis of the myofiber calibre distribution in hindlimb muscles of E17.5 *mdx.Aak1*$^{+/+}$ and *mdx.Aak1*$^{-/-}$ fetuses revealed a reduction in small-calibre myofibers, leading to a decreased proportion of smaller myofibers and an increased proportion of larger myofibers (**Figure 4.19F,G**). The myofibers were also denser on *mdx.Aak1*$^{-/-}$ fetal muscle cross-sections compared to *mdx.Aak1*$^{+/+}$ (**Figure 4.19F** and **Figure S2G**).

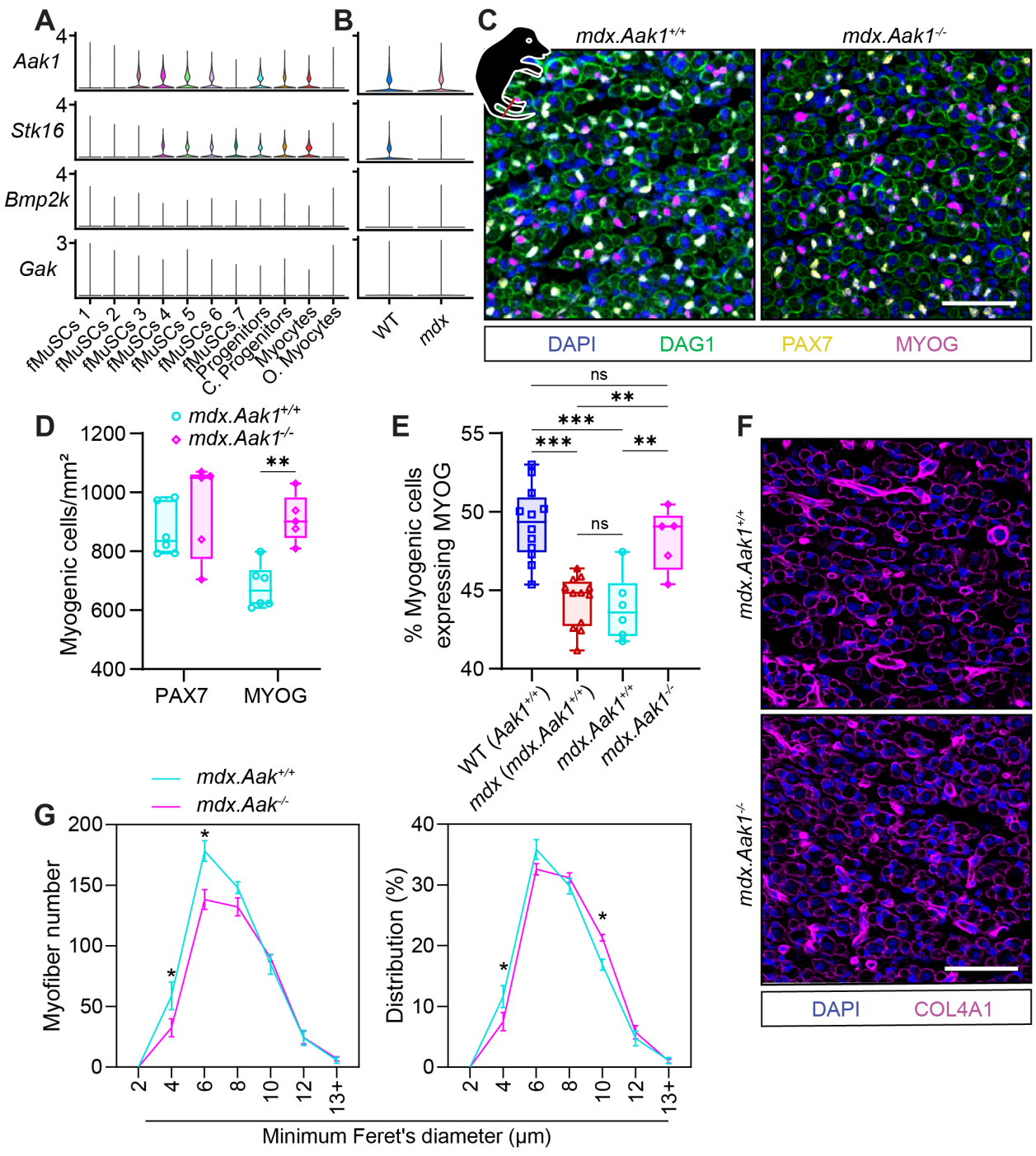
A
Aak1
Stk16
Bmp2k
Gak
fMuSCs 1
fMuSCs 2
fMuSCs 3
fMuSCs 4
fMuSCs 5
fMuSCs 6
fMuSCs 7
Progenitors
C. Progenitors
Myocytes
O. Myocytes
B
WT
mdx
C
mdx.Aak1+/+
mdx.Aak1-/-
DAPI
DAG1
PAX7
MYOG
D
mdx.Aak1+/+
mdx.Aak1-/-
Myogenic cells/mm²
PAX7
MYOG
E
% Myogenic cells expressing MYOG
ns
WT (Aak1+/+)
mdx (mdx.Aak1+/+)
mdx.Aak1+/+
mdx.Aak1-/-
F
mdx.Aak1+/+
mdx.Aak1-/-
DAPI
COL4A1
G
mdx.Aak+/+
mdx.Aak-/-
Myofiber number
Distribution (%)
Minimum Feret's diameter (µm)

Figure 4.19 Removal of AAK1 restores the progenitor generation in *mdx* fetal muscle.
A-B Violin plot depicting expression of the four mammalian NUMB-associated kinase (NAK) genes in single cell RNA-sequencing libraries and split by cluster (**A**) or genotype (**B**). Libraries derived from GFP^+ cells isolated from WT and *mdx* Pax7-nGFP limbs at E17.5. **C** Immunostaining illustration of the E17.5 *extensor digitorum longus* (EDL) on hindlimb cross-sections derived from *mdx.Aak1*$^{+/+}$ and *mdx.Aak1*$^{-/-}$ fetuses. PAX7 (yellow) marks fetal MuSCs, and MYOG (magenta) denotes differentiating myogenic cells. **D** Enumeration of myogenic cells expressing PAX7 and MYOG on *tibialis anterior* (TA) and EDL cross-sections, normalized to cross-section area (mm^2). n=6 *mdx.Aak1*$^{+/+}$ and n=5 *mdx.Aak1*$^{-/-}$. **E** Proportion of $MYOG^+$ cells relative to entire $PAX7^+$ and $MYOG^+$ cell population at E17.5. WT (*Aak1*$^{+/+}$) and *mdx* (*mdx.Aak1*$^{+/+}$) conditions repeated from **Figure 4.8**, and *mdx.Aak1*$^{+/+}$ and *mdx.Aak1*$^{-/-}$ hindlimb muscles were analyzed separately. **F** Representative immunostaining illustration of the E17.5 EDL on hindlimb cross-sections derived from *mdx.Aak1*$^{+/+}$ and *mdx.Aak1*$^{-/-}$ fetuses. Extracellular matrix marked by COL4A1 staining (magenta) and counterstained with DAPI (blue). **G** Distribution of myofiber size using minimum Feret's diameter by number of myofibers (left) and proportional distribution (right). For D,E, box plot whiskers indicate the maximum and minimum values. For G, data presented as mean values ± SEM. For D and G, two-way ANOVA followed by Sidak's multiple comparisons test. For E, one-way ANOVA followed by Tukey's test for multiple comparisons. Significance: $*p < 0.05$, $**p < 0.01$, $***p < 0.001$. Scale bars are 50μm.

We hypothesized that the loss of *Aak1* expression leads to increased asymmetric NUMB accumulation, thereby rescuing cell polarity and myogenic cell commitment. To investigate whether the loss of *Aak1* expression leads to increased NUMB polarization, we crossed the *mdx.Aak1*$^{-/-}$ and *Pax7-nGFP* lines to facilitate the isolation of fMuSCs. We then isolated GFP^{+} cells from *mdx.Pax7-nGFP.Aak1*$^{+/+}$ and *mdx.Pax7-nGFP.Aak1*$^{-/-}$ fetal limbs and assessed the expression of NUMB (**Figure 4.20A**). Interestingly, the loss of *Aak1* expression restored NUMB expression (**Figure 4.20B**) and the proportion of GFP^{+} cells expressing NUMB to WT levels (**Figure 4.20C)**. However, the ratio of polarized to non-polarized GFP^{+} NUMB^{+} cells remained unchanged (**Figure 4.20D**). Therefore, the overall increase in GFP^{+} NUMB^{+} cells led to a corresponding increase in GFP^{+} cells with polarized NUMB expression (**Figure 4.20E**).

Corroborating our histological findings, RT-qPCR analysis on GFP^{+} cells isolated from E17.5 *mdx.Pax7-nGFP.Aak1*$^{+/+}$ and *mdx.Pax7-nGFP.Aak1*$^{-/-}$ fetal limbs also revealed no difference in *Pax7* expression between genotypes, while *Myog* expression increased in the *mdx.Aak1*$^{-/-}$ cells (**Figure S6**). Together, our data suggests that modulating AAK1 activity in the *mdx* fetus restores NUMB expression and thus fMuSC polarity, which contributes to the formation of differentiation-competent progenitors during secondary myogenesis. This also supports the hypothesis that disrupted muscle development during secondary myogenesis is largely due to reduced fMuSC polarity.

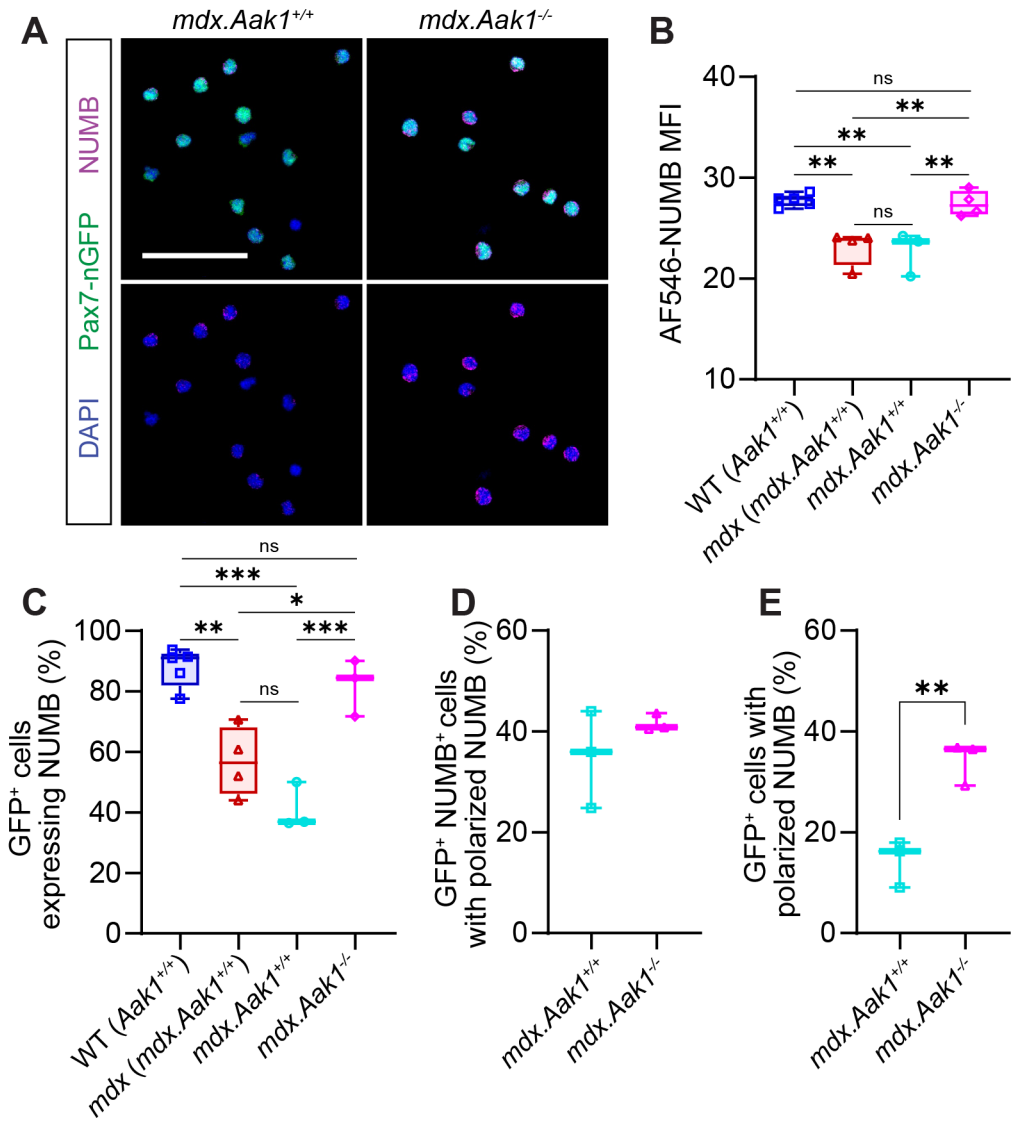

Figure 4.20 Fetal MuSC polarity rescued by the loss of AAK1 in *mdx* muscle.
A Immunofluorescence images of GFP$^+$ (green) cells isolated from E17.5 *mdx.Pax7nGFP.Aak1*$^{+/+}$ and *mdx.Pax7nGFP.Aak1*$^{-/-}$ fetal limbs. Cells express NUMB (magenta) and are counterstained with DAPI. Scale bar is 50µm. **B** Mean fluorescence intensity (MFI) of NUMB-Alexa Fluor 546 in GFP$^+$ cells. **C** Proportion of GFP$^+$ cells isolated expressing NUMB. For B,C, WT (*Aak1*$^{+/+}$) and *mdx* (*mdx.Aak1*$^{+/+}$) conditions repeated from Figure 4.19 and *mdx.Aak1*$^{+/+}$ and *mdx.Aak1*$^{-/-}$ hindlimb muscles were analyzed separately. **D** Proportion of GFP$^+$ NUMB$^+$ cells expressing polarized NUMB. **E** Percent of entire GFP$^+$ cells expressing polarized NUMB. Between 362 and 929 cells were assessed per replicate. Statistical analysis was performed using unpaired t-tests (* $p < 0.05$** $p < 0.01$, ***$p < 0.001$). Box plot whiskers indicate the maximum and minimum values.

4.9 Findings Summary

Chapter 4 demonstrates that, although primary myogenesis does not depend on dystrophin, intrinsic MuSCs impairment begins during secondary myogenesis in the *mdx* mouse. This aligns with the expression of dystrophin in $PAX7^{+}$ cells arising at E14.5. In developing *mdx* muscle, basal lamina formation is delayed at the onset of secondary myogenesis. Further, fetal muscle lacking dystrophin is hypotrophic compared to WT and has fewer progenitor cells, as indicated by histological and transcriptomic analyses. MARK2 and NUMB are also downregulated in *mdx* fMuSCs, and PARD3 polarization is disrupted. Importantly, the loss of AAK1 rescues NUMB expression in *mdx* fMuSCs and the number of myogenic progenitor cells in dystrophin-deficient fetal muscle. In summary, we find that polarity deficits in dystrophin-deficient MuSCs begin during fetal muscle development.

Chapter 5: Discussion

The current body of work aims to uncover the *in vivo* consequences of intrinsic MuSC dysfunction during muscle development and regeneration. First, we provide a comprehensive overview of muscular dystrophy progression, including changes in muscle architecture and myogenic cell behaviour in *mdx* skeletal muscle from the onset of muscle development to one year of age. Second, our analysis of muscle development and regeneration in postnatal and engrafted muscle reveals that DMD is an intrinsic MuSC disease with onset during secondary myogenesis, prior to the accumulation of necrotic myofibers, fibrosis, and inflammatory changes.[180] Collectively, our findings show that *mdx* MuSC dysfunction and skeletal muscle pathology are driven, not only by myofiber fragility and the resulting inflammatory environment,[182] but also intrinsic deficits in MuSC polarity that directly contribute to muscular pathology. These deficits lead to the generation of fewer progenitor cells, which impairs both muscle development and regeneration. Finally, we identify AAK1 as a potential therapeutic target for restoring MuSCs polarity in muscular dystrophy.

5.1 Progressive Morphological and Cellular Changes with Age in Adult *mdx* Muscle

Considering the finding that dystrophin is expressed in adult MuSCs where it regulates cell polarity and asymmetric cell division,[138] we first studied the morphological and functional changes that occur in *mdx* muscle from 13 to 52 weeks of age. Consistent with the literature, we find that Dp427m is essential for myofiber integrity and that the disease pathology worsens with age.[236,239] We observe hallmark pathological features of dystrophin-deficient muscle, including elevated mass and thickening, increased fibrosis, and changes in myofiber size distribution.[238,240,248,271] Morphological changes in the *mdx* diaphragm progress earlier and more severely than the TA,

likely resulting from ongoing respiratory requirements and related mechanical stress.[237,240,272] In the diaphragm of *mdx* mice, we see atrophy that is not evident in the TA, earlier onset of fibrotic deposition, and no myofiber hypertrophy. Conversely, hypertrophic *mdx* myofibers are maintained in the TA.[238,248] Given the diaphragm's significantly greater pathology compared to hindlimb muscles and its closer resemblance to human disease, our study underscores the importance of focusing on the *mdx* diaphragm as a model for advancing the development of novel therapeutics for DMD.[240,273,274] However, key differences in disease progression between species must still be considered.

In *mdx* mice, increases in myofibers and muscle mass precede severe fibrosis and atrophy, followed by concurrent reductions in intramuscular fat and body weight.[237,275] Unlike DMD patients, *mdx* mice experience delayed fibrosis, reduced intramuscular fat accumulation, and generally milder disease progression. Notably, intramuscular fat and muscle strength are inversely proportional in human patients, while mice are considerably leaner with more glycolytic myofibers.[275,276] As previously suggested, metabolism may play a key role in the differing progression of muscular dystrophy across species.[237,275,277] Despite these differences, the *mdx* mouse remains a valuable tool for studying disease mechanisms and potential therapeutics.

Myofiber branching, suspected to originate from aberrant muscle cell fusion during regeneration, contributes to increased myofiber numbers and decreased force production in *mdx* muscle.[278–282] However, we find that increases in small myofibers and elevated TA mass correlate with the preservation of maximum tetanic force beyond 20 weeks. Normalized force also does not decrease with age, which we would predict if muscle mass increases were attributed to pathogenic branching. We therefore theorize that the increase in small myofibers results from a combination of myofiber branching and beneficial hyperplasia resulting from ongoing muscle regeneration.

Advances in genomics have improved our understanding of DMD, highlighting the regenerative nature of dystrophin-deficient muscle. For example, RNA-seq of whole *mdx* muscle identified upregulated genes related to regenerating muscle and pathway enrichment pertaining to inflammation, fibrosis, proliferation, necrosis and apoptosis.[283] In another study, single nuclei RNA-seq of the dystrophin-deficient TA muscle observed changes in the cellular milieu and identified a regenerative myonuclear population.[247] The same study observed irregular expression of ubiquitin–proteasome-associated genes in myonuclei and decreased myonuclei. Our transcriptomic analysis provides further evidence of ongoing muscle regeneration by *mdx* MuSCs in homeostatic muscle. We see the entire trajectory of myogenic cells in *mdx* muscle and the upregulation of proliferation and differentiation markers in MuSCs. Moreover, in response to the chronic injury condition, we see the upregulation of immune response genes in the *mdx* myogenic cell libraries, supporting the previous finding that *mdx* MuSCs respond to the inflammatory microenvironment caused by myofiber fragility and cyclic muscle regeneration.[182]

Consistent with studies in mice and humans, we see hyperplasia of the MuSC pool in the homeostatic muscle of adult *mdx* mice.[138,174,244,245] However, while stem cell exhaustion is not a major contributor to muscular dystrophy progression,[174,244,245] we find that the total number of MuSCs decreases linearly in *mdx* muscle with age. Because MuSCs are highly regulated by their niche,[284] and chronic exposure to the dystrophic microenvironment contributes to MuSC dysfunction,[182] we theorize that the decline in MuSC numbers results from chronic exposure to the inflammatory niche.

Chronic inflammation induces cell senescence in dystrophic muscle. In young dystrophic mice, senescent cells are predominantly macrophages and endothelial cells, not $PAX7^{+}$ MuSCs.[285] Thus, the decreased number of *mdx* MuSCs could result from MuSCs becoming increasingly

dysfunctional due to the accumulation of non-myogenic senescent cells. However, the number of senescent MuSCs increases with age in WT mice and other muscle-wasting diseases.[286] Moreover, increased MuSC senescence in rodents and human dystrophin-deficient MuSCs have been reported.[287–289] Therefore, age-related decline in *mdx* MuSCs likely also results from MuSC senescence, which may worsen skeletal muscle pathology. Nonetheless, removing senescent cells with senolytics in aging mice improves acute injury outcomes.[290] Another likely contributor to the decline in MuSCs is that dystrophic MuSCs undergo another mechanism of non-apoptotic arrest through mitotic catastrophe related to defective MuSC polarity.[138] These results support previous findings that intrinsic and extrinsic factors contribute to MuSC dysfunction with age in muscular dystrophy.[138,139,182]

5.2 Delayed Functional Recovery Following Acute Insult to *mdx* Skeletal Muscle

Our study of acutely CTX-challenged muscle provides further insight into muscle regeneration in the *mdx* mouse and agrees with previous findings that the regenerative capacity of WT and *mdx* skeletal muscle is maintained following CTX injury.[291,292] In WT mice, branching occurs in about half of the regenerated myofibers following CTX injury.[278] Despite this, maximum titanic and specific force recovers in the WT TA by 21 dpi. In contrast, maximum tetanic force does not recover in the *mdx* TA until 90 dpi. Given that neither genotype experiences significant collagen deposition following CTX injury, fibrosis is an unlikely contributor to decreased force production in the *mdx* TA. Instead, the reduced force production may be attributed to increased myofiber branching in *mdx* regenerating muscle; however, myofiber branching was not assessed.

Increased TA weight between 21 and 90 dpi aligns with the finding that 5% of MuSCs are cycling a month after a CTX injury.[293] However, the morphometric myofiber changes following

acute injury differ between genotypes. We observe muscle and myofiber hypertrophy in the WT TA, and myofiber hyperplasia in the *mdx* TA. This is reminiscent of neonatal myogenesis when young *mdx* myofibers are hypotrophic and contain fewer myonuclei than WT controls until 3-4 weeks.[238,247,248] Considering our previous findings,[138,139] hypotrophic *mdx* myofibers are an *in vivo* indicator of deficient muscle regeneration in the *mdx* mouse.

5.3 Intrinsic Deficits Postnatal *mdx* MuSCs Lead to Impaired Muscle Regeneration

In line with reports in *mdx* mice and DMD patients, we observe an expansion of $PAX7^+$ cells in homeostatic conditions and following transplantation.[174,244,245] Our findings suggest this results from two mechanisms. First, we histologically and transcriptomically demonstrate that the dystrophic microenvironment's continual activation of MuSCs leads to elevated numbers of $PAX7^+$ progenitors. We also see the upregulation of immune and activation-related genes in *mdx* myogenic cells, which, as previously indicated, corroborates the previous findings that MuSCs respond to the extrinsic dystrophin microenvironment.[182] Second, our *in vivo* study of fetal, neonatal and CTX-challenged MuSCs combined with our engraftment data indicate that intrinsic polarity deficits cause *mdx* MuSCs to favour symmetric expansion over asymmetric cell division following activation.[138,139]

Using scRNA-seq analysis, we identify hyperplasia of uncommitted *mdx* MuSCs and fewer progenitor cells five days following CTX injury. Additionally, *mdx* MuSCs have impaired PARD3 polarity and generate fewer progenitor cells after CTX injury and in pre-necrotic day 7 neonatal muscle.[180] Finally, despite the similar engraftment of WT and *mdx* MuSCs, we also find that *mdx* MuSCs have significantly reduced regenerative potential, evidenced by smaller grafts and decreased numbers of myofibers, even in the absence of the dystrophic microenvironment. The

combined investigation of neonatal muscle growth and the postnatal response of *mdx* MuSCs to acute injury and transplantation assays demonstrates that *mdx* MuSCs possess intrinsic impairments. Thus, our study of acute and chronic myogenesis indicates that intrinsic and extrinsic factors play a role in *mdx* MuSC dysfunction.

5.4 Developmental Dysregulation Occurs in the Dystrophin-Deficient Embryo

Our study of postnatal myogenesis in the *mdx* mouse led us to question the developmental origin of polarity dysfunction in dystrophin-deficient MuSCs. Although a subtle delay in somitogenesis occurs at E10.5, our findings suggest that dystrophin does not play a role in primary myogenesis. In agreement, full-length dystrophin is undetectable by western blot at E10.5. Further, we find that full-length dystrophin is first upregulated in E14.5 *Pax7*$^{+}$ cells at the onset of secondary myogenesis. These observations align with the findings that embryonic myogenesis at E12.5 occurs without a developed basal lamina that later forms at E14.5,[93] and that fetal myogenic progenitors are enriched in adhesion-related genes.[89] Together, this reaffirms that distinct mechanisms govern embryonic, fetal and adult muscle growth and repair.

Unlike embryonic myofibers, a basal lamina surrounds the dermomyotome, and dermomyotome cells undergo symmetric and asymmetric cell divisions.[52,53,56,96] While full-length dystrophin is not expressed and does not regulate dermomyotome cell specification, dystroglycan and full-length utrophin are present at the dermomyotome basal lamina. Because both proteins are known interactors of the PAR complex and play a role in polarizing other epithelial structures,[186,294] dystroglycan and utrophin may regulate dermomyotome polarity.[295] However, while dystrophin has a high affinity for binding microtubules, utrophin does not, suggesting utrophin likely does not

play a role in mitotic spindle assembly.[296] Moreover, this does not explain the subtle delay in somitogenesis in the *mdx* embryo.

Recent modelling of somitogenesis using hiPSCs discovered the expression of a truncated 412kDA embryonic dystrophin isoform (Dp412e) during *in vitro* somitogenesis.[297] Similar experiments using DMD patient-derived hiPSCs observed the downregulation of somite markers, suggesting dystrophin plays a role upstream of primary myogenesis.[191] However, the promoter of Dp412e, located on exon 6 on the human *DMD* gene, is unique to select anthropods, including humans.[297] Interestingly, murine presomitic and somitic mesoderm cells extracted from a recently published E8.5 single cell sci-RNAseq3 dataset express the *Dmd* transcript.[254] However, the murine *Dmd* gene does not contain the exon 6 embryonic promoter, and the sci-RNA-seq3 technique enriches 3' RNA reads, necessitating further investigation. Nevertheless, an upstream role for dystrophin, perhaps in the presegmental plate, could explain the observed delay in somitogenesis. Alternatively, the absence of dystrophin in *mdx* dams could impact embryonic development.

Compared to the WT fetus, the pathology of *mdx* muscle differs at the beginning and end of secondary myogenesis. In addition to delayed basal lamina formation, we observe a more pronounced reduction in total myogenic cells in *mdx* muscle at E14.5 compared to E17.5. In contrast, the proportion of committed myogenic cells within the total myogenic cell population is more profoundly reduced in *mdx* muscle at E17.5. These differences may be explained by delayed somitogenesis, which could lead to altered migration of progenitor cells from the hypaxial dermomyotome and, in theory, a delay in the transition from primary to secondary myogenesis. However, the delay in somite formation is subtle, and several lines of evidence suggest the transition from primary to secondary myogenesis is not delayed in the *mdx* fetus. First, we find

that WT and *mdx* E14.5 fMuSCs expressed similar levels of *Nfix,* the transcriptional switch that regulates the transition from primary to secondary myogenesis.[91] This suggests that the myogenic program in fMuSCs is not transcriptionally delayed. Second, the same number of $MYH7^+$ myofibers was enumerated in WT and *mdx* fetal muscle. We propose that the phenotype differences between E14.5 and E17.5 result from a cumulative effect of polarity impairment beginning at E14.5 and persisting throughout secondary myogenesis. This is evidenced by the reduced PARD3 polarization in E14.5 *mdx* fMuSCs and the relatively fewer progenitor cells enumerated on E14.5 *mdx* cross-sections. However, the delay in basal lamina formation, potentially due to the absence of myofiber dystrophin, may also contribute to disrupted fMuSC polarity at E14.5.

In adult muscle, an increased number of FAPs is thought to result from chronic exposure to the dystrophin-deficient environment, contributing to progressive fibrosis with age.[298] Interestingly, in *mdx* and DMD fetal muscle, decreased myofiber density is accompanied by increased ECM deposition despite the absence of necrosis or muscular damage.[187,190] Similarly, *mdx* fetal muscle is visibly less dense than WT muscle. Moreover, our scRNA-seq analysis reveals a subtle increase in fFAP representation in the *mdx* fetal GFP^+ cell libraries. Given that fFAPs originate from $Pax7^+$ lineages,[258] whether this modest increase reflects a broader shift in $Pax7^+$ cell lineage specification remains unknown.

5.5 Intrinsic MuSC Deficits Begin During Secondary Myogenesis

Building on our discoveries, [1,138,139] we demonstrate that the polarity and commitment deficits observed in postnatal *mdx* MuSCs begin during secondary myogenesis. At E17.5, the loss of dystrophin-MARK2 interactions in fMuSCs leads to the downregulation of MARK2, disrupted PARD3 polarization, and the generation of fewer proliferating and committed progenitor cells in

fetal *mdx* muscle. Moreover, histological and single cell transcriptomic analysis shows an expansion of uncommitted *Myf5*^{Lo} fMuSCs in *mdx* fetal muscle. Thus, the overall reduction in PAX7^{+} cells that occurs during secondary myogenesis is a direct result of fewer proliferating progenitors and not depletion of the fMuSC pool. Moreover, unlike the libraries generated from adult MuSCs, no differences in the expression of immune response genes were detected in the WT and *mdx* myogenic cells by scRNA-seq. This is consistent with the notion that inflammation arises postnatally due to ambulation,[180] and corroborates the finding that the absence of dystrophin in fMuSCs directly causes intrinsic polarity deficits. Mirroring neonatal and regenerating CTX-injured muscle,[1,248] we also see hypotrophic myofibers in *mdx* fetal hindlimb muscle likely resulting from reduced myogenic cell commitment.

Notch pathway genes are highly expressed in fMuSCs, which is unsurprising given the importance of Notch signalling in maintaining the MuSC pool and promoting MuSC proliferation.[299] Conflicting with reports in postnatal MuSCs,[300,301] we find that *Hes1* is highly upregulated in *mdx* fMuSCs. This is likely explained by the altered proportion of fMuSCs and progenitor cells, as *Hes1* is most expressed in quiescence postnatal MuSCs, with its expression progressively reduced and then lost during myogenic cell differentiation.[111] Because *mdx* MuSCs become constitutively activated by the dystrophic microenvironment, it is plausible that the expression of quiescence-associated genes would be down-regulated. However, *Hes1* is likely upregulated in *mdx* cells due to the reduced number of progenitor cells in activation conditions. Interestingly, while *Numb* RNA is similarly expressed in WT and *mdx* fMuSCs, NUMB protein is downregulated in *mdx* fMuSCs. This suggests that NUMB downregulation occurs through post-translational mechanisms and not altered cell state.

Studies of mammalian neurogenesis find that PARD3 is an upstream regulator of Notch signalling that requires the expression of *Numb* and *Numbl* to promote asymmetric cell fate.[262] Ectopic expression of *Pard3* increases Notch signalling, while loss of *Pard3* expression leads to its downregulation. However, the loss of *Numb* and *Numbl* abolishes the effect of *Pard3* knockdown, leading to elevated Notch signalling in the absence of PARD3. Moreover, studies in mammalian cells demonstrate that NUMB is phosphorylated by the PAR-complex protein aPKC, which is dependent on PARD3 and leads to the asymmetric distribution of NUMB and aPKC/PARD3.[302,303] Thus, disrupted PARD3 polarity could lead to the downregulation of NUMB in the entire *mdx* fMuSC. The mechanistic relationship between the loss of MARK2-dystrophin interactions remains unclear, making it an interesting topic for future investigation.

While the loss of Notch signalling in MuSCs promotes precocious differentiation,[304] Notch pathway gene mutations can ameliorate dystrophic phenotypes. For instance, the Golden Retriever muscular dystrophy (GRMD) model of DMD typically displays a very severe pathology that leads to cardiorespiratory failure and death before 2 years of age. However, 'escaper' dogs carrying a disease-modifying mutation to the *Jag1* gene lived long and healthy lifespans.[305] Interestingly, we show that targeting the NUMB inhibitor gene *Aak1* rescues myogenic cell commitment in the *mdx* fetus. Ablation of *Aak1* increases NUMB expression and polarity in *mdx* fMuSCs, restoring the balance of $PAX7^+$ fMuSCs to committed $MYOG^+$ progenitors without depleting the stem cell pool. However, the mechanisms by which this occurs remain unknown.

One hypothesis is that the loss of *Aak1* expression counteracts the inhibitory effect of the PAR complex on NUMB, allowing fMuSCs to respond to asymmetric Notch ligand cues in the niche and undergo asymmetric division. This hypothesis is based on the finding that Notch ligands from the basal niche and apical myofiber module MuSC behaviour, and that self-renewing *Myf5*^{Lo}

MuSCs express higher levels of NOTCH3 than *Myf5*^{Hi} primed MuSCs.[134] Conceivably, DLL4 from endothelial cells modules the self-renewal of *Myf5*^{Lo} fMuSCs basally during asymmetric cell division, while either reduced DLL4 presented by the myofiber or expression of other Notch ligands stimulate proliferation and commitment of the *Myf5*^{Hi} fMuSCs. AAK1 and GAK also play a role in the clathrin-mediated endocytosis of EGFR, where the loss of either NAK reduces receptor internalization.[306] Therefore, another possibility is that the loss of AAK1 rescues *mdx* fMuSC asymmetric division through the EGFR-AURKA pathway, as seen by EGF treatment in postnatal *mdx* MuCSs. However, further study of the PAR complex and EGFR pathway following *Aak1* knockdown is required to investigate either hypothesis. Nevertheless, knocking out *Aak1* restores fMuSC NUMB expression and myogenic cell commitment in fetal *mdx* muscle (**Figure 5.1**).

Our study highlights AAK1 as a potential target for restoring dystrophin-deficient MuSCs polarity. However, AAK1 is widely expressed in the body and regulates diverse cellular processes. Despite this, inhibiting AAK1 kinase activity has shown preclinical therapeutic benefit in treating neuropathic pain and viral infection.[307] A potential explanation is that AAK1 regulates cellular processes through kinase-dependent and independent mechanisms. For instance, the AAK1 orthologue in *C. elegans*, SEL-5, contributes to neuroblast migration through mechanisms independent of its kinase activity.[308] Thus, inhibition of the AAK1 kinase domain, rather than complete ablation, may have greater therapeutic potential. Another possibility is that the phasic or partial inhibition of AAK1 may rescue fMuSC polarity but limit unintended effects. To investigate this further, experiments using kinase domain-specific inhibitors are required.

Of the two mammalian homologs, *Numb* and *Numbl*, only *Numb* was detected at notable levels in fMuSC and postnatal FiMuSC scRNA-seq libraries, suggesting that primarily NUMB

plays a role in MuSC polarity. From the mammalian *Numb* gene, at least 6 different alternatively spliced isoforms affected the amino-terminal phospho-tyrosine-binding (PTB) domain and the C-terminal proline-rich domain (PRR), each with overlapping and divergent roles.[309] NUMB1-4 play roles in notch inhibition, while the more transiently expressed NUMB5/6 have excitatory roles on NOTCH and are more often expressed in cancer cells.[310,311] Interestingly, NUMB isoforms with exon 12 in the PRR domain (NUMB1/3) promote proliferation in neuronal progenitor cells by activating notch signalling. Conversely, overexpression of isoforms with excised exon 12 (NUMB2/4) promotes differentiation, and these isoforms are highly expressed in adult tissues.[309] An interesting question remains regarding which NUMB isoforms are expressed in fetal and postnatal MuSCs and whether AAK1 preferentially inhibits select NUMB isoforms. This information could lead to more precise targeting of NUMB in dystrophin-deficient MuSCs.

While further investigation is required to evaluate the impact of inhibiting AAK1 on adult muscle regeneration, preliminary unpublished work using *ex vivo* myofiber culture corroborates our findings during fetal development. Western blot analysis shows that NUMB protein is downregulated in postnatal MuSCs, and treating myofibers isolated from the *mdx.Myf5-Cre.ROSA-YFP* EDL muscle with *siAak1* increases asymmetric MuSC divisions and the number of $MYOG^{+}$ progenitors without depleting the MuSC pool. Therefore, our studies using the *Aak1*-null mouse suggest that perturbed secondary myogenesis results from reduced fMuSC polarity and highlight AAK1 as a potential therapeutic target for DMD patients.

Beyond polarizing MuSCs, the role of dystrophin in cell polarity should be investigated in other cell types. In addition to musculoskeletal pathology, 1 in 3 DMD patients present with cognitive impairment.[180] Though less well characterized, the brain expresses full-length dystrophin splice isoforms. Cortical and Purkinje full-length dystrophin containing the MARK2 binding

domain are expressed in cortical neurons and Purkinje cells.[253] Interestingly, full-length brain dystrophin is highly co-expressed with genes related to a higher risk for autism spectrum disorders and significantly co-expressed with obsessive-compulsive disorder-related genes.[253] Oligodendrocytes and their progenitors also express full-length dystrophin, and *mdx* mice have delayed accumulation of mature oligodendrocytes and reduced myelination.[312] Moreover, dystrophin has been implicated in testis and epididymis development, and spermatogenesis. Interestingly, spermatogenic cells in *mdx* mice had reduced expression of MAKR2 alongside reduced proliferation and elevated apoptosis rates.[313] Therefore, the role of dystrophin in polarizing cells should be investigated in non-myogenic cell types that express dystrophin.

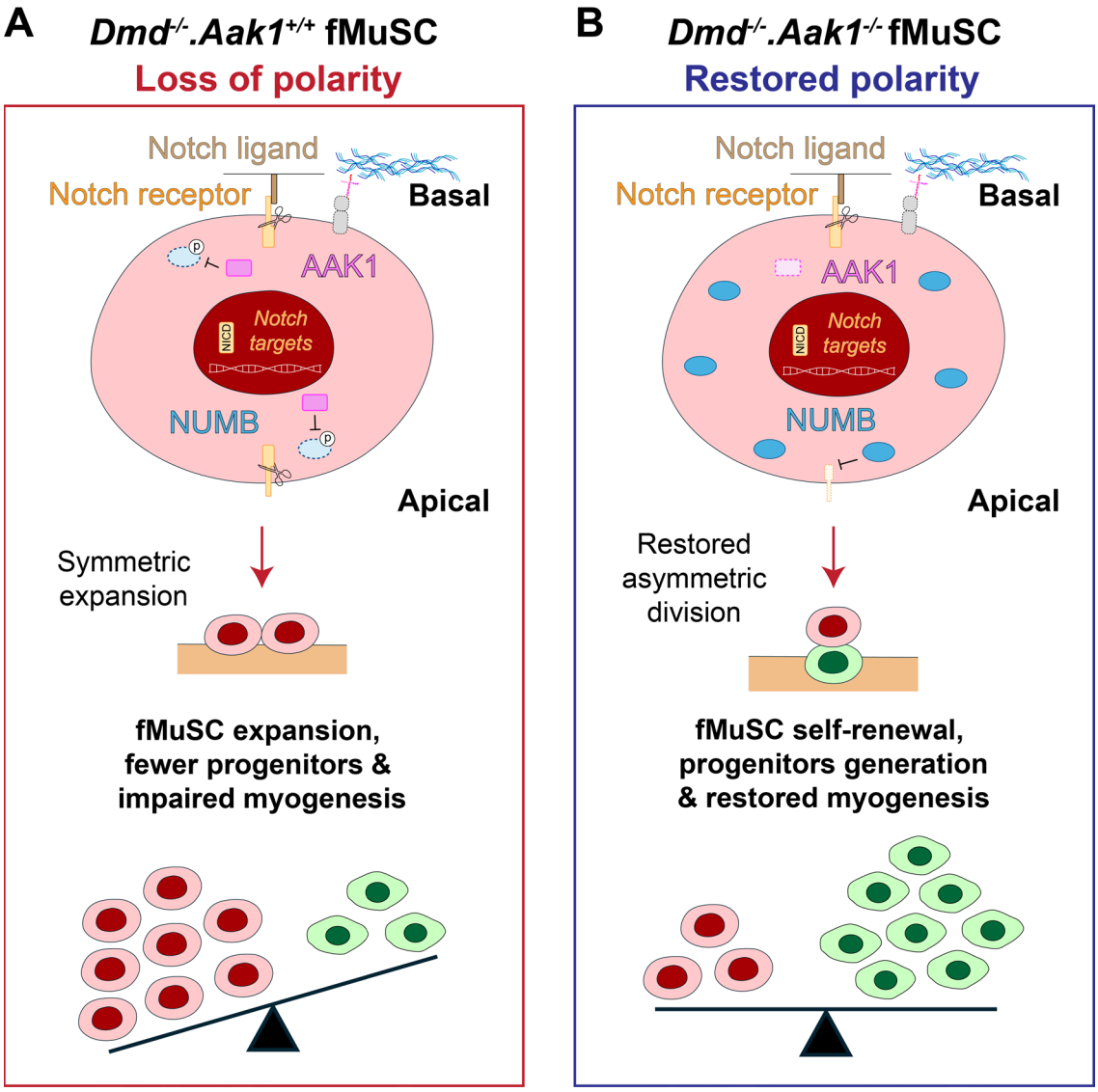

Figure 5.1 Graphical representation of proposed mechanism of rescued fMuSC polarity. **A** NUMB is downregulated in dystrophin-deficient fMuSCs, possibly by non-polarized PARD3/aPCK and the NUMB-associated kinase AAK1. This results in the expansion of the fMuSC pool and fewer MYOG^{+} progenitors. **B** Ablation of *Aak1* expression rescues fMuSC polarity, which restores asymmetric division and the generation of progenitor cells. This could result from two proposed mechanisms. First, the loss of *Aak1* balances the inhibitory effect of the non-polarized PARD3/aPCK. Second, the loss of Aak1 could reduce EGFR internalization, resulting in the restored asymmetric cell divisions and proportion of fMuSCs and progenitors.

5.6 Future Perspectives: The Therapeutic Restoration of Lost Polarity in DMD

Global incidence of DMD has dropped from 22.6 cases per 100,000 live male births in the 1950s-80s to 15.1–19.5 per 100,000 live male births reported in Europe, the USA, and Australia over the last few decades. However, epidemiological studies suggest that the global incidence has plateaued, likely due to the widespread adoption and diminishing returns of modern advancements in genetic screening and carrier detection.[314] In light of this, advancing therapeutic strategies to improve DMD patient outcomes is imperative.

The current work provides strong evidence that DMD skeletal muscle pathology and MuSC dysfunction are not only attributed to the inflammatory and degenerative mechanisms that result from myofiber fragility. In addition, the absence of dystrophin in MuSCs creates an intrinsic polarity deficit that impairs MuSC asymmetric division and commitment, resulting in both deficits in muscle development and perturbed muscle regeneration *in vivo*, as demonstrated by our fetal, neonatal and engraftment experiments. Interestingly, studies suggest that dystrophin deficiency in MuSCs and myofibers synergistically drives disease progression. Chronic MuSC activation and myogenesis exacerbate sarcolemma instability and, thus, myofiber fragility.[315–317] However, the fusion of *mdx* myocytes is imperative for the integrity of dystrophic muscle.[318] Therefore, an attractive therapeutic approach in DMD is targeting mechanisms that restore endogenous MuSC asymmetric division through DGC-independent mechanisms.[141] This provides a more nuanced intervention than mechanisms that induce MuCS activation, proliferation and differentiation. Moreover, restoring MuSC polarity and asymmetric division could address shortcomings of emerging gene therapies in clinical trials.

Despite promising early clinical data from Elividys, the first approved gene therapy for DMD, several concerns remain. First, the MuSC transduction efficiency by Elividys is unknown,

and AAVs are generally inefficient at infecting MuSCs due to the low endogenous expression of *Aavr*.[202] Given the ongoing muscle turnover and demand for regeneration by MuSCs, the long-term efficacy of gene therapy will likely rely on its ability to transduce MuSCs. Second, even with efficient transduction of MuSCs, 'micro' and 'mini' dystrophin gene therapies currently in clinical trial do not contain the MARK2 binding site on repeats 8 and 9, and would therefore not restore dystrophin-medicated MuSC polarity.[319] Finally, even with the integration of truncated dystrophin constructs carrying the MARK2 binding domain, the enhanced self-renewal capacity of *mdx* MuSCs, demonstrated by our transplantation assays, may result in a competitive growth advantage over corrected MuSCs. Consequently, dystrophin-deficient MuSCs that have undergone gene correction to restore polarity may eventually be lost to a competitive self-renewal disadvantage. Therefore, restoring dystrophin-deficient MuSC polarity by mechanisms not relying on dystrophin is essential and could potentially be leveraged as part of combination therapies.

5.7 MuSC Polarity as a Potential Therapeutic Target in Other Neuromuscular Diseases

Our research raises the intriguing question of whether therapeutic targeting of MuSCs to restore polarity could be relevant in other neuromuscular diseases. Several proteins involved in tethering the ECM to the intracellular actin cytoskeleton of myofibers are also expressed in MuSCs. Further, structural proteins play essential roles in cell signalling pathways, such as those that regulate the balance between MuSC self-renewal and commitment to sustain normal muscle regeneration.[138,139] To explore this further, muscular dystrophies and congenital myopathies should be investigated as potential secondary satellite cell-opathies.

One potential candidate is Congenital Merosin-Deficient 1a (MDC1A), caused by the complete loss of laminin α2 (LAMA2) function. Laminins are trimeric adhesion molecules of α,

β, and γ subunits that tether integrins and dystroglycan on cell membranes to the basal lamina. The expression of the laminin α chain is tissue and developmental timepoint-specific and is required for assembling the laminin complex. In muscle, laminin-211 and laminin-221 (α2β1γ1 and α2β2γ1) depend on the longer laminin α2 chain, encoded by *LAMA2*.[320] These interactions are essential for myofiber integrity and MuSC maintenance, as mutations to *LAMA2* have deleterious effects.[259,321]

Interestingly, laminin assembly is critical for MARK2-mediated cell polarity in muscle,[294] and loss of MuSC interaction with basal lamina results in a loss of polarity.[138] While the effects of *LAMA2* mutations on MuSC asymmetric division remain largely unexplored, MDC1A is likely a satellite cell-opathy. Moreover, gene therapies aimed at restoring *LAMA2* expression face similar challenges as those for DMD, including the large size of the *LAMA2* gene (9.5 kb), which exceeds the packaging capacity of adeno-associated virus (AAV) vectors,[322] and the limited transduction efficiency of AAV in MuSCs.[202] Thus, targeting MuSCs to restore polarity may hold therapeutic potential for MDC1A, though further experimentation is required to test this hypothesis.

5.8 Conclusion

Our findings provide compelling evidence that DMD is an intrinsic MuSC disorder characterized by deficits in MuSC polarity and myogenic commitment arising during secondary myogenesis. We further demonstrate that targeting AAK1 can restore myogenic cell commitment in the *mdx* fetus, highlighting the therapeutic potential of AAK1 inhibition to correct the MuSC deficits underlying DMD. Given that MuSC abnormalities and disrupted muscle architecture emerge *in utero*, it may be essential to implement newborn screening for DMD,[323] followed by MuSC-targeting therapies administered shortly after birth to leverage rapid neonatal muscle growth and enable timely

intervention. Overall, our study highlights the importance of investigating and targeting both myofibers and MuSCs in the treatment of DMD, and suggests that our findings should be explored in the context of other neuromuscular diseases.

References

1. Esper, M. E. *et al.* Intrinsic Muscle Stem Cell Dysfunction Contributes to Impaired Regeneration in the mdx Mouse. *Journal of Cachexia, Sarcopenia and Muscle* **16**, e13682 (2025).

2. Esper, M. E., Kodippili, K. & Rudnicki, M. A. Immunofluorescence Labeling of Skeletal Muscle in Development, Regeneration, and Disease. *Methods Mol Biol* **2566**, 113–132 (2023).

3. Frontera, W. R. & Ochala, J. Skeletal Muscle: A Brief Review of Structure and Function. *Calcif Tissue Int* **96**, 183–195 (2015).

4. Mukund, K. & Subramaniam, S. Skeletal muscle: A review of molecular structure and function, in health and disease. *WIREs Systems Biology and Medicine* **12**, e1462 (2020).

5. Schüler, S. C. *et al.* Extracellular matrix: Brick and mortar in the skeletal muscle stem cell niche. *Front Cell Dev Biol* **10**, 1056523 (2022).

6. Zhang, W., Liu, Y. & Zhang, H. Extracellular matrix: an important regulator of cell functions and skeletal muscle development. *Cell & Bioscience* **11**, 65 (2021).

7. Majchrzak, K., Hentschel, E., Hönzke, K., Geithe, C. & von Maltzahn, J. We need to talk—how muscle stem cells communicate. *Front. Cell Dev. Biol.* **12**, (2024).

8. Hoh, J. F. Y. Developmental, physiologic and phylogenetic perspectives on the expression and regulation of myosin heavy chains in mammalian skeletal muscles. *J Comp Physiol B* **193**, 355–382 (2023).

9. Bentzinger, C. F., Wang, Y. X. & Rudnicki, M. A. Building Muscle: Molecular Regulation of Myogenesis. *Cold Spring Harbor Perspectives in Biology* **4**, a008342–a008342 (2012).

10. Xi, H. *et al.* A Human Skeletal Muscle Atlas Identifies the Trajectories of Stem and Progenitor Cells across Development and from Human Pluripotent Stem Cells. *Cell Stem Cell* **27**, 158-176.e10 (2020).

11. White, R. B., Biérinx, A.-S., Gnocchi, V. F. & Zammit, P. S. Dynamics of muscle fibre growth during postnatal mouse development. *BMC Developmental Biology* **10**, 21 (2010).

12. Shahbazi, M. N. Mechanisms of human embryo development: from cell fate to tissue shape and back. *Development* **147**, dev190629 (2020).

13. Tani, S., Chung, U., Ohba, S. & Hojo, H. Understanding paraxial mesoderm development and sclerotome specification for skeletal repair. *Exp Mol Med* **52**, 1166–1177 (2020).

14. Grimaldi, A. & Tajbakhsh, S. Diversity in cranial muscles: Origins and developmental programs. *Current Opinion in Cell Biology* **73**, 110–116 (2021).

15. Yahya, I., Hockman, D., Brand-Saberi, B. & Morosan-Puopolo, G. New Insights into the Diversity of Branchiomeric Muscle Development: Genetic Programs and Differentiation. *Biology (Basel)* **11**, 1245 (2022).

16. Tzahor, E. Head Muscle Development. in *Vertebrate Myogenesis: Stem Cells and Precursors* (ed. Brand-Saberi, B.) 123–142 (Springer, Berlin, Heidelberg, 2015). doi:10.1007/978-3-662-44608-9_6.

17. Manning, E. & Placzek, M. Chapter Four - Organizing activities of axial mesoderm. in *Current Topics in Developmental Biology* (ed. Stern, C. D.) vol. 157 83–123 (Academic Press, 2024).

18. Hofmann, M. *et al.* WNT signaling, in synergy with T/TBX6, controls Notch signaling by regulating Dll1 expression in the presomitic mesoderm of mouse embryos. *Genes Dev.* **18**, 2712–2717 (2004).

19. Takada, S. *et al.* Wnt-3a regulates somite and tailbud formation in the mouse embryo. *Genes Dev* **8**, 174–189 (1994).

20. Wittler, L. *et al.* Expression of Msgn1 in the presomitic mesoderm is controlled by synergism of WNT signalling and Tbx6. *EMBO Rep* **8**, 784–789 (2007).

21. Yamaguchi, T. P., Takada, S., Yoshikawa, Y., Wu, N. & McMahon, A. P. T (Brachyury) is a direct target of Wnt3a during paraxial mesoderm specification. *Genes Dev* **13**, 3185–3190 (1999).

22. Yoon, J. K. & Wold, B. The bHLH regulator pMesogenin1 is required for maturation and segmentation of paraxial mesoderm. *Genes Dev* **14**, 3204–3214 (2000).

23. Chal, J. & Pourquié, O. Making muscle: skeletal myogenesis *in vivo* and *in vitro*. *Development* **144**, 2104–2122 (2017).

24. Tam, P. P. L. The control of somitogenesis in mouse embryos. *Development* **65**, 103–128 (1981).

25. Sanaki-Matsumiya, M. *et al.* Periodic formation of epithelial somites from human pluripotent stem cells. *Nat Commun* **13**, 2325 (2022).

26. Oates, A. C., Morelli, L. G. & Ares, S. Patterning embryos with oscillations: structure, function and dynamics of the vertebrate segmentation clock. *Development* **139**, 625–639 (2012).

27. Schubert, F. R. *et al.* Early mesodermal phenotypes in splotch suggest a role for Pax3 in the formation of epithelial somites. *Developmental Dynamics* **222**, 506–521 (2001).

28. Dequéant, M.-L. *et al.* A Complex Oscillating Network of Signaling Genes Underlies the Mouse Segmentation Clock. *Science* **314**, 1595–1598 (2006).

29. Hubaud, A. & Pourquié, O. Signalling dynamics in vertebrate segmentation. *Nat Rev Mol Cell Biol* **15**, 709–721 (2014).

30. Aulehla, A. *et al.* Wnt3a plays a major role in the segmentation clock controlling somitogenesis. *Dev Cell* **4**, 395–406 (2003).

31. Dubrulle, J., McGrew, M. J. & Pourquié, O. FGF Signaling Controls Somite Boundary Position and Regulates Segmentation Clock Control of Spatiotemporal *Hox* Gene Activation. *Cell* **106**, 219–232 (2001).

32. Naiche, L. A., Holder, N. & Lewandoski, M. FGF4 and FGF8 comprise the wavefront activity that controls somitogenesis. *Proceedings of the National Academy of Sciences* **108**, 4018–4023 (2011).

33. Wahl, M. B., Deng, C., Lewandoski, M. & Pourquié, O. FGF signaling acts upstream of the NOTCH and WNT signaling pathways to control segmentation clock oscillations in mouse somitogenesis. *Development* **134**, 4033–4041 (2007).

34. Saga, Y., Hata, N., Koseki, H. & Taketo, M. M. Mesp2: a novel mouse gene expressed in the presegmented mesoderm and essential for segmentation initiation. *Genes Dev* **11**, 1827–1839 (1997).

35. Takahashi, J. *et al.* Analysis of Ripply1/2-deficient mouse embryos reveals a mechanism underlying the rostro-caudal patterning within a somite. *Developmental Biology* **342**, 134–145 (2010).

36. Moreno, T. A., Jappelli, R., Belmonte, J. C. I. & Kintner, C. Retinoic acid regulation of the Mesp–Ripply feedback loop during vertebrate segmental patterning. *Developmental Biology* **315**, 317–330 (2008).

37. Saga, Y. The mechanism of somite formation in mice. *Current Opinion in Genetics & Development* **22**, 331–338 (2012).

38. Rhinn, M. & Dollé, P. Retinoic acid signalling during development. *Development* **139**, 843–858 (2012).

39. Bessho, Y. *et al.* Dynamic expression and essential functions of Hes7 in somite segmentation. *Genes Dev* **15**, 2642–2647 (2001).

40. Forsberg, H., Crozet, F. & Brown, N. A. Waves of mouse Lunatic fringe expression, in four-hour cycles at two-hour intervals, precede somite boundary formation. *Current Biology* **8**, 1027–1030 (1998).

41. Morimoto, M., Takahashi, Y., Endo, M. & Saga, Y. The Mesp2 transcription factor establishes segmental borders by suppressing Notch activity. *Nature* **435**, 354–359 (2005).

42. Chalamalasetty, R. B. *et al.* The Wnt3a/β-catenin target gene Mesogenin1 controls the segmentation clock by activating a Notch signalling program. *Nat Commun* **2**, 390 (2011).

43. González, A., Manosalva, I., Liu, T. & Kageyama, R. Control of Hes7 expression by Tbx6, the Wnt pathway and the chemical Gsk3 inhibitor LiCl in the mouse segmentation clock. *PLoS One* **8**, e53323 (2013).

44. Meijer, W. H. M. & Sonnen, K. F. From signalling oscillations to somite formation. *Current Opinion in Systems Biology* **39**, 100520 (2024).

45. Oginuma, M., Niwa, Y., Chapman, D. L. & Saga, Y. Mesp2 and Tbx6 cooperatively create periodic patterns coupled with the clock machinery during mouse somitogenesis. *Development* **135**, 2555–2562 (2008).

46. Niwa, Y. *et al.* Different types of oscillations in Notch and Fgf signaling regulate the spatiotemporal periodicity of somitogenesis. *Genes Dev* **25**, 1115–1120 (2011).

47. Buckingham, M. Myogenic progenitor cells and skeletal myogenesis in vertebrates. *Current Opinion in Genetics & Development* **16**, 525–532 (2006).

48. Deries, M., Schweitzer, R. & Duxson, M. J. Developmental fate of the mammalian myotome. *Dev Dyn* **239**, 2898–2910 (2010).

49. Hernández-Hernández, J. M., García-González, E. G., Brun, C. E. & Rudnicki, M. A. The myogenic regulatory factors, determinants of muscle development, cell identity and regeneration. *Seminars in Cell & Developmental Biology* **72**, 10–18 (2017).

50. Buckingham, M. & Relaix, F. PAX3 and PAX7 as upstream regulators of myogenesis. *Semin. Cell Dev. Biol.* **44**, 115–125 (2015).

51. Cinnamon, Y., Kahane, N. & Kalcheim, C. Characterization of the early development of specific hypaxial muscles from the ventrolateral myotome. *Development* **126**, 4305–4315 (1999).

52. Venters, S. J. & Ordahl, C. P. Asymmetric cell divisions are concentrated in the dermomyotome dorsomedial lip during epaxial primary myotome morphogenesis. *Anatomy and Embryology* **209**, 449–460 (2005).

53. Ben-Yair, R. & Kalcheim, C. Lineage analysis of the avian dermomyotome sheet reveals the existence of single cells with both dermal and muscle progenitor fates. *Development* **132**, 689–701 (2005).

54. Holowacz, T., Zeng, L. & Lassar, A. B. Asymmetric localization of numb in the chick somite and the influence of myogenic signals. *Dev. Dyn.* **235**, 633–645 (2006).

55. Cinnamon, Y., Ben-Yair, R. & Kalcheim, C. Differential effects of N-cadherin-mediated adhesion on the development of myotomal waves. *Development* **133**, 1101–1112 (2006).

56. Jory, A. *et al.* Numb promotes an increase in skeletal muscle progenitor cells in the embryonic somite. *Stem Cells* **27**, 2769–2780 (2009).

57. Hirsinger, E. *et al.* Notch signalling acts in postmitotic avian myogenic cells to control MyoD activation. *Development* **128**, 107–116 (2001).

58. Schuster-Gossler, K., Cordes, R. & Gossler, A. Premature myogenic differentiation and depletion of progenitor cells cause severe muscle hypotrophy in Delta1 mutants. *PNAS* **104**, 537–542 (2007).

59. Vasyutina, E. *et al.* RBP-J (Rbpsuh) is essential to maintain muscle progenitor cells and to generate satellite cells. *Proc Natl Acad Sci U S A* **104**, 4443–4448 (2007).

60. Reshef, R., Maroto, M. & Lassar, A. B. Regulation of dorsal somitic cell fates: BMPs and Noggin control the timing and pattern of myogenic regulator expression. *Genes Dev* **12**, 290–303 (1998).

61. von Maltzahn, J., Chang, N. C., Bentzinger, C. F. & Rudnicki, M. A. Wnt Signaling in Myogenesis. *Trends Cell Biol* **22**, 602–609 (2012).

62. Melendez, J. *et al.* TGFβ signalling acts as a molecular brake of myoblast fusion. *Nat Commun* **12**, 749 (2021).

63. Bajard, L. *et al.* A novel genetic hierarchy functions during hypaxial myogenesis: Pax3 directly activates Myf5 in muscle progenitor cells in the limb. *Genes & Development* **20**, 2450 (2006).

64. L'Honoré, A., Ouimette, J.-F., Lavertu-Jolin, M. & Drouin, J. Pitx2 defines alternate pathways acting through MyoD during limb and somitic myogenesis. *Development* **137**, 3847–3856 (2010).

65. Relaix, F. *et al.* Six Homeoproteins Directly Activate Myod Expression in the Gene Regulatory Networks That Control Early Myogenesis. *PLOS Genetics* **9**, e1003425 (2013).

66. Lagha, M. *et al.* Pax3 regulation of FGF signaling affects the progression of embryonic progenitor cells into the myogenic program. *Genes Dev* **22**, 1828–1837 (2008).

67. Hutcheson, D. A., Zhao, J., Merrell, A., Haldar, M. & Kardon, G. Embryonic and fetal limb myogenic cells are derived from developmentally distinct progenitors and have different requirements for β-catenin. *Genes Dev* **23**, 997–1013 (2009).

68. Seale, P. *et al.* Pax7 Is Required for the Specification of Myogenic Satellite Cells. *Cell* **102**, 777–786 (2000).

69. Seale, P., Ishibashi, J., Scimè, A. & Rudnicki, M. A. Pax7 Is Necessary and Sufficient for the Myogenic Specification of CD45+:Sca1+ Stem Cells from Injured Muscle. *PLoS Biology* **2**, e130 (2004).

70. Oustanina, S., Hause, G. & Braun, T. Pax7 directs postnatal renewal and propagation of myogenic satellite cells but not their specification. *EMBO J* **23**, 3430–3439 (2004).

71. Lepper, C., Partridge, T. A. & Fan, C.-M. An absolute requirement for Pax7-positive satellite cells in acute injury-induced skeletal muscle regeneration. *Development* **138**, 3639–3646 (2011).

72. Sambasivan, R. *et al.* Pax7-expressing satellite cells are indispensable for adult skeletal muscle regeneration. *Development* **138**, 3647–3656 (2011).

73. von Maltzahn, J., Jones, A. E., Parks, R. J. & Rudnicki, M. A. Pax7 is critical for the normal function of satellite cells in adult skeletal muscle. *Proc Natl Acad Sci U S A* **110**, 16474–16479 (2013).

74. Braun, T., Rudnicki, M. A., Arnold, H. H. & Jaenisch, R. Targeted inactivation of the muscle regulatory gene Myf-5 results in abnormal rib development and perinatal death. *Cell* **71**, 369–382 (1992).

75. Kablar, B. *et al.* MyoD and Myf-5 differentially regulate the development of limb versus trunk skeletal muscle. *Development* **124**, 4729–4738 (1997).

76. Rudnicki, M. A., Braun, T., Hinuma, S. & Jaenisch, R. Inactivation of MyoD in mice leads to up-regulation of the myogenic HLH gene Myf-5 and results in apparently normal muscle development. *Cell* **71**, 383–390 (1992).

77. Rudnicki, M. A. *et al.* MyoD or Myf-5 is required for the formation of skeletal muscle. *Cell* **75**, 1351–1359 (1993).

78. Kassar-Duchossoy, L. *et al.* Mrf4 determines skeletal muscle identity in Myf5:Myod double-mutant mice. *Nature* **431**, 466–471 (2004).

79. Hasty, P. *et al.* Muscle deficiency and neonatal death in mice with a targeted mutation in the myogenin gene. *Nature* **364**, 501–506 (1993).

80. Nabeshima, Y. *et al.* Myogenin gene disruption results in perinatal lethality because of severe muscle defect. *Nature* **364**, 532–535 (1993).

81. Braun, T. & Arnold, H. H. Inactivation of Myf-6 and Myf-5 genes in mice leads to alterations in skeletal muscle development. *EMBO J* **14**, 1176–1186 (1995).

82. Rawls, A. *et al.* Overlapping functions of the myogenic bHLH genes MRF4 and MyoD revealed in double mutant mice. *Development* **125**, 2349–2358 (1998).

83. Bröhl, D. *et al.* Colonization of the Satellite Cell Niche by Skeletal Muscle Progenitor Cells Depends on Notch Signals. *Developmental Cell* **23**, 469–481 (2012).

84. Kanisicak, O., Mendez, J. J., Yamamoto, S., Yamamoto, M. & Goldhamer, D. J. Progenitors of skeletal muscle satellite cells express the muscle determination gene, MyoD. *Dev Biol* **332**, 131–141 (2009).

85. Lahmann, I. *et al.* Oscillations of MyoD and Hes1 proteins regulate the maintenance of activated muscle stem cells. *Genes Dev* **33**, 524–535 (2019).

86. Schiaffino, S., Rossi, A. C., Smerdu, V., Leinwand, L. A. & Reggiani, C. Developmental myosins: expression patterns and functional significance. *Skeletal Muscle* **5**, 22 (2015).

87. Narusawa, M. *et al.* Slow myosin in developing rat skeletal muscle. *Journal of Cell Biology* **104**, 447–459 (1987).

88. Pin, C. L. & Merrifield, P. A. Embryonic and fetal rat myoblasts express different phenotypes following differentiation in vitro. *Dev Genet* **14**, 356–368 (1993).

89. Biressi, S. *et al.* Intrinsic phenotypic diversity of embryonic and fetal myoblasts is revealed by genome-wide gene expression analysis on purified cells. *Developmental Biology* **304**, 633–651 (2007).

90. Taglietti, V. *et al.* Nfix Induces a Switch in Sox6 Transcriptional Activity to Regulate MyHC-I Expression in Fetal Muscle. *Cell Reports* **17**, 2354–2366 (2016).

91. Messina, G. *et al.* Nfix regulates fetal-specific transcription in developing skeletal muscle. *Cell* **140**, 554–566 (2010).

92. Daou, N. *et al.* A new role for the calcineurin/NFAT pathway in neonatal myosin heavy chain expression via the NFATc2/MyoD complex during mouse myogenesis. *Development* **140**, 4914–4925 (2013).

93. Collins, B. C. *et al.* Three-dimensional imaging studies in mice identify cellular dynamics of skeletal muscle regeneration. *Developmental Cell* **59**, 1457-1474.e5 (2024).

94. Relaix, F., Rocancourt, D., Mansouri, A. & Buckingham, M. A Pax3/Pax7-dependent population of skeletal muscle progenitor cells. *Nature* **435**, 948–953 (2005).

95. Kassar-Duchossoy, L. *et al.* Pax3/Pax7 mark a novel population of primitive myogenic cells during development. *Genes Dev* **19**, 1426–1431 (2005).

96. Gros, J., Manceau, M., Thomé, V. & Marcelle, C. A common somitic origin for embryonic muscle progenitors and satellite cells. *Nature* **435**, 954–958 (2005).

97. Schienda, J. *et al.* Somitic origin of limb muscle satellite and side population cells. *Proceedings of the National Academy of Sciences* **103**, 945–950 (2006).

98. Tajbakhsh, S. Skeletal muscle stem cells in developmental versus regenerative myogenesis. *Journal of Internal Medicine* **266**, 372–389 (2009).

99. Allbrook, D. B., Han, M. F. & Hellmuth, A. E. Population of muscle satellite cells in relation to age and mitotic activity. *Pathology* **3**, 223–243 (1971).

100. Schultz, E. Satellite Cell Proliferative Compartments in Growing Skeletal Muscles. *Developmental Biology* **175**, 84–94 (1996).

101. Bansal, D. *et al.* Defective membrane repair in dysferlin-deficient muscular dystrophy. *Nature* **423**, 168–172 (2003).

102. Schmalbruch, H. & Lewis, D. M. Dynamics of nuclei of muscle fibers and connective tissue cells in normal and denervated rat muscles. *Muscle Nerve* **23**, 617–626 (2000).

103. Feige, P., Brun, C. E., Ritso, M. & Rudnicki, M. A. Orienting Muscle Stem Cells for Regeneration in Homeostasis, Aging, and Disease. *Cell Stem Cell* **23**, 653–664 (2018).

104. Low, S., Barnes, J. L., Zammit, P. S. & Beauchamp, J. R. Delta-Like 4 Activates Notch 3 to Regulate Self-Renewal in Skeletal Muscle Stem Cells. *Stem Cells* **36**, 458–466 (2018).

105. Eliazer, S., Sun, X., Barruet, E. & Brack, A. S. Heterogeneous levels of delta-like 4 within a multinucleated niche cell maintains muscle stem cell diversity. *eLife* **11**, e68180 (2022).

106. Verma, M. *et al.* Muscle Satellite Cell Cross-Talk with a Vascular Niche maintains quiescence via VEGF and Notch Signaling. *Cell Stem Cell* **23**, 530-543.e9 (2018).

107. Fujimaki, S. *et al.* The endothelial Dll4–muscular Notch2 axis regulates skeletal muscle mass. *Nat Metab* **4**, 180–189 (2022).

108. Mourikis, P., Gopalakrishnan, S., Sambasivan, R. & Tajbakhsh, S. Cell-autonomous Notch activity maintains the temporal specification potential of skeletal muscle stem cells. *Development* **139**, 4536–4548 (2012).

109. Mourikis, P. *et al.* A Critical Requirement for Notch Signaling in Maintenance of the Quiescent Skeletal Muscle Stem Cell State. *Stem Cells* **30**, 243–252 (2012).

110. Wen, Y. *et al.* Constitutive Notch Activation Upregulates Pax7 and Promotes the Self-Renewal of Skeletal Muscle Satellite Cells. *Mol Cell Biol* **32**, 2300–2311 (2012).

111. Bjornson, C. R. R. *et al.* Notch signaling is necessary to maintain quiescence in adult muscle stem cells. *Stem Cells* **30**, 232–242 (2012).

112. Baghdadi, M. B. *et al.* Reciprocal signalling by Notch-Collagen V-CALCR retains muscle stem cells in their niche. *Nature* **557**, 714–718 (2018).

113. Cheung, T. H. *et al.* Maintenance of muscle stem-cell quiescence by microRNA-489. *Nature* **482**, 524–528 (2012).

114. Baghdadi, M. B. *et al.* Notch-Induced miR-708 Antagonizes Satellite Cell Migration and Maintains Quiescence. *Cell Stem Cell* **23**, 859-868.e5 (2018).

115. Crist, C. G., Montarras, D. & Buckingham, M. Muscle Satellite Cells Are Primed for Myogenesis but Maintain Quiescence with Sequestration of Myf5 mRNA Targeted by microRNA-31 in mRNP Granules. *Cell Stem Cell* **11**, 118–126 (2012).

116. Zismanov, V. *et al.* Phosphorylation of eIF2α Is a Translational Control Mechanism Regulating Muscle Stem Cell Quiescence and Self-Renewal. *Cell Stem Cell* **18**, 79–90 (2016).

117. Eliazer, S. *et al.* Wnt4 from the Niche Controls the Mechano-Properties and Quiescent State of Muscle Stem Cells. *Cell Stem Cell* **25**, 654-665.e4 (2019).

118. Yamaguchi, M. *et al.* Calcitonin Receptor Signaling Inhibits Muscle Stem Cells from Escaping the Quiescent State and the Niche. *Cell Reports* **13**, 302–314 (2015).

119. García-Prat, L. *et al.* FoxO maintains a genuine muscle stem-cell quiescent state until geriatric age. *Nat Cell Biol* **22**, 1307–1318 (2020).

120. Yue, F. *et al.* Pten is necessary for the quiescence and maintenance of adult muscle stem cells. *Nat Commun* **8**, 14328 (2017).

121. Peng, Y. *et al.* Mechano-signaling via Piezo1 prevents activation and p53-mediated senescence of muscle stem cells. *Redox Biol* **52**, 102309 (2022).

122. Brun, C. E. *et al.* GLI3 regulates muscle stem cell entry into GAlert and self-renewal. *Nat Commun* **13**, 3961 (2022).

123. Li, W. *et al.* Primary cilia in satellite cells are the mechanical sensors for muscle hypertrophy. *Proc Natl Acad Sci U S A* **119**, e2103615119 (2022).

124. Rodgers, J. T. *et al.* mTORC1 controls the adaptive transition of quiescent stem cells from G0 to GAlert. *Nature* **510**, 393–396 (2014).

125. Rodgers, J. T., Schroeder, M. D., Ma, C. & Rando, T. A. HGFA Is an Injury-Regulated Systemic Factor that Induces the Transition of Stem Cells into GAlert. *Cell Reports* **19**, 479–486 (2017).

126. Lee, G. *et al.* Fully reduced HMGB1 accelerates the regeneration of multiple tissues by transitioning stem cells to GAlert. *Proceedings of the National Academy of Sciences* **115**, E4463–E4472 (2018).

127. Machado, L. *et al.* In Situ Fixation Redefines Quiescence and Early Activation of Skeletal Muscle Stem Cells. *Cell Rep* **21**, 1982–1993 (2017).

128. Pietrosemoli, N. *et al.* Comparison of multiple transcriptomes exposes unified and divergent features of quiescent and activated skeletal muscle stem cells. *Skelet Muscle* **7**, 28 (2017).

129. van den Brink, S. C. *et al.* Single-cell sequencing reveals dissociation-induced gene expression in tissue subpopulations. *Nat Methods* **14**, 935–936 (2017).

130. van Velthoven, C. T. J., de Morree, A., Egner, I. M., Brett, J. O. & Rando, T. A. Transcriptional Profiling of Quiescent Muscle Stem Cells In Vivo. *Cell Rep* **21**, 1994–2004 (2017).

131. Relaix, F. *et al.* Perspectives on skeletal muscle stem cells. *Nat Commun* **12**, 692 (2021).

132. Webster, M. T., Manor, U., Lippincott-Schwartz, J. & Fan, C.-M. Intravital Imaging Reveals Ghost Fibers as Architectural Units Guiding Myogenic Progenitors During Regeneration. *Cell Stem Cell* **18**, 243–252 (2016).

133. Shinin, V., Gayraud-Morel, B., Gomès, D. & Tajbakhsh, S. Asymmetric division and cosegregation of template DNA strands in adult muscle satellite cells. *Nat. Cell Biol.* **8**, 677–687 (2006).

134. Kuang, S., Kuroda, K., Le Grand, F. & Rudnicki, M. A. Asymmetric Self-Renewal and Commitment of Satellite Stem Cells in Muscle. *Cell* **129**, 999–1010 (2007).

135. Goel, A. J., Rieder, M.-K., Arnold, H.-H., Radice, G. L. & Krauss, R. S. Niche Cadherins Control the Quiescence-to-Activation Transition in Muscle Stem Cells. *Cell Reports* **21**, 2236–2250 (2017).

136. Irintchev, A., Zeschnigk, M., Starzinski-Powitz, A. & Wernig, A. Expression pattern of M-cadherin in normal, denervated, and regenerating mouse muscles. *Dev Dyn* **199**, 326–337 (1994).

137. Urciuolo, A. *et al.* Collagen VI regulates satellite cell self-renewal and muscle regeneration. *Nat Commun* **4**, 1964 (2013).

138. Dumont, N. A. *et al.* Dystrophin expression in muscle stem cells regulates their polarity and asymmetric division. *Nature Medicine* **21**, 1455–1463 (2015).

139. Chang, N. C. *et al.* The Dystrophin Glycoprotein Complex Regulates the Epigenetic Activation of Muscle Stem Cell Commitment. *Cell Stem Cell* **22**, 755-768.e6 (2018).

140. Le Grand, F., Jones, A. E., Seale, V., Scimè, A. & Rudnicki, M. A. Wnt7a activates the planar cell polarity pathway to drive the symmetric expansion of satellite stem cells. *Cell Stem Cell* **4**, 535–547 (2009).

141. Wang, Y. X. *et al.* EGFR-Aurka Signaling Rescues Polarity and Regeneration Defects in Dystrophin-Deficient Muscle Stem Cells by Increasing Asymmetric Divisions. *Cell Stem Cell* **24**, 419-432.e6 (2019).

142. Fujimaki, S. *et al.* Notch1 and Notch2 Coordinately Regulate Stem Cell Function in the Quiescent and Activated States of Muscle Satellite Cells. *Stem Cells* **36**, 278–285 (2018).

143. Kitamoto, T. & Hanaoka, K. Notch3 Null Mutation in Mice Causes Muscle Hyperplasia by Repetitive Muscle Regeneration. *Stem Cells* **28**, 2205–2216 (2010).

144. Conboy, I. M. & Rando, T. A. The regulation of Notch signaling controls satellite cell activation and cell fate determination in postnatal myogenesis. *Dev Cell* **3**, 397–409 (2002).

145. George, R. M. *et al.* Numb-deficient satellite cells have regeneration and proliferation defects. *Proc Natl Acad Sci U S A* **110**, 18549–18554 (2013).

146. Zhang, P. *et al.* mTOR is necessary for proper satellite cell activity and skeletal muscle regeneration. *Biochem Biophys Res Commun* **463**, 102–108 (2015).

147. Jash, S., Dhar, G., Ghosh, U. & Adhya, S. Role of the mTORC1 Complex in Satellite Cell Activation by RNA-Induced Mitochondrial Restoration: Dual Control of Cyclin D1 through MicroRNAs. *Molecular and Cellular Biology* **34**, 3594–3606 (2014).

148. Pawlikowski, B., Vogler, T. O., Gadek, K. & Olwin, B. B. Regulation of skeletal muscle stem cells by fibroblast growth factors. *Developmental Dynamics* **246**, 359–367 (2017).

149. Bischoff, R. Proliferation of muscle satellite cells on intact myofibers in culture. *Developmental Biology* **115**, 129–139 (1986).

150. Yablonka-Reuveni, Z., Seger, R. & Rivera, A. J. Fibroblast growth factor promotes recruitment of skeletal muscle satellite cells in young and old rats. *J Histochem Cytochem* **47**, 23–42 (1999).

151. Shefer, G., Van de Mark, D. P., Richardson, J. B. & Yablonka-Reuveni, Z. Satellite-cell pool size does matter: Defining the myogenic potency of aging skeletal muscle. *Developmental Biology* **294**, 50–66 (2006).

152. Liu, Y. FGF2 activates TRPC and Ca2+ signaling leading to satellite cell activation. *Frontiers in Physiology* **5**, (2014).

153. Yin, H., Price, F. & Rudnicki, M. A. Satellite Cells and the Muscle Stem Cell Niche. *Physiol Rev* **93**, 23–67 (2013).

154. Kuang, S., Chargé, S. B., Seale, P., Huh, M. & Rudnicki, M. A. Distinct roles for Pax7 and Pax3 in adult regenerative myogenesis. *J Cell Biol* **172**, 103–113 (2006).

155. Scaramozza, A. *et al.* Lineage Tracing Reveals a Subset of Reserve Muscle Stem Cells Capable of Clonal Expansion under Stress. *Cell Stem Cell* **24**, 944-957.e5 (2019).

156. Der Vartanian, A. *et al.* PAX3 Confers Functional Heterogeneity in Skeletal Muscle Stem Cell Responses to Environmental Stress. *Cell Stem Cell* **24**, 958-973.e9 (2019).

157. Yin, H. *et al.* MicroRNA-133 controls brown adipose determination in skeletal muscle satellite cells by targeting Prdm16. *Cell Metab* **17**, 210–224 (2013).

158. Chakkalakal, J. V. *et al.* Early forming label-retaining muscle stem cells require p27kip1 for maintenance of the primitive state. *Development* **141**, 1649–1659 (2014).

159. Tierney, M. T., Stec, M. J., Rulands, S., Simons, B. D. & Sacco, A. Muscle Stem Cells Exhibit Distinct Clonal Dynamics in Response to Tissue Repair and Homeostatic Aging. *Cell Stem Cell* **22**, 119-127.e3 (2018).

160. Porpiglia, E. *et al.* Elevated CD47 is a hallmark of dysfunctional aged muscle stem cells that can be targeted to augment regeneration. *Cell Stem Cell* **29**, 1653-1668.e8 (2022).

161. Ganassi, M., Muntoni, F. & Zammit, P. S. Defining and identifying satellite cell-opathies within muscular dystrophies and myopathies. *Exp Cell Res* **411**, 112906 (2022).

162. Deprez, A., Orfi, Z., Rieger, L. & Dumont, N. A. Impaired muscle stem cell function and abnormal myogenesis in acquired myopathies. *Biosci Rep* **43**, BSR20220284 (2023).

163. Ganassi, M. & Zammit, P. S. Involvement of muscle satellite cell dysfunction in neuromuscular disorders: Expanding the portfolio of satellite cell-opathies. *Eur J Transl Myol* **32**, 10064 (2022).

164. Koenig, M. *et al.* Complete cloning of the Duchenne muscular dystrophy (DMD) cDNA and preliminary genomic organization of the DMD gene in normal and affected individuals. *Cell* **50**, 509–517 (1987).

165. Tennyson, C. N., Klamut, H. J. & Worton, R. G. The human dystrophin gene requires 16 hours to be transcribed and is cotranscriptionally spliced. *Nat Genet* **9**, 184–190 (1995).

166. Sadoulet-Puccio, H. M. & Kunkel, L. M. Dystrophin and its isoforms. *Brain Pathol* **6**, 25–35 (1996).

167. LaPelusa, A., Asuncion, R. M. D. & Kentris, M. Muscular Dystrophy. in *StatPearls* (StatPearls Publishing, Treasure Island (FL), 2025).

168. Duan, D., Goemans, N., Takeda, S., Mercuri, E. & Aartsma-Rus, A. Duchenne muscular dystrophy. *Nat Rev Dis Primers* **7**, 1–19 (2021).

169. Garcia, S. *et al.* Identification of de novo Mutations of Duchénnè/Becker Muscular Dystrophies in Southern Spain. *Int J Med Sci* **11**, 988–993 (2014).

170. Haldane, J. B. S. The rate of spontaneous mutation of a human gene. 1935. *J Genet* **83**, 235–244 (2004).

171. Tang, A. & Yokota, T. Duchenne muscular dystrophy: promising early-stage clinical trials to watch. *Expert Opin Investig Drugs* **33**, 201–217 (2024).

172. Hoffman, E. P., Brown, R. H. & Kunkel, L. M. Dystrophin: the protein product of the Duchenne muscular dystrophy locus. *Cell* **51**, 919–28 (1987).

173. Ibraghimov-Beskrovnaya, O. *et al.* Primary structure of dystrophin-associated glycoproteins linking dystrophin to the extracellular matrix. *Nature* **355**, 696–702 (1992).

174. Kodippili, K. & Rudnicki, M. A. Satellite cell contribution to disease pathology in Duchenne muscular dystrophy. *Front Physiol* **14**, 1180980 (2023).

175. Alexander, M. S. *et al.* CD82 Is a Marker for Prospective Isolation of Human Muscle Satellite Cells and Is Linked to Muscular Dystrophies. *Cell Stem Cell* **19**, 800–807 (2016).

176. Bulfield, G., Siller, W. G., Wight, P. A. & Moore, K. J. X chromosome-linked muscular dystrophy (mdx) in the mouse. *Proc. Natl. Acad. Sci. U.S.A.* **81**, 1189–1192 (1984).

177. Hoffman, E. P., Monaco, A. P., Feener, C. C. & Kunkel, L. M. Conservation of the Duchenne muscular dystrophy gene in mice and humans. *Science* **238**, 347–350 (1987).

178. Ryder-Cook, A. S. *et al.* Localization of the mdx mutation within the mouse dystrophin gene. *EMBO J.* **7**, 3017–3021 (1988).

179. Sicinski, P. *et al.* The molecular basis of muscular dystrophy in the mdx mouse: a point mutation. *Science* **244**, 1578–1580 (1989).

180. McGreevy, J. W., Hakim, C. H., McIntosh, M. A. & Duan, D. Animal models of Duchenne muscular dystrophy: from basic mechanisms to gene therapy. *Disease Models & Mechanisms* **8**, 195–213 (2015).

181. Crone, M. & Mah, J. K. Current and Emerging Therapies for Duchenne Muscular Dystrophy. *Curr Treat Options Neurol* **20**, 31 (2018).

182. Robertson, R., Li, S., Filippelli, R. L. & Chang, N. C. Chapter Four - Muscle stem cell dysfunction in rhabdomyosarcoma and muscular dystrophy. in *Current Topics in Developmental Biology* (eds. Rudnicki, M. A. & Dilworth, F. J.) vol. 158 83–121 (Academic Press, 2024).

183. Starosta, A. & Konieczny, P. Therapeutic aspects of cell signaling and communication in Duchenne muscular dystrophy. *Cell. Mol. Life Sci.* **78**, 4867–4891 (2021).

184. Pelosi, L. *et al.* Functional and Morphological Improvement of Dystrophic Muscle by Interleukin 6 Receptor Blockade. *EBioMedicine* **2**, 285–293 (2015).

185. Tierney, M. T. *et al.* STAT3 signaling controls satellite cell expansion and skeletal muscle repair. *Nat Med* **20**, 1182–1186 (2014).

186. Yamashita, K. *et al.* The 8th and 9th tandem spectrin-like repeats of utrophin cooperatively form a functional unit to interact with polarity-regulating kinase PAR-1b. *Biochem. Biophys. Res. Commun.* **391**, 812–817 (2010).

187. Farini, A. *et al.* Inositol 1,4,5-trisphosphate (IP3)-dependent Ca2+ signaling mediates delayed myogenesis in Duchenne muscular dystrophy fetal muscle. *Development* **143**, 658–669 (2016).

188. Nguyen, F., Cherel, Y., Guigand, L., Goubault-Leroux, I. & Wyers, M. Muscle lesions associated with dystrophin deficiency in neonatal golden retriever puppies. *J. Comp. Pathol.* **126**, 100–108 (2002).

189. Bassett, D. I. *et al.* Dystrophin is required for the formation of stable muscle attachments in the zebrafish embryo. *Development* **130**, 5851–5860 (2003).

190. Merrick, D., Stadler, L. K. J., Larner, D. & Smith, J. Muscular dystrophy begins early in embryonic development deriving from stem cell loss and disrupted skeletal muscle formation. *Disease Models & Mechanisms* **2**, 374–388 (2009).

191. Mournetas, V. *et al.* Myogenesis modelled by human pluripotent stem cells: a multi-omic study of Duchenne myopathy early onset. *J Cachexia Sarcopenia Muscle* **12**, 209–232 (2021).

192. Mozin, E. *et al.* Dystrophin deficiency impairs cell junction formation during embryonic myogenesis from pluripotent stem cells. *iScience* **27**, (2024).

193. Pescatori, M. *et al.* Gene expression profiling in the early phases of DMD: a constant molecular signature characterizes DMD muscle from early postnatal life throughout disease progression. *The FASEB Journal* **21**, 1210–1226 (2007).

194. Broomfield, J., Hill, M., Guglieri, M., Crowther, M. & Abrams, K. Life Expectancy in Duchenne Muscular Dystrophy. *Neurology* **97**, e2304–e2314 (2021).

195. Bushby, K. *et al.* Diagnosis and management of Duchenne muscular dystrophy, part 1: diagnosis, and pharmacological and psychosocial management. *Lancet Neurol* **9**, 77–93 (2010).

196. Eser, G. & Topaloğlu, H. Current Outline of Exon Skipping Trials in Duchenne Muscular Dystrophy. *Genes (Basel)* **13**, 1241 (2022).

197. Burnette, W. B. Survival in eteplirsen-treated Duchenne Muscular Dystrophy patients: Are there benefits beyond steroids? *Muscle Nerve* **70**, 4–5 (2024).

198. Agrawal, P. *et al.* Role of CRISPR/Cas9 in the treatment of Duchenne muscular dystrophy and its delivery strategies. *Life Sci* **330**, 122003 (2023).

199. Mendell, J. R. *et al.* Practical Considerations for Delandistrogene Moxeparvovec Gene Therapy in Patients With Duchenne Muscular Dystrophy. *Pediatric Neurology* **153**, 11–18 (2024).

200. Hoy, S. M. Delandistrogene Moxeparvovec: First Approval. *Drugs* **83**, 1323–1329 (2023).

201. Pozsgai, E. R., Griffin, D. A., Heller, K. N., Mendell, J. R. & Rodino-Klapac, L. R. Systemic AAV-Mediated β-Sarcoglycan Delivery Targeting Cardiac and Skeletal Muscle

Ameliorates Histological and Functional Deficits in LGMD2E Mice. *Mol Ther* **25**, 855–869 (2017).

202. Zengel, J. *et al.* Hardwiring tissue-specific AAV transduction in mice through engineered receptor expression. *Nat Methods* **20**, 1070–1081 (2023).

203. Houzelstein, D., Lyons, G. E., Chamberlain, J. & Buckingham, M. E. Localization of dystrophin gene transcripts during mouse embryogenesis. *The Journal of cell biology* **119**, 811–21 (1992).

204. Durand, M., Suel, L., Barbet, J. P., Beckmann, J. S. & Fougerousse, F. Sequential expression of genes involved in muscular dystrophies during human development. *Morphologie* **86**, 9–12 (2002).

205. Tajbakhsh, S. *et al.* Gene targeting the myf-5 locus with nlacZ reveals expression of this myogenic factor in mature skeletal muscle fibres as well as early embryonic muscle. *Dev Dyn* **206**, 291–300 (1996).

206. Sambasivan, R. *et al.* Distinct regulatory cascades govern extraocular and pharyngeal arch muscle progenitor cell fates. *Dev Cell* **16**, 810–821 (2009).

207. Prigge, J. R. *et al.* Nuclear double-fluorescent reporter for in vivo and ex vivo analyses of biological transitions in mouse nuclei. *Mamm Genome* 10.1007/s00335-013-9469–8 (2013) doi:10.1007/s00335-013-9469-8.

208. Tallquist, M. D., Weismann, K. E., Hellström, M. & Soriano, P. Early myotome specification regulates PDGFA expression and axial skeleton development. *Development* **127**, 5059–5070 (2000).

209. Bowl, M. R. *et al.* A large scale hearing loss screen reveals an extensive unexplored genetic landscape for auditory dysfunction. *Nat Commun* **8**, 886 (2017).

210. Charles, J. P., Cappellari, O., Spence, A. J., Hutchinson, J. R. & Wells, D. J. Musculoskeletal Geometry, Muscle Architecture and Functional Specialisations of the Mouse Hindlimb. *PLoS One* **11**, e0147669 (2016).

211. Feige, P. & Rudnicki, M. A. Isolation of satellite cells and transplantation into mice for lineage tracing in muscle. *Nat Protoc* **15**, 1082–1097 (2020).

212. Heyne, G. W. *et al.* A Simple and Reliable Method for Early Pregnancy Detection in Inbred Mice. *J Am Assoc Lab Anim Sci* **54**, 368–371 (2015).

213. McFarlane, L., Truong, V., Palmer, J. S. & Wilhelm, D. Novel PCR Assay for Determining the Genetic Sex of Mice. *Sexual Development* **7**, 207–211 (2013).

214. Musy, M. *et al.* A quantitative method for staging mouse embryos based on limb morphometry. *Development* **145**, (2018).

215. Rouillard, A. D. *et al.* The harmonizome: a collection of processed datasets gathered to serve and mine knowledge about genes and proteins. *Database* **2016**, baw100 (2016).

216. Rossi, G. *et al.* Silencing Nfix rescues muscular dystrophy by delaying muscle regeneration. *Nat Commun* **8**, 1055 (2017).

217. Smith, L. R. & Barton, E. R. SMASH – semi-automatic muscle analysis using segmentation of histology: a MATLAB application. *Skeletal Muscle* **4**, 1–16 (2014).

218. Renier, N. *et al.* iDISCO: A Simple, Rapid Method to Immunolabel Large Tissue Samples for Volume Imaging. *Cell* **159**, 896–910 (2014).

219. Sincennes, M. C., Wang, Y. X. & Rudnicki, M. A. Primary Mouse Myoblast Purification using Magnetic Cell Separation. in *Muscle Stem Cells: Methods and Protocols* (eds. Perdiguero, E. & Cornelison, D.) 41–50 (Springer, New York, NY, 2017). doi:10.1007/978-1-4939-6771-1_3.

220. Patro, R., Duggal, G., Love, M. I., Irizarry, R. A. & Kingsford, C. Salmon provides fast and bias-aware quantification of transcript expression. *Nature Methods* **14**, 417–419 (2017).

221. Zhu, A., Ibrahim, J. G. & Love, M. I. Heavy-tailed prior distributions for sequence count data: removing the noise and preserving large differences. *Bioinformatics* **35**, 2084–2092 (2019).

222. Ashburner, M. *et al.* Gene Ontology: tool for the unification of biology. *Nat Genet* **25**, 25–29 (2000).

223. The Gene Ontology Consortium *et al.* The Gene Ontology knowledgebase in 2023. *Genetics* **224**, iyad031 (2023).

224. Wu, T. *et al.* clusterProfiler 4.0: A universal enrichment tool for interpreting omics data. *The Innovation* **2**, 100141 (2021).

225. Hao, Y. *et al.* Integrated analysis of multimodal single-cell data. *Cell* **184**, 3573-3587.e29 (2021).

226. Germain, P.-L., Lun, A., Garcia Meixide, C., Macnair, W. & Robinson, M. D. Doublet identification in single-cell sequencing data using scDblFinder. *F1000Res* **10**, 979 (2021).

227. Korsunsky, I. *et al.* Fast, sensitive and accurate integration of single-cell data with Harmony. *Nat Methods* **16**, 1289–1296 (2019).

228. Zhou, Y. *et al.* Metascape provides a biologist-oriented resource for the analysis of systems-level datasets. *Nat Commun* **10**, 1523 (2019).

229. Blanco-Carmona, E. Generating publication ready visualizations for Single Cell transcriptomics using SCpubr. 2022.02.28.482303 Preprint at https://doi.org/10.1101/2022.02.28.482303 (2022).

230. Marsh, S., Salmon, M. & Hoffman, P. scCustomize: Custom Visualizations & Functions for Streamlined Analyses of Single Cell Sequencing. Zenodo https://doi.org/10.5281/zenodo.10724532 (2024).

231. Hao, Y. *et al.* Dictionary learning for integrative, multimodal and scalable single-cell analysis. *Nat Biotechnol* **42**, 293–304 (2024).

232. Hafemeister, C. & Satija, R. Normalization and variance stabilization of single-cell RNA-seq data using regularized negative binomial regression. *Genome Biology* **20**, 296 (2019).

233. Choudhary, S. & Satija, R. Comparison and evaluation of statistical error models for scRNA-seq. *Genome Biology* **23**, 27 (2022).

234. Kolberg, L. *et al.* g:Profiler—interoperable web service for functional enrichment analysis and gene identifier mapping (2023 update). *Nucleic Acids Research* **51**, W207–W212 (2023).

235. Pastoret, C. & Sebille, A. mdx mice show progressive weakness and muscle deterioration with age. *Journal of the Neurological Sciences* **129**, 97–105 (1995).

236. Lynch, G. S., Hinkle, R. T., Chamberlain, J. S., Brooks, S. V. & Faulkner, J. A. Force and power output of fast and slow skeletal muscles from mdx mice 6-28 months old. *J Physiol* **535**, 591–600 (2001).

237. Beastrom, N. *et al.* mdx5cv Mice Manifest More Severe Muscle Dysfunction and Diaphragm Force Deficits than Do mdx Mice. *Am J Pathol* **179**, 2464–2474 (2011).

238. Coulton, G. R., Morgan, J. E., Partridge, T. A. & Sloper, J. C. The mdx mouse skeletal muscle myopathy: I. A histological, morphometric and biochemical investigation. *Neuropathol Appl Neurobiol* **14**, 53–70 (1988).

239. Hayes, A. & Williams, D. A. Contractile function and low-intensity exercise effects of old dystrophic (mdx) mice. *Am J Physiol* **274**, C1138-1144 (1998).

240. Stedman, H. H. *et al.* The mdx mouse diaphragm reproduces the degenerative changes of Duchenne muscular dystrophy. *Nature* **352**, 536–539 (1991).

241. Guardiola, O. *et al.* Induction of Acute Skeletal Muscle Regeneration by Cardiotoxin Injection. *JoVE* 54515 (2017) doi:10.3791/54515.

242. Heslop, L., Morgan, J. E. & Partridge, T. A. Evidence for a myogenic stem cell that is exhausted in dystrophic muscle. *Journal of Cell Science* **113**, 2299–2308 (2000).

243. Luz, M. a. M., Marques, M. J. & Santo Neto, H. Impaired regeneration of dystrophin-deficient muscle fibers is caused by exhaustion of myogenic cells. *Braz J Med Biol Res* **35**, 691–695 (2002).

244. Ribeiro, A. F. *et al.* Muscle satellite cells and impaired late stage regeneration in different murine models for muscular dystrophies. *Sci Rep* **9**, 11842 (2019).

245. Kottlors, M. & Kirschner, J. Elevated satellite cell number in Duchenne muscular dystrophy. *Cell Tissue Res* **340**, 541–548 (2010).

246. Ryall, J. G. *et al.* The NAD+-Dependent SIRT1 Deacetylase Translates a Metabolic Switch into Regulatory Epigenetics in Skeletal Muscle Stem Cells. *Cell Stem Cell* **16**, 171–183 (2015).

247. Chemello, F. *et al.* Degenerative and regenerative pathways underlying Duchenne muscular dystrophy revealed by single-nucleus RNA sequencing. *PNAS* **117**, 29691–29701 (2020).

248. Duddy, W. *et al.* Muscular dystrophy in the mdx mouse is a severe myopathy compounded by hypotrophy, hypertrophy and hyperplasia. *Skeletal Muscle* **5**, 1–18 (2015).

249. Boldrin, L., Zammit, P. S. & Morgan, J. E. Satellite cells from dystrophic muscle retain regenerative capacity. *Stem Cell Res* **14**, 20–29 (2015).

250. Bentzinger, C. F., Wang, Y. X. & Rudnicki, M. A. Building Muscle: Molecular Regulation of Myogenesis. *Cold Spring Harb Perspect Biol* **4**, a008342 (2012).

251. Resende, T. P., Andrade, R. P. & Palmeirim, I. Timing Embryo Segmentation: Dynamics and Regulatory Mechanisms of the Vertebrate Segmentation Clock. *Biomed Res Int* **2014**, 718683 (2014).

252. Bajanca, F. *et al.* Integrin α6β1-laminin interactions regulate early myotome formation in the mouse embryo. *Development* **133**, 1635–1644 (2006).

253. Doorenweerd, N. *et al.* Timing and localization of human dystrophin isoform expression provide insights into the cognitive phenotype of Duchenne muscular dystrophy. *Scientific Reports* **7**, 1–12 (2017).

254. Qiu, C. *et al.* Systematic reconstruction of cellular trajectories across mouse embryogenesis. *Nat Genet* **54**, 328–341 (2022).

255. Wilson, D. G. S., Tinker, A. & Iskratsch, T. The role of the dystrophin glycoprotein complex in muscle cell mechanotransduction. *Commun Biol* **5**, 1–18 (2022).

256. Greenbaum, M. P., Iwamori, N., Agno, J. E. & Matzuk, M. M. Mouse TEX14 Is Required for Embryonic Germ Cell Intercellular Bridges but Not Female Fertility. *Biol Reprod* **80**, 449–457 (2009).

257. Aloisio, G. M. *et al.* PAX7 expression defines germline stem cells in the adult testis. *J Clin Invest* **124**, 3929–3944 (2014).

258. Fung, C. W. *et al.* Cell fate determining molecular switches and signaling pathways in Pax7-expressing somitic mesoderm. *Cell Discov* **8**, 1–21 (2022).

259. Rayagiri, S. S. *et al.* Basal lamina remodeling at the skeletal muscle stem cell niche mediates stem cell self-renewal. *Nat Commun* **9**, 1075 (2018).

260. Girardi, F. *et al.* TGFβ signaling curbs cell fusion and muscle regeneration. *Nat Commun* **12**, 750 (2021).

261. Cayouette, M. & Raff, M. Asymmetric segregation of Numb: a mechanism for neural specification from Drosophila to mammals. *Nat Neurosci* **5**, 1265–1269 (2002).

262. Bultje, R. S. *et al.* Mammalian Par3 Regulates Progenitor Cell Asymmetric Division via Notch Signaling in the Developing Neocortex. *Neuron* **63**, 189–202 (2009).

263. Uemura, T., Shepherd, S., Ackerman, L., Jan, L. Y. & Jan, Y. N. numb, a gene required in determination of cell fate during sensory organ formation in Drosophila embryos. *Cell* **58**, 349–360 (1989).

264. Gulino, A., Di Marcotullio, L. & Screpanti, I. The multiple functions of Numb. *Experimental Cell Research* **316**, 900–906 (2010).

265. Gupta-Rossi, N. *et al.* The Adaptor-associated Kinase 1, AAK1, Is a Positive Regulator of the Notch Pathway. *J Biol Chem* **286**, 18720–18730 (2011).

266. McGill, M. A. & McGlade, C. J. Mammalian numb proteins promote Notch1 receptor ubiquitination and degradation of the Notch1 intracellular domain. *J Biol Chem* **278**, 23196–23203 (2003).

267. Ruiz Gómez, M. & Bate, M. Segregation of myogenic lineages in Drosophila requires numb. *Development* **124**, 4857–4866 (1997).

268. Chien, C., Wang, S., Rothenberg, M., Jan, L. Y. & Jan, Y. N. Numb-Associated Kinase Interacts with the Phosphotyrosine Binding Domain of Numb and Antagonizes the Function of Numb In Vivo. *Molecular and Cellular Biology* **18**, 598 (1998).

269. Huang, C., Ji, C. & Wang, J. Current thoughts on cellular functions of numb-associated kinases. *Mol Biol Rep* **50**, 4645–4652 (2023).

270. Sorensen, E. B. & Conner, S. D. AAK1 Regulates Numb Function at an Early Step in Clathrin-Mediated Endocytosis. *Traffic* **9**, 1791–1800 (2008).

271. Giovarelli, M. *et al.* Characterisation of Progressive Skeletal Muscle Fibrosis in the Mdx Mouse Model of Duchenne Muscular Dystrophy: An In Vivo and In Vitro Study. *Int J Mol Sci* **23**, 8735 (2022).

272. Delaney, R. & O'Halloran, K. D. Respiratory performance in Duchenne muscular dystrophy: Clinical manifestations and lessons from animal models. *Experimental Physiology* **109**, 1426–1445 (2024).

273. Bruin, P. F. D. *et al.* Diaphragm thickness and inspiratory strength in patients with Duchenne muscular dystrophy. *Thorax* **52**, 472–475 (1997).

274. Laviola, M., Priori, R., D'Angelo, M. G. & Aliverti, A. Assessment of diaphragmatic thickness by ultrasonography in Duchenne muscular dystrophy (DMD) patients. *PLOS ONE* **13**, e0200582 (2018).

275. Strakova, J. *et al.* Integrative effects of dystrophin loss on metabolic function of the mdx mouse. *Sci Rep* **8**, 13624 (2018).

276. Norris, A. M. *et al.* Studying intramuscular fat deposition and muscle regeneration: insights from a comparative analysis of mouse strains, injury models, and sex differences. *Skeletal Muscle* **14**, 1–19 (2024).

277. Tsonaka, R., Seyer, A., Aartsma-Rus, A. & Spitali, P. Plasma lipidomic analysis shows a disease progression signature in mdx mice. *Sci Rep* **11**, 12993 (2021).

278. Pichavant, C. & Pavlath, G. K. Incidence and severity of myofiber branching with regeneration and aging. *Skeletal Muscle* **4**, 1–11 (2014).

279. Massopust, R. T. *et al.* Lifetime analysis of mdx skeletal muscle reveals a progressive pathology that leads to myofiber loss. *Sci Rep* **10**, 17248 (2020).

280. Faber, R. M., Hall, J. K., Chamberlain, J. S. & Banks, G. B. Myofiber branching rather than myofiber hyperplasia contributes to muscle hypertrophy in mdx mice. *Skeletal Muscle* **4**, 10 (2014).

281. Chan, S., Head, S. I. & Morley, J. W. Branched fibers in dystrophic mdx muscle are associated with a loss of force following lengthening contractions. *American Journal of Physiology-Cell Physiology* **293**, C985–C992 (2007).

282. Branched fibres in old dystrophic mdx muscle are associated with mechanical weakening of the sarcolemma, abnormal Ca2+ transients and a breakdown of Ca2+ homeostasis during fatigue. *Experimental Physiology* **95**, 641–656 (2010).

283. Yanay, N. *et al.* Pax7, Pax3 and Mamstr genes are involved in skeletal muscle impaired regeneration of dy2J/dy2J mouse model of Lama2-CMD. *Human Molecular Genetics* **28**, 3369–3390 (2019).

284. Dinulovic, I., Furrer, R. & Handschin, C. Plasticity of the Muscle Stem Cell Microenvironment. *Adv Exp Med Biol* **1041**, 141–169 (2017).

285. Young, L. V. *et al.* Loss of dystrophin expression in skeletal muscle is associated with senescence of macrophages and endothelial cells. *Am J Physiol Cell Physiol* **321**, C94–C103 (2021).

286. Saito, Y. & Chikenji, T. S. Diverse Roles of Cellular Senescence in Skeletal Muscle Inflammation, Regeneration, and Therapeutics. *Front. Pharmacol.* **12**, (2021).

287. Le Roux, I., Konge, J., Le Cam, L., Flamant, P. & Tajbakhsh, S. Numb is required to prevent p53-dependent senescence following skeletal muscle injury. *Nat Commun* **6**, 8528 (2015).

288. Cardone, N. *et al.* Myopathologic trajectory in Duchenne muscular dystrophy (DMD) reveals lack of regeneration due to senescence in satellite cells. *Acta Neuropathologica Communications* **11**, 167 (2023).

289. Sugihara, H. *et al.* Cellular senescence-mediated exacerbation of Duchenne muscular dystrophy. *Sci Rep* **10**, 16385 (2020).

290. Moiseeva, V. *et al.* Senescence atlas reveals an aged-like inflamed niche that blunts muscle regeneration. *Nature* **613**, 169–178 (2023).

291. Irintchev, A., Zweyer, M. & Wernig, A. Impaired functional and structural recovery after muscle injury in dystrophic mdx mice. *Neuromuscul Disord* **7**, 117–125 (1997).

292. Reimann, J., Irintchev, A. & Wernig, A. Regenerative capacity and the number of satellite cells in soleus muscles of normal and mdx mice. *Neuromuscul Disord* **10**, 276–282 (2000).

293. Hardy, D. *et al.* Comparative Study of Injury Models for Studying Muscle Regeneration in Mice. *PLoS One* **11**, e0147198 (2016).

294. Masuda-Hirata, M. *et al.* Intracellular polarity protein PAR-1 regulates extracellular laminin assembly by regulating the dystroglycan complex. *Genes to Cells* **14**, 835–850 (2009).

295. Anderson, C., Winder, S. J. & Borycki, A.-G. Dystroglycan protein distribution coincides with basement membranes and muscle differentiation during mouse embryogenesis. *Developmental Dynamics* **236**, 2627–2635 (2007).

296. Belanto, J. J. *et al.* Microtubule binding distinguishes dystrophin from utrophin. *Proc Natl Acad Sci U S A* **111**, 5723–5728 (2014).

297. Massouridès, E. *et al.* Dp412e: a novel human embryonic dystrophin isoform induced by BMP4 in early differentiated cells. *Skelet Muscle* **5**, 40 (2015).

298. Molina, T., Fabre, P. & Dumont, N. A. Fibro-adipogenic progenitors in skeletal muscle homeostasis, regeneration and diseases. *Open Biol* **11**, 210110 (2021).

299. Vargas-Franco, D. *et al.* The Notch signaling pathway in skeletal muscle health and disease. *Muscle & Nerve* **66**, 530 (2022).

300. Jiang, C. *et al.* Notch signaling deficiency underlies age-dependent depletion of satellite cells in muscular dystrophy. *Dis Model Mech* **7**, 997–1004 (2014).

301. Sun, Z. *et al.* Bioprinted Notch ligand to function as stem cell niche improves muscle regeneration in dystrophic muscle. *Int J Bioprint* **9**, 711 (2023).

302. Smith, C. A. *et al.* aPKC-mediated phosphorylation regulates asymmetric membrane localization of the cell fate determinant Numb. *EMBO J.* **26**, 468–480 (2007).

303. Nishimura, T. & Kaibuchi, K. Numb Controls Integrin Endocytosis for Directional Cell Migration with aPKC and PAR-3. *Developmental Cell* **13**, 15–28 (2007).

304. Lin, S. *et al.* Brief report: Blockade of Notch signaling in muscle stem cells causes muscular dystrophic phenotype and impaired muscle regeneration. *Stem Cells* **31**, 823–828 (2013).

305. Vieira, N. M. *et al.* Jagged 1 rescues the Duchenne muscular dystrophy phenotype. *Cell* **163**, 1204 (2015).

306. Neveu, G. *et al.* AP-2-Associated Protein Kinase 1 and Cyclin G-Associated Kinase Regulate Hepatitis C Virus Entry and Are Potential Drug Targets. *J Virol* **89**, 4387–4404 (2015).

307. Xin, X. *et al.* Development and therapeutic potential of adaptor-associated kinase 1 inhibitors in human multifaceted diseases. *European Journal of Medicinal Chemistry* **248**, 115102 (2023).

308. Knop, F., Zounarová, A., Šabata, V., Middelkoop, T. C. & Macůrková, M. Caenorhabditis elegans SEL-5/AAK1 regulates cell migration and cell outgrowth independently of its kinase activity. *eLife* **13**, e91054 (2024).

309. Choi, H. Y., Seok, J., Kang, G.-H., Lim, K. M. & Cho, S.-G. The role of NUMB/NUMB isoforms in cancer stem cells. *BMB Rep* **54**, 335–343 (2021).

310. Dho, S. E., French, M. B., Woods, S. A. & McGlade, C. J. Characterization of four mammalian numb protein isoforms. Identification of cytoplasmic and membrane-associated variants of the phosphotyrosine binding domain. *J. Biol. Chem.* **274**, 33097–33104 (1999).

311. Karaczyn, A. *et al.* Two novel human NUMB isoforms provide a potential link between development and cancer. *Neural Dev* **5**, 1–15 (2010).

312. Arreguin, A. J., Shao, Z. & Colognato, H. Dmd mdx mice have defective oligodendrogenesis, delayed myelin compaction and persistent hypomyelination. *Dis Model Mech* **17**, dmm050115 (2024).

313. Chen, H.-C. *et al.* Utrophin Compensates dystrophin Loss during Mouse Spermatogenesis. *Sci Rep* **7**, 7372 (2017).

314. Kariyawasam, D. *et al.* Incidence of Duchenne muscular dystrophy in the modern era; an Australian study. *Eur J Hum Genet* **30**, 1398–1404 (2022).

315. Granata, A. L. *et al.* Gamma irradiation can reduce muscle damage in mdx dystrophic mice. *Acta Neuropathol* **96**, 564–568 (1998).

316. Rossi, G. *et al.* Silencing Nfix rescues muscular dystrophy by delaying muscle regeneration. *Nat Commun* **8**, 1055 (2017).

317. Boyer, J. G. *et al.* Depletion of skeletal muscle satellite cells attenuates pathology in muscular dystrophy. *Nat Commun* **13**, 2940 (2022).

318. Petrany, M. J., Song, T., Sadayappan, S. & Millay, D. P. Myocyte-derived Myomaker expression is required for regenerative fusion but exacerbates membrane instability in dystrophic myofibers. *JCI Insight* **5**, e136095 (2020).

319. Tang, A. & Yokota, T. Is Duchenne gene therapy a suitable treatment despite its immunogenic class effect? *Expert Opin Drug Saf* 1–17 (2024) doi:10.1080/14740338.2024.2447072.

320. Barraza-Flores, P., Bates, C. R., Oliveira-Santos, A. & Burkin, D. J. Laminin and Integrin in LAMA2-Related Congenital Muscular Dystrophy: From Disease to Therapeutics. *Front Mol Neurosci* **13**, 1 (2020).

321. Brancaccio, A. A molecular overview of the primary dystroglycanopathies. *J Cell Mol Med* **23**, 3058–3062 (2019).

322. Packer, D. & Martin, P. T. Micro-laminin gene therapy can function as an inhibitor of muscle disease in the dyW mouse model of MDC1A. *Mol Ther Methods Clin Dev* **21**, 274–287 (2021).

323. Moat, S. J., Bradley, D. M., Salmon, R., Clarke, A. & Hartley, L. Newborn bloodspot screening for Duchenne muscular dystrophy: 21 years experience in Wales (UK). *Eur J Hum Genet* **21**, 1049–1053 (2013).

Chapter 6: Appendix

6.1 Supplemental Figures

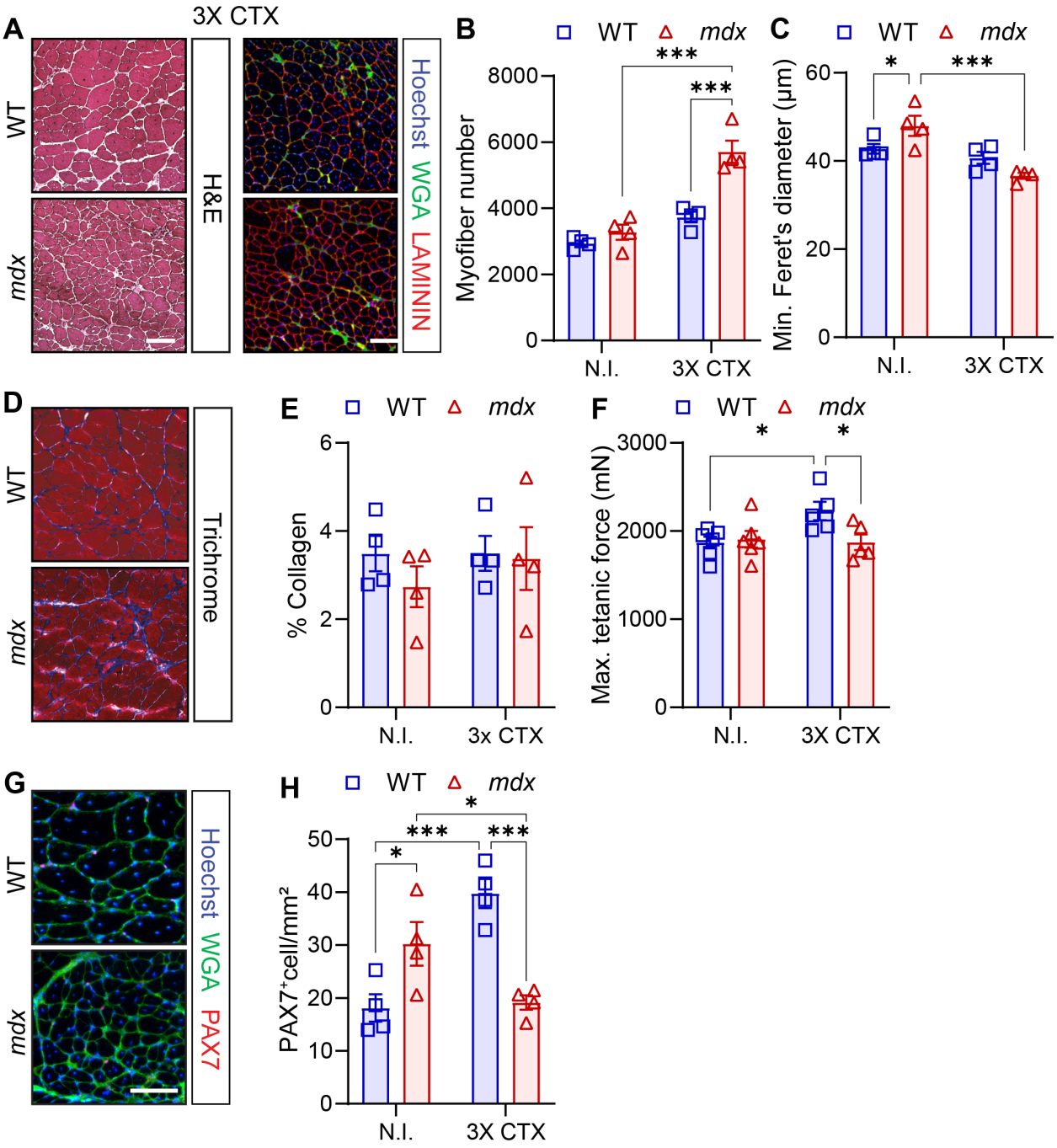

Figure S1 Disrupted regeneration after triple cardiotoxin-injury of *mdx tibialis anterior*.
A Representative hematoxylin and eosin (H&E) and immunofluorescence images of transversal sections of non-injured (N.I.) and triple cardiotoxin (CTX)-injured (3X CTX) *tibialis anterior* (TA) muscle from wild type (WT) and *mdx* mice. Re-injury conduced every 21 days for a total experiment length of 63 days (3X CTX). LAMININ (red) delineates the myofibers, WGA (green) stains the connective tissues and Hoechst (blue) labels the nuclei. **B** Cross-section TA myofiber quantification after 3X CTX compared to N.I. **C** Mean WT and *mdx* TA myofiber size using the minimum Feret's diameter in N.I. and 3X CTX muscles. **D** Representative Trichrome staining images of N.I. and 3X CTX WT and *mdx* TA muscle cross-sections. **E** Quantification of collagen content (blue staining) in Trichrome-stained TA muscle sections. **F** Maximum tetanic force of TA muscle from N.I. and 3X CTX WT and *mdx* mice. **G** Representative immunofluorescence images of WT and *mdx* N.I. and 3X CTX TA cross-sections from WT and *mdx* mice. PAX7 (red) marks the muscle stem cells (MuSCs), WGA (green) stains the connective tissues and Hoechst (blue) labels the nuclei. **H** PAX7-expressing MuSC number per mm² on TA cross-sections. n = 4 mice/genotype. Data presented as mean values ± SEM. Two-way ANOVA corrected for multiple comparisons using Sidak's test (*$p < 0.05$; **$p < 0.01$; ***$p < 0.001$).

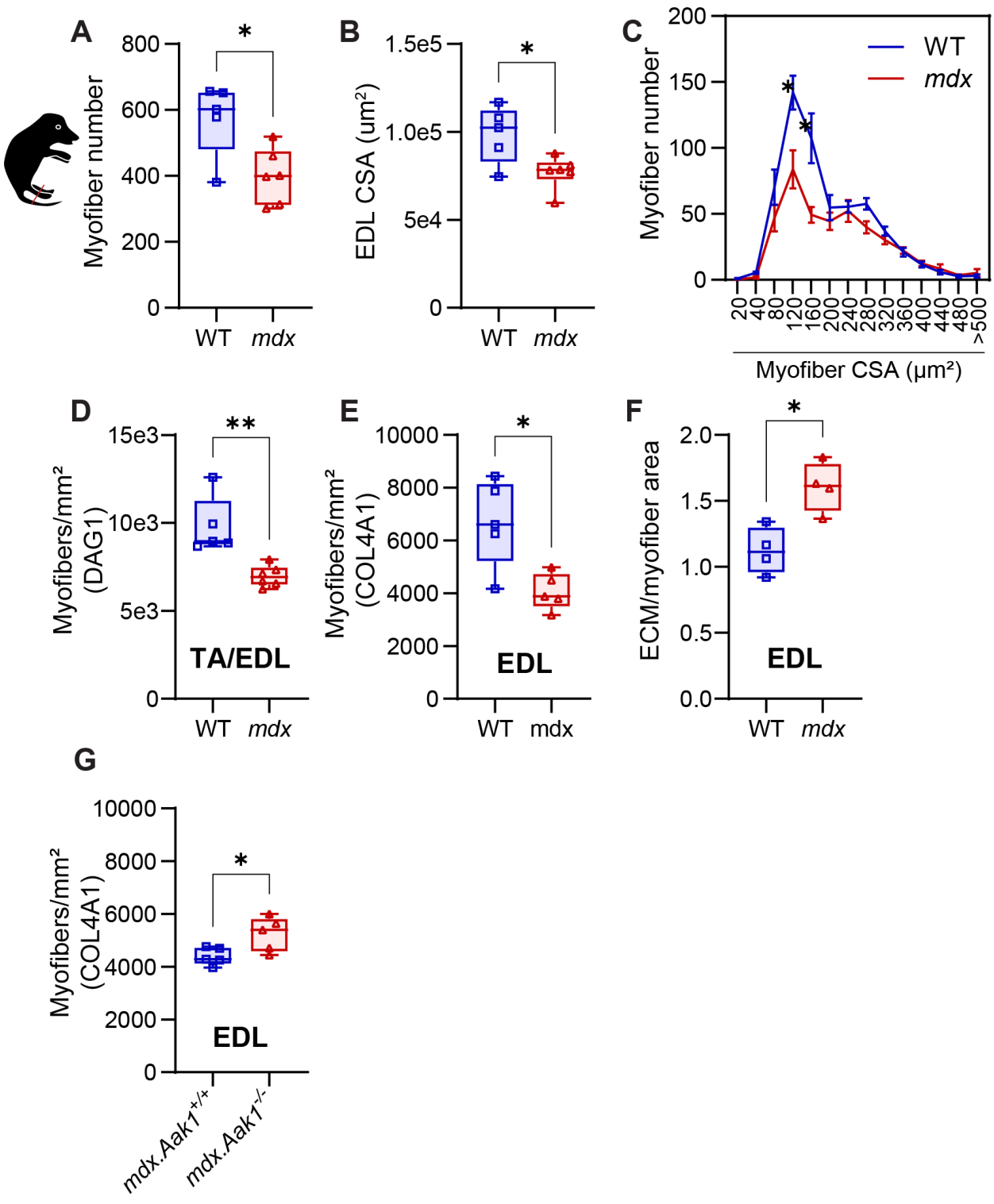
A
Myofiber number
800
600
400
200
0
WT
mdx
*
B
EDL CSA (um²)
1.5e5
1.0e5
5e4
0
WT
mdx
*
C
Myofiber number
200
150
100
50
0
WT
mdx
20
40
80
120
160
200
240
280
320
360
400
440
480
>500
Myofiber CSA (µm²)
D
Myofibers/mm²
(DAG1)
15e3
10e3
5e3
0
TA/EDL
WT
mdx
**
E
Myofibers/mm²
(COL4A1)
10000
8000
6000
4000
2000
0
EDL
WT
mdx
*
F
ECM/myofiber area
2.0
1.5
1.0
0.5
0.0
EDL
WT
mdx
*
G
Myofibers/mm²
(COL4A1)
10000
8000
6000
4000
2000
0
EDL
mdx.Aak1+/+
mdx.Aak1-/-
*

Figure S2 Fewer myofibers and decreased myofiber density in E17.5 *mdx* muscle.
A,B Total number of myofibers (A) and cross-section area (CSA; μm^2) (B) enumerated from wild type (WT) and *mdx extensor digitorum longus* (EDL) cross-sections at E17.5 based on COL4A1 staining. **C** Size distribution of E17.5 myofibers using myofiber CSA (μm^2) based on COL4A1 staining. n=5 for WT and n=6 for *mdx*. **D,E** Myofiber density as number of myofibers per mm^2 using DAG1 (D; EDL/*tibialis anterior* [TA]) and COL4A1 (E; EDL) staining of WT and *mdx* fetal E17.5 muscle. **F** Density of myofibers presented as ECM/myofiber area. **G** Myofiber density as the number of myofibers per mm^2 using COL4A1 staining of the *mdx.Aak1*$^{+/+}$ and *mdx.Aak1*$^{-/-}$ EDL muscle. Statistical analysis performed using unpaired t-tests (A,B,E-G) and two-way ANOVA followed by Sidak's test for multiple comparisons (C) (*$p < 0.05$). Box plot whiskers indicate the maximum and minimum values. Related to **Figure 4.6** and **Figure 4.19**.

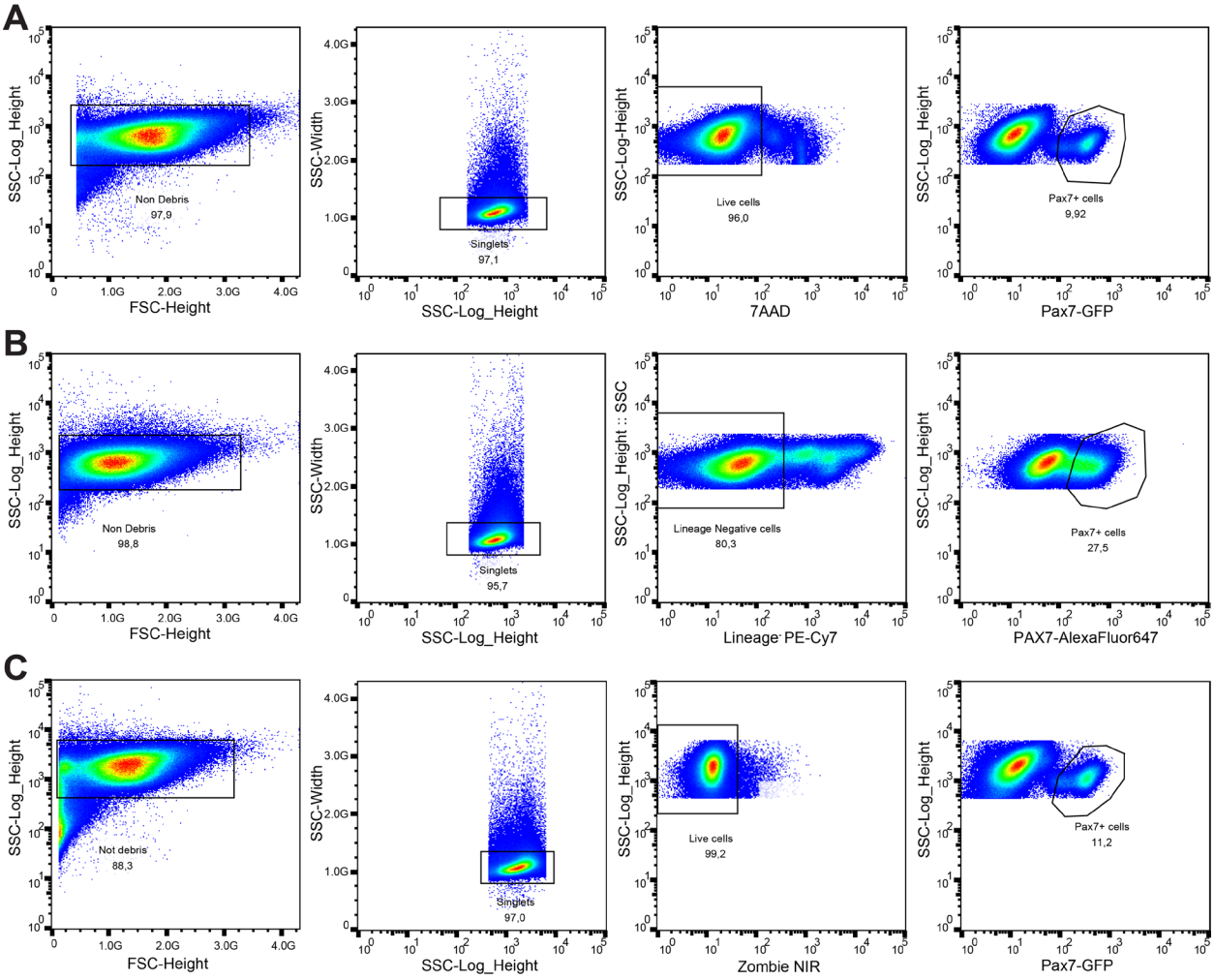

Figure S3 Fetal MuSC isolation strategy.

A Experimental design for fluorescence sorting GFP$^+$ freshly isolated (Fi) and activated (A) and fetal (f) muscle stem cells (MuSCs) from the wild type (WT) and *mdx Pax7-nGFP* mice. **B** Sort strategy to isolate formaldehyde-fixed fMuSCs using PAX7-Alexa Fluor 647 staining. **C** Isolation of formaldehyde-fixed GFP$^+$ fMuSCs from *Pax7-nGFP* fetal tissue.

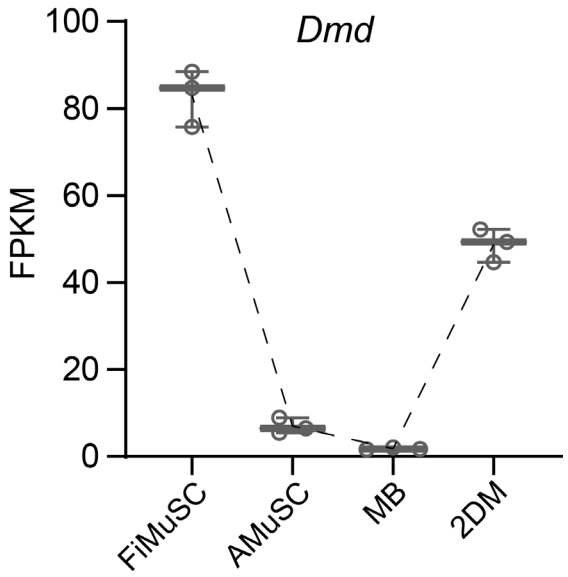

Figure S4 FPKM of *Dmd* gene from bulk RNA-seq of myogenic cells.
Libraries were generated in biological duplicate from freshly isolated MuSCs (FiMuSC), activated MuSCs from 3 days following CTX-injury (AMuSC), cultured myoblasts (MB) and two-day differentiated myotubes (2DM). Related to **Figure 3.12.**

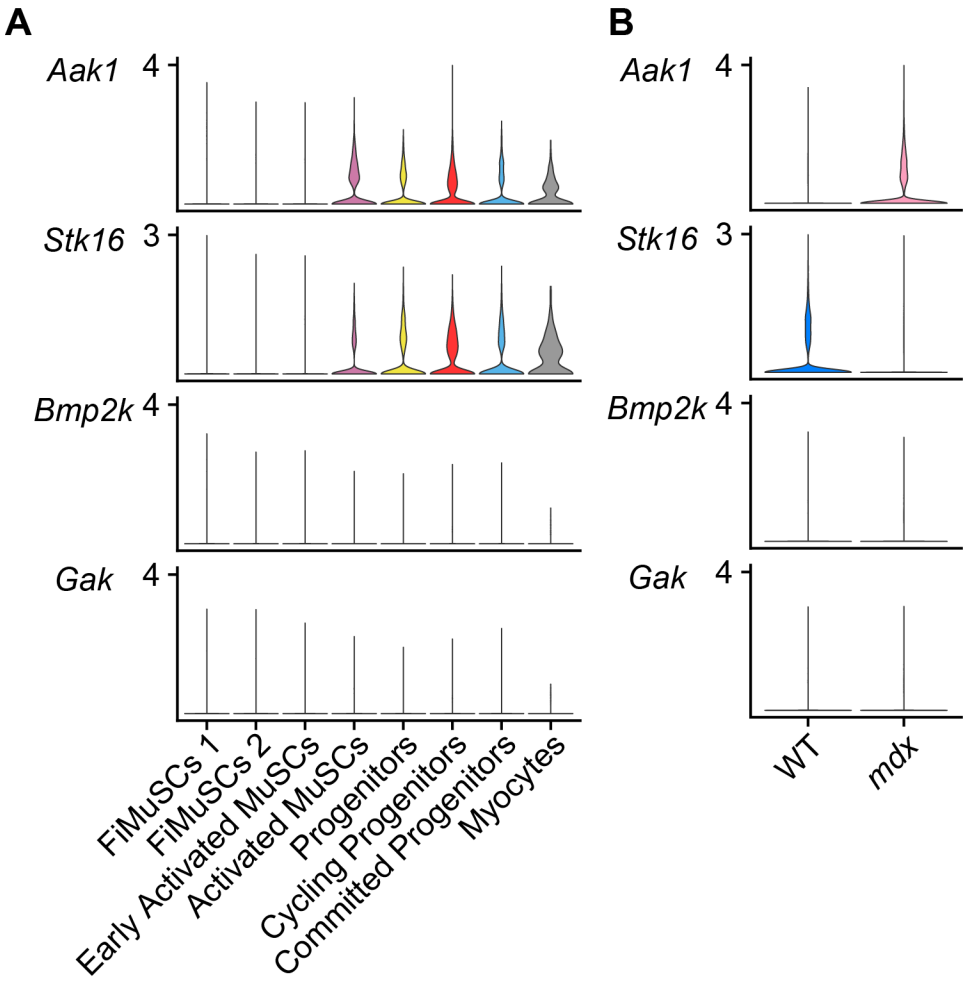

Figure S5 Postnatal myogenic cells express NUMB-associated kinases.
A-B Violin plot depicting expression of the four mammalian NUMB-associated kinase (NAK) genes in single cell RNA-sequencing libraries and split by cluster (**A**) or genotype (**B**).

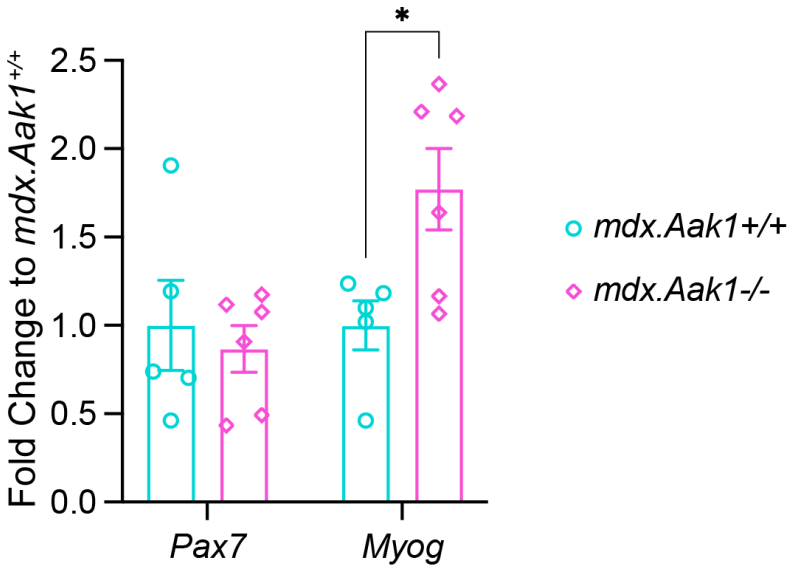

Figure S6 Increased expression of *Myog* RNA in *mdx.Aak1*$^{-/-}$ GFP^{+} fMuSCs.
RT-qPCR analysis of *mdx.Aak1*$^{+/+}$ and *mdx.Aak1*$^{-/-}$ GFP^{+} fMuSCs isolated from E17.5 *Pax7-nGFP* fetal limbs. Data presented as fold change to *mdx.Aak1*$^{+/+}$. Error bars represent SEM. *mdx.Aak1*$^{+/+}$ n=5 and *mdx.Aak1*$^{-/-}$ n=6. Data analyzed using two-way ANOVA corrected for multiple comparisons using Sidak's test, where * $p < 0.05$.

6.2 List of Supplemental Data Files

Data File S1 Differential gene expression testing of bulk RNA-seq libraries.

Data File S2 GO term analysis of postnatal bulk RNAseq libraries.

Data File S3 Cluster markers for postnatal MuSC libraries.

Data File S4 Cluster markers for combined fetal MuSC libraries.

Data File S5 Myogenic cell subset cluster markers for combined fetal MuSC libraries.

Data File S6 Differentially expressed genes between wild type and *mdx* fetal libraries.

Data File S7 GO terms identified from downregulated genes in *mdx* fetal MuSC libraries.

6.3 Immunofluorescence Labelling of Skeletal Muscle in Development, Regeneration, and Disease

Marie E. Esper[1,2], Kasun Kodippili[1,2], Michael A. Rudnicki[1,2*]

1. The Sprott Centre for Stem Cell Research
   Regenerative Medicine Program
   Ottawa Hospital Research Institute
   Ottawa, Ontario
   Canada, K1H 8L6

2. Department of Cellular and Molecular Medicine
   Faculty of Medicine, University of Ottawa
   Ottawa, Ontario
   Canada, K1H 8M5

*Corresponding author: mrudnicki@ohri.ca

Abstract

Skeletal muscle is composed of long multinucleated cells, termed myofibers, that are formed through the activation and differentiation of resident muscle stem cells, called satellite cells. In healthy individuals, skeletal muscle enables voluntary locomotion, while also playing a role in energy metabolism and thermoregulation. As skeletal muscle is integral to everyday processes, perturbations to skeletal muscle function can have devastating consequences. Here we describe an integral tool in biomedical research of skeletal muscle regeneration and disease, the immunofluorescence staining of myogenic cells. We highlight useful techniques for immunostaining myogenic cells, and we list validated antibodies for the staining of muscle proteins across different species and multiple developmental time points. This includes methods for unmasking antigens following formaldehyde fixation (using Myosin Heavy Chain staining as an example), and practices for preserving endogenous fluorescent proteins by cardiac perfusion fixation.

Key Words: Skeletal Muscle, Satellite Cell, Muscle Stem Cell, Immunohistochemistry, Immunofluorescence, Regeneration, Differentiation, Myogenesis, Antibodies, Myosin Heavy Chain, Pax7, Heat Induced Antigen Retrieval

1. Introduction

Skeletal muscle is the most abundant tissue in the human body, accounting for approximately 40% of total body mass. It is critical for many bodily functions, such as voluntary locomotion, force generation and energy metabolism. It also exhibits remarkable plasticity and regenerative potential [A1]. Unsurprisingly, diseases that affect skeletal muscle function and regeneration can profoundly impact health and well-being, and are common focuses of biomedical research [A2].

The study of skeletal muscle frequently relies on the visualization of myogenic cells by immunofluorescent staining. Markers of myogenic cells that are expressed during development and regeneration are also evolutionarily conserved. In mammals, somite-derived embryonic muscle stem cells (eMuSCs) expressing Pax3 and Pax7 give rise to all skeletal muscles of the trunk and limbs. Pax7 expression is maintained in a population of eMuSCs that give rise to adult muscle stem cells, while Pax3 is only maintained in a small subpopulation of MuSCs [A3]. Following injury or in diseased conditions, quiescent MuSCs become activated and enter the cell cycle and differentiate in a process reminiscent of muscle development. During differentiation, progenitor cells transiently amplify as myoblasts, differentiate into mononuclear myocytes and either fuse to damaged myofibers or form new myofibers to facilitate muscle development or regeneration. Both processes are regulated by the hierarchical expression of the muscle regulatory factors (MRFs) Myf5, MyoD, Myogenin and Mrf4, while terminally differentiated myofibers are identified by the expression of contractile proteins such as Myosin Heavy Chain (MyHC) and Actin [A3].

The immunofluorescence labelling of eMuSCs, MuSCs and derivative cells is an important tool for studying myogenesis in the context of regeneration and disease. However, probing new antigens and testing new antibodies is time consuming and expensive. Moreover, many

commercially available antibodies do not robustly react with their target antigen, or do not recognize the target antigen following formaldehyde tissue fixation. This is problematic when formaldehyde-fixation is required, such as for paraffin embedding or to preserve the location of endogenous proteins in transgenic animals and MuSC transplantation assays [A4].

Antigens however can be routinely recovered using heat induced antigen retrieval (HIAR). Interestingly, while heating is absolutely necessary for non-enzymatic antigen retrieval, the pH and composition of the retrieval solution can profoundly impact the success of different antibody stains [A5]. For example, commonly used antibodies raised against different Myosin Heavy Chain (MyHC) isotypes are highly specific when staining fresh or methanol fixed mouse tissue, but do not recognize their antigens following cardiac perfusion fixation. HIAR with conventional citrate buffer pH6 retrieves the MyHCI antigen recognized by the monoclonal antibody BAF8 but causes nonspecific tissue binding of the antibody clones SC-71 and BF-F3 which normally recognize MyHCIIa and MyHCIIb respectively. However, when the citrate buffer is adjusted to pH 7, all three monoclonal antibodies are highly specific for their target antigens (Fig. A4). The current chapter describes techniques for the immunofluorescence labelling of myogenic cells; methods for preserving endogenously expressed fluorophores in transgenic mouse tissue; and lists useful reagents and validated antibodies for the study of mouse, dog, and human skeletal muscle tissue.

2. Materials

2.1 Cardiac Perfusion Fixation

1. Paraformaldehyde (PFA) 4%: add 100 mL of 10x PBS and 800 mL of distilled deionized H_2O (ddH_2O) into a glass beaker. While stirring, add 40 g of PFA powder and 10 drops of 2N NaOH. Heat the solution to 60°C while stirring to dissolve the powder but do not let the solution heat above 70°C. Adjust the pH to 7.4 using HCl and adjust the volume to 1 L using ddH_2O. Filter the solution through a 0.2 μM filter and store at 4°C for up to one month or freeze aliquots (*see* **Note** 1).
2. PBS 1x, pH 7.4 stored at 4°C.
3. Anesthesia/euthanasia agent: Euthanyl (sodium pentobarbital) at >120 mg/kg for mouse administered by intraperitoneal injection to euthanize mice (*see* **Note** 2).
4. 70% Ethanol.
5. 15% sucrose solutions in PBS 1x stored at 4°C.
6. 30% sucrose solutions in PBS 1x stored at 4°C.
7. Needles (25 gauge for mouse).
8. Surgical instruments (hemostat, sharp dissection scissors, Vannas spring scissors, forceps).
9. Peristaltic pump and silicon tubing (we use MCP3000 series 13-310-661; Fisher Scientific) (*see* **Note** 3).
10. Chemical fume hood.
11. Masking tape.
12. Large weighing dish.
13. 15 mL Falcon tubes.

2.2 Immersion Fixation

1. PFA 4%: refer to section 2.1 (*see* **Note** 1).
2. PBS 1x, pH 7.4 stored at 4℃.
3. 70% Ethanol.
4. Dissection instruments (sharp dissection scissors, Vannas spring scissors, forceps, fine forceps).
5. 15 mL Falcon tubes.

2.2 Tissue Cryopreservation, Embedding and Sectioning

1. Tissue-Tek OCT compound.
2. Tinfoil cryomold (*see* **Note** 4).
3. Liquid nitrogen.
4. 2-methylbutane.
5. Dry ice.
6. Superfrost Microscope Slides.
7. Cryostat.
8. Slide box.

2.3 Deparaffinization of Paraffin Sections (*see* **Note** 5) (*see* **Note** 6)

1. Xylene.
2. 100%, 95%, 70% and 50% Ethanol.
3. ddH_2O.
4. Staining jars.

2.4 Antigen Retrieval

1. Citrate Buffer (10 mM sodium citrate, 0.05% Tween 20, pH 6 or pH 7) (*see* **Note** 7): dissolve 2.94 g of Tri-sodium citrate (dihydrate) in 900 mL of ddH_2O by mixing. Adjust to pH 6 or 7 using 2M HCl. Add 0.5 mL of Tween 20 and adjust to 1 L total volume using ddH_2O. Store at room temperature for short term use or at 4°C for longer than one month.
2. Tris-EDTA Buffer (10 mM Tris Base, 1 mM EDTA, 0.05% Tween 20, pH 9) (*see* **Note** 8): dissolve 1.21 g Tris Base and 0.37 g of EDTA in 900 mL of ddH_2O by mixing. Adjust to pH 9 using 2M NaOH. Add 0.5 mL of Tween 20 and adjust volume to 1 L. Store at room temperature or at 4°C for longer than one month.
3. Autoclavable staining jar.
4. Pressure cooker (and rack) that reaches 12 psi (*see* **Note** 9).

2.5 Immunofluorescence Staining

1. PFA 4%: refer to section 2.1 (*see* **Note** 10).
2. PBS 1x (*see* **Note** 11).
3. Hydrophobic PAP pen (*see* **Note** 12).
4. Mouse on Mouse (M.O.M.) blocking reagent (*see* **Note** 13).
5. TrueBlack Lipofuscin Autofluorescence Quencher (*see* **Note** 14).
6. Blocking solution: 5% goat serum, 2% bovine serum albumin (BSA) in 1x PBS (0.22 µm syringe filtered) (*see* **Note** 15) (*see* **Note** 16).
7. Permeabilization solution: 0.1 M Glycine, 0.1% Triton X-100, in PBS 1x (0.22µm syringe filter) (*see* **Note** 13).
8. Primary antibodies (see Table 2) (*see* **Note** 17).
9. Cross absorbed fluorescence conjugated secondary antibodies (*see* **Note** 18).
10. DAPI (4',6-diaminidino-phenylindole dihydrochloride).

11. Aqueous mounting medium (*see* **Note** 19).

12. Glass coverslip (#1.5).

13. Clear nail varnish.

14. Epifluorescence microscope.

3. Methods

Extensive formaldehyde fixation of tissue prevents some antibodies from recognizing their target antigens, making immunofluorescence staining of fresh frozen tissue sections the simplest method for examining myogenic cells. In this workflow, tissue sections are briefly fixed prior to immunostaining, or fixation is omitted (Fig. A1A) (*see* **Note** 10). However, when formaldehyde fixation by cardiac perfusion fixation (Fig.A1B) or by immersion fixation (Fig. A1C) is necessary (either to preserve the location of endogenous fluorescent proteins or when embedding tissue in paraffin) heat-induced antigen retrieval (HIAR) can effectively retrieve antigens while preserving tissue morphology. Table A1 summarizes the tissue processing and embedding strategies that best suit most myogenic samples. Table A2 lists validated antibodies for the study of myogenic antigens and the appropriate HIAR method when required. Finally, the workflow from tissue processing to immunostaining of myogenic cells is schematically represented in Fig. A1. Sample images are provided to illustrate immunofluorescence staining of common myogenic markers (Fig. A3) and the effectiveness of HIAR on retrieving the Myosin Heavy Chain epitopes from formaldehyde-fixed tissues (Fig. A4). While this chapter covers the processing and staining of paraffin tissue sections, the embedding and sectioning steps are not described.

3.1 Cryopreservation of Muscle Tissue

3.1.1. Harvesting and Cryopreservation of Fresh Tissue in OCT (Fig. A1A)

1. Perform all animal experiments in accordance with your institution's animal care and usage protocols and guidelines. We use CO_2 or isoflurane followed by cervical dislocation for mouse euthanization.
2. Wet the animal's fur by spraying 70% ethanol.
3. Harvest muscles, embed in Tissue-Tek OCT compound, and freeze in 2-methylbutane cooled in liquid nitrogen (*see* **Note** 20). To prevent cracking, remove the tissue block from the 2-methylbutane before the OCT completely freezes and place it on dry ice. Store embedded tissues at -80°C.
4. Using a cryostat, section the OCT-embedded tissue (perpendicular to the direction in which the myofibers traverse) at 10 μm thickness, and then carefully transfer the section onto a SuperFrost microscope slide. Proceed directly to immunostaining or store the slides at -20°C.

3.1.2 Cardiac Perfusion Fixation and Cryopreservation of Mouse Tissue in OCT (Fig A1B)

1. Set up peristaltic pump in a chemical fume hood with a 25-gauge needle affixed to silicon tubing. Run ddH_2O through the pump tubing to clear it out, then switch to collecting tube to ice cold PBS. Set the machine to 48.5 RPMs (~4 mL/min) and pause the PBS flow.
2. Anesthetize or euthanize the animal according to your institution standard operation procedures and confirm by loss of pedal withdraw. We administer euthanyl (sodium pentobarbital) at >120mg/kg by intraperitoneal injection. Place the animal on a large weighing dish in a supine position and tape down the limbs (Fig. A2A). This allows for safe collection of the fixative.
3. Spray the mouse with 70% ethanol.

4. Lift the skin at the sternum using blunt forceps and create a lateral incision below the rib cage using sharp dissection scissors (Fig. A2A). Hold the sternum with forceps and cut laterally to expose the diaphragm (Fig. A2B). If the liver adheres to the body wall, gently push it downwards with blunt forceps and avoid piercing it. Cut into the rib cage, but do not cut the lungs.
5. Cut back the diaphragm using Vannus spring scissors and expose the plural cavity and heart (Fig. A2C). Clamp the sternum using a hemostat and rest it over the animal's head. Gently remove connective tissue from around the heart.
6. Locate the left ventricle and right atrium. The right site of the heart will be a deeper red (Fig. A2C). Confirm there are no bubbles in the perfusion tubing and that the machine is paused. Gently insert the needle into the bottom of the left ventricle pointing towards the left atrium. The needle should only be inserted to directly above the bevel to prevent it from puncturing the left atrium or right ventricle, which will detrimentally impact fixation. Affixing tape directly above the bevel can prevent the needle from being inserted too deeply.
7. Using Vannas spring scissors, create a small incision in the right atrium. Deep red blood should immediately drain into the chest cavity (Fig. A2D).
8. Turn on the perfusion machine and flush the animal with ice cold PBS until the buffer leaving the animal is no longer red and the liver lightens from deep red to pink (approximately 20-30 mL of PBS per mouse) (Fig. A2E). Turn off the machine and switch tubing to ice cold 4% PFA and turn it back on. Perfuse the mouse for 10-15 min (approximately 50 mL of 4% PFA). The liver and tail should become stiff.

9. Harvest the hind limb muscle and immerse them in 2% PFA overnight at 4℃ (*see* **Note** 21).
10. Wash muscle in PBS three times for 5 min.
11. Prepare sucrose gradient by placing 30% sucrose in a falcon tube. Break the end of a serological pipet and gently place 15% sucrose above the 30% sucrose in the same tube. Two separate layers should be easily observed.
12. Gently place the fixed muscle at the top of the sucrose gradient and wait until the muscle sinks to the bottom of the tube before embedding. The muscles can be left in sucrose overnight, but no longer than 24 h, as this can detrimentally impact the tissue.
13. Remove the muscle from sucrose and gently tap dry with Kim wipe. Embed the muscle in OCT and let it rest for 1 min.
14. Freeze the muscle in 2-methylbutane cooled in liquid nitrogen (*see* **Note** 16). Remove the tissue block from the 2-methylbutane before the OCT completely freezes to prevent cracking. Place the tissue block on dry ice. Store the embedded tissue at -80℃.
15. Using a cryostat, section the OCT-embedded muscle (perpendicular to the direction of myofibers) at 10 μm thickness and carefully transfer the sections onto a SuperFrost microscope slide. Proceed directly to immunostaining or store the slides at -20℃.

3.1.3 Immersion Fixation for Paraffin Embedding

A detailed description of paraffin embedding and sectioning is beyond the scope of this chapter. However, there are numerous readily available resources online for more information, and many institutions provide histology core services that routinely perform paraffin embedding for a nominal fee.

1. Euthanize the animal according to your institution's animal care and usage protocols and guidelines. We use CO_2 or isoflurane followed by cervical dislocation for mouse euthanasia.
2. Sterilize and wet the animal's fur by spraying 70% ethanol.
3. Harvest muscle or embryos. To isolate embryos, remove the uterine lining, the yolk sac, and the amniotic sac. If necessary, save the yolk sac or placenta for genotyping, as both are derived from embryo and not maternal DNA.
4. Wash tissues 3 times for 5 min in PBS.
5. Fix muscles or E9.5-E11.5 embryos for 24 to 48 h in 4% PFA depending on tissue size. For embryos older than E11.5, remove the head prior to tissue fixation to help with penetration of the PFA (*see* **Note** 22).
6. Wash tissues 3 times for 5 min in PBS.
7. Consult your institution's histology core services for paraffin embedding and sectioning.

3.2 Heat Induced Antigen Retrieval

Refer to Table 2 for the appropriate antigen retrieval solution based on the selected antibody panel (*see* **Note** 7) (*see* **Note** 23). If the antibody is not listed in Table 2 and does not recognize its target with conventional immunostaining, different pH and buffer combinations can be tested with HIAR.

1. Insert the metal rack into the pressure cooker pot and fill with enough ddH_2O to reach the rack. Fill an autoclavable staining jar with the appropriate antigen retrieval solution. With a loosely fitted lid, place the jar atop the pressure cooker rack and preheat the ddH_2O and antigen retrieval solution (*see* **Note** 9).
2. Perform the appropriate slide preparatory step listed below.

a. Paraffin sections: deparaffinize slides by sequential immersion in jars containing the following chemicals (Fig. A1C) (*see* **Note** 6).
    i. Xylene 10 min.
    ii. 100% Ethanol, 2 x 10 min.
    iii. 95%, 70% 50% ethanol, 5 min each.
    iv. ddH_2O, 1 min.
    v. Place slides in the jar containing preheated antigen retrieval solution.
b. Fixed frozen (Fig. A1B): air dry slides at room temperature for 5 min or longer to ensure there is no residual moisture (*see* **Note** 24). Place slides in the jar containing preheated antigen retrieval solution.

3. With the staining jar atop the rack, set the pressure cooker to 12 psi (or max) for 5-15 min. The time can be adjusted, but 10 min is routinely sufficient (*see* **Note** 25).
4. When the pressure cooker is sufficiently cooled to handle the staining jar safely, remove the jar from the pressure cooker. Gently run tap water into the jar for 2 min. Place the slides in PBS for 5 min at room temperature.
5. Remove the slides, one at a time, from the water and gently tap them. It is important that the tissues do not dry out (residual PBS should still surround the tissue sections). Use a Kim-wipe to remove any moisture where the hydrophobic barrier will be applied. Using a PAP pen, surround the tissues and cover the slide in PBS. If the glass slide is wet, the hydrophobic barrier will not adhere properly.
6. Proceed directly to permeabilization in the immunofluorescence staining section (steps 5-15). Do not fix the tissues again, and do not let the tissues dry out.

3.3 Immunofluorescence Staining

Immunofluorescence staining is effective for examining multiple antigens simultaneously (*see* **Note** 27) (*see* **Note** 23). Consult Table 2 for primary antibody concentrations and the corresponding immunostaining method. If Table 2 indicates an antibody does not work following formaldehyde fixation and HIAR is not performed, skip tissue fixation (step 3-4) and proceed with permeabilization. Select secondary antibodies that are compatible with the epifluorescence or confocal microscope available at your institution (*see* **Note** 17). All steps are performed at room temperature unless otherwise indicated.

1. Remove slides from the freezer and let them air dry for 5 min. Ensure there is no residual moisture before beginning immunostaining.
2. Surround tissue sections with a hydrophobic barrier using a PAP pen.
3. Cover tissues with 4% PFA and incubate for 5 min (*see* **Note** 10).
4. Aspirate PFA and wash three times with PBS for 5 min.
5. Incubate slides in permeabilization buffer for 10 min (*see* **Note** 26).
6. Wash three times with PBS for 5 min if using TrueBlack, otherwise proceed directly to blocking (*see* **Note** 14).
7. (*Optional*) Treat slides with TrueBlack autofluorescence quencher. Dilute 20x Trueblack in 70% ethanol and apply generously to the slide for 30 s and ensure the tissues do not dry out. It is okay if residual buffer is left on the slide when applying TrueBlack. Wash slides three times with PBS for 5 min, ensuring no black remains in PBS when done. Do not use reagents containing detergents (*i.e*. Triton X-100 or Tween 20) for the remainder of the protocol.

8. Cover the slides in blocking solution and incubate for at least 1 h at room temperature. Include M.O.M. blocking reagent 1:40 when staining mouse tissue with antibodies raised in mouse (*see* **Note** 13) (*see* **Note** 27).
9. Dilute primary antibodies in blocking solution (see Table 2 for antibody dilutions). It is acceptable to dilute antibodies in hybridoma supernatant when targeting multiple antigens.
10. Aspirate the blocking buffer and cover slide with the primary antibody solution without washing. Incubate the slides overnight at 4°C (*see* **Note** 28).
11. Wash three times with PBS for 5 min.
12. Cover slides with secondary antibodies diluted in blocking buffer for 1 h at room temperature in the dark (*see* **Note** 17). Keep slides in the dark for the remainder of protocol.
13. Wash slides three times with PBS for 5 min.
14. Incubate with 1 μg/mL DAPI diluted in PBS for 5 min.
15. Wash once in PBS for 5 min.
16. Aspirate PBS and place 1-2 drops of mounting media (*see* **Note** 19). Carefully place a coverslip on the slide. Take care to avoid introducing air bubbles. Let the slides dry in the dark for a 1-2 h before sealing the slides with clear nail polish. Store the slides at 4°C and visualize within 2 weeks.

4. Notes

1. Personal protective equipment and a chemical fume hood are required to safely handle PFA. Make sure to consult the available MSDS. PFA 8% or 16% can also be purchased and diluted to 4% with 1x PBS (for example, 10 mL 8% PFA, 2 mL 10x PBS, 8 mL ddH_2O).
2. All animal protocols must be approved by your institute's animal care committee. We use Euthanyl (sodium pentobarbital) at >120mg/kg administered by intraperitoneal injection to

euthanize mice. Euthanyl is a controlled substance and must be used according to your institution's standard operating procedures and approved animal protocols. Ketamine/xylazine mixtures can also be used for anesthesia.

3. Syringes connected to silicone pump tubing can be used for cardiac perfusion fixation as an alternative to the automated peristaltic pump.
4. For muscles such as the tibialis anterior or the gastrocnemius, we create cryomolds using tin foil. These tin foil molds fit perfectly in the wells of a 48-well tissue culture dish which is ideal for organization and storage. For embryos or smaller muscles, small plastic molds can be purchased.
5. For the purposes of this methods chapter, paraffin embedding and sectioning are not covered. However, resources are readily available, and many institutions have core facilities that perform paraffin embedding.
6. Deparaffinization solutions can be used multiple times but should be replaced when volumes change, as ethanol and xylene do evaporate.
7. Citrate buffer pH 6 is a standard retrieval buffer that works for many antigens; however, if an antibody does not recognize its target with conventional immunostaining, different pH and buffer combinations can be tested. When citrate buffer at pH 6 creates excessive background, try increasing to pH 7 or switching to Tris-EDTA pH 9. Reducing the pH of citrate buffer to 3 or 4 can also improve retrieval of antigens but often creates significant background signal. Generally, citrate buffer pH 6 is superior for staining of nuclear antigens [5].
8. Heat induced antigen retrieval using Tris-EDTA pH 9 buffer is effective at retrieving antigens that are not retrieved using an acidic or neutral retrieval solution. However, Tris-

EDTA can negatively impact tissue morphology, especially on frozen sections, and thus may not be suited for examining small structures. For perfusion fixed tissues, morphology is improved when the sections are fixed after thawing and before performing antigen retrieval.

9. A microwave can be used in lieu of a pressure cooker. However, we highly recommend the use of a pressure cooker if antigen retrieval is performed routinely. Most commercially available pressure cookers will work for this step.
10. Ice cold 100% methanol or acetone is an effective fixative for cryosections, and more suited to some antigens. Acetone is less harsh than methanol, and they are both precipitating fixatives. For conventional immunostaining, 4% PFA, 100% methanol or 100% acetone are applied following cryosectioning.
11. TBS or PBS can be used as wash buffers. Further, when high background is observed after immunostaining, 0.1 % Tween-20 can be added to PBS or TBS wash buffers to reduce nonspecific binding of antibodies. However, detergents can negate the effectiveness of some hydrophobic barriers, thus caution should be used to ensure slides do not dry out due to barrier failure.
12. The barrier created by the hydrophobic PAP pen (RPI, 195505) will be disrupted if reagents containing detergents like Tween-20 or Triton X-100 come into direct contact. The ImmEdge hydrophobic pen is less susceptible to solutions containing Tween 20 or Triton X-100 when applied and dried appropriately.
13. When staining mouse tissue with primary antibodies raised in mouse, add a 1:40 dilution of the Mouse on Mouse (M.O.M.) blocking reagent (Vector laboratories, MKB-2213) to

the blocking solution. Omit M.O.M. reagent when staining tissues from other species or when using antibodies raised in species other than mouse.

14. TrueBlack Lipofuscin Autofluorescence Quencher (Biotium, Cat# 23007) is a new iteration of Sudan Black that provides less background autofluoresence in the far-red channel. While TrueBlack is a lipofuscin autofluorescence quencher, it is also a good general background blocking agent. TrueBlack is particularly useful for reducing background fluorescence in the green channel when immunofluorescence staining paraffin sections. Ensure that slides do not dry out when using this reagent, as this will detrimentally impact the immunostain, and it is important not to use any reagents containing detergents (i.e. Triton X-100 or Tween 20) for the remainder of the protocol.
15. The animal serum should match species in which secondary antibodies are raised.
16. When blocking or permeabilization solutions are stored longer than one week, either add 0.02% sodium azide or freeze aliquots at -20 ℃.
17. When planning the primary antibody panel, ensure the primary antibodies are raised in different species or possess different IgG isotypes. For example, it is okay to combine a Pax7 mouse IgG1 primary antibody with a Myogenin mouse IgG2a.
18. Fluorophore selections should match the microscope configuration at your institution. For wide field epifluorescence microscopes, this depends on the light source and filter sets, while the laser and detector combinations must be considered for confocal microscopy. Many tools are available to help identify the best combination of fluorophore-conjugated secondary antibodies. FBbase is an open-source tool that lists most fluorophores and their emission and absorption spectra (https://www.fpbase.org/spectra/). Generally, we use Alexa Fluor dyes, as most are bright and photostable, and the Fisher Scientific website

provides information on stability in buffer and fluorophore brightness to dye recommendations based on your filter set and more. Alternatively, the CF dyes by Biotium offer antibody isotypes conjugated to less common fluorphores. For example, CF405 is available in goat anti-mouse IgG1, while the comparable Alexa Fluor dye is only available in goat anti-Mouse IgG. The most common panel our lab uses is DAPI, Alexa Fluor 488/546/647.

19. PermaFluor (Fisher Scientific, TA-030-FM) is our preferred mounting media, but other mounting media can be substituted. It is a good idea to note the resolution and the refractive index of your microscope objective when choosing an appropriate mounting media.
20. Ensure the 2-methylbutane begins solidifying prior to freezing the muscle tissues. If the 2-methylbutanol is not sufficiently cooled, the muscles will not freeze fast enough. This causes ice crystal to form in the tissues and can detrimentally impact tissue morphology and immunostaining.
21. When performing cardiac perfusion, an improperly placed needle can detrimentally impact fixation (i.e., if the needle perforates the right ventricle). When muscles are insufficiently fixed, immersion fix the muscle for 48 hours at 4°C prior to the sucrose gradient.
22. To improve penetration of PFA, 0.05% NP-40 can be added to the fixative overnight.
23. If tissues containing fluorescence reporters require antigen retrieval, antibodies raised against the fluorescent proteins must be included in the primary antibody panel, as heat induced antigen retrieval quenches endogenous fluorophores (see Table 2).
24. Heat induced antigen retrieval using Tris-EDTA pH 9 buffer is effective at retrieving antigens that are not retrieved using an acidic or neutral retrieval solution. However, Tris-EDTA can negatively impact tissue morphology, especially on frozen sections, and thus

may not be suited for examining small structures. For cardiac perfusion fixed tissues, morphology is improved when the sections are fixed again in 4% PFA after thawing and before antigen retrieval.

25. Fixed frozen sections can be more sensitive than paraffin sections. If sections detach or morphology is impacted, consider reducing the time in the pressure cooker. Properly dried samples rarely detach from superfrost slides.
26. When using permeabilization buffer, take care to keep the solution away from the hydrophobic barrier, otherwise it negates its hydrophobicity. If this happens, wash the slide well with PBS.
27. Controls, including secondary only and antibody isotype in lieu of primary antibodies should be included when possible. Positive and negative controls for the antigen of interest are also important when testing new antibodies or tissues.
28. We do not generally recommend incubating slides in primary antibodies for only 2-3 hours at room temperature, except for unfixed muscle tissue with MyHC antibodies.

Acknowledgments

We thank Dr. Dongsheng Duan at University of Missouri-Columbia for providing us with dog tissue. M.A.R. holds a Canada Research Chair in Molecular Genetics. These studies were carried out with the support of grants from the Canadian Institutes of Health Research [FDN-148387], the US National Institutes for Health [R01AR044031], E-Rare-3 (Canadian Institutes of Health Research/Muscular Dystrophy Canada), the Foundation for Gene & Cell Therapy, and the Stem Cell Network.

References

A1. Dumont NA, Bentzinger CF, Sincennes M-C, Rudnicki MA (2015) Satellite Cells and Skeletal Muscle Regeneration. In: Comprehensive Physiology. American Cancer Society, pp 1027–1059

A2. Mercuri E, Bönnemann CG, Muntoni F (2019) Muscular dystrophies. The Lancet 394:2025–2038. https://doi.org/10.1016/S0140-6736(19)32910-1

A3. Bentzinger CF, Wang YX, Rudnicki MA (2012) Building Muscle: Molecular Regulation of Myogenesis. Cold Spring Harbor Perspectives in Biology 4:a008342–a008342. https://doi.org/10.1101/cshperspect.a008342

A4. Feige P, Rudnicki MA (2020) Isolation of satellite cells and transplantation into mice for lineage tracing in muscle. Nat Protoc 15:1082–1097. https://doi.org/10.1038/s41596-019-0278-8

A5. Shi SR, Imam SA, Young L, et al (1995) Antigen retrieval immunohistochemistry under the influence of pH using monoclonal antibodies. J Histochem Cytochem 43:193–201. https://doi.org/10.1177/43.2.7822775

Tissue Processing and Immunostaining Workflow

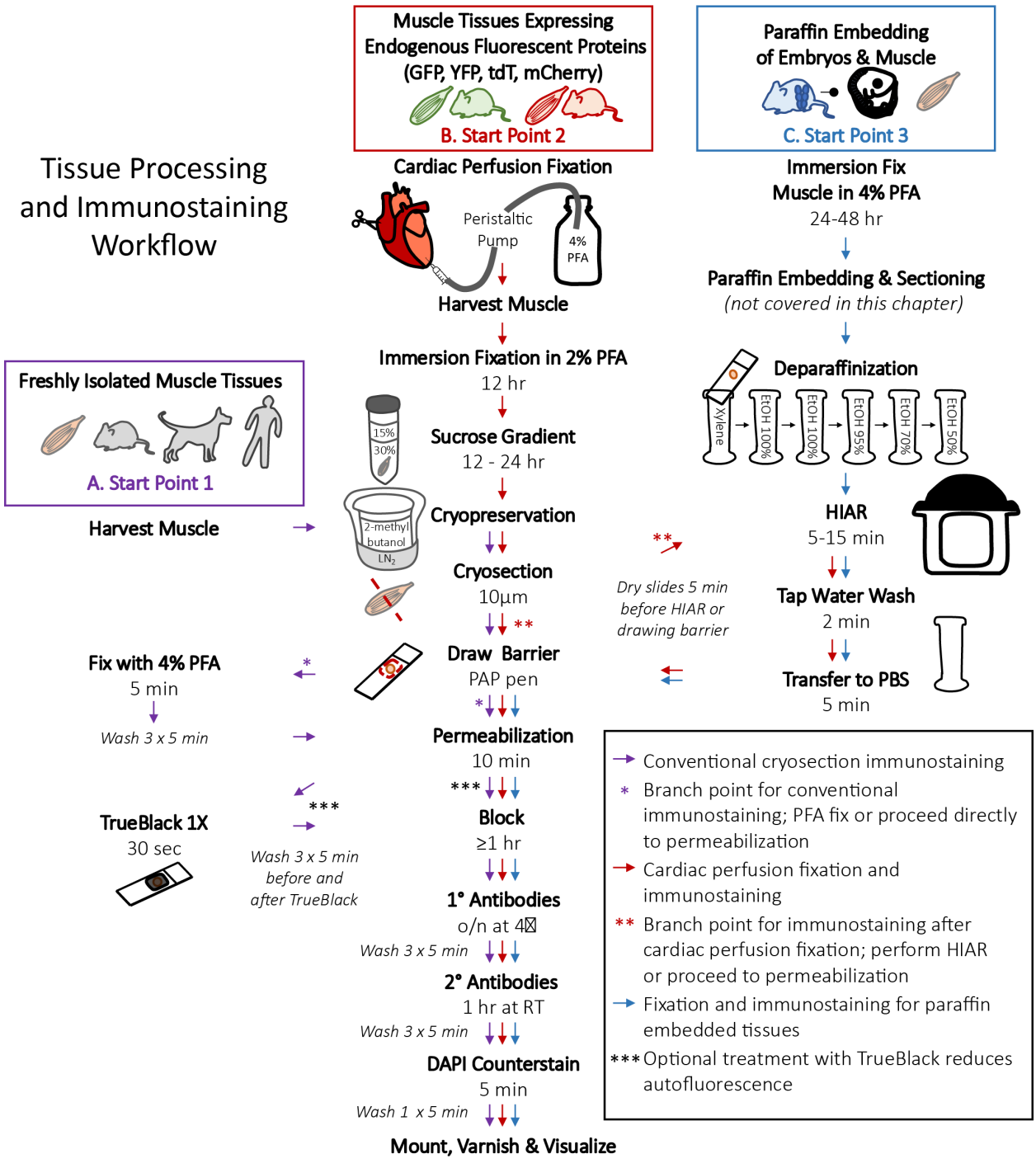

Fig. A1 Schematic representation of the workflow for myogenic tissue processing and immunofluorescence staining.
(**A**) Begin from Start Point 1 to process fresh tissue for immunostaining (purple arrows). After surrounding tissues with the hydrophobic barrier, PFA-fixation can be omitted for antigens that are highly sensitive to formaldehyde (purple asterisk). (**B**) The processing and immunostaining of muscle that requires cardiac perfusion fixation begins at Start Point 2 (red arrows). Heat Induced Antigen Retrieval (HIAR) is not always required for perfusion fixed tissues but is necessary for some primary antibodies (red asterisks). (**C**) Select Start Point 3 for fixing tissues prior to paraffin embedding and for the subsequent immunostaining of paraffin embedded tissue sections. HIAR is almost always recommended when immunostaining paraffin embedding tissues. Treating tissues with TrueBlack is optional but particularly useful for quenching autofluorescence in the green channel (triple asterisks). Start points A-C correspond to Table 1.

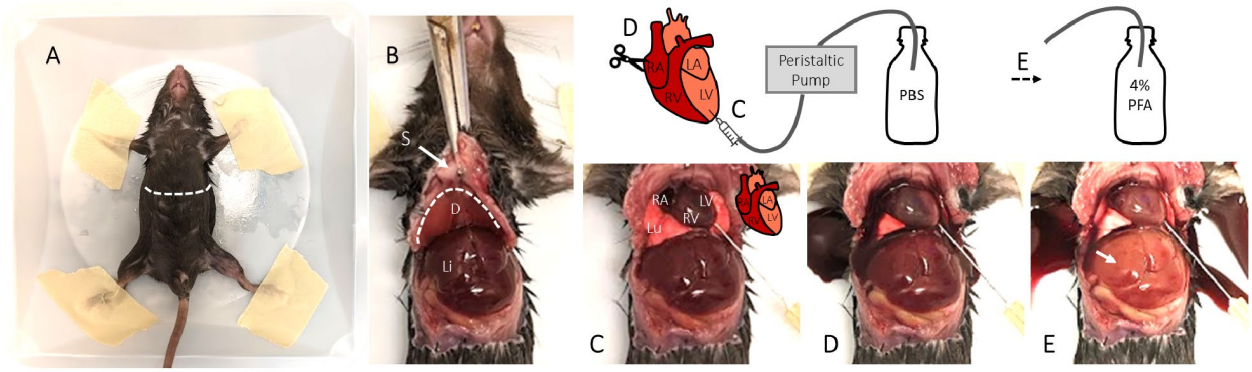

Fig. A2 Visual guide for cardiac perfusion fixation of mice.
(**A**) Following euthanasia, affix the mouse to a weighing dish using masking tape. (**B**) Make a lateral incision below the sternum and rib cage to expose the diaphragm and liver. Cut back the diaphragm using Vannus spring scissors and expose the plural cavity and heart. (**C**) Identify the left ventricle and insert the needle bevel. (**D**) Create a small incision in the right atrium and turn on the peristaltic pump to flush the circulatory system with PBS. (**E**) Once the blood has cleared from the circulatory system and the liver has lightened, switch the tubing to collect 4% PFA. Sternum (S), diaphragm (D), liver (Li), lung (Lu).

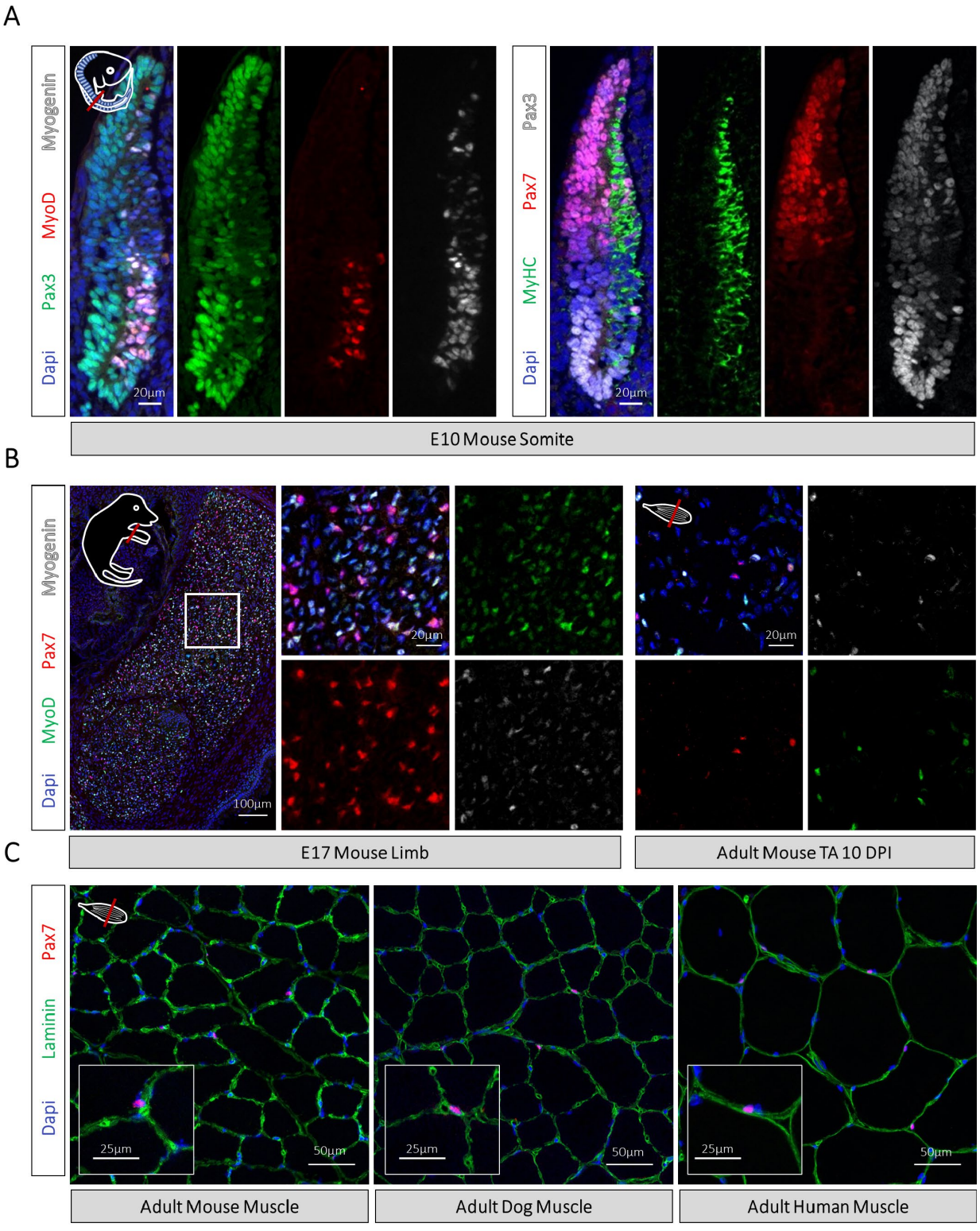
A
Dapi
Pax3
MyoD
Myogenin
20µm
Dapi
MyHC
Pax7
Pax3
20µm
E10 Mouse Somite
B
Dapi
MyoD
Pax7
Myogenin
100µm
20µm
20µm
E17 Mouse Limb
Adult Mouse TA 10 DPI
C
Dapi
Laminin
Pax7
25µm
50µm
25µm
50µm
25µm
50µm
Adult Mouse Muscle
Adult Dog Muscle
Adult Human Muscle

Fig. A3 Immunofluorescence staining of myogenic cells.
(A) Visualization of myogenic cells in E10.5 murine embryos following deparaffinization and antigen retrieval in citrate buffer pH6 for 10 min. Corresponds to Start Point 3, Fig A1. Images taken with widefield Zeiss D1 microscope (B) Immunostaining of myogenic cells on fresh frozen E17.5 mouse embryo limbs and adult muscle following 4% PFA fixation and blocking with M.O.M. blocking reagent. Corresponds to Start Point 1, Fig A1. (C) Immunostaining of Pax7 muscle stem cells on fresh frozen mouse, dog, and human tissues following tissue fixation in 4% PFA. Corresponds to Start Point 1, Fig A1. Days post injury (DPI). Images acquired on an LSM900 confocal microscope.

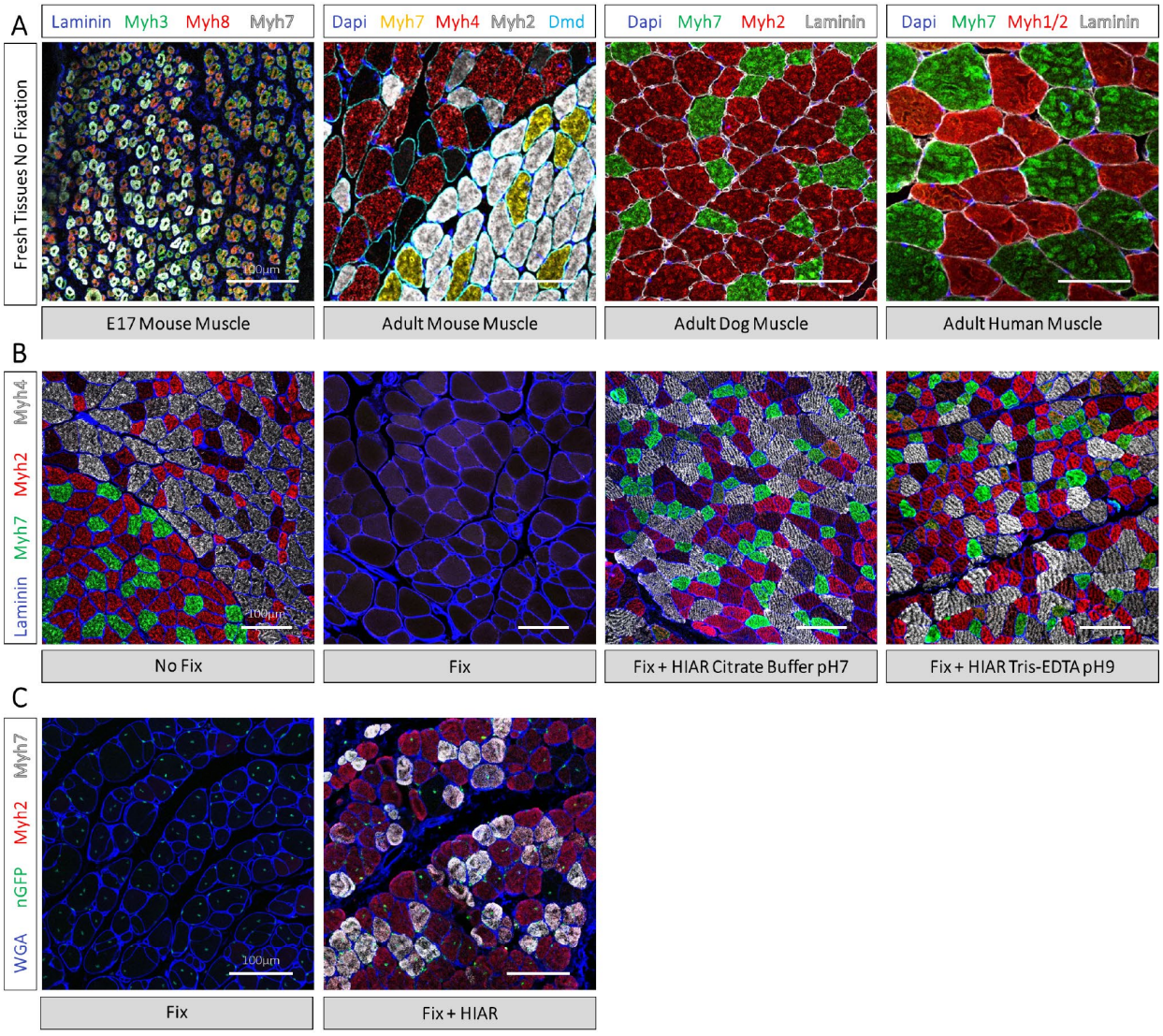

Fig. A4 Visualization of musclefibre type by immunofluorescence histochemistry.
(**A**) Immunostaining of Myosin Heavy Chain isotypes on E17 and adult mouse, adult dog, and adult human muscle with no formaldehyde fixation. Corresponds to Start Point 1, Fig A1. (**B**) Myosin Heavy Chain immunostaining of adult mouse tissue without formaldehyde fixation, after cardiac perfusion fixation, and after cardiac perfusion fixation with heat induced antigen retrieval (HIAR) in Citrate buffer pH7 and Tris-EDTA pH9 for 10 min. Corresponds to Start Point 2, Fig A1. (**C**) Myosin Heavy Chain immunostaining of recipient mouse tissue 28 days after muscle stem cell transplantation. Cardiac perfusion fixation preserves donor cell nuclear GFP expression but masks the Myosin Heavy chain epitope (left). Cardiac perfusion fixation followed by HIAR in Tris-EDTA pH9 and immunostaining with a GFP antibody highlights transplanted myofibers and musclefibre type (right). Corresponds to Start Point 2, Fig A1. Images taken with comparable laser intensity and master gain by confocal microscopy on the LSM900. All scale bars represent 100 µm.

6.4 Academic Summary

Education

PhD in Cellular and Molecular Medicine, University of Ottawa 2025

- Supervisor: Dr. Michael A. Rudnicki, Ottawa Hospital Research Institute

MSc in Cellular and Molecular Medicine, University of Ottawa 2019

- Transferred to PhD program from MSc

BSc (honours) in Translational and Molecular Medicine, University of Ottawa 2019

- *Summa Cum Laude*; Dean's honour list

BSc (honours) in Human Kinetics, University of Ottawa, Ottawa ON 2015

- *Magna Cum Laude*; Dean's honour list

Publications and Works in Progress

- **Esper ME**, Lin AYT, Bennett B, Rudnicki MA. (2025). Lack of dystrophin disrupts fetal muscle stem cell polarity and commitment during secondary myogenesis. *Nat Comm*. Revisions requested.
- **Esper ME***, Brun CE*, Lin AYT, Feige F, Catenacci M, Sincennes MC, Ritso M, Rudnick MA. Intrinsic Muscle Stem Cell Dysfunction Contributes to Impaired Regeneration in the *mdx* Mouse. *Journal of Cachexia, Sarcopenia and Muscle*. 2025;16(1):e13682.

  *Contributed equally to this work.
- Gurriaran-Rodriguez U, Datzkiw D, Radusky LG, **Esper ME**, Javandoost E, Xiao F, Ming H, Fisher S, Marina A, De Repentigny Y, Kothary R, Azkargorta M, Elortza F, Rojas AL, Serrano L, Hierro A, Rudnicki MA. Identification of the Wnt signal peptide that directs secretion on extracellular vesicles. *Sci Adv*. 2024 Dec 13;10(50):eado5914.
- **Esper ME**, Saber J, Rudnicki MA. (2025). Satellite cells in Regeneration and Disease. Muscle Biology; *Cold Spring Harbor Perspectives*. Submitted.
-

- Lin AYT, Ancel S, **Esper ME**, Ritso M, Hernández-Hernández JM, Bentzinger CF, Stuelsatz P, Tsai1 EC, Feige JN, Rudnicki MA. (2025). Identification of long term self-renewing muscle stem cells characterized by low metabolic requirements. Manuscript in preparation.
- **Esper ME,** Kodippili K, Rudnicki MA. Immunofluorescence Labeling of Skeletal Muscle in Development, Regeneration, and Disease. *Methods Mol Biol*. 2023;2566:113-132.
- **Esper ME**, Lin YTA, Brun CE, Rudnicki MA. *Myf5*-expressing muscle stem cells have greater propensity to form oxidative myofibers. *Ongoing research.*

Conference Presentations

- Gordon Myogenesis Conference | Lucca, Italy | 2025
- Till & McCulloch Meetings, Annual | Vancouver, Toronto, Montreal, Canada | Poster | 2021-2024
- Ottawa Hospital Research Institute Research Day | Ottawa, Canada | Poster | 2019-2024
- Frontiers in Myogenesis Conference | São Paulo, Brazil | Seminar | 2023

Awards and Recognitions

- Stem Cell Network Travel Award, 2024 Till & McCulloch Meeting
- Queen Elizabeth II graduate scholarships in science and technology (QEII - GSST), 2024-2025
- Poster Presentation Award, 1st place, OHRI research day, 2023
- Stem Cell Network Travel Award 2023 Till & McCulloch Meeting
- Ontario Graduate Scholarship (OGS), 2023-2024
- Stem Cell Network Travel Award, 2022 Till & McCulloch Meeting
- Queen Elizabeth II graduate scholarships in science and technology (QEII - GSST), 2022-2023
- Queen Elizabeth II graduate scholarships in science and technology (QEII - GSST), 2021-2022
- Poster Presentation Award, 2nd place, CMM Research Day, 2021

- Canada Graduate Scholarship-Masters (CGS M), Canadian Institute of Health Research, 2019-2020
- PhD Admissions Scholarship, University of Ottawa, 2020-2025
- Excellence Scholarship, University of Ottawa, 2020
- Masters Admissions Scholarship, University of Ottawa, 2019